Computational Structural Analysis as a Tool
Develop Valved Stent Applications and Techn

Silvia Schievano

Submitted for the degree of Doctor of Philosophy
of the University of London

London, February 2008

ProQuest LLC
789 East Eisenhower Parkway
P.O. Box 1346
Ann Arbor, MI 48106-1346

If I have seen farther than others,
it is because I was standing on the shoulders
of giants.

Sir Isaac Newton

DECLARATION OF ORIGINALITY

The contents of this thesis are original material, except where indicated in the text for illustrations and background material recreated from referenced sources.

This thesis is solely my own work, except where indicated in the case of work done in collaboration with others, in particular:

- Percutaneous pulmonary valve implantations were performed by Prof. Philipp Bonhoeffer, Dr Younes Boudjemline and Dr. Sachin Kambadkone;
- Echocardiogram examinations were carried out by Dr. Sachin Kambadkone, Dr. Louise Coats, Dr. Johannes Nordmeyer and Dr. Philipp Lurz;
- Magnetic resonance images were performed by Dr. Andrew Taylor;
- Rapid prototyping models were built by Dr. Giuseppe Sala, Silvio Ferragina and Antonio Armillotta from the Aerospace and Mechanical Engineering Departments of Politecnico di Milano, Milan – Italy;
- Design of Experiment analyses were designed with engineers from Medtronic, Inc. – USA.

Silvia Schievano

ABSTRACT

Percutaneous pulmonary valve implantation is an innovative technique for the treatment of right ventricular outflow tract dysfunction. This procedure is available for a limited group of patients with very specific anatomy. Finite element analyses, together with computer aided design technology and imaging processing software, were used in this study to broaden the range of patients who might benefit from this procedure.

Three-dimensional reconstruction of patient right ventricular outflow tracts, derived from magnetic resonance data, was performed by image elaboration to assess the implantation site anatomy. A morphological classification was created to analyse the criteria for percutaneous pulmonary valve implantation subject selection. Physical models of the right ventricular outflow tracts from patients with borderline anatomy for percutaneous procedure were built using the rapid prototyping technique. These models provided a complete appreciation of the three-dimensional anatomy and aided patient selection for percutaneous pulmonary valve implantation more accurately than magnetic resonance images. Moreover, they enabled trial implantation of devices to test their deployment and anchoring force into the right ventricular outflow tract.

Computer aided design models of different stents were created: the early generation device employed for percutaneous pulmonary valve implantation, the device currently in use and a new possible stent design made of nitinol. Virtual simulation of the inflation of these devices was performed using the finite element method to study the mechanical behaviour and risk of fracture in these devices. The stress and strain distributions were evaluated to numerically compare the performance of the first generation device, with the current stent. A finite element model of a selected patient right ventricular outflow tract was created to computationally investigate the stent/implantation site interaction. Finite element analyses aided the optimisation of a nitinol ring to be employed in the next generation stent.

ACKNOWLEDGEMENTS

First and foremost, I would like to thank the patients who took part in the studies which constitute much of the thesis and the British Heart Foundation for providing financial support to this research.

I would like to acknowledge the following people for their support and advice during my work at GOSH: Philipp Bonhoeffer, who has provided me with expert guidance, brilliant ideas, constructive criticism, food and moral support throughout; Andrew Taylor, for his continued advice and for proof reading my final manuscript and pretty much everything else (except probably for these acknowledgements!); Francesco Migliavacca, Lorenza Petrini and Gabriele Dubini, who pioneered the biomedical engineering research at GOSH and have provided invaluable inputs to this study; and Louise Coats, for her friendship and emotional support.

Furthermore, I would like to thank the other members of the PPVI team, who have supported my work and life during these 3 years: Sachin Khambadkone, Younes Boudjemline, Romana Pedrali, Giovanni Parenzan, Tracey Humphreys, Twin Yen Lee, Johannes Nordmeyer, Philipp Lurz, Pauline Whitmore, Vivek Muthurangu and Michael Hansen. Without your help this thesis would not have been possible.

I am also grateful to 3 friends, amongst many, who have shared the GOSH experience with me: Angelo, for his unconditional help, Savi, for her cheerful friendship, and Jacob, for his English lessons and for tolerating my OCD tidiness in the 'research café'.

A huge and sincere "thank you!" goes to all those 'persons' who have filled up the rest of my London life with their indispensable friendship; especially, I would like to credit Ferdinando, Sarah, Alessandro and Nausicaa for keeping me sane!

Last, but by no means least, I would like to thank (in Italian) my family, without whom none of this would have been possible: grazie per il vostro supporto morale e incondizionato affetto. Quello che sono oggi lo devo soprattutto a voi.

CONTENTS

LIST OF FIGURES

LIST OF TABLES

LIST OF ABBREVIATIONS

1D	One-dimensional
2D	Two-dimensional
3D	Three-dimensional
AP	Antero-posterior
ASD	Atrial Septal Defect
CAD	Computer Aided Design
CT	Computerized Tomography
DOE	Design Of Experiments
ECG	Electrocardiogram
FDM	Fused Deposition Modelling
FE	Finite Element
FSF	Fatigue Safety Factor
MR	Magnetic Resonance
PA	Pulmonary Artery
PDE	Partial Differential Equations
PFO	Patent Foramen Ovale
PPVI	Percutaneous Pulmonary Valve Implantation
RF	Regurgitant Fraction
RP	Rapid Prototyping
RV	Right Ventricle

RVOT	Right Ventricular Outflow Tract
SMA	Shape Memory Alloy
SSFP	Steady State Free Precession
STL	Solid To Layer
TE	Echo Time
TR	Repetition Time
VSD	Ventricular Septal Defect

CHAPTER 1

INTRODUCTION

1.1 INTRODUCTION

Biomedical engineering is the application of engineering principles and techniques to the medical field. It combines the design and problem solving skills of engineering with the medical and biological sciences, to help improve patient health care and the quality of life of individuals. As a relatively new discipline, much of the work in biomedical engineering consists of research and development, covering an array of fields: bioinformatics, medical imaging, image processing, physiological signal processing, biomechanics, biomaterials, systems analysis, etc. Examples of concrete applications of biomedical engineering are the development and manufacture of biocompatible prostheses, medical devices, diagnostic devices, pharmaceutical drugs, and imaging equipment.

Biomechanics is the branch of biomedical engineering that researches and analyses the mechanics of living organisms or the application and derivation of mechanical engineering principles to and from biological systems [1,2]. The research and analysis can be carried forth on multiple levels, from the molecular all the way up to the tissue and organ level. By applying the laws of mechanics and concepts of physics to human biological functions and performance, biomechanics science studies, models, simulates, and measures human mechanisms and structures.

In the cardiovascular field, biomechanics seeks to understand how the composition, structure, electrical activation, geometry, and hemodynamic environment of the heart interact to produce known physiological behaviour, and to apply this knowledge to understand and modify pathophysiological responses that arise as various disease processes affect the heart [3-6]. In this context, biomechanics research aims to: develop theoretical, computational, and experimental methodologies to quantify anatomical structure and physiological responses of the cardiac system under normal, diseased, and surgically-altered states; implement methods for improving vascular disease diagnosis, surgical planning, and prosthesis design; and create transferable technology for use by medical professionals and disseminate results to scientific and medical communities.

1.2 BIOMECHANICS IN THE THESIS

In this research, the principles of biomechanics have been applied to the study of percutaneous pulmonary valve implantation (PPVI), a new, non-surgical technique of heart valve replacement, developed in the late 1990's by Professor Philipp Bonhoeffer. This technique was based on the concept that a heart valve sewn inside a stent could be reduced in size by crimping it onto a balloon catheter, and then introduced through a peripheral vessel to the desired implantation site in the heart. Inflation of the balloon would deploy the valved stent and anchor it within the old dysfunctional valve. This simple principle has formed the basis for a successful clinical programme, which to date has treated more than 400 patients with dysfunction of the pulmonary valve and represents the largest experience of percutaneous valve implantation in the world.

My research, which is sponsored by the British Heart Foundation [BHF Fellowship FS/05/039], started during the initial phases of PPVI clinical applications. It focuses on two key points related to this interventional technique: the implantation site and the device. The interaction between these two components determines the success of the procedure, but also defines the limits of its clinical application. Indeed, the device is only suitable for patients with specifically defined anatomy and patient selection is critical both to ensure procedural success and to optimise long-term treatment outcome, thus avoiding stent fracture, a common complication observed in our population.

For the purpose of this research, a broad range of different techniques and methodologies has been employed: magnetic resonance (MR) imaging to collect implantation site morphological information; image processing tools to define three-dimensional (3D) volumes and dimensions of patient right ventricular outflow tracts (RVOTs); rapid prototyping (RP) techniques to build realistic, physical models of the implantation sites; finite element (FE) modelling for the study of stent mechanical behaviour; computer aided design (CAD) software, along with biplane fluoroscopy images, for the assessment of stent shape and deformations post-implantation; and Design of Experiment (DOE) tool to analyse the parameters involved in the mechanical performance of a new possible shape memory alloy (SMA) stent for PPVI.

1.3 AIMS AND OBJECTIVES

The aim of this research is to improve the success of PPVI and to extend the percutaneous approach treatment to a wider patient population.

The objectives of the research presented herein are:

- To thoroughly categorise patients' RVOTs for a better understanding of the implantation site morphology and dimensions.
- To identify characteristic sub-groups that can be used for better patient selection and that can guide future device design for PPVI.
- To create physical models of the implantation site to aid the cardiologist's decision and that can be used to test new PPVI devices.
- To analyse the current PPVI stent mechanical performance in terms of short- and long-term fracture.
- To establish the real loading conditions of the stent once implanted into the RVOT.
- To investigate the feasibility of stent/implantation site interaction analysis using the FE method.
- To optimise the design of a SMA ring to be employed in the next generation of PPVI device.

1.4 OUTLINE OF THE THESIS

The remainder of this thesis is organized in the following way.

Chapters 2 to 5 are introductory to the thesis: Chapters 2 and 3 provide a clinical background to the problem, whilst Chapters 4 and 5 describe the main technical tools used for the purpose of this thesis. Specifically, Chapter 2 briefly reviews the most common congenital heart disease conditions encountered in the patients who are referred to our centre for PPVI, and introduces the clinical problem that is the subject of this research: RVOT dysfunction. Chapter 3 focuses on the PPVI procedure, its development since the first human application and the clinical outcomes of the current experience. This chapter also introduces the complications incurred in PPVI to date, in particular stent fracture. This problem is a technical challenge for the engineering development of the PPVI device and the understanding of fracture in PPVI is one of the central subjects of my thesis. Moreover, Chapter 3 underlines the limitations of the current device in relation to the dimensions of those RVOT which are unsuitable for the

current percutaneous treatment. Patient selection for PPVI plays a key role in the success of the procedure; refining and enhancing the process of RVOT assessment is one of the main goals of my research. Chapter 4 centres upon the use of MR imaging for the assessment of patients pre- and post-PPVI. The data resulting from these clinical investigations are a fundamental input for the development of this research. Chapter 5 provides a brief description of the numerical principles that form the basis of the FE method. This computational technique is used in this thesis to study the mechanical performance of the current PPVI stent in comparison with new devices which are different in material and design properties.

Chapters 6 and 7 focus on the implantation site. Chapter 6 describes a retrospective analysis of the origin and nature of RVOT morphologies and dimensions that develop after surgical repair of congenital heart disease. Chapter 7 introduces the use of RP methodologies to establish the precise morphology of the implantation site in borderline PPVI cases for a more accurate selection of patients. The outcomes of the RVOT morphological analysis help to identify criteria for better patient selection and to outline the necessary requirements for the design of future PPVI devices.

Chapter 8 centres upon the current device for PPVI and the understanding of its mechanical properties, in particular elastic recoil, radial strength and fracture resistance in static and cyclic loading conditions. In this chapter, an innovative solution to reduce the rate of device fracture and increase the success of the percutaneous procedure, without compromising its technical ease, is described. A comparison between the early generation device, the current stent, and an innovative multi-element device is carried out. The results of this study give indications towards a better understanding of the stent mechanical properties and fracture site. However, the main limitation of this comparison in Chapter 8 is the absence of the RVOT boundary. This problem and a solution to the study of the device *in-situ* are presented in the next chapter.

Chapter 9 analyses the interactions between the device and the implantation site, from angiographic data using FE modelling. Biplane fluoroscopy data are used to reconstruct the 3D shape and deformations of the device *in-situ*. The FE model of the interaction between device and implantation site exploits the feasibility of contact problem analyses in FE codes and accounts for more realistic loading conditions of the device. The results obtained from the implantation of the stent into a realistic RVOT are

compared with the free expansion of the device. The non-uniform deployment of the stent in the implantation site situation significantly influences its mechanical performance.

Chapter 10 introduces a new design for a PPVI stent made of SMA. The peculiar behaviour of SMA materials is explained and modelled in FE, as well as the different loading phases that a nitinol stent is subjected to. An optimal stent ring to be employed in the peripheral part of this new device is proposed from the result of the DOE analysis based on 9 possible different designs. The next generation stent, made of optimized nitinol rings, may be able to treat a wider range of RVOTs, especially those which present large diameters and distensible properties.

Chapter 11 summarizes the results of this thesis and outlines a number of remaining research issues, which have been identified as areas for future work.

CHAPTER 2

RIGHT VENTRICULAR OUTFLOW TRACT DYSFUNCTION

Congenital heart disease is a defect of the heart that exists primarily at birth. It is common, affecting about 1% of all live births. Nowadays, due to excellent advancements in cardiac surgery, 85% of children born with congenital cardiac defects survive into adult life, leading normal or relatively normal lives. However, in many patients, surgical treatment is only palliative. In particular those patients who require pulmonary valve related surgery (including those who have insertion of a conduit) develop pulmonary valve dysfunction – regurgitation and/or stenosis – associated with detrimental clinical sequelae. This has led to an increasing proportion of patients requiring operative replacement of the stenosed and/or regurgitant pulmonary valve in later life. At present, this is performed surgically with the concomitant complications and serious risks associated with open heart surgery. Sometimes, in the setting of the RVOT obstruction, bare metal stenting is performed to prolong conduit lifespan. However this causes free pulmonary regurgitation with detrimental effects on right ventricular function and risk of arrhythmia. As a result, the majority of patients with repaired congenital heart disease undergo multiple open-heart operations. In this context, a new technique of non-surgical valve implantation for the treatment of pulmonary valve dysfunction has recently been introduced into clinical practise: PPVI.

2.1 INTRODUCTION

This chapter provides a brief description of the normal cardiovascular system in adults and fetuses, and the abnormalities that can develop during the fetal gestation, called congenital heart disease. In particular, the most recurrent congenital heart diseases seen in the patients who are referred as potential candidates for PPVI are described in Section 2.4. The most common complications and recent findings about RVOT dysfunction post cardiac surgery are documented, with relevant references, in Section 2.5. A concise overview of the current treatment alternatives for these dysfunctions is presented in Section 2.6. Percutaneous pulmonary valve implantation is exhaustively described in the next chapter (Chapter 3). The illustrations of this chapter have been adapted from Everett AD, *et al.* [7].

2.2 THE NORMAL HEART

The normal human heart is a hollow muscular organ that receives blood from the veins and pumps it into the arteries. It is divided by muscular walls (septae) into two halves, right and left, each of which is subdivided into two chambers (Figure 2.1). The upper chambers – atria – receive blood and pass it on to the lower chambers – ventricles – which then pump it out of the heart.

The left atrium receives freshly oxygenated (red in the illustrations) blood from the lungs. This blood passes through the mitral valve and enters the left ventricle (LV), which is the heart's main pumping chamber. It propels the red blood through the aorta to the arterial system, which carries it to the body's tissues. The coronary arteries depart from the root of the aorta and carry blood for the nourishment of the heart itself.

After delivering its supply of oxygen and picking up waste materials along the way, the blood (blue in the illustrations), deoxygenated, enters the venous system and is carried back to the heart. The blood from the lower body enters the right atrium through the vein known as the inferior vena cava; the blood from the upper body enters the right atrium through the superior vena cava. The right atrium also receives flow of deoxygenated blood from the coronary sinus.

The right atrium passes the blood through the tricuspid valve into the right ventricle (RV), which pumps it into the pulmonary artery (PA). The PA divides into two

branches that carry the blood to the lungs. After releasing carbon dioxide as waste material and absorbing a fresh supply of oxygen, this blood is carried back to the left atrium of the heart by four pulmonary veins and the cycle continues.

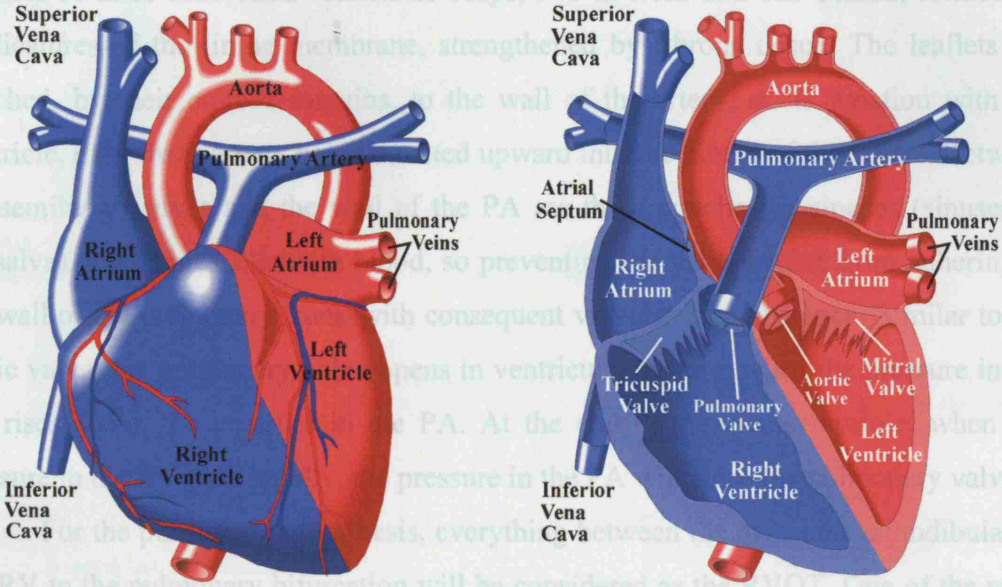

Figure 2.1 External and internal, frontal views of the normal heart. The red and blue colours denote the presence of oxygenated and de-oxygenated blood respectively.

2.2.1 The Pulmonary Artery

The PA conveys the venous deoxygenated blood from the RV of the heart to the lungs. In the human heart, the main PA or pulmonary trunk is a short, wide vessel, about 5 cm in length and 3 cm in diameter, arising from the RV. It extends obliquely upward and backward, passing at first in front and then to the left of the ascending aorta, as far as the under surface of the aortic arch, where it divides into right and left branches of nearly equal size. The right branch of the PA, longer and larger than the left, runs horizontally to the right, behind the ascending aorta and superior vena cava and in front of the right bronchus, to the root of the right lung, where it divides into two branches. The lower and larger of these goes to the middle and lower lobes of the lung; the upper and smaller is distributed to the upper lobe. The left branch of the PA, shorter and somewhat smaller than the right, passes horizontally in front of the descending aorta and left bronchus to the root of the left lung, where it divides into two branches, one for each lobe of the lung.

The pulmonary valve is the semilunar valve of the heart that lies between the RV and the PA. It lies slightly antero-superior to the aortic valve at the superior end of the RV. The diameter of the valve is 2-3 cm at its annulus. The pulmonary valve consists of three semi-lunar leaflets or cusps, two in front and one behind, formed by duplicatures of the lining membrane, strengthened by fibrous tissue. The leaflets are attached, by their convex margins, to the wall of the artery, at its junction with the ventricle, their free borders being directed upward into the lumen of the vessel. Between the semilunar valves and the wall of the PA are three pouches or sinuses (sinuses of Valsalva). Each sinus fills with blood, so preventing the valve leaflet from adhering to the wall of the pulmonary trunk with consequent valvular incompetence. Similar to the aortic valve, the pulmonary valve opens in ventricular systole, when the pressure in the RV rises above the pressure in the PA. At the end of ventricular systole, when the pressure in the RV falls rapidly, the pressure in the PA will close the pulmonary valve.

For the purposes of this thesis, everything between the muscular infundibular of the RV to the pulmonary bifurcation will be considered as the RVOT. One of the main reasons for choosing this term is that it can also be used to describe those patients who have been treated surgically with either homografts or conduits.

2.3 THE FETAL HEART

The circulatory system of an unborn infant, or fetus, functions differently from that of a baby after birth (Figure 2.2) or an adult. The most significant difference is that, while a baby after birth acquires oxygen from its lungs, a fetus derives oxygen from its mother through the placenta. Oxygenated blood travels from the placenta to the fetus's heart (inferior vena cava and right atrium) by way of the umbilical vein (ductus venosus). The heart structure of the fetus differs from the normal postnatal heart in that there is an opening in the atrial septum called the foramen ovale. This allows most of the blood that enters the right atrium to flow straight into the left atrium instead of into the RV. From the left atrium, the oxygenated blood is pumped into the LV and into the aorta, which carries it to the body tissues. From there, it returns to the placenta via the umbilical arteries. Deoxygenated blood returning via the superior vena cava is preferentially directed across the tricuspid valve and into the RV. The RV pumps this blood into the pulmonary arteries, and across the patent ductus arteriosus into the

descending aorta. The lungs in a fetus are non-functional and filled with fluid. The presence of this fluid makes the lungs resistant to the flow of blood into them and, therefore, they receive only enough blood for their own nourishment.

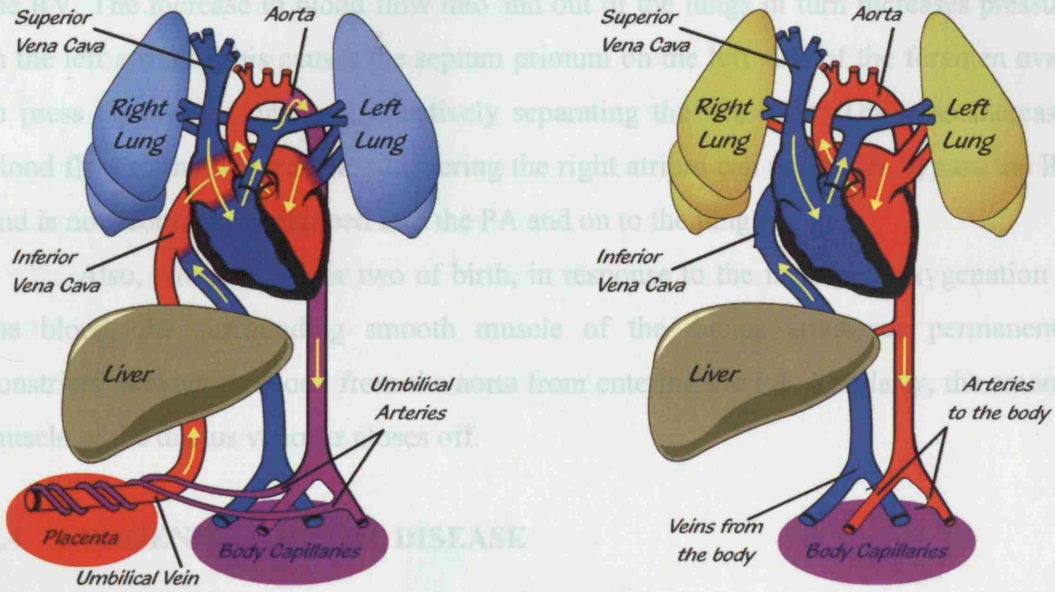

Figure 2.2 Fetal and normal post-natal circulation.

2.3.1 Shunts in Fetal Circulation

In summary there are 4 unique structures that differentiate the fetal circulatory system from the normal circulation: placenta, ductus venosus, foramen ovale and ductus arteriosus.

The ductus venosus shunts oxygenated blood from the umbilical vein to the inferior vena cava, bypassing the liver.

The foramen ovale is formed by a flap of tissue, called septum primum, that is pushed open by the flow of blood from the right to the left atrium. Oxygenated blood from the ductus venosus is directed toward the foramen ovale, and into the left heart. This shunts the blood with the highest oxygen content to the left heart for perfusion of the coronary arteries and brain. From the left atrium, the oxygenated blood is pumped into the LV and into the aorta, which carries it to the body.

The ductus arteriosus connects the PA to the aorta. This ductus shunts deoxygenated caval blood from the RV to the descending aorta bypassing the non-aerated lungs.

2.3.2 Postnatal Changes

At birth, a dramatic change in the circulatory pattern occurs. The lungs inflate decreasing pulmonary vascular resistance, which tends to draw blood into them from the RV. The increase in blood flow into and out of the lungs in turn increases pressure in the left atrium. This causes the septum primum on the left side of the foramen ovale to press against the opening, effectively separating the two atria. This also increases blood flow to the lungs as blood entering the right atrium can no longer bypass the RV and is now completely pumped into the PA and on to the lungs.

Also, within a day or two of birth, in response to the increased oxygenation of the blood, the surrounding smooth muscle of the ductus arteriosus permanently constricts, preventing blood from the aorta from entering the PA. Similarly, the smooth muscle of the ductus venosus closes off.

2.4 CONGENITAL HEART DISEASE

Congenital heart disease occurs when the heart or blood vessels near the heart do not develop properly before birth. Therefore, the heart does not pump because it is not completely developed. Also, the blood flow is obstructed in the heart by the undeveloped vessels nearby, causing an abnormal flow of blood through the heart. Blood flow obstructions put a strain on the heart muscle causing the heart to work harder and beat faster. For example, if the foramen ovale remains open (patent foramen ovale, PFO) or if the ductus arteriosus remains open (patent ductus arteriosus), heart failure may occur.

Current knowledge about the causes of congenital heart disease is scanty and largely based on small studies (<1,000 patients). Potential identified factors include environmental factors, such as chemicals, drugs, or infection, and genetic factors. Though many patients with congenital heart disease do not have an underline genetic syndrome, progress in the field of gene identification will undoubtedly reveal the genetic make-up of congenital heart diseases in the future.

Congenital heart disease can describe a wide variety of different abonrmalities. The most recurrent congenital heart diseases encountered in the patients who are referred to our centre for PPVI have been described in the following paragraphs.

2.4.1 Tetralogy of Fallot

The commonest cyanotic congenital heart disorder is tetralogy of Fallot which accounts for 10% of the cases of congenital heart disease, affecting boys and girls equally. It has been described as 4 cardiac anomalies (Figure 2.3):

- A large malalignment ventricular septal defect (VSD).
- Stenosis of the RVOT (infundibular stenosis) with associated pulmonary valve stenosis. The severity of the RVOT obstruction may vary from localised sub-valvular obstruction to atresia of the pulmonary trunk.
- The aorta is enlarged and displaced to the right such that it overrides the VSD.
- RV hypertrophy.

A right-sided aortic arch is present in a quarter to a third of patients. Patients may also have an atrial septal defect (ASD).

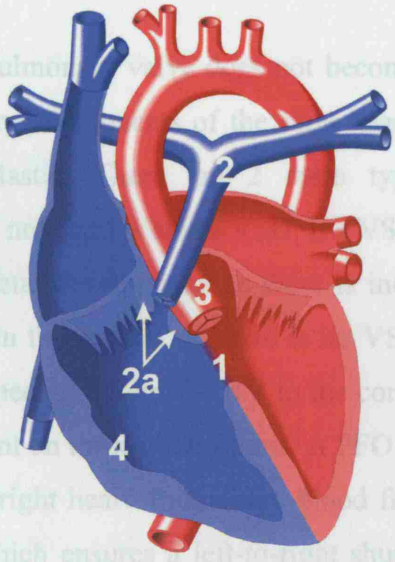

Figure 2.3 Tetralogy of Fallot: 1. VSD; 2. Stenotic pulmonary valve and artery; 2a. Infundibular stenosis; 3. Enlarged aorta overriding VSD; 4. RV hypertrophy.

The degree of cyanosis in tetralogy of Fallot is largely dependent on the degree of pulmonary stenosis. Infants with minimal stenosis may have a large left to right shunt across the VSD and may have little to no cyanosis, while infants with severe stenosis of the PA will be severely cyanotic, with ductal dependent pulmonary blood flow.

Thus at birth, the predominant dysfunction of the RVOT is one of obstruction, involving either the muscular infundibulum, and/or the PV, and/or the proximal branch

PAs. After birth, severely cyanotic infants require drug treatment to maintain ductal patency and pulmonary perfusion. To provide adequate pulmonary blood flow to the lungs, in selected cases, a modified Blalock-Taussing shunt may be performed. This palliative procedure involves interposing a graft between the innominate or subclavian artery and the right or left PA. Complete surgical repair of tetralogy of Fallot is indicated between 4-6 months of age, or with progression of cyanosis. The principles of repair of tetralogy of Fallot are closure of the VSD and provision of a less obstructed blood flow from the RV to the pulmonary arteries. This latter goal is accomplished by resection of obstructing infundibular muscle bands and RVOT patch reconstruction as necessary. Therefore, immediately following this surgical correction, infants are often left with no pulmonary valve function. Thus, the dysfunction of the RVOT is now predominately one of incompetence.

2.4.2 Pulmonary Atresia

In pulmonary atresia, the pulmonary valve does not become patent (Figure 2.4). As a result, the other two primary components of the right heart, the RV and the tricuspid valve, are usually hypoplastic. There are 2 main types of pulmonary atresia, distinguished by whether or not there is also a VSD. If a VSD is present, it may promote growth of the RV during fetal development as there is increased blood flow into this chamber through the hole in the septum. If there is no VSD, severe hypoplasia of the RV results in fistulous connections from the RV to the coronary arteries. The coronary circulation may be dependent on these connections. A PFO or ASD is usually present to decompress the obstructed right heart. Pulmonary blood flow is dependent on patency of the ductus arteriosus, which ensures a left-to-right shunt. The obligate right-to-left shunt at the PFO/ASD results in systemic cyanosis.

After diagnosis, drug treatment is performed to maintain ductal patency. In patients with right ventricular dependent coronaries and a restrictive atrial septum, balloon atrial septostomy may be necessary to produce a larger ASD. In the absence of right ventricular dependent coronaries, primary repair can be accomplished by opening the atretic pulmonary valve with transcatheter perforation or surgical valvotomy. In many patients, another source of pulmonary blood flow (either a surgically placed aorto-pulmonary shunt or a patent ductus) is required until RV compliance improves.

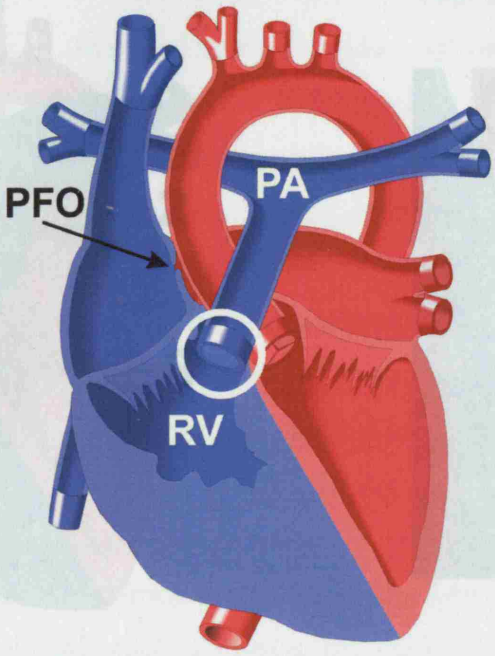

Figure 2.4 Pulmonary atresia with intact ventricular septum.

2.4.3 Absent Pulmonary Valve

In this rare defect, the pulmonary valve tissue is poorly formed (Figure 2.5) and there is significant insufficiency. This can result in massive dilatation of the pulmonary arteries, which leads to the extrinsic compression of the bronchial airway. There can also be associated VSD. In cases with significant degree of bronchial compression, there is marked respiratory impediment. In the presence of VSD, right to left shunt can occur leading to systemic desaturation.

Plication of the pulmonary arteries, pulmonary valve replacement and closure of the VSD are the goals of surgical therapy (Figure 2.5).

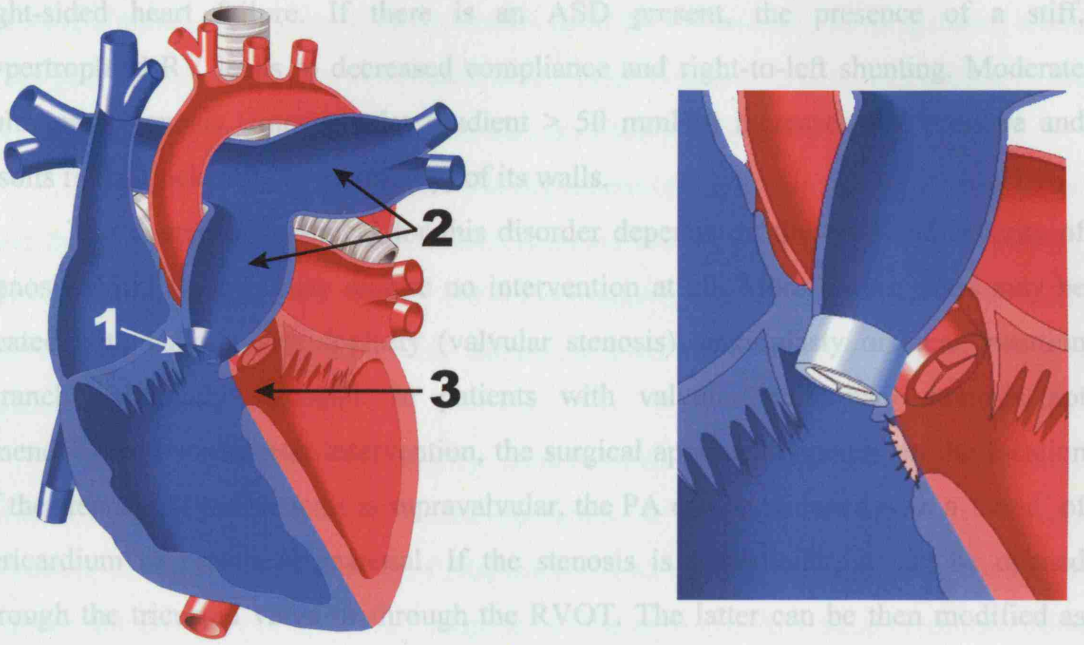

Figure 2.5 1. Absent or insufficient pulmonary valve; 2. Dilatation of the pulmonary arteries; 3. VSD. The illustration on the right shows a zoom of the surgical repair by insertion of a prosthetic pulmonary valve (light blue) and a VSD patch (pink).

2.4.4 Pulmonary Stenosis

In this defect, the pulmonary valve opening and/or the RVOT is restricted (Figure 2.6). This is one of the most common congenital heart defects and exists as a spectrum from mild to severe.

Three types of pulmonary valve stenosis have been described, according to the location of the stenosis relative to the valve:

- In supravalvular stenosis, the PA lumen above the valve is narrowed. Obstruction can be in the main or branch pulmonary arteries.
- In valvular pulmonary stenosis, the leaflets of the pulmonary valve are abnormally thickened and fused at their edges so that the valve does not open fully. Often there is post-stenotic dilatation of the main PA. The valve is often bicuspid or can be dysplastic with redundant tissue.
- In subvalvular or infundibular stenosis, the outflow tract of the RV, below the pulmonary valve, is narrow or obstructed by excess tissue.

Pulmonary stenosis, unless severe, is well tolerated and children are often asymptomatic. Children with severe stenosis (suprasystemic RV pressure) may develop

right-sided heart failure. If there is an ASD present, the presence of a stiff, hypertrophied RV leads to decreased compliance and right-to-left shunting. Moderate pulmonary stenosis (transvalvular gradient > 50 mmHg) increases RV pressure and results in the thickening (hypertrophy) of its walls.

The course of treatment for this disorder depends on the type and severity of stenosis. Mild stenosis may require no intervention at all. More severe cases may be treated with balloon valvuloplasty (valvular stenosis), angioplasty or stent insertion (branch pulmonary stenosis). In patients with valvular pulmonary stenosis not amendable to transcatheter intervention, the surgical approach depends on the location of the stenosis. If the stenosis is supravalvular, the PA can be widened with a 'hood' of pericardium or prosthetic material. If the stenosis is subvalvular, it can be opened through the tricuspid valve or through the RVOT. The latter can be then modified as mentioned above. Should the stenosis involve the valve with a small annulus of the pulmonary valve, the incision is carried out proximal and distal to the valve and is covered with a transannular patch.

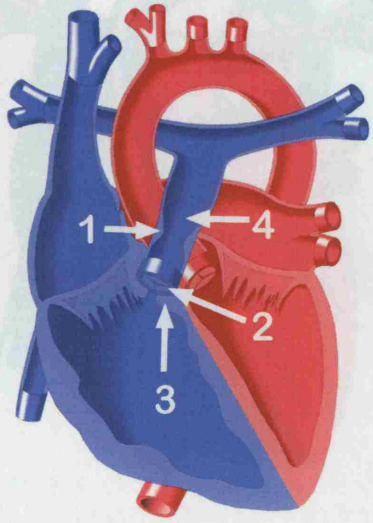

Figure 2.6 Pulmonary stenosis: 1. supravalvular, 2. valvular, 3. subvalvular or 4. infundibular.

2.4.5 Transposition of the Great Arteries

In this defect, which accounts for 5% of the cases of congenital heart disease, the ventricular-arterial relationship is discordant (Figure 2.7). The aorta is anterior and to the right of the PA. It arises from the RV and returns de-oxygenated blood to the

systemic circulation. Similarly, the PA arises from the LV and returns oxygenated blood to the pulmonary circulation. Associated defects can include VSD and coarctation of the aorta. Coronary artery abnormalities are also common in this defect.

Adequate systemic oxygenation is dependent upon mixing of oxygenated blood from the pulmonary circulation with de-oxygenated blood from the systemic circulation. This can occur at the atrial septum via a PFO, and/or at the great arterial level via a patent ductus arteriosus. The atrial communication may be restricted, leading to significant systemic cyanosis.

This defect will require surgery, usually in the first week of life. The current definitive repair is an arterial switch operation. It involves connecting the distal ascending aorta to the LV and the distal main PA to the RV, as in a normal heart. In addition, the coronary arteries are transposed to the neoaorta. Any atrial communication is closed and the patent ductus arteriosus is divided.

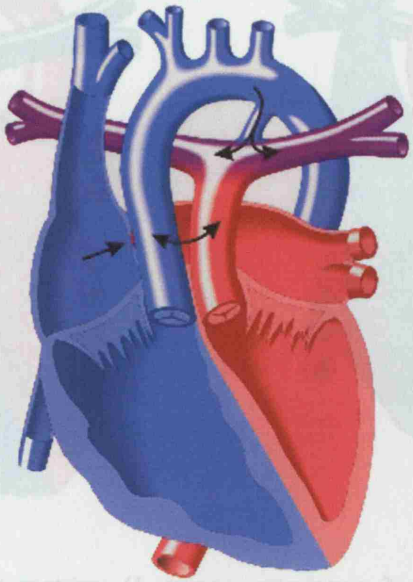

Figure 2.7 Transposition of the great arteries: the arrows indicate the PFO (left), the transposition of arteries (central) and the blood flow direction through patent ductus arteriosus (right). The purple colour denotes the presence of mixed blood.

2.4.6 Truncus Arteriosus

In this rare defect, which can occur with other genetic disorders, the aorta and PA leave the heart as a common trunk, known as the truncus arteriosus (Figure 2.8,left). In addition, there is a large VSD, which the truncus arteriosus overrides.

The truncal valve is often abnormal in form, sometimes with two, four, or five valve leaflets rather than the normal three. The valve can also be both stenotic and insufficient. Rarely, truncus arteriosus is associated with aortic arch or branch PA abnormalities.

Surgical treatment of this defect involves closure of the VSD (patch) with detachment of the pulmonary arteries from the common trunk and placement of RV to PA conduit (Figure 2.8,right). The truncus now assumes the functional role of the aorta carrying blood from the LV to the body. This is among the more complicated procedures to be performed on a newborn. In patients with significantly stenotic or insufficient truncal valves, surgical repair of the valve itself has limited success, and many require replacement of the dysfunctional valve with a prosthetic valve.

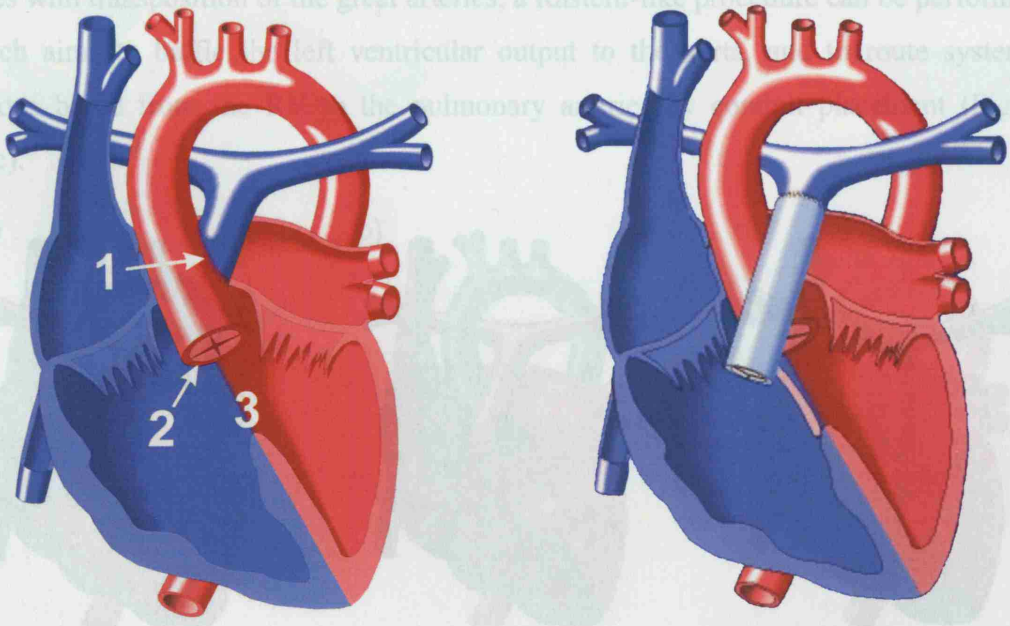

Figure 2.8 Truncus arteriosus anatomy (1. truncus arteriosus; 2. Abnormal truncal valve with 4 leaflets; and 3. VSD) and surgical repair by insertion of a valved tube or conduit (light blue) and a VSD patch (pink).

2.4.7 Double Outlet Right Ventricle

Double outlet right ventricle is an uncommon congenital heart defect in which both the aorta and the PA arise from the RV. This lesion can also be described as the presence of muscular conal tissue (CT in the illustration) under both PA and aorta, with fibrous discontinuity between the aortic and mitral valves. There is a VSD, which can be sub-

aortic, sub-pulmonary, doubly-committed, or remote in location. The great vessels may be normally related (Figure 2.9a) or malposed in orientation (Figure 2.9b). Rarely, there can be hypoplasia of the mitral valve and LV.

The haemodynamic and physiological effects of this lesion depend on the position of the VSD and the degree of pulmonary valve stenosis. Infants with this lesion may show the spectrum from pulmonary over-circulation to transposition-like physiology. Transposition-like physiology occurs with inadequate circulatory mixing due to streaming of oxygenated blood from the LV back to the PA.

Surgery is the mainstay of therapy for this lesion. In patients with normally related great vessels and sub-aortic VSD, primary repair can be accomplished by patching the VSD to the aorta. However, if the aorta is remote from the VSD and in cases with transposition of the great arteries, a Rastelli-like procedure can be performed, which aims to baffle the left ventricular output to the aorta, and to route systemic venous blood from the RV to the pulmonary arteries by conduit placement (Figure 2.9c).

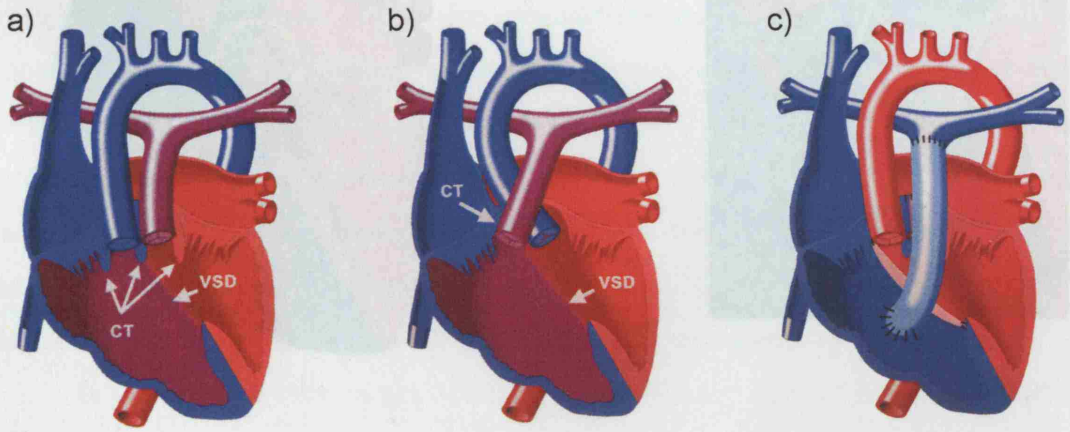

Figure 2.9 Double outlet right ventricle with **a)** transposed great arteries and **b)** normal orientation of the great vessels (CT – conal tissue). **c)** Rastelli procedure result with a valved conduit (light blue) and a VSD patch (pink).

2.4.8 Aortic Stenosis

In valvular aortic stenosis, the outflow tract leading from the heart into the aorta, which carries oxygen-rich blood to the body, is obstructed (Figure 2.10). The most common type of aortic stenosis, known as valve stenosis, involves a narrowing of the aortic valve itself. This may be caused by the aortic valve leaflets being too small or too thick, or the

valve may be bicuspid or rarely unicuspid. There can be associated defects such as patent ductus arteriosus or coarctation of the aorta. Left ventricular hypertrophy is present. Occasionally, the obstruction does not involve the aortic valve itself but consists of a narrowing of the proximal aortic lumen above (supravalvular) or of the left ventricular outflow tract below it (subvalvular). Supravalvular aortic stenosis can be associated with coronary artery abnormalities, while subvalvular aortic stenosis can lead to insufficiency of the aortic valve. The natural history of aortic valvular stenosis is progressive. This results in increased afterload on the LV, resultant hypertrophy, increased myocardial oxygen demand and subendocardial ischemia. Ventricular arrhythmia and sudden cardiac death can occur in moderate to severe cases.

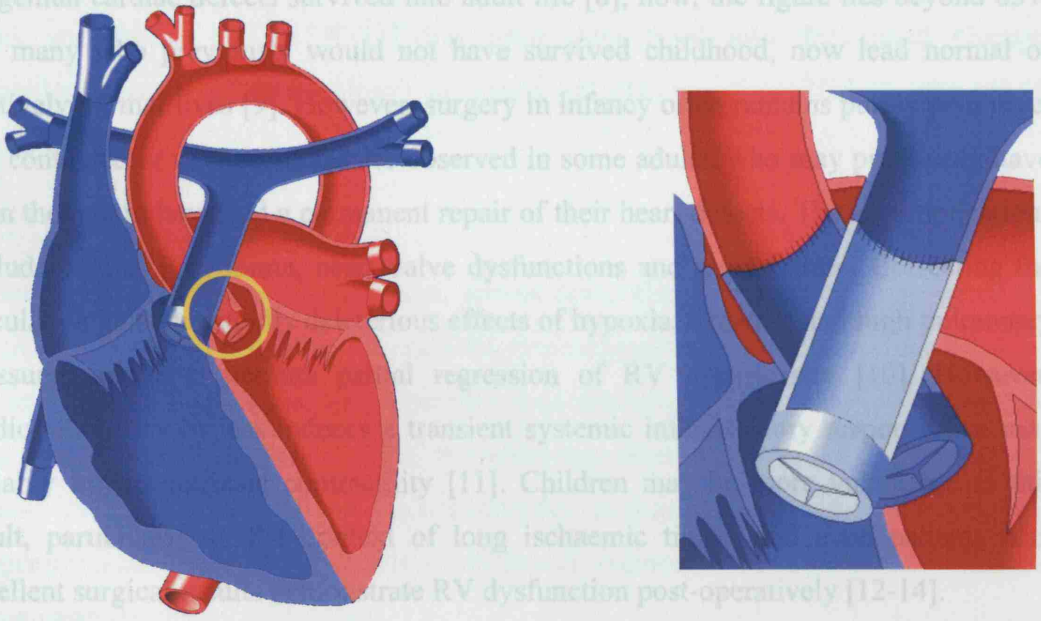

Figure 2.10 Aortic stenosis marked in the illustration by the yellow circle and zoom of the Ross surgical repair by placement of the pulmonary valve and lower portion of the PA into the aortic position, and insertion of an artificial valve into the pulmonary position.

For patients with severe obstruction due to valvular aortic stenosis (peak-to-peak gradient > 70 mmHg or > 50 mmHg with symptoms), intervention is warranted to decrease the risk of sudden death. Balloon valvuloplasty is an excellent palliative procedure, but most patients will ultimately require surgical valve replacement. Surgical possibilities include mechanical valve prosthesis or the Ross procedure. In the latter, the patient's own pulmonary valve root is transposed into the aortic position. The patient's

RVOT is reconstructed with a pulmonary homograft (Figure 2.10). As part of the procedure, the coronary arteries need to be detached and re-implanted into the autograft as well. The Ross procedure is the only aortic valve replacement option that provides the possibility of growth and thus is useful in the paediatric population.

2.5 CONSEQUENCES OF CONGENITAL HEART DISEASE SURGICAL REPAIR

All the conditions described in Section 2.4 may require surgical repair in infancy that will lead to a common problem late in life: RVOT dysfunction.

Prior to the advent of cardiac surgery, less than 20% of children born with congenital cardiac defects survived into adult life [8]; now, the figure lies beyond 85% and many who previously would not have survived childhood, now lead normal or relatively normal lives [9]. However, surgery in infancy often remains purely palliative, and continued or new problems are observed in some adults, who may previously have been thought to have had a permanent repair of their heart defects. These complications include cardiac arrhythmia, heart valve dysfunctions and heart failure. Correcting the circulation halts the rapidly deleterious effects of hypoxia, cyanosis and high pulmonary pressures and also permits partial regression of RV hypertrophy [10]. However, cardiopulmonary bypass induces a transient systemic inflammatory response that may variably impair intrinsic contractility [11]. Children may be more vulnerable to this insult, particularly in the context of long ischaemic times, and even patients with excellent surgical results demonstrate RV dysfunction post-operatively [12-14].

In the early era of tetralogy of Fallot surgical repair, relief of RVOT obstruction was achieved by aggressive resection of infundibular muscle bands or liberal transannular patch reconstruction. However, as time passed, it became clear that this strategy resulted in RVOT aneurysms and associated severe pulmonary regurgitation that had detrimental consequences for RV function. Consequently, extensive transannular patch repairs have now been abandoned and limited outflow tract patching with preservation of pulmonary valve competence has become the key goal. Nevertheless, surgical reconstruction inevitably leads to some degree of morphological change in the RVOT. Similarly, in those conditions where conduits are required to re-establish continuity between the RV and the pulmonary arteries, patch augmentation of

the RVOT is often necessary to achieve an adequate anastomosis. Furthermore, homograft, bioprosthetic or other synthetic materials used to fashion such patches and/or conduits are susceptible to degeneration and calcification and may variably influence the outflow tract shape.

From the above discussion it can be seen that patients who present late after initial repair of their RVOTs (which encompasses a large number of congenital heart diseases, the most common of which is tetralogy of Fallot) will present with a wide variety of RVOT dysfunction. One of the aims of this thesis is to try and classify these patients according to the morphology they have developed late after repair, such that individual patient specific treatment options can be defined and used in the future.

Dysfunctions of the RVOT are many fold: however, for the purposes of this thesis, dysfunction of the RVOT has been categorized into anatomical changes (dilatation, change in morphology) or functional changes simplified to stenosis or regurgitation

2.5.1 Pulmonary Regurgitation

Pulmonary regurgitation is a common, almost invariable consequence of many of the surgical procedures employed to palliate the congenital heart defects described in Section 2.4 [15-18]. Significant pulmonary regurgitation also develops in patients who have required implantation of a RV to pulmonary arterial conduit (e.g. patients with truncus arteriosus). Indeed, over the past decades, as more and more patients with these congenital heart defects have survived childhood, pulmonary regurgitation has become an increasingly common problem.

Although once thought to be a relatively benign condition [15,19], the clinical significance and sometimes ominous implications of chronic pulmonary regurgitation have recently become recognized and appreciated [16,20-27]. Pulmonary incompetence and the associated RV volume overload can cause RV dysfunction, which can in turn lead to symptoms of reduced exercise tolerance [28], and increased risk of ventricular tachyarrythmias [20], and sudden death [24,29]. Furthermore, moderate to severe pulmonary regurgitation has been demonstrated to have consequences for LV size and function [30-33] even if minimal or no change LV findings have been found in the presence of mild pulmonary regurgitation [34,35]. These reports indicate an increase in LV end diastolic and end systolic volumes, when compared to controls that positively

correlates with pulmonary regurgitation severity and is associated with an impaired ejection fraction. Serial follow-up of patients with pulmonary regurgitation suggests that deterioration in right and LV ejection fraction is progressive and thus contributes to the rationale for replacing the pulmonary valve in this population [21].

2.5.2 Right Ventricular Outflow Tract Obstruction

Focus over recent years has centred mainly on the problems of pulmonary regurgitation, perhaps because of its frequency in the context of transannular patch repair of tetralogy of Fallot. Right ventricular outflow tract obstruction is a cause of haemodynamic instability and has been rarely described in non-congenital cardiac surgery. Right ventricular pressure overload caused by the obstruction, if mild to moderate, has been considered to be a benign condition and the limited MR studies available have suggested no difference in RV volumes and function from controls [36,37]. This supposition, however, is based mainly on evidence from patients with isolated congenital pulmonary stenosis who may never have been exposed to hypoxia, cyanosis or cardio-pulmonary bypass [38,39]. Pressure overloaded ventricles develop compensatory RV hypertrophy in order to negate increased wall stress and utilise more oxygen than volume loaded ventricles [40]. Chronic RV pressure overload has been associated with impaired RV diastolic function, septal displacement, altered LV geometry and reduced LV end-diastolic volume [41-44]. However, in comparison to the volume overloaded RV, LV ejection fraction is preserved [45].

Little work has been done to investigate the validity of any of these findings in the context of late RVOT obstruction, often resulting as a consequence of conduit degeneration, following repair of complex congenital heart conditions.

2.6 MANAGEMENT ALTERNATIVES

The growing recognition of the detrimental effects of chronic RV volume and/or pressure overload has resulted in a shift towards a strategy of re-operation in patients with the incompetent and/or stenosed pulmonary valves and conduits.

2.6.1 Surgical Pulmonary Valve Replacement

Surgical pulmonary valve replacement is now a low-risk intervention with a peri-operative mortality of 1-4% and excellent mid-term survival [46-48]. Current choices

for replacement include bioprosthetic homografts and xenografts, and mechanical valves. These valve substitutes offer adequate function, but also present several disadvantages: limited availability of homografts, gradual degeneration over time of bioprosthetic xenografts, and the need for lifetime anticoagulation therapy for mechanical valves. When undertaken in young subjects, pulmonary valve replacement has been found to decrease RV dimensions, reduce symptoms, and improve exercise function [25,49-51]. However, the results of pulmonary valve replacement in older subjects have, in some studies, been disappointing, perhaps because delayed valve replacement has resulted in irreversible RV dysfunction [52,53].

Thus, surgical replacement is a balance between the operative risk of the procedure, the finite life span of any conduit inserted and the risk of irreversible RV dysfunction if the operation is performed too late. The optimal timing and method of restoring pulmonary valve function are important issues that are yet to be resolved.

2.6.2 Bare Stenting

Though the treatment of RVOT stenosis is possible surgically, the amenability of conduit stenosis to stenting has meant that this is the preferred method. Early attempts with percutaneous balloon angioplasty showed marginal efficacy in relieving the obstruction, diminishing the pressure gradient and avoiding surgical intervention [54,55]. With developments in intervention, stent implantation proved superior and resulted in immediate and sustained haemodynamic improvement, effectively prolonging conduit life [56-59]. An important consideration, however, is the significant pulmonary regurgitation, which invariably follows placement of a bare stent. Whilst patients report symptomatic improvement, there has been little investigation into the consequences of this intervention for objective exercise capacity and arrhythmia propensity.

2.6.3 Percutaneous Pulmonary Valve Implantation

From the analysis of RVOT dysfunction presented in this chapter, it is therefore apparent that there is a demand for a potential alternative to surgery to treat this condition. Indeed, enthusiasm for repeated surgery is tempered by the limited longevity of surgically implanted valves or conduits. For those with obstructed outflow tracts, bare stenting can delay surgery but at the cost of pulmonary regurgitation. Therefore,

recently, a novel non-surgical procedure for heart valve replacement, which can relieve both regurgitation and/or stenosis in the RVOT, has been introduced. Percutaneous pulmonary valve implantation will be extensively described in the next chapter.

CHAPTER 3

PERCUTANEOUS PULMONARY VALVE IMPLANTATION

Percutaneous pulmonary valve implantation is a novel, non-surgical treatment for patients with RVOT dysfunction. Between September 2000 and August 2007, 178 patients with RVOT stenosis and/or regurgitation underwent PPVI at our centre. The procedure has been demonstrated technically feasible with low risk and has had sustained clinical results to date. Indeed, PPVI leads to significant reduction in RV systolic pressure and RVOT gradient, by restoring pulmonary valve competence and, at the same time, relieving RVOT obstruction.

There are limitations to the application of this technique in young and small patients and patients with either too small or too large outflow tracts. The major technical pitfall of this procedure is stent fracture, which can, however, be treated with further PPVI or surgical intervention.

Thus, the use of PPVI, to delay surgical RVOT revision, might lead to a reduction in the number of open heart procedures required over the total lifetime of patients with RV to PA conduits.

3.1 INTRODUCTION

The treatment of congenital heart disease has become increasingly interventional as the armamentarium of tools has grown. Bare stenting during percutaneous catheterisation has emerged as an efficient technique to re-open pulmonary conduit obstructions, thereby delaying the need for surgery. However, this technique is not entirely satisfactory because the valve in the conduit has to be sacrificed, which then leads to pulmonary insufficiency. A non-surgical technique to correct the conduit obstruction without compromising the competence of the valve is therefore attractive. By preserving adequate long-term RV function, this option potentially diminishes the number of surgical interventions in patients who need numerous open-heart operations during their life. Our group performed the first successful human transcatheter valve replacement in the pulmonary position in 2000 [60]. This chapter describes our experience with PPVI, that to date has treated over 175 patients with dysfunction of the pulmonary valve.

3.2 PERCUTANEOUS PULMONARY VALVE IMPLANTATION

3.2.1 Historical review

Percutaneous valve intervention represents a fast-growing and very young field in cardiology. The first implantation of a heart valve without cardiac arrest was reported more than 50 years ago [61]. Hufnagel et al. described insertion of a valve into the descending aorta, after clamping of the aorta, for treatment of aortic regurgitation. This pioneering work was performed before the era of cardiopulmonary bypass. In 1992, with recent advances in catheter technology, two separate investigators readdressed this concept and made attempts to design a non-surgical technique for mechanical and biological aortic valve replacement [62]. Andersen reported on valve implantation in pigs without thoracotomy. A porcine aortic valve was mounted onto a balloon-expandable stent and positioned into the aortic root [63]. Pavcnik et al. approached the concept of non-surgical heart valve implantation with a crimpable mechanical valve [62], but valvular competency was maintained for no longer than 1-3 hours. Andersen's work was largely overlooked at that time and the concept came to fruition only 8 years later when the first percutaneous pulmonary valve approaches were developed [64]. In September 2000, the first PPVI in man was performed by our group with the aim of

avoiding surgery in a 12-year-old boy whose dysfunctional conduit would have conventionally necessitated open heart surgery [60]. The initial design of a biological valve mounted on an expandable stent proposed by Andersen is still current. The first transcatheter aortic valve described by Cribier et al. in 2002 used the same concept and design [65]. Over the last six years, devices have been implanted percutaneously in all four heart valves in animal experimental studies [66,67]. Human applications started with the pulmonary implantation because of its lower complexity and to date are limited to this and the aortic valve. The technical difficulty of aortic implantations and the fragile patient population, initially limited to patients with surgical contraindications, led to relatively high morbidity and mortality rates [68-70], which have been in rapid decline over the last few years due to evolving technology and better understanding of patient selection [71,72]. Percutaneous pulmonary valve implantation has also shown a marked learning curve over the last 6 years, with proven improvement in safety and efficacy. This finally led to the first approval of a transcatheter heart valve by European regulatory bodies at the end of 2006 for the pulmonary valve, followed in 2007 by two devices for aortic valve implantation.

3.2.2 The Device

The PPVI device is composed of a segment of bovine jugular vein with a native central valve that is sutured inside a balloon expandable stent (Figure 3.1). Bovine jugular venous valves can have perfectly formed bicuspid or tricuspid arrangements. Bovine jugular venous valves are available only up to 22 mm of diameter. Therefore, only RVOTs smaller than 22mm of diameter can be treated with this percutaneous device. However, in borderline cases, with larger or high compliance outflow tracts, the device can be over-deployed up to 24 mm. The valve venous segment, which is thinned down and fixed in buffered glutaraldehyde, is attached to the stent by continuous 5-0 polypropylene sutures around the entire circumference of the inflow and outflow zones and also discretely at each strut intersection. The suture is clear for all points except the outflow line, which is blue to signify the outflow end of the device and to facilitate orientation on the delivery system.

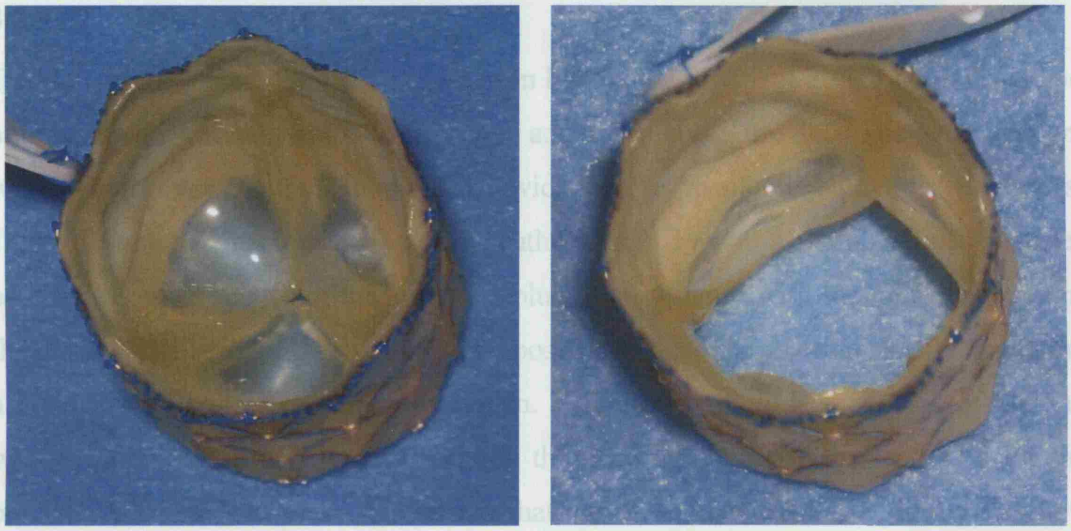

Figure 3.1 Melody^{TM} percutaneous pulmonary valve device with the valve in the close and open position.

The first device used for PPVI was developed from commercially available products (Contegra: Medtronic, Minneapolis, MN and CP stent: NuMed Inc, Hopkinton, NY) with proven utility in the clinical setting [73]. The CP stent was created by a platinum-10%iridium wire, formed into a zig-zag shaped pattern. The individual segments were joined together at the crowns to create the full stent, by welding of the platinum. Since the platinum welds were prone to fracture, this device was modified in design by introducing a gold braising process to reinforce the crowns of the stent (Figure 3.2).

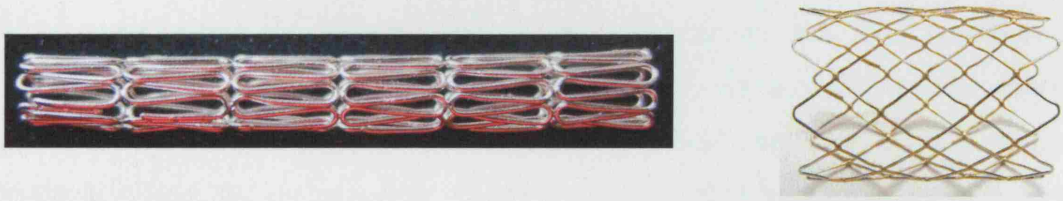

Figure 3.2 Platinum-10% Iridium stent and the gold reinforced current device.

The stent can be crimped to a size of 6 mm before being re-expanded up to 24 mm. The valve itself can undergo multiple compressions and re-expansions inside the stent. The combined device undergoes a final sterilization step using a proprietary sterilant containing glutaraldehyde and isopropyl alcohol, in which it is then packaged. The valved stent assembly is crimped on a custom made delivery system, based on a front-loading mechanism.

3.2.3 The Delivery System

The delivery system comprises a balloon in balloon deployment design at its distal end onto which the valved stent is front-loaded and crimped (Figure 3.3). The outer balloon, which determines the final implanted device size, is available with three diameters: 18mm, 20mm and 22mm. The tip of the catheter is 21 Fr (7mm) with an inner diameter of 18 Fr (6mm). The tip of the system is blue to correspond with the outflow suture of the device. The body of the system is composed of a one-piece Teflon sheath containing a braided-wire reinforced elastomer lumen. This design minimises the risk of kinking whilst optimising flexibility and retaining the necessary 'pushability' required for the procedure. There is a retractable sheath that covers the stented valve during its entry through the skin and delivery, and is pulled back just prior to deployment at the implantation site. The distal part of the sheath is not radio-opaque and a marker at the proximal end of the sheath indicates that the stent is uncovered before deployment. Contrast can be delivered via the retracted sheath from a side port to confirm positioning of the device prior to deployment. Proximally, there are three ports, one for the guidewire (green), one to deploy the inner balloon (indigo), and one to deploy the outer balloon (orange). The balloons are inflated in succession, the inner balloon first, which helps further in positioning the stent, followed by the outer balloon, which fully deploys the device.

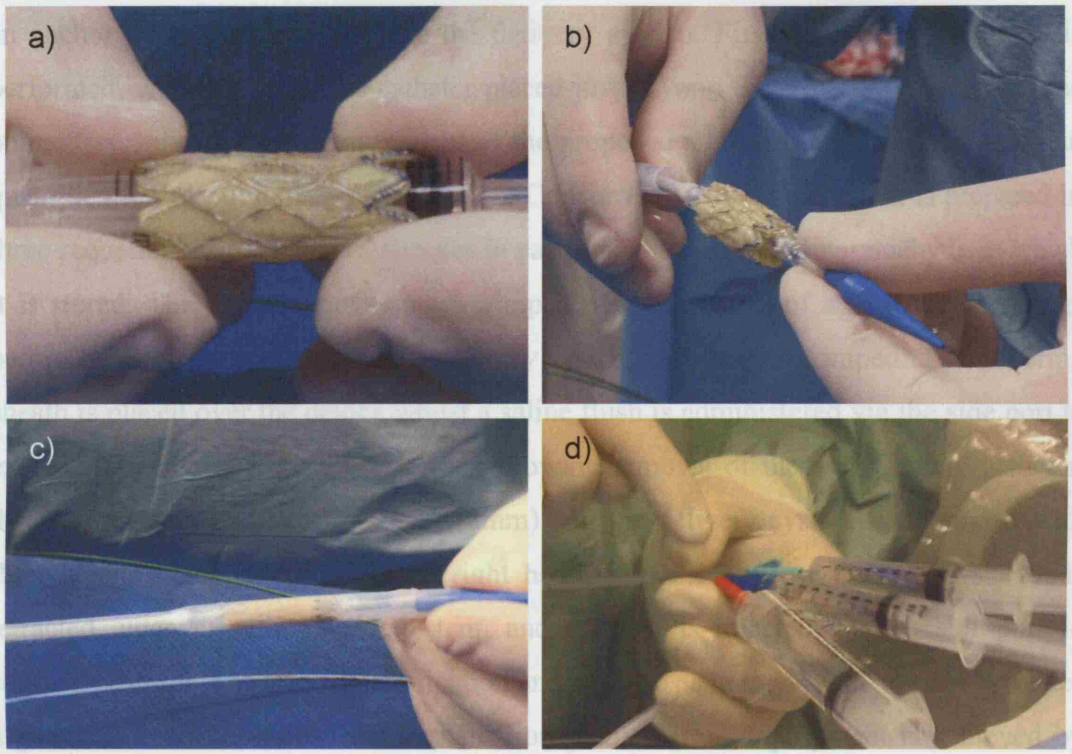

Figure 3.3 Loading of the PPVI stent onto the delivery catheter: a) initial crimping of the device onto a syringe; b) loading of the device on the balloon-in-balloon system; c) a retractable sheath covers the device to protect it during the delivery; d) the three ports at the other extremity of the delivery system, one for the guidewire (green), one to deploy the inner balloon (indigo) and one to deploy the outer balloon (orange).

3.2.4 The Procedure

Percutaneous pulmonary valve implantation involves transcatheter placement of a valved stent within the existing degenerated valve or conduit. The procedure is performed under general anaesthesia, predominantly via a right femoral venous approach, with invasive blood pressure monitoring. A full aseptic technique to surgical standards is used and a single dose of broad-spectrum intravenous antibiotics is given for endocarditis prophylaxis. Heparin is administered routinely at the beginning of the procedure and repeated hourly thereafter as required. Right heart catheterisation is performed according to standard techniques to assess pressures and saturations in the RV, PA and aorta with additional measurements, for example in the branch pulmonary arteries, made as appropriate. Angiography is performed in frontal, lateral and oblique projections to determine the anatomy of RVOT and the branch PAs in order to confirm feasibility, select the appropriate site of deployment and aid the choice of delivery system (Figure 3.4a). A stiff guidewire is positioned into a distal branch PA to provide

an anchor from which to advance the delivery system. First, biplane angiography is performed, with the tip of the catheter placed just beyond the expected position of the pulmonary valve, to allow assessment of the proposed site for device implantation and quantification of pulmonary regurgitation. Concurrently, the valved stent is prepared in three sequential saline baths (5 minutes in each) to wash off the glutaraldehyde in which it is stored. The valved stent is hand-crimped over the barrel of a sterile 2ml syringe before being front-loaded onto the delivery system and further crimped. The covering sheath is placed over the device whilst a saline flush is administered via the side port to exclude air bubbles from the system. Following removal of the angiography catheter, the femoral vein is dilated to 24 Fr (8mm) and the delivery system is advanced with fluoroscopic guidance, through the right heart, into the outflow tract. The sheath is retracted, uncovering the valved stent, and contrast is injected via the side-port to confirm position. The area of calcification and/or stenosis in the RVOT usually provides a good landmark to choose the implantation point. Partial deployment is achieved by hand inflation of the inner balloon and after final confirmation of the position the outer balloon is hand inflated to complete deployment. The balloons are deflated and the delivery system carefully withdrawn, keeping the guidewire position intact. Repeat angiography and pressure measurements are made to confirm a positive outcome (Figure 3.4b).

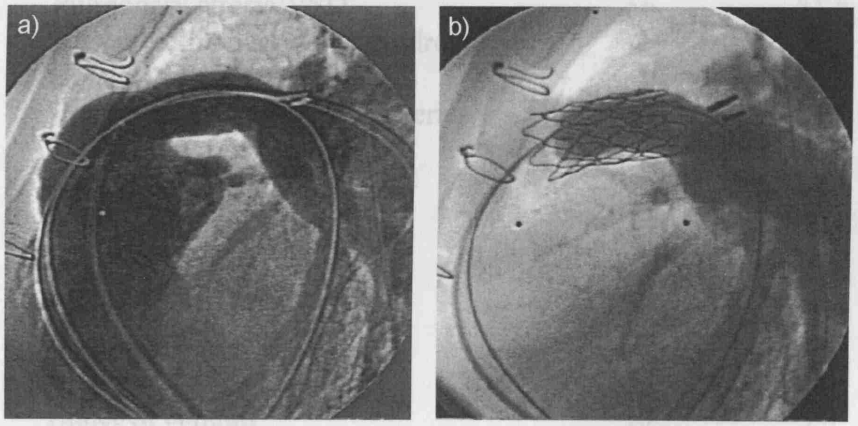

Figure 3.4 **a)** Pre- and **b)** post-PPVI angiograms.

The nature and position of RV to PA conduits is heterogeneous and cannulation with the large delivery system can be challenging. In calcified, stenosed conduits pre-dilatation with a high-pressure balloon and placement of a bare stent can ease

implantation and optimise outcome. Equally, if further dilatation of the valved stent is required following implantation, this is performed using a high-pressure balloon with inflation up to 8-10 atm. Post-dilatation of the device has not been observed to cause any damage to valve leaflets or affect valve competency.

3.2.5 Current Clinical Experience

The clinical programme of PPVI began at Hôpital Necker Enfants Malades (Paris, France) and continued at Great Ormond Street Hospital for Children, The Heart Hospital, and Harley Street Clinic (London, United Kingdom). The local research ethics committees approved the study, and all subjects (and/or a parent/guardian) gave informed consent.

Between September 2000 and August 2007 our group has implanted 202 percutaneous valves into 178 patients. Characteristics of this patient population are shown in Table 3.1.

Characteristic	**n (=178)**	**%**
Male	103	57.9
Median age [years]	21 (range 7-71)	
Primary diagnosis:		
Tetralogy of Fallot	48	27.0
Pulmonary atresia/VSD	56	31.5
Absent pulmonary valve syndrome	7	3.9
Isolated pulmonary stenosis	4	2.2
Transposition of the great arteries	21	11.8
Truncus arteriosus	15	8.4
Double outlet right ventricle	6	3.4
Aortic valve disease (Ross)	13	7.3
Others	8	4.5
Outflow tract type:		
Homograft	140	78.7
Homograft + Patch	7	3.9
Hancock conduit	10	5.6
Carpentier-Edwards conduit	4	2.3
Native	5	2.8
Others	12	6.7

Table 3.1 Characteristics of the patient population who underwent PPVI between September 2000 and August 2007.

3.3 PATIENT SELECTION

The surgical indications for RVOT dysfunction are probably the most controversial topic in congenital heart disease. Whereas most institutions treat outflow tract obstruction according to symptoms, no unified criteria exist for the timing of valve replacement in the context of pulmonary regurgitation. Recently, finding the right parameter to detect the point of no return in RV volume overload has been described as the Holy Grail of paediatric cardiology and in particular grown up congenital heart disease [74], emphasising the complexity of this issue. The detrimental effects of longstanding pulmonary regurgitation have been shown beyond doubt. However, due to the limited longevity of surgical interventions, the risk of multiple open-heart operations has to be taken into account and influence the clinical management of patients.

3.3.1 Clinical Indications

Percutaneous pulmonary valve implantation is not proposed as an alternative to surgery, rather as a less invasive opportunity to preserve RV function by extending conduit life and potentially reducing the number of operations a patient may have to undergo during a lifetime. Criteria for bare stenting and surgical pulmonary valve replacement have provided general guidance when determining indications for this new technique. Patients are considered for PPVI if they had previously undergone surgery of the RVOT during repair of congenital heart disease and have symptoms or RVOT dysfunction of a sufficient degree to warrant further surgical intervention, based on conventional practices for surgical indications (Section 3.3.3). With feasibility demonstrated in the early patient series [75], indications were also extended to patients who were unfit for surgery (pulmonary hypertension, severe kypho-scoliosis and those 'in extremis') and to patients with milder disease who were symptomatic. All potential candidates are discussed in a multi-disciplinary meeting of cardiologists, cardiothoracic surgeons and intensivists and the decision to proceed to PPVI is reached by consensus. Importantly, PPVI does not affect subsequent suitability for surgery. Inclusion and exclusion criteria are outlined in detail for patients requiring treatment of RVOT obstruction or pulmonary regurgitation in Section 3.3.3.

3.3.2 Anatomical Suitability

The main limitation of the currently available transcatheter valve device is the maximum diameter to which it can be deployed (22mm) before compromising valvular competence. Selection of patients with suitable anatomy is, therefore, critical to ensure both procedural success and to optimise long-term outcome. The surgical history and nature of the RVOT provide important baseline information as to the likely anatomical suitability of the patient. We have found that homografts or other circumferential conduits (Hancock, Carpentier-Edwards) provide the optimal implantation target because of their tendency to deform in a predictable manner. Those with transannular patches or native outflow tracts are rarely suitable, as they deform asymmetrically and thus risk device stability. One exception to this is following the arterial switch operation when the obstructed native RVOT does offer a safe environment for PPVI. Even when the predominant indication for intervention is pulmonary regurgitation, the presence of some level of obstruction or at least calcification of the conduit is essential to achieve device stability.

Establishing the precise morphology of the proposed implantation site, by echocardiography, is often difficult because of limited echo windows and two-dimensional imaging planes. Assessment of these patients with MR (or computerised tomography (CT) if contra-indicated) is extremely valuable with gadolinium contrast-enhanced angiography able to provide a complete appreciation of the overall morphology [Chapter 4].

At the time of catheterisation, patients with borderline dimensions on MR imaging (20-24mm) undergo balloon sizing of their conduit prior to proceeding. This permits assessment of the distensibility of the conduit wall and the likelihood of device stability. The course of the coronary circulation with respect to the RVOT is defined if this is not known. An aortogram, with or without simultaneous injection into the RVOT, is usually sufficient to alleviate uncertainty. If concern remains with regard to the proximity of these structures, selective coronary angiography with simultaneous balloon inflation in the outflow tract designed to mimic valve implantation is carried out (Figure 3.5). Potential compression of the coronary artery can thus be identified prospectively allowing safe termination of the procedure and referral for surgery.

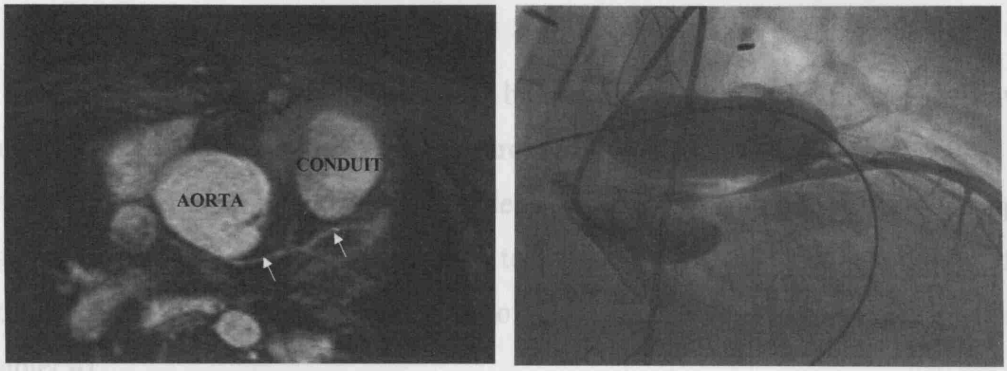

Figure 3.5 In patients with uncertain coronary circulation, selective coronary angiography with simultaneous balloon inflation is performed.

3.3.3 Inclusion and Exclusion Criteria

Acceptance for valve implantation requires suitable outflow tract anatomy (potential device implantation site diameter >14x14mm and <22x22mm) as well as a clinical indication for intervention. For predominant obstruction (outflow tract gradient >50mmHg with no more than mild regurgitation on echocardiography), patients with RV systolic pressure >3/4 systemic pressure are accepted irrespective of symptoms. Right ventricular pressure is assessed by echocardiography, systemic pressure by non-invasive blood pressure measurements. In addition, patients with RV systolic pressure >2/3 systemic pressures are accepted, but are required to be symptomatic. For predominant regurgitation (gradient <50mmHg with moderate or severe pulmonary regurgitation on echocardiography), one of the following is required: symptoms, impaired exercise capacity (peak oxygen uptake of less than 65% of predicted), or moderate/severe RV dysfunction or dilatation (the cut-off point in these patients who are suitable for MR imaging is a RV to LV end-diastolic volume ratio of 1.5). Patients with mixed lesions are discussed on an individual basis with consideration to the above clinical inclusion criteria.

Exclusion criteria include pregnancy, occluded central veins, active infection and outflow tracts with "unfavorable" morphology (obstructed conduits less than 16 mm at surgical insertion or RVOT diameter greater than 22 mm on angiography). Patients less than five years of age or weighing less than 20 kg are not suitable for this procedure due to the size of the delivery system.

3.4 CLINICAL ASSESSMENT

All patients undergoing PPVI are studied before and after intervention. They have a detailed clinical examination, electrocardiogram (ECG), chest radiograph and echocardiography including colour Doppler, continuous- and pulsed-wave Doppler. Magnetic resonance imaging is performed to assess RV volume and function, outflow obstruction, pulmonary regurgitation, outflow tract morphology, and exercise capacity [Chapter 4].

Cardiopulmonary exercise testing is performed to evaluate exercise capacity using a mechanically braked bicycle ergometer Sensormedics, Ergoline 800, Blitz, Germany) and respiratory gas exchange analysis via a mouthpiece or facemask (Medgraphics, St. Paul, Minnesota, USA). Patients under seven years, below 119 cm in height, with gross motor or neurological deficiency, mental or behavioural deficiency or contagious illness do not undergo exercise testing. Maximum work rate, peak minute ventilation, heart rate and blood pressure response are assessed.

During catheterization, RV systolic and end diastolic pressures, and PA systolic and diastolic pressures (beyond the obstruction) are measured before and after the procedure.

Postero-anterior and lateral chest x-rays after implantation are carried out to assess stent patency and monitor for stent fractures. New York Heart Association functional classification is used to subjectively assess the clinical status of the patients before intervention and at the 1 and 3 month follow-up.

During follow-up, patients are subject to clinical review, electrocardiography, antero-posterior and lateral chest x-ray and trans-thoracic echocardiography at 1 month, 3 months, 6 months and 1 year following the procedure and at yearly intervals thereafter.

3.5 RESULTS

Since the first implant in 2000, PPVI has been shown to be feasible and very safe, with nearly 400 implants performed worldwide to date. So far, no procedure-related death has been reported. In our series of implantation (202 PPVIs into 178 patients), successful device deployment was achieved in the majority of cases [Section 3.5.1].

However, procedural complications occurred, particularly in the early experience [Section 3.6].

3.5.1 Immediate Procedural Outcome

Median procedure time was 94 minutes (range 43-240) and fluoroscopy time was 19 minutes (range 4-129). 95.9% procedures were performed from a femoral approach, with all others performed via the internal jugular vein. Failure to deliver the valved stent occurred on 3 occasions (1.7%): 2 patients subsequently underwent successful implantations following a design change in the delivery system, the third was referred for surgery. Fourteen patients underwent pre-stenting of the conduit/PA prior to PPVI. Additional procedures performed concurrently included stenting of a branch PA, second valve implantation, VSD closure, paravalvular leak closure, coarctation stenting and device closure of a PA aneurysm. Twenty-three patients (13%) subsequently went on to have further valve implantations, 16 using a stent-in-stent technique, for a variety of indications. All the patients with successful valve implantation were ambulatory within 24 hours of the procedure.

Acutely, PPVI has been proven to reduce significantly RV pressures and the gradient across the outflow tract. In addition, diastolic PA pressures rise after stent deployment, indicating restoration of valvular competence. Angiography prior to and after valve insertion showed a significant reduction in pulmonary regurgitation [76,77]. There were no patients with more than mild pulmonary regurgitation after the procedure. A symptomatic improvement has been observed after the procedure in the vast majority of our patients. Magnetic resonance imaging performed after the procedure [Chapter 4] showed a reduction in RV volumes and an increase in effective right and LV stroke volumes.

3.5.2 Follow-up

During follow-up, valvular competency was well maintained with freedom from moderate or severe pulmonary regurgitation on echocardiography at one year more than 97%. Significant pulmonary regurgitation was predominantly associated with endocarditis. The more common problem, presented with RVOT obstruction, was an increase in the pressure gradient across the valved stent. This was predominantly related to early device failure. Two important device-related complications were seen: the

'hammock' effect and the appearance of stent fractures, which will be described in detail in Sections 3.6.2 and 3.6.3 respectively.

3.5.3 Mortality

Four deaths have occurred following PPVI. In two of these patients, who both presented in cardiogenic shock and multi-organ failure, PPVI was performed as a palliative strategy. The first patient, who had undergone 5 previous surgeries, was in chronic atrial fibrillation with ascites and had pleural effusions. Despite a successful procedure the patient deteriorated 6 weeks later following a chest infection and died. The second patient presented in a coma with multi-organ failure and severe fluid overload with critical supravalvular aortic stenosis and RVOT obstruction. Despite technically successful transcatheter treatment of re-coarctation and RVOT obstruction, the patient died 24 hours later from intractable pulmonary oedema.

Fatal arrhythmia was the cause for the two other deaths, late after valve implantation. The first patient (who had repaired pulmonary atresia) died suddenly 35 months after PPVI. At autopsy, the valved stent was appropriately seated in the conduit and had shown good function throughout the follow-up. The second patient (with double outlet right ventricle and Rastelli procedure) had a long history of RV pressure overload. After several unsuccessful balloon dilatations of the obstructed conduit in the past, he underwent percutaneous valve insertion. Despite a good haemodynamic result with a low velocity on Doppler across the stent at latest follow-up, he died 8 months after valve insertion; no reason other than arrhythmia could be found.

3.6 COMPLICATIONS

3.6.1 Procedure Related

Major procedure related complications, usually necessitating conversion to surgery, have included device instability in 2 patients (1.1%), homograft rupture in 3 patients (1.7%), compression of the left main coronary artery in one patient who have had previous bare metal stenting (0.6%), and obstruction of the origin of the right branch PA in 1 case (0.6%) (Figure 3.6).

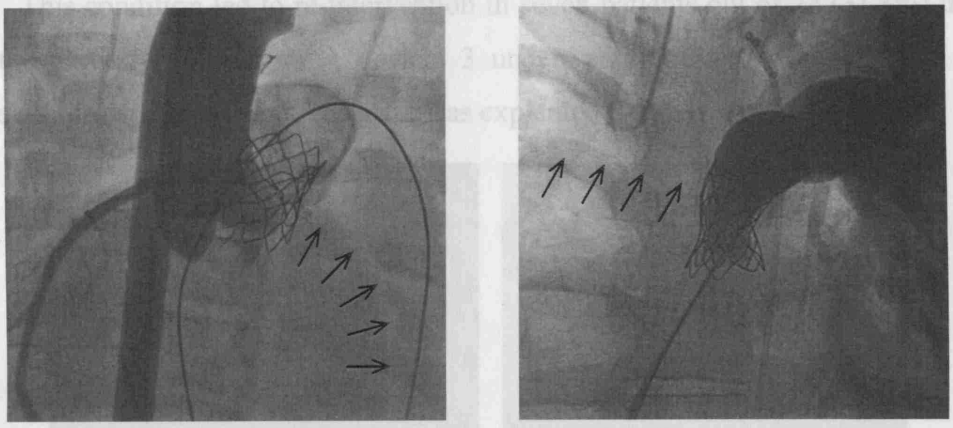

Figure 3.6 Left main coronary artery compression and right PA obstruction. The arrows map the course of the left coronary artery and the right PA respectively.

Minor complications have included limited perforation of a distal PA by the guidewire resulting in minor bronchial bleeding (2 cases, 1.1%), partial homograft rupture (1 case, 0.6%), and damage to the tricuspid valve probably due to entrapment of the delivery system in the chordae (2 cases, 1.1%).

Six patients (3.4%) who had major complications required surgical intervention; none of them led to mortality. Whereas coronary obstruction and device dislodgement in distensible and dilated RVOTs occurred rather early in our experience, they are avoidable by 3D imaging prior to the procedure [68,78]. Risks for homograft ruptures, however, remain unclear. Although not fatal, resuscitation, auto-transfusion and subsequent open-heart surgery were necessary in one patient. Fortunately, early neurological sequelae showed good recovery 6 months after the procedure.

3.6.2 'Hammock' Effect

This phenomenon became apparent in the early cohort of patients undergoing valve implantation, when a high incidence of in-stent stenosis was noted. The 'hammock' effect describes the appearance of the venous wall hanging through the stent (Figure 3.7). Originally, the venous segment of the bovine valve was sutured to the stent only at its distal extremities. This permitted passage of blood between the wall of the vein and the recipient outflow tract resulting in an effective stenosis. Recognition of this problem led to additional sutures being placed at all strut intersections, which resolved the issue with no further cases being seen.

This condition led to re-intervention in seven patients out of 22 (31.8%) treated with the partially sutured valve device; 3 underwent repeated valve insertion (new device design) and in 4 the valved stent was explanted.

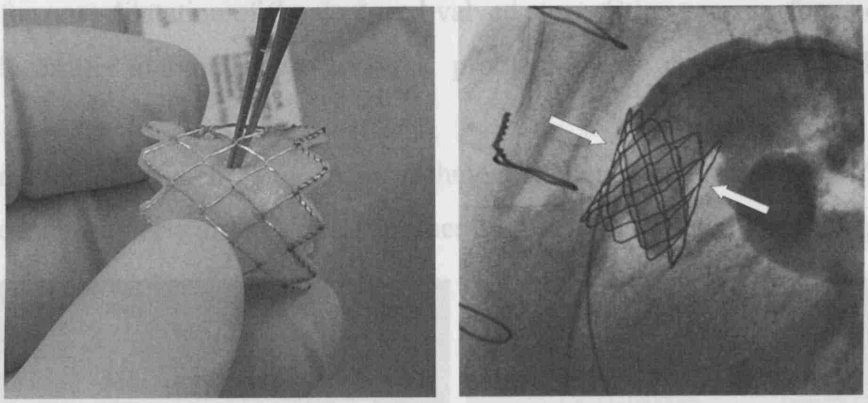

Figure 3.7 'Hammock' effect in the early patients.

3.6.3 Stent Fractures

This finding is well-recognised following stent implantation for all cardiovascular applications. Aetiology is likely to be multi-factorial and depends both on the nature of the stent as well as the characteristics of the implantation site.

Following PPVI, stent fracture has been detected in 20.2% (36 cases) of our patients at varying intervals (Figure 3.8). In most cases, this has been an incidental finding detected on routine chest x-ray. Fractures appeared to be clinically silent with no increase in gradient across the valved stent. In a small proportion of patients (5.2%), however, new outflow tract obstruction developed and in one device embolization into the right PA occurred 9 months after the implantation. In these cases further percutaneous (second PPVI) or surgical intervention was required.

Careful chest x-ray examination has been introduced in patient follow-up to monitor the device structure and to prevent the embolization of the device due to stent failure. In fact, second stent implantation is advisable in cases with loss of stent integrity, even in absence of stenosis. Fluoroscopy may add benefit by grading of stent fractures and by gaining information about stent stability [79]. The lack of circumferential calcification increases the risk of stent fractures, indicating the impact of implantation site distensibility throughout the cardiac cycle [79].

Whereas early device failure was treated mainly by second device implantation, residual stenosis represents the most common indication for re-operation in our series. This occurred particularly in the early experience, before the use of high-pressure balloons for post-dilatation of the deployed valved stent. Other reasons for re-operation were endocarditis and outgrown conduits, problems seen also in surgically placed conduits.

Fracture of the stent is the major technical challenge of the current PPVI and is one of the main subjects of this thesis – further discussed in Chapter 8 and Chapter 9.

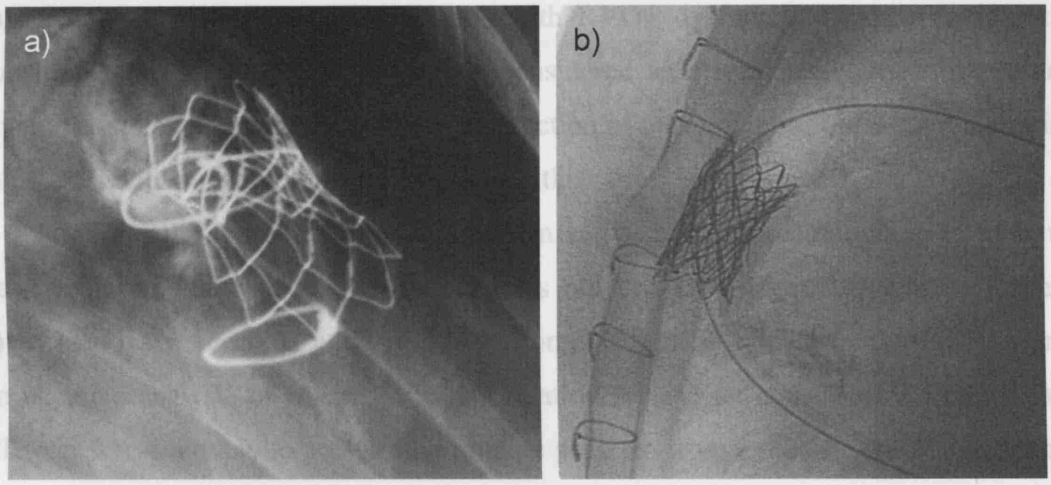

Figure 3.8 **a)** X-rays of a patient presented with extensive stent fracture; **b)** stent-in-stent treatment.

3.6.4 Haemolysis

One patient (0.6%), in whom sequential balloon dilatation and valve implantation failed to adequately relieve obstruction in a small conduit (15mm homograft), developed dark urine containing free haemoglobin the day after the procedure. Following transfusion, he went forward to uneventful surgery at 21 days post-PPVI.

3.6.5 Endocarditis

Infection of the valved stent has been seen in 5 patients (2.8%) at a median of 4.93 (range 1.9 to 23.2) months after PPVI, and can occur either on the venous wall or the valve itself. In these patients, endocarditis occurred in the context of unprotected dental treatment (1 case), reactivation of previously treated fungal infection (1 case), and septic wound after arm trauma (1 case). Two patients had histories of endocarditis treated medically before PPVI. Of these 5 patients, 3 patients developed pulmonary

regurgitation, 1 developed obstruction and 1 had no consequences for device function. Endocarditis led to valve explantation in 3 patients; 2 patients were successfully treated medically.

3.7 FUTURE DIRECTIONS

Percutaneous pulmonary valve implantation, due to the CE mark approval by regulatory bodies within Europe at the end of 2006, is nowadays available to a broader patient population and will be used more commonly. In our opinion, PPVI represents the non-invasive treatment of choice in patients with RVOT dysfunction and, even if not a substitute of cardiac surgery, it can be considered as a treatment option to prolong conduit function. This should result in a reduction of the number of open-heart surgeries in patients with congenital heart disease over their lifespan.

Although significant improvements in early and late outcome after PPVI have been achieved, the risk of stent fractures is not understood yet sufficiently. Further investigations are necessary to avoid these complications. Finite element modelling and an accurate analysis of *in-situ* stent deformation are the tools used in Chapter 8 and Chapter 9 respectively to analyse the fracture problem from a mechanical point of view and better understand the underlying basis for this important technical failure.

Moreover, at present, the device can only be safely implanted in patients with circumferential conduits, which do not exceed 22 mm in diameter. Development of new devices that can assure no failure in both short- and long-term and that can be suitable for a larger patient population requiring RVOT dysfunction treatment need to be advanced [80-82]. A first approach to the design of the next generation of devices is proposed in Chapter 10, where SMAs are used to develop a new stent suitable for large RVOTs.

Ultimately, evolution of the treatment of RVOT dysfunction can only be achieved by close co-operation between cardiologists, surgeons, imaging specialists and biomedical engineers.

CHAPTER 4

CARDIOVASCULAR MAGNETIC RESONANCE IMAGING

Magnetic resonance is becoming an important imaging modality for the assessment of cardiovascular disease in both congenital and acquired heart disease. Using this non-invasive technique, cardiovascular anatomy can be assessed in 3 dimensions along with the other structures of the thorax, thus enabling accurate description of cardiac anatomy in relation to these structures. Furthermore, MR imaging currently provides the best available, non invasive, quantifiable assessment of both cardiac function and great vessel blood flow. Therefore, cardiovascular MR imaging can be used to define cardiac and great vessel anatomy, and ventricular and valve function to plan the intervention of RVOT treatment for incompetence and/or obstruction, with either percutaneous technique or surgery. This approach reduces the need for diagnostic cardiac catheterization and can provide important data for the clinical decision-making process, without exposure to x-rays.

Cardiovascular MR was introduced in the PPVI protocol of investigation to assess the implantation site size, in order to guarantee safe anchoring of the device, and the degree of stenosis and/or regurgitation of the candidate's RVOT.

Post-intervention cardiovascular MR imaging is used to assess the results of the procedure in terms of patency and function of the PPVI valve, and the physiological response of the RV to relief of obstruction and regurgitation.

4.1 INRODUCTION

Magnetic resonance imaging is an imaging technique used primarily in medical settings to produce high quality images of the inside of the human body. Magnetic resonance is based on the principles of nuclear magnetic resonance, a spectroscopic technique used by scientists to obtain microscopic chemical and physical information about molecules. The technique was called magnetic resonance imaging, rather than nuclear magnetic resonance imaging, because of the negative connotations associated with the word nuclear in the late 1970's. Felix Bloch and Edward Purcell, both of whom were awarded the Nobel Prize in 1952, discovered the MR phenomenon independently in 1946 [83-90]. Since then, the development of MR spectrometers and scanners has led to the opening up of whole new branches of physics, chemistry, biology and medicine. Almost 50 years later MR has become an important imaging modality for the assessment of cardiovascular disease, in both congenital and acquired heart dysfunctions [91,92]. The anatomical and functional significance of the disease process can be defined using a single non-invasive imaging modality without exposure to x-rays or to the nephrotoxic effects of iodinated contrast agents.

The aim of the present chapter is to provide an overview of the MR imaging techniques that are used for the purpose of this thesis. The protocol clinically used for MR assessment of right heart and PA before and after PPVI provide a series of data that are used as input for the morphological and dimensional study of the implantation site developed in Chapter 6 and Chapter 7.

4.2 MAGNETIC RESONANCE OF THE PULMONARY VALVE

Cardiovascular MR assessment of the pulmonary valve is usually performed in subjects who have undergone surgical intervention to the RVOT. Echocardiography is the first-line investigation in these subjects, but visualization of the RVOT, pulmonary trunk, and branch pulmonary arteries is often difficult due to the lack of an acoustic window (structures behind the sternum) and changes secondary to multiple operations. Cardiac catheterization is considered the second-line investigation in many centres. However, if access to cardiovascular MR is available, MR imaging can provide much of the information of a diagnostic cardiac catheter, with the exception of hemodynamic

pressure traces and accurate imaging of coronary artery disease. Cardiovascular CT is currently less commonly used due to issues of radiation exposure in a group of patients who will need life-long follow-up of their clinical condition.

Thus, 3D anatomy of the right-sided cardiac and vascular structures can be depicted, and RV and pulmonary valve/conduit function accurately assessed, by MR. These parameters, in conjunction with clinical findings, echocardiography and exercise testing data, can be used to help monitor subjects, define the timing of interventions, and, when intervention is necessary, select the appropriate treatment option – surgery or PPVI.

4.2.1 Right Ventricular Outflow Tract Anatomy

4.2.1.1 'Black-blood' imaging

'Black-blood' spin echo imaging was the earliest technique used to image congenital heart disease [93,94]. In this sequence, flowing fluids give no MR signal, whilst stationary tissue returns MR signal, allowing excellent delineation between, for example, the blood pool (black) and either the vessel wall or myocardium (white). MR data acquisition is performed during a defined portion of the cardiac cycle to 'freeze' cardiac motion (usually the diastolic diastasis). Most spin echo sequences are now acquired rapidly using fast spin echo imaging algorithms, which enables images to be acquired in a single breath-hold [95]. The main disadvantage of the 'black-blood' spin echo sequences is that data is acquired in two-dimensional (2D) slices, and skill is required for image acquisition and interpretation. However, although gradient echo sequences (cine imaging and MR angiography) are increasingly used in cardiovascular MR (see 2.1.2 & 2.1.3), the 'black-blood' spin echo sequence remains important in two situations:

- For accurate sizing of severe valvular and vascular stenosis [96-98]. With these lesions, gradient echo sequences are prone to signal loss, due to turbulent flow, whilst for 'black-blood' imaging contrast improves when the blood flow velocity is high.
- When imaging vessels after metallic stent insertion. The majority of stents are safe to image [99], but cause marked artifacts on gradient-echo sequences secondary to T2* field inhomogeneity. Due to the refocusing pulse, spin-echo sequences are not as

susceptible to these phenomena, and imaging of the vessel within the stent can be achieved (Figure 4.1a,b).

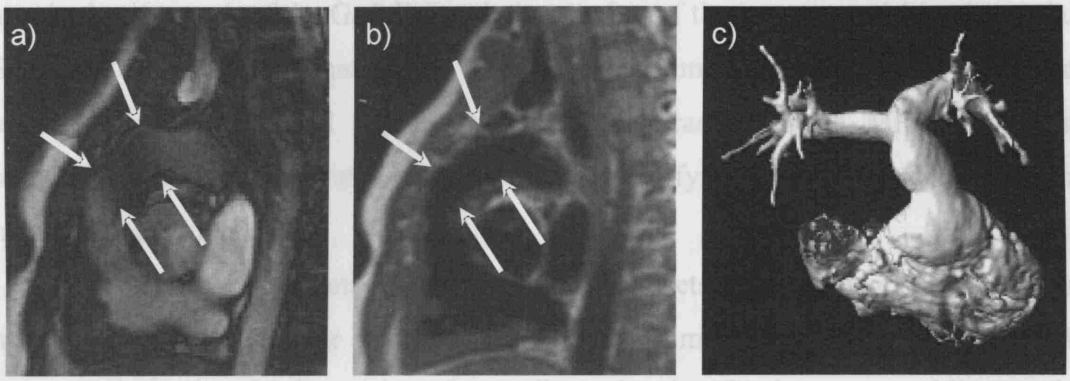

Figure 4.1 Sagittal image through the RVOT post-PPVI in a) balanced-steady state free precession image and b) black-blood spin echo image. The arrows identify the extent of the stent. c) 3D volume-rendered reconstruction of a patient RVOT from coronal view [100].

4.2.1.2 Two-dimensional 'white-blood' cine imaging

In gradient echo imaging, signal from the blood-pool is recovered, and blood appears white. Data are acquired rapidly with high temporal resolution, enabling acquisition of multiple phases of the cardiac cycle.

More recently, balanced steady state free precession (balanced-SSFP) sequences have become available [101]. These sequences have very short MR parameters, which place high demands on MR hardware. Balanced-SSFP images provide improved blood-pool homogeneity throughout the cardiac cycle and faster acquisition times than conventional gradient echo images [102,103]. Two-dimensional balanced-SSFP imaging has become widely used in cardiac imaging, and allows qualitative assessment of the cardiac chambers, valvular dysfunction, and dynamic vascular anatomy. Importantly, as information is acquired over the entire cardiac cycle, the dynamic nature of the structure being imaged can be assessed. This information can be crucial in sizing of the RVOT/pulmonary trunk prior to PPVI, as underestimation of the dimension may lead an inappropriate attempt of implantation.

4.2.1.3 Gadolinium contrast-enhanced MR angiography

Use of contrast agents in MR can ease image acquisition, enhance image quality and improve diagnostic specificity and sensitivity. At present, gadolinium contrast-enhanced MR angiography is the most popular has been shown to be useful in delineating thoracic

vascular anatomy [13]. Acquisition is during a single breath hold and utilises 'bolus tracking' to time the arrival of the gadolinium at the site of interest. A 3D data set is acquired at the peak of the Gadolinium bolus: timing of the image acquisition is crucial. Sequence design ensures that tissues without Gadolinium enhancement are suppressed, leaving contrast enhanced vessels prominent. Contrast-enhanced MR angiography images have been demonstrated to be accurate at identifying stenotic vessels even in the neonatal population [104].

The ability of MR imaging to acquire 3D data sets, enables reconstruction of the heart, and in particular the great vessels, in three-dimensions, that are more easily interpreted than multiple stacks of two-dimensional (2D) images, enabling easier communication of the information between imagers and clinicians (Figure 4.1c) [105,106].

The major drawback of contrast-enhanced MR angiography is that it is usually performed without cardiac synchronization. This has two effects: image blurring due to cardiac motion, which reduces the ability of this technique to visualize intra-cardiac anatomy [105]; error in the measurement of vessel size, which represents an average size over the cardiac cycle. This can lead to underestimation of the maximum systolic dimension of a vessel, which may be crucial for PPVI sizing.

4.2.1.4 Three-dimensional 'white-blood' imaging

One potential method to overcome the disadvantage of lack of cardiac synchronization in MR angiography, whilst maintaining the 3D nature of the acquired data set, is to use a new 3D balanced SSFP technique [105,106]. With this sequence, axial balanced-SSFP ('white-blood') slices are acquired in multiple 3D chunks over several breath-holds. The entire data set is then summed to give complete coverage of the heart and great vessels, with near isotropic resolution (1.0x1.0x1.3mm).

The simplicity of the technique enables image acquisition to be performed without expert planning. The improved contrast and resolution of the balanced-SSFP technique allows simpler volume rendering based on thresholding techniques. In addition, the almost isotropic dataset allows accurate multi-planar reformatting, which is particularly useful for delineating the complex anatomy of congenital heart disease. Thus, image data can be assessed using slice-by-slice examination, multi-planar reformatting, and 3D reconstruction of the entire cardiac and great vessel volume.

The acquisition is ECG gated, with a current temporal resolution of 40-80ms, and it is possible to acquire multiple phases of the cardiac cycle (currently ~ 10 frames), enabling four-dimensional dataset reconstruction [107].

4.2.2 Pulmonary Valve Function

4.2.2.1 RVOT and pulmonary valve MR imaging planes

The imaging planes for the RVOT and assessment of pulmonary flow are outlined in Figure 4.2. The RVOT is visualized by aligning a plane that passes through the pulmonary trunk/ conduit and the RV from a set of axial images (Figure 4.2a,b). An alternative way to obtain the RVOT view is by aligning a plane that passes through the pulmonary trunk/ conduit and descending aorta. This is usually a sagittal, or oblique sagittal plane. A plane perpendicular to this, in an axial or oblique axial orientation, will give a second view through the RVOT (Figure 4.2d). A plane through the pulmonary trunk/ conduit, just above the pulmonary valve, perpendicular to both RVOT views, can be used to assess through-plane pulmonary flow (Figure 4.2e).

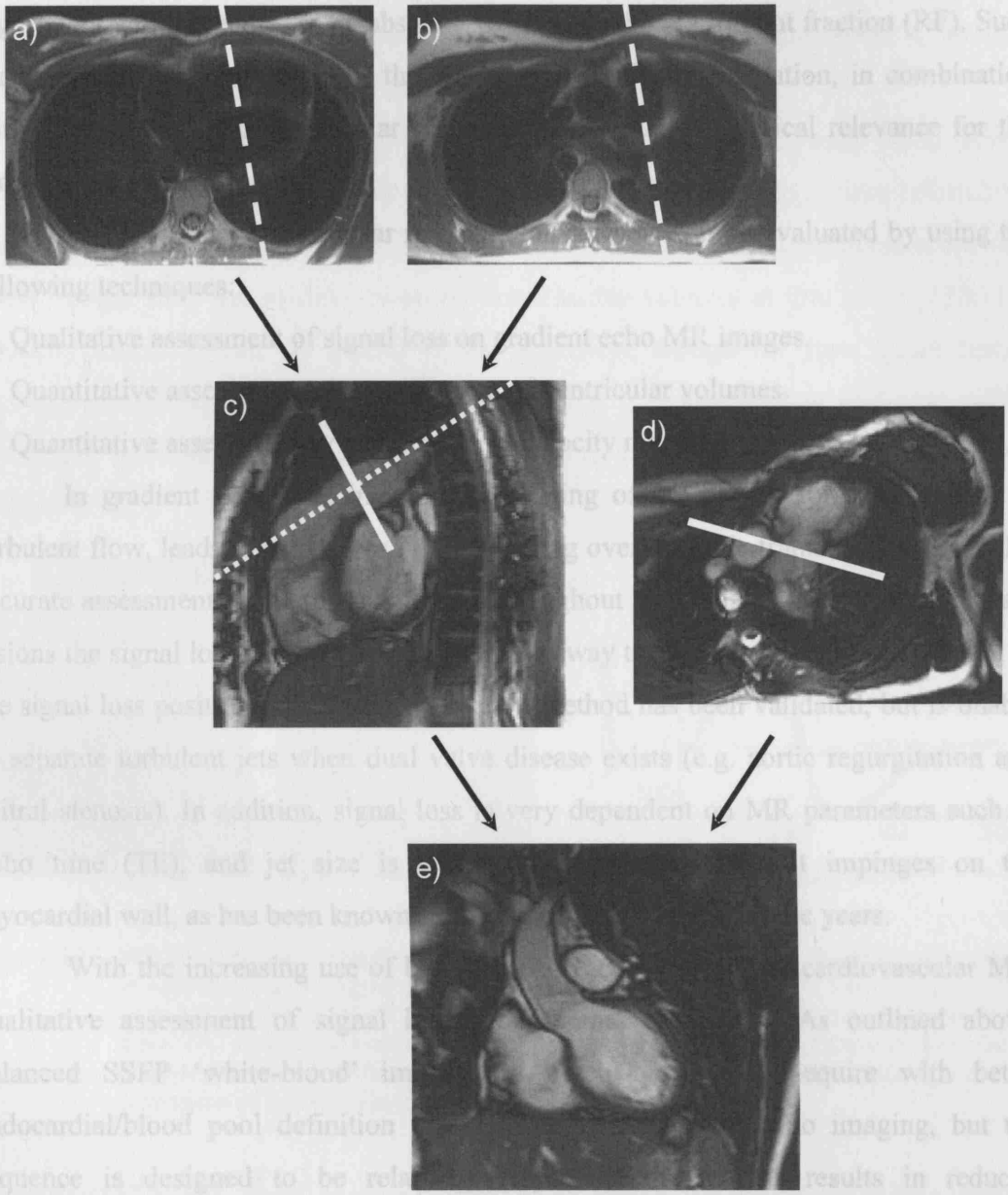

Figure 4.2 Imaging planes for the RVOT. The first RVOT view (c) is prescribed as an oblique plane through the main PA and RV on a set of axial images (a & b, dashed lines). The second RVOT plane (d) is prescribed perpendicular to the first RVOT view (dotted line on c). The imaging plane for pulmonary flow assessment (e) is aligned perpendicular to both RVOT views (solid lines on c & d). The imaging plane should be placed just above the pulmonary valve if visible [100].

4.2.2.2 Pulmonary incompetence

Currently, none of the conventional imaging techniques can accurately define valvular regurgitation, but MR which can image the regurgitant jet in any plane, and thus a 3D appreciation of the jet can be acquired. Furthermore, MR imaging can quantify the

regurgitant volume, either as an absolute value or as the regurgitant fraction (RF). Such a non-invasive quantification of the degree of valvular regurgitation, in combination with information about ventricular function, is of particular clinical relevance for the timing of valve replacement.

MR assessment of valvular regurgitation severity can be evaluated by using the following techniques:

- Qualitative assessment of signal loss on gradient echo MR images.
- Quantitative assessment by measurement of ventricular volumes.
- Quantitative assessment by phase contrast velocity mapping.

In gradient echo cine imaging, de-phasing of the proton spins, secondary to turbulent flow, leads to signal loss [108]. Imaging over multiple frames (20-40) enables accurate assessment of the turbulent flow, throughout the cardiac cycle. For regurgitant lesions the signal loss can be graded in a similar way to x-ray angiography according to the signal loss position [109]. This qualitative method has been validated, but is unable to separate turbulent jets when dual valve disease exists (e.g. aortic regurgitation and mitral stenosis). In addition, signal loss is very dependent on MR parameters such as echo time (TE), and jet size is easily underestimated when it impinges on the myocardial wall, as has been known from echocardiography for some years.

With the increasing use of balanced-SSFP cine imaging in cardiovascular MR, qualitative assessment of signal loss has become less useful. As outlined above, balanced SSFP 'white-blood' images are much quicker to acquire with better endocardial/blood pool definition than conventional gradient echo imaging, but the sequence is designed to be relatively flow insensitive. This results in reduced visualization of flow disturbance secondary to valvular regurgitation, in particular when regurgitation is mild. Thus, in subjects who are being imaged for other reasons, incidental detection of mild valvular regurgitation may not be apparent on balanced-SSFP cine imaging.

Magnetic resonance imaging can now be regarded as the best available *in-vivo* technique for the measurement of ventricular volumes [91]. In normal individuals there is a 1:1 relationship between the 2 ventricle stroke volumes. Any discrepancy between the ventricular stroke volumes in a patient with regurgitation will identify the

regurgitant volume. The main limitation of this technique, when used alone, is that only patients with a single regurgitant valve can be assessed.

The most accurate quantitative method for assessing great vessel blood flow is to use MR phase contrast velocity mapping. For velocity mapping, phase information and not magnitude information is displayed. Each point in the imaging plane is encoded with a phase shift that is directly proportional to the velocity at that point [110,111]. Velocity encoding can be applied in any direction, though for flow quantification through plane imaging is used. Stationary material is represented as mid-gray, whilst increasing velocities in either direction are shown in increasing grades of black or white (Figure 4.3a,b).

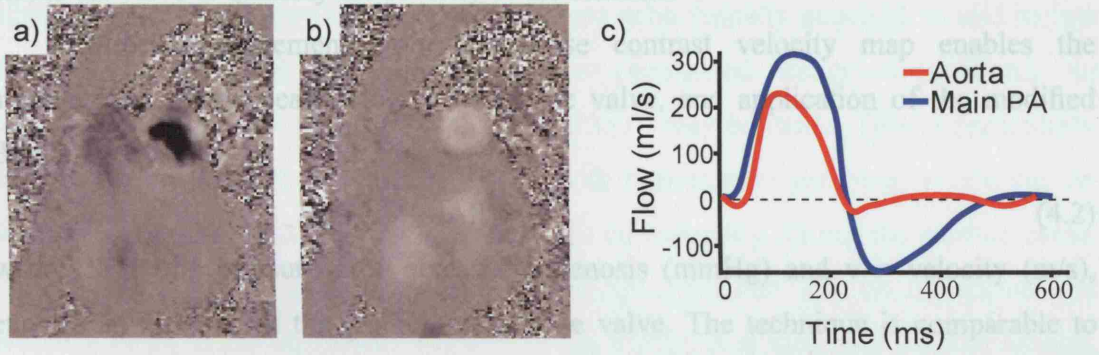

Figure 4.3 MR phase contrast velocity mapping during diastole (a) and systole (b). Stationary material is represented as mid-gray, flow towards the lungs by white pixels, and regurgitant flow back into the RV by black pixels; c) plot of blood flow volume vs. time in the aorta and main PA during the cardiac cycle. Negative values represent retrograde flow during diastole. Integration of the area under the curve for antegrade and retrograde flow enables calculation of the regurgitant volume per cardiac cycle (ml/beat).

Measurement of the spatial mean velocity for all pixels in a region of interest enables the calculation of the instantaneous flow volume at any point in the cardiac cycle. Calculation of the flow volume per heart beat can be made by integrating the instantaneous flow volumes for all frames throughout the cardiac cycle (area under the curve, Figure 4.3c). The pulmonary RF is given by:

$$\mathrm{RF}(\%) = \frac{\text{Pulmonary retrograde flow (ml/beat)}}{\text{Pulmonary forward flow (ml/beat)}} \times 100 \qquad (4.1)$$

This technique has been validated *in-vitro* and *in-vivo*, and is extremely accurate and reproducible [112-114]. The severity of regurgitation can be defined as follows [115]:

- Mild: RF = 15-20%
- Moderate: RF = 20-40%
- Severe: RF > 40%

Conventionally, phase contrast gradient echo images are acquired during shallow respiration over several minutes. Faster imaging can be performed, and it is now possible to acquire the real-time phase contrast data [116].

4.2.2.3 Pulmonary valvular or conduit stenosis

The presence of valvular stenosis can be identified by signal loss seen in gradient echo cine images. Velocity mapping may then be used to establish an accurate peak velocity across the valve to quantify the severity of the stenosis.

Direct measurement from the phase contrast velocity map enables the measurement of the peak velocity across the valve, and application of the modified Bernoulli equation,

$$\Delta P = 4v^2 \tag{4.2}$$

where ΔP = the pressure drop across the stenosis (mmHg) and v = velocity (m/s), enables an estimate of the gradient across the valve. The technique is comparable to Doppler echocardiography valvular stenosis measurements [117] with the main advantage of having no limitation of acoustic windows. Therefore, the velocity jet can be easily aligned in any direction.

Imaging can be performed through plane (velocity jet perpendicular to the imaging plane) or in-plane (velocity jet parallel to the imaging plane) [118,119]. Selection of the correct velocity encode gradient is essential to maintain sensitivity and accuracy of measurements, whilst avoiding aliasing. Most scanners now have a fast phase contrast velocity mapping sequence that can be acquired in approximately 15-20s. This enables an estimate of the peak velocity to be made before progressing to the more time-consuming conventional phase contrast velocity mapping sequence.

4.3 MAGNETIC RESONANCE ASSESSMENT PRE-PERCUTANOUS PULMONARY VALVE IMPLANTATION

As feasibility of PPVI became clear, the protocol for investigating the RVOT prior to intervention was improved and cardiovascular MR was introduced – after 30 PPVI – to assess the implantation site morphology and function.

The most important current limitation for PPVI is size. The size assessment of RVOT is difficult on echocardiography, and cardiovascular MR can be used to avoid diagnostic cardiac catheterization in a number of patients. MR assessment of the RVOT dimensions is best made on the 2 perpendicular RVOT cine images (Figure 4.2c,d), as it is the maximum (systolic) diameter that is most important to guarantee safe anchoring of the device. Using only the 'black-blood' spin echo (usually acquired in mid to late diastole) or the MR angiography images (non-gated image acquisition), an underestimation of the maximum size of the RVOT may be made. This is particularly true for native tissue that has been treated with transannular patching, which can be extremely dynamic, and can change dimension considerably during the cardiac cycle. Dynamic changes are less pronounced in conduits, but can still be significant and preclude PPVI. If the maximum diameter of the RVOT is at the upper limit of normal, PPVI may be attempted, but with the use of an accurate sizing balloon prior to actual implantation [Chapter 3]. If the RVOT diameter is too narrow, with marked conduit thickening, PPVI may not be possible, as the dimensions may be too small to enable the implanted pulmonary valve to open. The pre-PPVI MR is also used to quantify the degree of pulmonary incompetence, the gradient across any stenoses, the RV and LV dimensions and function, the presence of distal PA stenoses, and other cardiovascular problems (aortic incompetence, aortic root dilatation, aortic coarctation, airway narrowing, etc.). The complete MR protocol can be performed in approximately 1 hour. To date, the majority of patients we have studied for PPVI have been symptomatic, and treatment has been deemed necessary on clinical grounds. In the future, MR imaging may be able to help select asymptomatic patients, in whom future RV dysfunction may occur, for optimal timing of PPVI or surgical treatment.

4.4 MAGNETIC RESONANCE ASSESSMENT POST-PERCUTANEOUS PULMONARY VALVE IMPLANTATION

In our own practice, post-PPVI MR is performed soon after the procedure and at 1, 3 and 5 year follow-up, as part of a research study. The protocol for MR imaging following PPVI is as for the pre-PPVI assessment, with the exception that MR angiography is not performed, due to the stent artifact. 'Black-blood' spin echo imaging across the valve stent is the most useful sequence, as this allows the patency of the PPVI to be defined (Figure 4.1b). Pulmonary flow measurements are performed to confirm that the pulmonary valve functions properly (no pulmonary incompetence) and to define any residual peak velocity across the PPVI. The plane for the pulmonary flow measurements is positioned at the distal end of the PPVI to avoid stent artifact. Assessment of ventricular indices is also performed to establish the acute effects of PPVI.

4.5 CONCLUSION

The recent improvement in non-invasive cardiovascular MR imaging has resulted in a change in our approach to the definition of anatomy and physiology in subjects with congenital and acquired heart disease. The precise role of this imaging modality is to assess the right heart, pulmonary valve and pulmonary arteries for planning intervention to the RVOT for stenosis or incompetence, with either trans-catheter techniques or surgery. Cardiovascular MR imaging can be used to define intra-cardiac and great vessel anatomy, and ventricular and valvular function. This approach reduces the need for diagnostic cardiac catheterization and can provide important data for clinical decision-making.

In the future, routinely performed scans for MR assessment of RV and PAs will include new sequences that aim to investigate distensibility and deformations of the heart structures. For example, nowadays, little information is gained on the 3D deformations of the RVOT. Two-dimensional cine images present estimation errors due to the out-of-plane movement of the heart and the deformation of the 3D RVOT structure is not acquired otherwise. MR tagging, a technique which permits assessment of regional myocardial deformation and contraction movement in 3D, has already been shown to be successful in quantifying regional RV function in patients with tetralogy of

Fallot and might be used in the future to enhance the understanding of RVOT distensibility characteristics.

Further MR data collection should enable refinement of patient selection for treatment (PPVI vs. surgery) of pulmonary stenosis and/or incompetence, and optimise timing of intervention, a balance between the risk of the procedure, the finite life span of any valve or conduit inserted, and the risk of irreversible RV dysfunction if re-intervention is performed too late.

CHAPTER 5

FINITE ELEMENT METHOD

Engineering analysis can be simplified as a two stage process. In the first step, a physical system is represented with a mathematical model (equations of equilibrium, stress-strain relationships, etc.), followed by an approximate numerical solution of the mathematical model. The FE method is a simple, robust and efficient method of obtaining a numerical approximate solution for a given mathematical model of a structure. The essence of the FE method is to take a complex problem whose solution may be difficult to obtain, and decompose it into pieces (elements) upon each of which a simple approximation of the solution may be constructed, and then put the local approximate solutions together to obtain a global approximate solution. The method is applicable to a wide range of physical and engineering problems and is employed in many industrial fields to understand the complex behaviour of assemblies, explore some concepts for new designs, and simulate manufacturing processes. More recently, the FE method has been introduced in the cardiovascular arena for the design and development of medical devices such as stents, vascular and heart valve prostheses, and instruments. In this thesis, FE analyses have been used to study the fracture of current devices in static and fatigue conditions, and to assess the performance of coupled devices (stent-in-stent), and of a possible new stent design.

5.1 INTRODUCTION

Structural analysis comprises the set of physical laws and mathematics required to study and predict the behaviour of structures. From a theoretical perspective the primary goal of structural analysis is the computation of deformations, internal forces, and stresses in structures. In practice, structural analysis can be viewed more abstractly as a method to drive the engineering design process and/or prove the soundness of a product design without a dependence on directly testing it. To perform an accurate structural analysis, specific characteristics must initially be determined and hypothesized such as geometry, material properties, structural loads and support conditions. The results of the analysis typically include support reactions, stresses, displacements and deformations. This information is then compared to criteria that indicate the conditions of failure for the analysed product. There are three approaches to structural analysis: the mechanics of materials approach (also known as strength of materials), the elasticity theory approach (which is actually a special case of the more general field of continuum mechanics), and the FE approach. The first two make use of analytical formulations which apply mostly to simple linear elastic models, lead to closed-form solutions, and can often be solved by hand. The FE approach is actually a numerical method for solving differential equations generated by theories of mechanics such as elasticity theory and strength of materials, and is more applicable to structures of arbitrary size and complexity.

Regardless of approach, the formulation is based on the same three fundamental relations: equilibrium, constitutive, and compatibility. The solutions are approximate when any of these relations are only approximately satisfied, or only an approximation of reality. Each method has noteworthy limitations. The method of mechanics of materials is limited to very simple structural elements under relatively simple loading conditions. The allowed structural elements and loading conditions, however, are sufficient to solve many useful engineering problems. The theory of elasticity allows the solution of structural elements of general geometry under general loading conditions, in principle. Analytical solution, however, is limited to relatively simple cases. The solution of elasticity problems also requires the solution of a system of partial differential equations (PDEs), which is considerably more mathematically demanding than the solution of mechanics of materials problems, which require at most the solution

of an ordinary differential equation. The FE method is perhaps the most restrictive and most useful at the same time. This method itself relies upon other structural theories (such as the other two discussed here) for equations to solve. It does, however, make it generally possible to solve these equations, even with highly complex geometry and loading conditions, with the restriction that there is always some numerical error. Effective and reliable use of this method requires a solid understanding of its limitations. Moreover, the FE method depends heavily on the processing power of computers.

5.1.1 Mechanics of Materials Method

The simplest of the three methods here discussed, the mechanics of materials method, is available for simple structural members subject to specific loadings such as axially loaded bars, prismatic beams in a state of pure bending, and circular shafts subject to torsion. The solutions can under certain conditions be obtained using the superposition principle to analyze a member undergoing combined loading. Solutions for special cases exist for common structures such as thin-walled pressure vessels.

For the analysis of entire systems, this approach can be used in conjunction with statics, giving rise to the method of sections and method of joints for truss analysis, moment distribution for small rigid frames, and portal frame and cantilever method for large rigid frames. Except for moment distribution, which came into use in the 1930s, these methods were developed in their current forms in the second half of the nineteenth century. They are still used for small structures and for preliminary design of large structures.

The solutions are based on linear isotropic infinitesimal elasticity and Euler-Bernoulli beam theory. In other words, they contain the assumptions (among others) that the materials in question are elastic, that stress is related linearly to strain, that the material (but not the structure) behaves identically regardless of direction of the applied load, that all deformations are small, and that beams are long relative to their depth. As with any simplifying assumption in engineering, the more the model strays from reality, the less useful (and more dangerous) the result.

5.1.2 Elasticity Method

Elasticity methods are available generally for an elastic solid of any shape. Individual members such as beams, columns, shafts, plates and shells may be modelled. The solutions are derived from the equations of linear elasticity. The equations of elasticity are a system of 15 PDEs. Due to the nature of the mathematics involved, analytical solutions may only be produced for relatively simple geometries. For complex geometries, a numerical solution method such as the FE method is necessary.

5.2 FINITE ELEMENT METHOD

The FE method models a structure as an assembly of elements or components with various forms of connection between them. Thus, a continuous system such as a plate or shell is modelled as a discrete system with a finite number of elements interconnected at finite number of nodes. The behaviour of individual elements is characterised by the element's stiffness or flexibility relation, which altogether leads to the system's stiffness or flexibility relation. To establish the element's stiffness or flexibility relation, the mechanics of materials approach for simple one-dimensional (1D) bar elements, and the elasticity approach for more complex 2D and 3D elements can be used. The analytical and computational developments are best effected throughout by means of matrix algebra.

Early applications of matrix methods were for articulated frameworks with truss, beam and column elements; later and more advanced matrix methods, referred to as FE analysis, model an entire structure with 1D, 2D, and 3D elements and can be used for articulated systems together with continuous systems such as a pressure vessel, plates, shells, and 3D solids. Commercial computer software for structural analysis typically uses matrix FE analysis, which can be further classified into 2 main approaches: the displacement or stiffness method, and the force or flexibility method. The stiffness method is the most popular by far, due to its ease of implementation as well as of formulation for advanced applications. The FE technology is now sophisticated enough to handle just about any system as long as sufficient computing power is available. Its applicability includes, but is not limited to, linear and non-linear analysis, solid and fluid interactions, materials that are isotropic, orthotropic, or anisotropic, and external effects that are static, dynamic, and environmental factors. This, however, does not

imply that the computed solution will automatically be reliable because much depends on the model and the reliability of the data input [120].

5.3 MATHEMATICAL FORMULATION OF THE FINITE ELEMENT METHOD FOR STRUCTURAL ANALYSIS

Consider the equilibrium of a general 3D body located in a fixed coordinate system X, Y, Z (Figure 5.1). Consider that the body is subjected on a certain surface traction f^S on the area S^f and a certain body force f^B, and a portion of the external area S^u has a prescribed displacement U^S. The displacement of the body from the unloaded configuration is measured in the coordinate system X, Y, Z and is denoted as **U**, where

$$\mathbf{U}(X,Y,X) = \begin{bmatrix} U \\ V \\ W \end{bmatrix} \tag{5.1}$$

and $\mathbf{U} = \mathbf{U}^S$ on the surface area S^u.

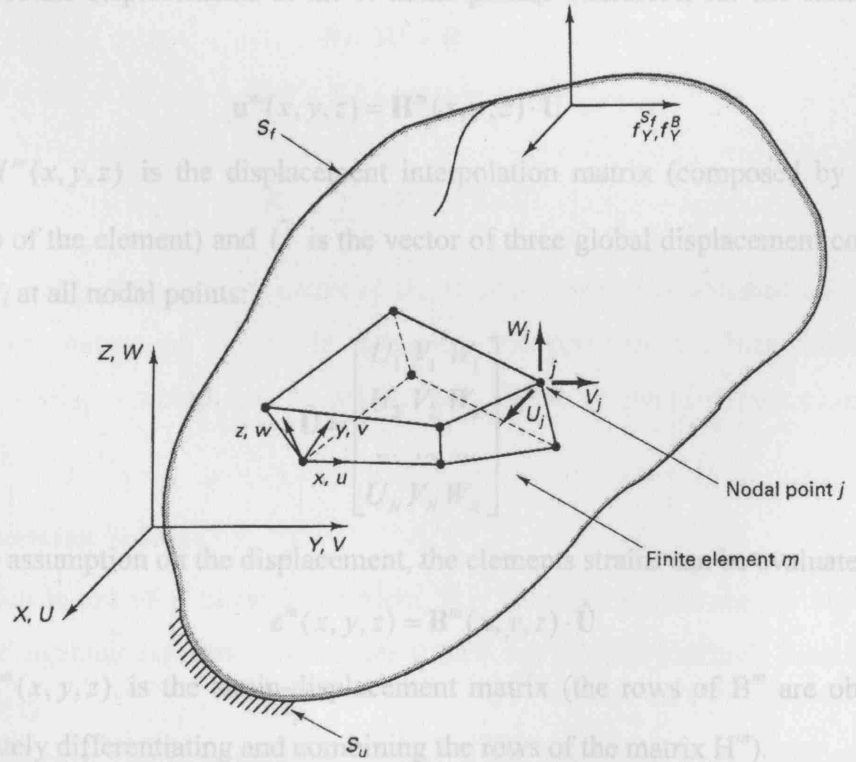

Figure 5.1 Schematic diagram of a 3D volume in a Cartesian coordinate system.

The strains corresponding to **U** are denoted as ε and the stresses corresponding to ε are denoted as τ. For a certain material, the relationship between ε and τ is denoted as:

$$\boldsymbol{\tau} = \mathbf{C} \cdot \boldsymbol{\varepsilon} \tag{5.2}$$

where C is the stress-strain material matrix for a linear elastic continuum. The Principle of Virtual Work states that the equilibrium of the body requires that, for any compatible small virtual displacement imposed on the body in its state of equilibrium, the total internal virtual work is equal to the total external virtual work:

$$\int_V \bar{\boldsymbol{\varepsilon}}^T \cdot \boldsymbol{\tau} dV = \int_V \bar{\mathbf{U}}^T \cdot \mathbf{f}^B dV + \int_{S^f} \bar{\mathbf{U}}^S \cdot \mathbf{f}^S dS \tag{5.3}$$

where **U** is the virtual displacement and ε is the corresponding virtual strain. τ is the stress in equilibrium with the applied loads.

In the FE analysis, we approximate the body as an assemblage of discrete finite elements interconnected at nodal points on the element boundaries. The displacement measured in a local coordinate system x, y, z within each element is assumed to be a function of the displacements at the N nodal points. Therefore, for the element *m* we have:

$$\mathbf{u}^m(x,y,z) = \mathbf{H}^m(x,y,z) \cdot \hat{\mathbf{U}} \tag{5.4}$$

where $H^m(x,y,z)$ is the displacement interpolation matrix (composed by the shape functions of the element) and $\hat{U}$ is the vector of three global displacement components U_i, V_i, W_i at all nodal points:

$$\hat{\mathbf{U}} = \begin{bmatrix} U_1 & V_1 & W_1 \\ U_2 & V_2 & W_2 \\ \cdots & \cdots & \cdots \\ U_N & V_N & W_N \end{bmatrix} \tag{5.5}$$

With this assumption on the displacement, the elements strains can be evaluated as

$$\boldsymbol{\varepsilon}^m(x,y,z) = \mathbf{B}^m(x,y,z) \cdot \hat{\mathbf{U}} \tag{5.6}$$

where $B^m(x,y,z)$ is the strain-displacement matrix (the rows of B^m are obtained by appropriately differentiating and combining the rows of the matrix H^m).

The relationships (5.4) and (5.6) can be rewritten using virtual displacements and strains:

$$\bar{\mathbf{u}}^m(x,y,z) = \mathbf{H}^m(x,y,z) \cdot \bar{\hat{\mathbf{U}}} \tag{5.7}$$

$$\bar{\varepsilon}^m(x,y,z) = B^m(x,y,z)\cdot\bar{\hat{U}} \tag{5.8}$$

Substituting in (5.3) and hypothesizing the validity of (5.8), it is possible to obtain:

$$\bar{\hat{\mathbf{U}}}^T\left[\sum_m \int_{V^m} \mathbf{B}^{mT}\mathbf{C}^m\mathbf{B}^m dV^m\right]\hat{\mathbf{U}} = \bar{\hat{\mathbf{U}}}^T\left[\left\{\sum_m \int_{V^m} \mathbf{H}^{mT}\mathbf{f}^{Bm} dV^m\right\} + \left\{\sum_m \int_{S^m} \mathbf{H}^{SmT}\mathbf{f}^{Sm} dS^m\right\}\right] \tag{5.9}$$

Since this equation has to be valid for every displacement $\bar{\hat{U}}$, it can be simplified in the form:

$$\mathbf{KU} = \mathbf{R} \tag{5.10}$$

where

$$\mathbf{U} = \hat{\mathbf{U}} \tag{5.11}$$

$$\mathbf{K} = \sum_m \int_{V^m} \mathbf{B}^{mT}\mathbf{C}^m\mathbf{B}^m dV^m \tag{5.12}$$

$$\mathbf{R} = \mathbf{R}^B + \mathbf{R}^S \tag{5.13}$$

$$\mathbf{R}^B = \sum_m \int_{V^m} \mathbf{H}^{mT}\mathbf{f}^{Bm} dV^m \tag{5.14}$$

$$\mathbf{R}^S = \sum_m \int_{S^m} \mathbf{H}^{SmT}\mathbf{f}^{Sm} dS^m \tag{5.15}$$

The matrix K is the stiffness matrix of the structure, which is obtained assembling all the stiffness matrix of the single elements. The problem has been reduced to an algebraic problem which can be solved with direct or iterative numerical methods [121,122].

5.3.1 Iteration Scheme

For the resolution of a physical problem, the FE method requires the solution of a system of algebraic equations which are solved using iterate methods because of their non linearity.

The most common iterative method is the Newton-Raphson method: let **X**(t) denote the vector of all the unknowns at the time step *t*, the equation for the solution of the physical problem can be written as:

$$\mathbf{F}(\mathbf{X}(t)) = 0 \tag{5.16}$$

where **F** is the equation vector. For this scheme, a solution increment $\Delta\mathbf{X}$ is solved from a linearized equation and the solution vector **X** is then updated accordingly. The linearized equation can be expressed as:

$$\mathbf{A}\Delta\mathbf{X} = \mathbf{B} \tag{5.17}$$

and the new solution is updated as:

$$\mathbf{X} \rightarrow \mathbf{X} + \Delta\mathbf{X} \tag{5.18}$$

where **A** is the coefficient matrix and **B** is called the right-hand side vector. They are calculated as:

$$\mathbf{A} = \frac{\partial \mathbf{F}(\mathbf{X})}{\partial \mathbf{X}} \tag{5.19}$$

$$\mathbf{B} = -\mathbf{F}(\mathbf{X}) \tag{5.20}$$

The convergence of the Newton-Raphson scheme strongly depends on the initial guess $\mathbf{X}_0$ which is usually the solution calculated in the previous solution time step.

5.4 FINITE ELEMENT MODELLING IN THE THESIS

The FE method is employed in many industrial fields to understand the complex behaviour of assemblies, explore some concepts for new designs, and simulate the manufacturing processes. Traditionally, new products have been developed by prototyping and evaluation; however this process is very time consuming and often does not fully reveal potential failures. Finite element modelling and analysis can greatly reduce testing and the time to market by allowing the designer to examine any number of scenarios in optimizing the design and to 'virtually' test (in silico) the product before any physical building occurs. Simulation and modelling can also provide detailed insight into the mechanical behaviour of the design, which may not be discoverable through normal testing and experimentation. However, simulation cannot be done without physical properties and some simplifying assumptions are inevitably made. Thus simulations act to complement, rather than substitute, testing.

Nowhere is this in better evidence than in the development of advanced biomedical implants, since medical technology continues to advance rapidly as physicians and engineers move closer to and understand better each other's needs. In the cardiovascular arena, the FE method has been introduced for the design of medical devices such as stents, vascular and heart valve prostheses, and instruments [123-141].

Nowadays, FE analyses are also part of the preclinical testing process for new medical devices, required by the US Food and Drug Administration before the launch of a new product in the market [142-144].

In this thesis, the FE method has been used to analyze some of the factors responsible for current device fracture in static, fatigue and *in-situ* conditions [Chapter 8 and 9], to assess the performance of coupled devices (stent-in-stent) [Chapter 8], and to study a possible new stent design [Chapter 10]. The analyses have been performed using the FE commercial code ABAQUS/Standard 6.4 (Hibbit Karlsson & Sorenses, Inc., Pawtucket, RI, USA), which was installed on a dedicated Dell Precision Workstation (Dual Intel® Xeon™ Processor – 3.2GHz, 800MHz FSB, 1MB cache).

Finite element method and FE codes are extremely versatile and powerful tools, but, in spite of the significant recent advances that have been made in developing FE packages, the obtained results and the accuracy of the solutions are always a function of the mesh resolution [Section 8.2.2 and Section 8.3.1] and of the hypotheses adopted for the model. The complexity of the real problem is always simplified in a numerical model that tries to describe the reality as best as is possible. In particular, if biological structures are involved in the model, mandatory approximations have to be made and a validation process is not always available. This is the major limit of the FE method.

In this thesis, FE modelling is used as a tool to gain information about the behaviour of complicated structures, such as stents, through the measurement of some characteristic parameters. However, these parameters are not evaluated in their absolute value, but as a comparison between different stent designs and different loading conditions. Therefore, each FE stent analysis performed in the thesis is still subject to the adopted simplifications intrinsic to modelling, but these assumptions and restrictions are the same for each compared model, thus having the same effects.

CHAPTER 6

RIGHT VENTRICULAR OUTFLOW TRACT MORPHOLOGICAL CLASSIFICATION

The aim of this chapter is to identify sub-groups of RVOT morphology that would be suitable for PPVI and to document their prevalence in our patient population. Therefore, 83 consecutive patients referred to our centre for MR investigation of RVOT dysfunction were retrospectively studied. A morphological classification was created according to visual assessment of 3D reconstructions and detailed measurement. Diagnosis, RVOT type, surgical history and treatment outcomes were documented. RVOT morphology resulted heterogeneous; nevertheless, 5 patterns were visually identified. Type I, a pyramidal morphology, was most prevalent (49%) and related to the presence of a transannular patch. Other types (II–V) were seen more commonly in patients with conduits. Two patients had unclassifiable morphology. Ninety-five percent of patients were assigned to the correct morphological classification by visual assessment alone. Percutaneous pulmonary valve implantation was performed successfully in 10 patients with Type II–V morphology and in 1 patient with unclassifiable morphology. Percutaneous implantation was not performed in patients with Type I morphology because of the high risk of device dislodgement. In conclusion, we have created a morphological classification of the RVOT in patients referred for assessment of RVOT dysfunction. Though only 13% of our patients underwent PPVI, >50% of RVOT morphologies may be suitable for this approach, in particular with the development of new devices appropriate for larger RVOTs.

6.1 INTRODUCTION

In the past few years the number of patients requiring interventions to their pulmonary valve and referred to our centre for possible percutaneous treatment has been increasing exponentially. However, among these patients, only a few are selected for PPVI. Therefore, as a starting point for this thesis, I wanted to understand the morphological constraints of the RVOT for PPVI treatment. In order to achieve this, I selected a cohort of patients who had undergone MR assessment of their RVOT to visualise their RVOT anatomy and identify sub-groups of RVOT morphology that would be suitable for PPVI and to document their prevalence in our patient population. The methodology I developed for the RVOT morphology assessment is described in Section 6.2. This initial study also enabled me to familiarize myself with the clinical problems related to the treatment of RVOT dysfunction and with the imaging methods (advantages and limitations) that are currently used to acquire data for RVOT assessment. The resulting morphological classification is documented in Section 6.3, and further discussed in Section 6.4.

6.2 METHODS

6.2.1 Study Population

Eighty-three consecutive patients with RVOT dysfunction following previous repair of congenital heart disease, who were referred to our institution for MR imaging between March 2003 and February 2005, were retrospectively studied. Clinical indications for PPVI mirror the conventional criteria for surgical re-intervention. Therefore, the analysed cohort of patients included pulmonary regurgitation with increasing RV size, substantial tricuspid regurgitation, arrhythmia and/or impairment in exercise capacity or RVOT obstruction with RV pressure greater than 2/3 systemic. Patients < 5 years old were not included as they are currently unsuitable for PPVI on account of size alone. Patient characteristics are shown in Table 6.1. Institutional ethical approval for MR imaging was obtained and all subjects (and/or a parent/guardian) gave informed consent for retrospective data analysis of the MR images.

Characteristic	N	%
Male	45	54.2
Age at scan:		
5-12 years	30	36.1
12-18 years	38	45.8
> 18 years	15	18.1
Primary diagnosis:		
Tetralogy of Fallot	48	48.2
Pulmonary atresia/VSD	19	22.9
Truncus arteriosus	7	8.4
Transposition of the great arteries	6	7.2
Isolated pulmonary stenosis	5	6.0
Double outlet right ventricle	4	4.8
Others	2	2.4
RVOT type:		
Transannular patch	40	48.2
Homograft	23	27.7
Native	9	10.8
RVOT patch	8	9.6
Others	3	3.6
Open operations:		
1	67	80.7
2	13	15.7
3	2	2.4
4	1	1.2

Table 6.1 Patient characteristics.

6.2.2 Magnetic Resonance Imaging

MR imaging was performed as described in Chapter 4. A 1.5T scanner (Siemens Medical Systems, Erlangen, Germany) was used with a 4-element body phased array coil. Pulmonary artery through-plane flow data was acquired using a flow sensitive gradient echo sequence (TR 8ms, TE 3.8ms, flip angle 30°, 3 averages, parallel imaging (iPAT) factor 2, resolution 1.3 x 1.3 x 5mm) and retrospective cardiac gating during free breathing. The image plane was located at the midpoint of the pulmonary trunk. Pulmonary flow and velocity was calculated from the phase contrast images using a semi-automatic vessel edge detection algorithm with operator correction. Regurgitant fraction was calculated as the percent backward flow over forward flow. A 3D gradient echo sequence was used to acquire the MR angiography after the administration of 0.4

mL/kg of Gadolinium – imaging parameters: TR 3.7ms, TE 1.4ms, flip angle 25°, resolution 1.3 x 1.3 x 1.3mm.

6.2.3 Three-Dimensional Reconstruction

Reconstruction from MR images was performed using the image processing package Mimics 9.0 (Materialise Inc., Ann Arbor, MI, USA). Segmentation and editing tools were used to detect the region of interest, the RVOT, and create its 3D volume.

The raw DICOM data of the patient's MR angiogram were imported into Mimics where they can be viewed in 2D (automatic axial, coronal and sagittal slices) and in 3D after segmentation. Segmentation masks were used to detect the region of interest, the RVOT (Figure 6.1). The first action performed to create a segmentation mask was thresholding. The region of interest was selected by defining a range of gray values. The boundaries of this range were the lower and upper threshold value. All pixels with a gray value in this range were highlighted in the mask. Thus, to detect the inner arterial wall, 2 suitable threshold values were chosen. Next, the Region Growing algorithm was used to eliminate noise and separate structures that were not connected. Finally, Manual Editing functions were used to draw, erase or restore parts of the image, by clicking on single pixels. When the region of interest was completely selected, the software calculated a 3D model of the structure by means of pattern recognition and interpolation algorithms.

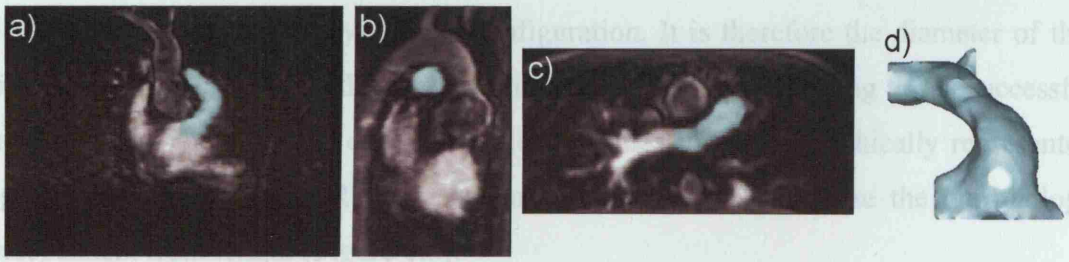

Figure 6.1 Two-dimensional MR images of the heart in the a) coronal, b) sagittal and c) axial view. The cyan mask represents the selected region of interest, the RVOT; d) Mimics 3D volume render of the selected RVOT.

6.2.4 Three-Dimensional Volume Analysis

Mimics software enables rotation and scaling of 3D objects. This allows complete appreciation of the 3D RVOT anatomy. First, a morphological classification was created based on visualization of the patients' RVOT alone. Five types of RVOT

morphology were identified (Figure 6.2). Type I had a pyramidal shape (wide proximally and narrow distally). Type II had a constant diameter. Type III had an inverted pyramidal shape (narrow proximally and wide distally). Type IV was wide centrally but narrowed proximally and distally. Type V was narrowed centrally but wide proximally and distally. The 83 patients were classified in these groups by myself, blinded to the assessment of the clinician.

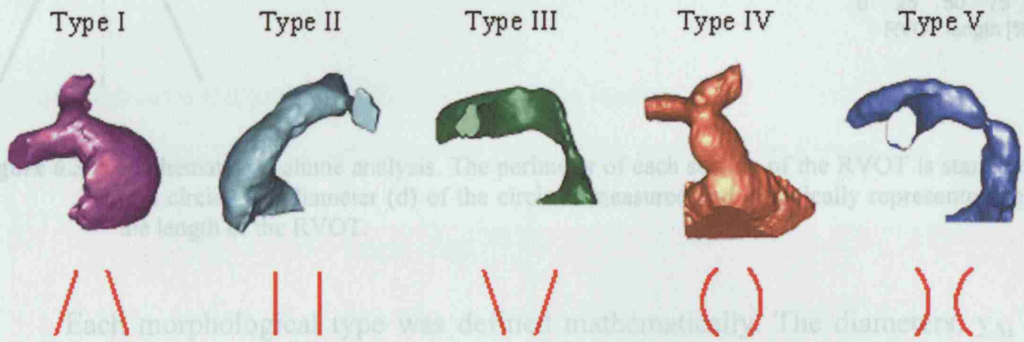

Figure 6.2 Five types of RVOT morphology.

The centre axis of the 3D RVOT volume was identified and, starting from the pulmonary bifurcation, divided into 10 mm segments. The RVOT volume was then sectioned by planes orthogonal to the centre axis at each of these points. The perimeter of each of these sections was measured, and the shape of the cross-sectional area standardized to a circle. During PPVI, pressure inflation of the balloon deploying the device usually achieves a cylindrical configuration. It is therefore the diameter of this final circle which will influence stability of the device, resulting in a successful implantation. The diameter of these circles was measured and graphically represented against the length of the RVOT, standardized in order to visualize the morphology independent from length (Figure 6.3).

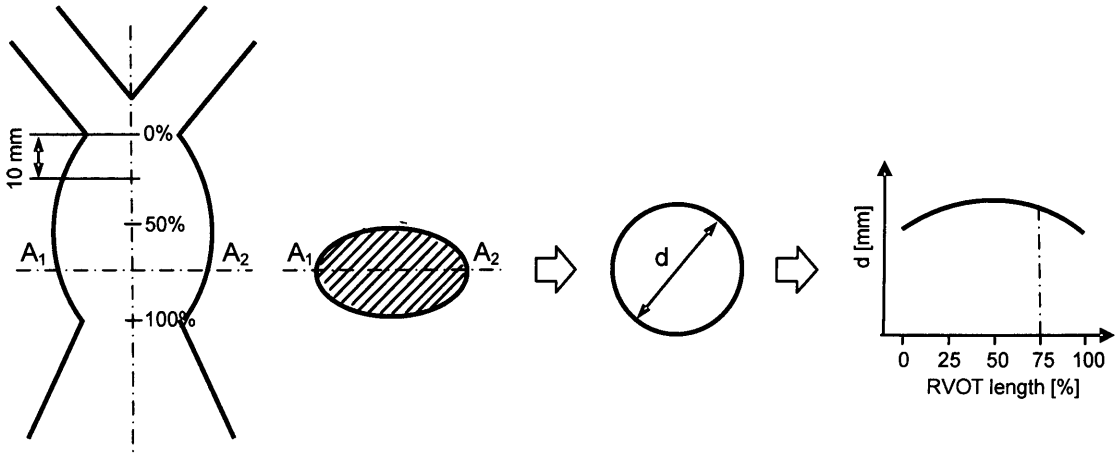

Figure 6.3 Mathematical volume analysis. The perimeter of each section of the RVOT is standardized to a circle. The diameter (d) of the circle is measured and graphically represented against the length of the RVOT.

Each morphological type was defined mathematically. The diameters, y_A, and y_C, were measured at 0% and 100% of the RVOT length, respectively for all morphological types. The diameter, y_B was measured at 50% of the RVOT length in patients with Type I, II or III morphology. In patients with Types IV morphology, y_B was measured at the point of maximum diameter, irrespective of its position along the length of the RVOT. In Type V morphology, y_B was measured at the point of minimum diameter. The average diameter $\bar{y}$ along the RVOT length was determined. The difference between diameters were calculated and expressed as a percentage of the average RVOT diameter:

$$\Delta y_1 = \frac{y_B - y_A}{\bar{y}} \cdot 100 \qquad \text{and} \qquad \Delta y_2 = \frac{y_C - y_B}{\bar{y}} \cdot 100$$

The mathematical rules defining each morphological type are described by the following systems and use the two unknowns Δy_1 and Δy_2:

$$\text{Type I}: \begin{cases} \Delta y_1 > -10\% \\ \Delta y_2 > -10\% \\ \Delta y_1 + \Delta y_2 > 10\% \quad \vee \quad \Delta y_1 > 10\% \quad \vee \quad \Delta y_2 > 10\% \end{cases}$$

$$\text{Type II}: \begin{cases} -10\% \le \Delta y_1 \le 10\% \\ -10\% \le \Delta y_2 \le 10\% \\ -10\% \le \Delta y_1 + \Delta y_2 \le 10\% \end{cases}$$

$$\text{Type III}: \begin{cases} \Delta y_1 < 10\% \\ \Delta y_2 < 10\% \\ \Delta y_1 + \Delta y_2 < -10\% \quad \vee \quad \Delta y_1 < -10\% \quad \vee \quad \Delta y_2 < -10\% \end{cases}$$

$$\text{Type IV}: \begin{cases} \Delta y_1 > 10\% \\ \Delta y_2 < -10\% \end{cases}$$

$$\text{Type V}: \begin{cases} \Delta y_1 < -10\% \\ \Delta y_2 > 10\% \end{cases}$$

where $\vee$ indicates the inclusive disjunction of the terms.

The above mathematical descriptions are graphically presented in Figure 6.4.

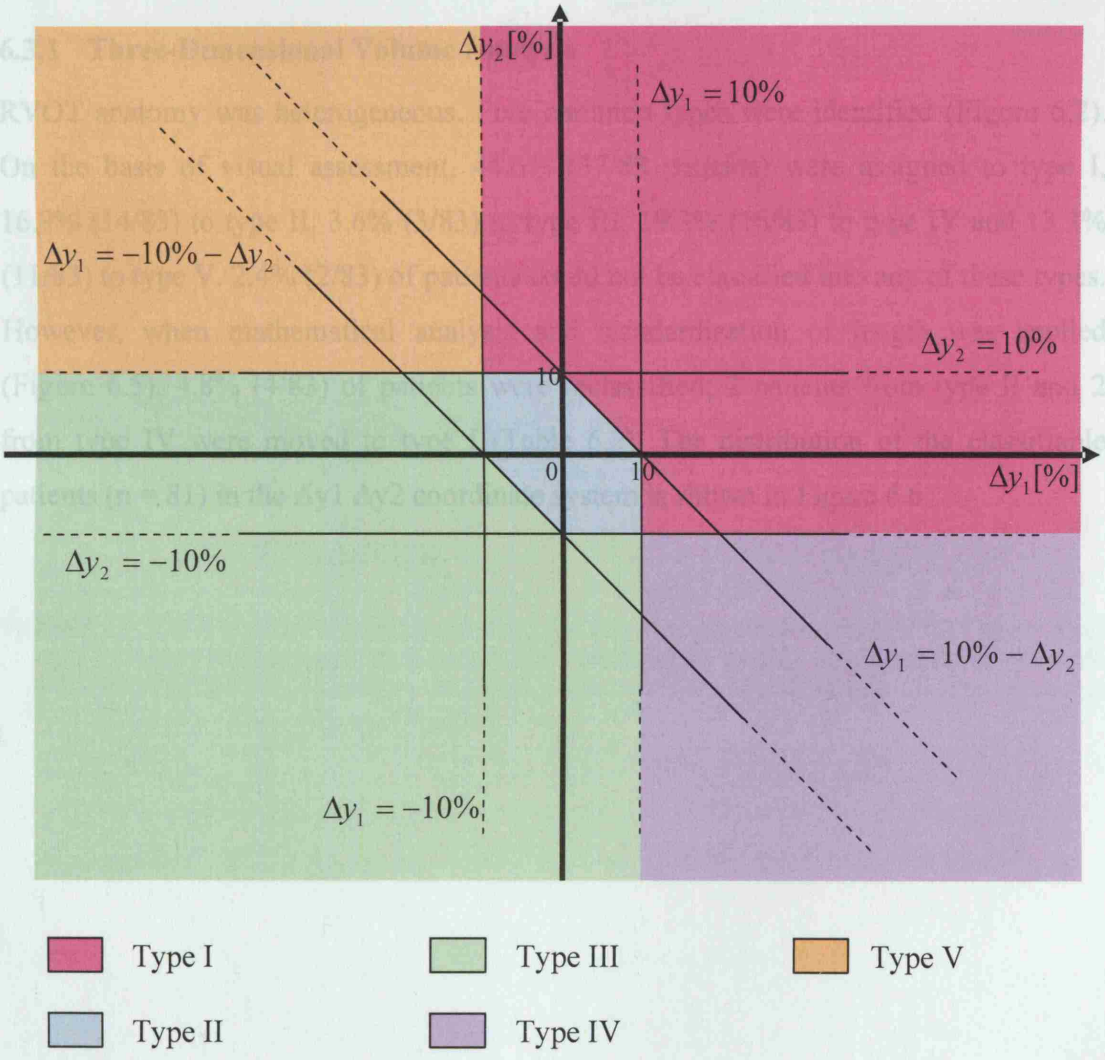

Figure 6.4 Graphical representation of the systems' solutions which mathematically describe the 5 morphological types.

6.2.5 Statistical Analysis

The following clinical data were collected for the patient population and correlations between these and the morphological groups were sought: primary diagnosis, RVOT type, surgical history and treatment outcomes, RVOT peak velocity and pulmonary RF.

All categorical variables were expressed as an absolute number and a percentage. Comparison between categories and calculation of the odds ratio were made using the Fisher's exact test. Significance was accepted if $p < 0.05$ with 95% confidence intervals.

6.3 RESULTS

6.3.1 Three-Dimensional Volume Analysis

RVOT anatomy was heterogeneous. Five common types were identified (Figure 6.2). On the basis of visual assessment, 44.6% (37/83 patients) were assigned to type I, 16.9% (14/83) to type II, 3.6% (3/83) to type III, 19.3% (16/83) to type IV and 13.3% (11/83) to type V. 2.4% (2/83) of patients could not be classified into any of these types. However, when mathematical analysis and standardization of length was applied (Figure 6.5), 4.8% (4/83) of patients were reclassified; 2 patients from type II and 2 from type IV were moved to type I (Table 6.2). The distribution of the classifiable patients ($n = 81$) in the $\Delta y1$ $\Delta y2$ coordinate system is shown in Figure 6.6.

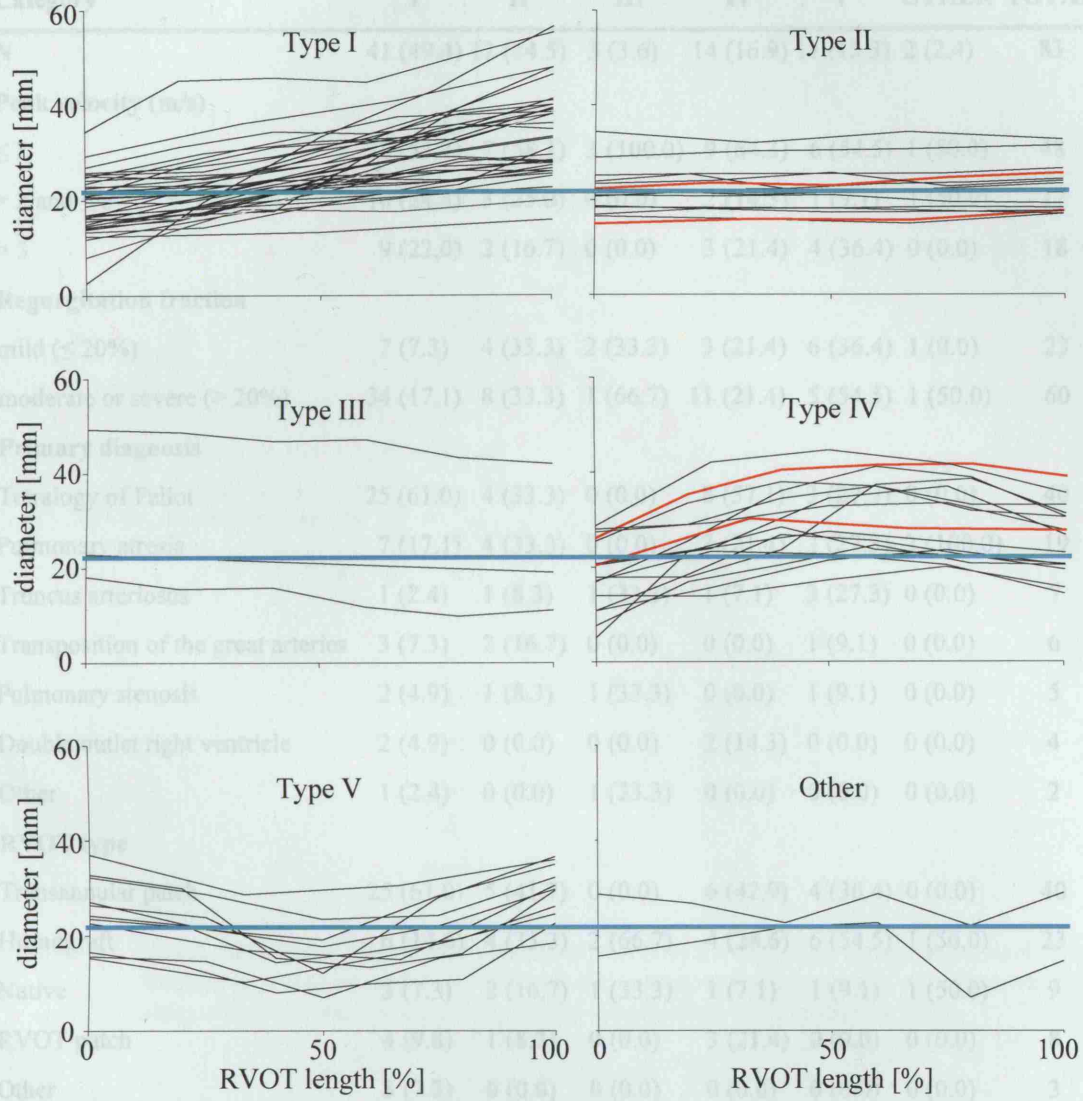

Figure 6.5 RVOT profiles divided by morphological types and standardized along RVOT length. Only RVOT diameters <22mm in diameter (blue lines) are suitable for the current PPVI device. The red lines represent patients who were wrongly assigned to their morphological type using visualization of 3D geometry alone.

Category	I	II	III	IV	V	OTHER	TOTAL
N	41 (49.4)	12 (14.5)	3 (3.6)	14 (16.9)	11 (13.3)	2 (2.4)	83
Peak velocity (m/s)							
≤ 2	22 (53.7)	7 (58.3)	3 (100.0)	9 (64.3)	6 (54.5)	1 (50.0)	48
> 2 and ≤ 3	10 (24.4)	3 (25.0)	0 (0.0)	2 (14.3)	1 (9.1)	1 (50.0)	17
> 3	9 (22.0)	2 (16.7)	0 (0.0)	3 (21.4)	4 (36.4)	0 (0.0)	18
Regurgitation fraction							
mild (≤ 20%)	7 (7.3)	4 (33.3)	2 (33.3)	3 (21.4)	6 (36.4)	1 (0.0)	23
moderate or severe (> 20%)	34 (17.1)	8 (33.3)	1 (66.7)	11 (21.4)	5 (54.5)	1 (50.0)	60
Primary diagnosis							
Tetralogy of Fallot	25 (61.0)	4 (33.3)	0 (0.0)	8 (57.1)	3 (27.3)	0 (0.0)	40
Pulmonary atresia	7 (17.1)	4 (33.3)	0 (0.0)	3 (21.4)	3 (27.3)	2 (100.0)	19
Truncus arteriosus	1 (2.4)	1 (8.3)	1 (33.3)	1 (7.1)	3 (27.3)	0 (0.0)	7
Transposition of the great arteries	3 (7.3)	2 (16.7)	0 (0.0)	0 (0.0)	1 (9.1)	0 (0.0)	6
Pulmonary stenosis	2 (4.9)	1 (8.3)	1 (33.3)	0 (0.0)	1 (9.1)	0 (0.0)	5
Double outlet right ventricle	2 (4.9)	0 (0.0)	0 (0.0)	2 (14.3)	0 (0.0)	0 (0.0)	4
Other	1 (2.4)	0 (0.0)	1 (33.3)	0 (0.0)	0 (0.0)	0 (0.0)	2
RVOT type							
Transannular patch	25 (61.0)	5 (41.7)	0 (0.0)	6 (42.9)	4 (36.4)	0 (0.0)	40
Homograft	6 (14.6)	4 (33.3)	2 (66.7)	4 (28.6)	6 (54.5)	1 (50.0)	23
Native	3 (7.3)	2 (16.7)	1 (33.3)	1 (7.1)	1 (9.1)	1 (50.0)	9
RVOT patch	4 (9.8)	1 (8.3)	0 (0.0)	3 (21.4)	0 (0.0)	0 (0.0)	8
Other	3 (7.3)	0 (0.0)	0 (0.0)	0 (0.0)	0 (0.0)	0 (0.0)	3
Procedure							
Surgery	30 (73.2)	5 (41.7)	0 (0.0)	3 (21.4)	4 (36.4)	0 (0.0)	42
PPVI	0 (0.0)	2 (16.7)	2 (66.7)	3 (21.4)	3 (27.3)	1 (50.0)	11
Other percutaneous	3 (7.3)	1 (8.3)	0 (0.0)	1 (7.1)	0 (0.0)	1 (50.0)	6
Surgery + other percutaneous	1 (2.4)	0 (0.0)	0 (0.0)	0 (0.0)	1 (9.1)	0 (0.0)	2
No intervention	7 (17.1)	4 (33.3)	1 (33.3)	7 (50.0)	3 (27.3)	0 (0.0)	22

Table 6.2 Summary of results. The numbers in brackets indicate the percentage values [%].

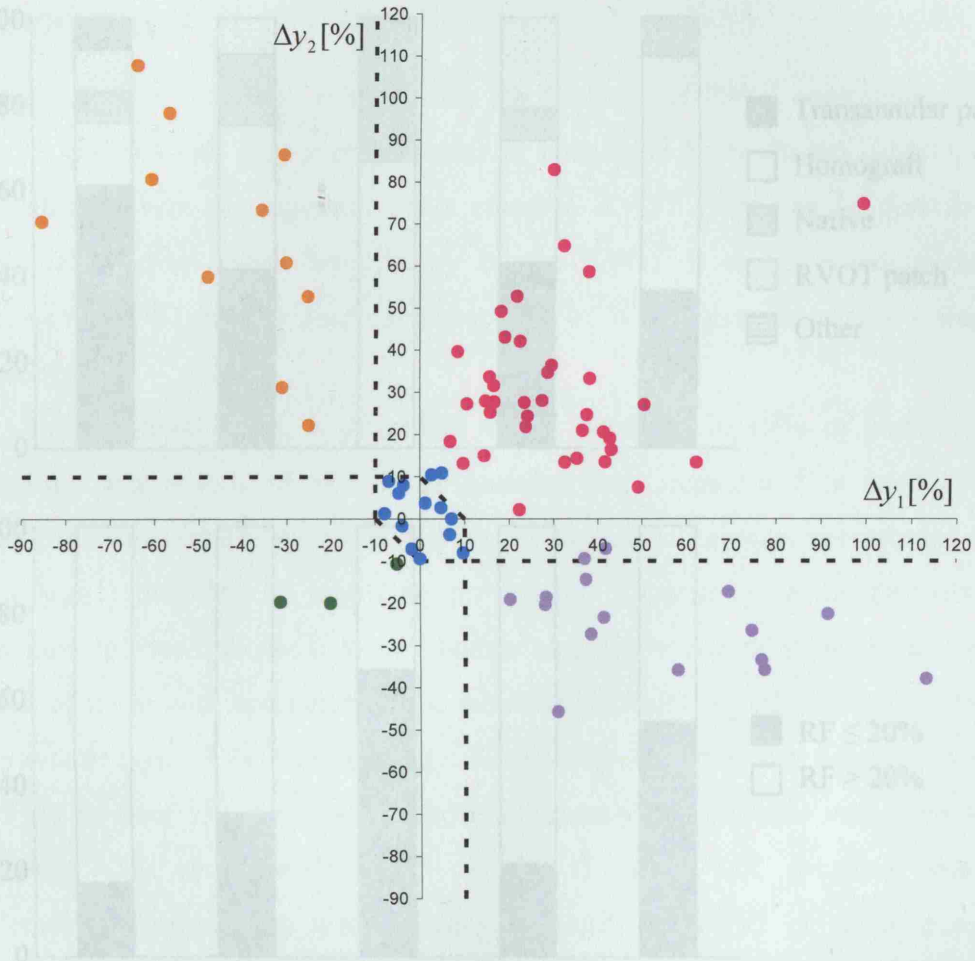

Figure 6.6 Distribution of the classifiable patients (n = 81) in the Δy1-Δy2 coordinate system. Four datasets (2 turquoise and 2 lavender points) corresponded to patients who were wrongly assigned to their morphological type using visualization of 3D geometry alone.

6.3.2 Clinical Correlates

The majority of patients in our population had tetralogy of Fallot and the commonest outflow tract was a transannular patch. The prevalence of different diagnoses and RVOT types is shown in Table 6.2. No direct correlation was found between surgical history or underlying diagnosis and morphological type. Transannular patch was more commonly seen in patients with type I morphology compared to those with types II-V (Figure 6.7a, Odds Ratio 0.28, $p < 0.05$). Furthermore, type I morphology was associated with a higher RF than types II-V (Figure 6.7b, Odds Ratio 0.33, $p < 0.05$).

Eleven patients underwent PPVI: 2 patients with type II morphology, 2 with type III, 3 with type IV and 3 with type V and 1 patient whose morphology was unclassifiable. All had a homograft outflow tract and none had type I morphology which was felt unsuitable because of the risk of proximal device dislodgement.

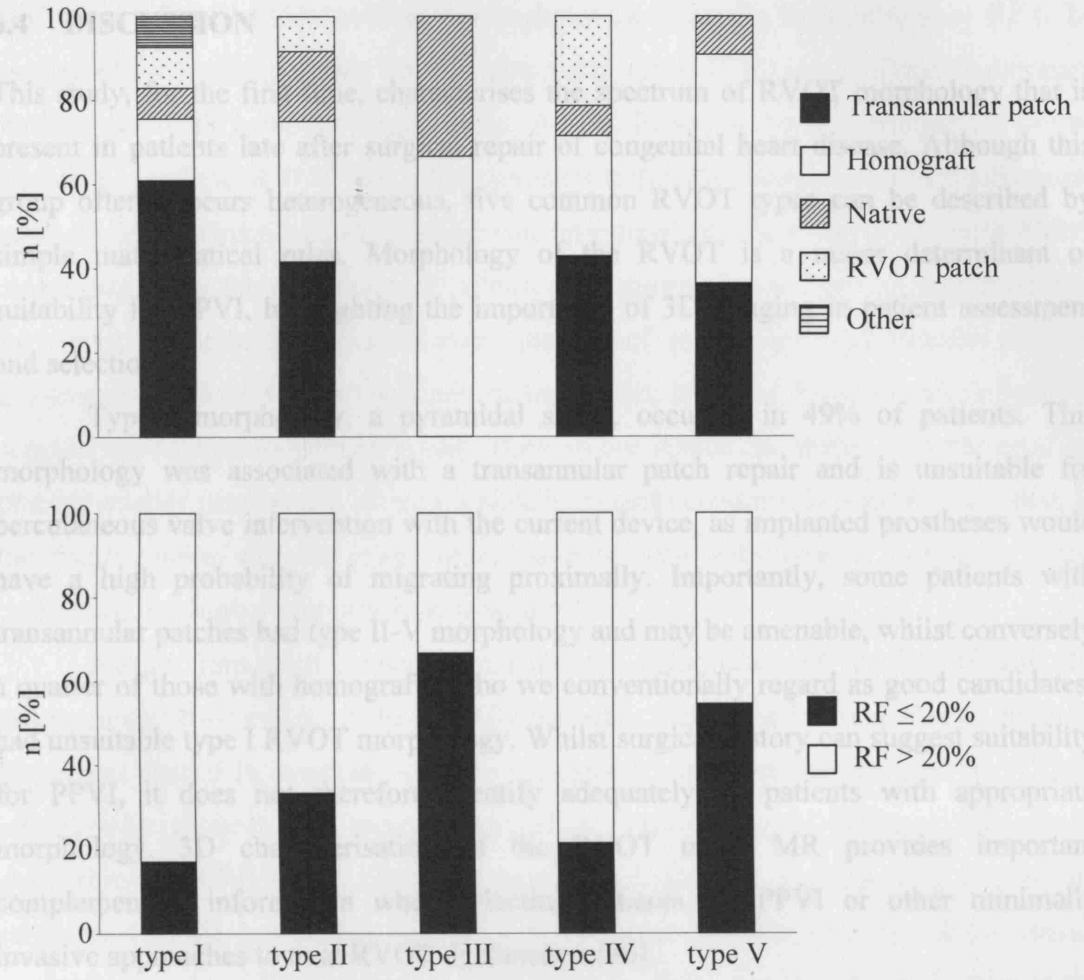

Figure 6.7 Distribution of a) outflow tract type and b) RF in the 5 morphological types (n = 81 classifiable patients, %).

Twelve patients had homograft outflow tracts but did not undergo PPVI. Homograft outflow tracts are often appropriate for PPVI because of their circumferential nature and tendency to calcify and comprise much of the clinical experience [68]. Importantly, however, 6 patients in this population had homograft conduits with type I morphology and thus were unsuitable for PPVI with the current device. These patients represent 26% (6/23) of all those with homograft conduits in our patient population. Three patients had insufficient valvular/conduit dysfunction to warrant intervention to the RVOT, but all had stents placed to treat branch pulmonary artery stenosis. Two patients underwent surgery as PPVI was not widely available at the time of their referral. One patient was followed-up medically as there was no clinical indication for intervention.

6.4 DISCUSSION

This study, for the first time, characterises the spectrum of RVOT morphology that is present in patients late after surgical repair of congenital heart disease. Although this group often appears heterogeneous, five common RVOT types can be described by simple mathematical rules. Morphology of the RVOT is a major determinant of suitability for PPVI, highlighting the importance of 3D imaging in patient assessment and selection.

Type I morphology, a pyramidal shape, occurred in 49% of patients. This morphology was associated with a transannular patch repair and is unsuitable for percutaneous valve intervention with the current device, as implanted prostheses would have a high probability of migrating proximally. Importantly, some patients with transannular patches had type II-V morphology and may be amenable, whilst conversely a quarter of those with homografts, who we conventionally regard as good candidates, had unsuitable type I RVOT morphology. Whilst surgical history can suggest suitability for PPVI, it does not therefore identify adequately all patients with appropriate morphology. 3D characterisation of the RVOT using MR provides important complementary information when selecting patients for PPVI or other minimally invasive approaches to treat RVOT dysfunction [80].

The assessment of RVOT dimensions from MR data is generally performed measuring the maximum and minimum diameter of some relevant selected sections. An average of these 2 dimensions is then used to calculate the diameter of the RVOT. This way of assessment is qualitative and does not account accurately for the shape of the sections. The measurement of the section perimeter, proposed in this study, and the subsequent standardization of the section shape to a circle, better quantify the maximum diameter of the RVOT. Furthermore, the three point system simplification of the RVOT shape variations along the axis, developed in this chapter, allowed the description of 98% (81/83) of all morphologies. Mathematical analysis of MR data, therefore, has enabled us to optimize identification of the correct morphological sub-type and better select patients for PPVI.

Type I morphology was associated with a higher pulmonary RF than other morphological sub-types. The detrimental effect of chronic pulmonary regurgitation on RV function, exercise capacity and arrhythmia potential has already been documented

in Chapter 2 [24,30,145]. Previous investigators have found a high pulmonary RF to be associated with the presence of a transannular patch [146] or a dilated pulmonary annulus [147]. We would suggest that this is likely to be a consequence of the morphology of the RVOT that often develops following placement of a transannular patch. Fluid dynamics studies could provide an insight into the effect of different RVOT morphologies on the generation of pulmonary regurgitation and are an important area for future research. The clinical consequences of pulmonary regurgitation and the growing availability of new transcatheter treatments, however, have already influenced surgical approaches to primary repair. Thus, in our institution, there is a preference for placing smaller patches and where possible homograft conduits. It is most likely that, in the future, there will be fewer older patients seen with type I morphology and consequently a higher proportion suitable for PPVI.

Further important considerations are the compliance of the RVOT and the displacement/deformation of the RVOT/pulmonary trunk junction (e.g. due to strain in the tissues caused by attachment to the ventricles), which are not assessed by 3D MR angiography [Chapter 4]. A patient with type II-V morphology of < 22 mm, may still be unsuitable for PPVI if the RVOT distends significantly at implantation, as stability cannot be assured. In practice, balloon sizing, performed at the time of catheterization, currently provides a 2D assessment of distensibility that can aid decision-making. In the future, this information could be derived non-invasively, with development of different MR imaging sequences, thus avoiding catheterization of patients who subsequently prove unsuitable for PPVI. Furthermore, our experience to date suggests that stent fractures are more commonly seen following PPVI in non-calcified outflow tracts or conduits [79]. Again, this may be difficult to assess by MR angiography. Both the dynamic nature of the outflow tract and the wall thickness (consistent with calcification) may be assessed with gradient echo cine imaging trough the outflow tract or conduit.

From a morphological perspective, we could have attempted PPVI in all types of RVOT except the pyramidal type (type I). In fact, we only performed PPVI in 11 patients from 42 with suitable morphologies, as other factors influence patient selection for this procedure. The current clinical device is only suitable for those patients whose outflow tracts are <22mm in diameter. The development of larger devices and new device designs that permit downsizing of dilated outflow tracts to the size of

biologically available valves is underway [Chapter 10 and 11] and will increase the number of patients that could benefit from a percutaneous approach in the future [80]. The characteristic sub-groups identified in this study can be used to guide the design of these new devices for PPVI, which can be optimized according to the requirements outlined in the RVOT classification in terms of morphological suitability, size and safe anchoring.

Finally, although MR imaging is performed for all our patients referred with symptomatic RVOT dysfunction, our patient population may be biased. Though the exact percentages for each morphology may differ between different Institutional practices, we believe that the 5 main morphologies we have described will be consistent.

6.5 CONCLUSION

The conclusion of this part of my thesis is that patient selection for PPVI on the basis of surgical history alone is not sufficient; 3D assessment of the RVOT with 3D volume reconstruction and mathematical analysis provides important additional information. The type of morphology, in combination with RVOT size and distensibility, informs selection for the current generation of PPVI device. Indeed, patients with RVOT maximum dimensions smaller than 22mm can be safely treated with the current generation device. However, patients with borderline dimensions need further investigation to assess and guarantee the anchoring of the device [Chapter 7].

For a variety of reasons, more than 85% of patients requiring treatment of RVOT dysfunction cannot benefit from the current PPVI procedure. A detailed knowledge and understanding of the morphologies of this large group of patients, as carried out in this part of the thesis could help us identify the necessary characteristics of new devices that will extend the PPVI indications to this growing patient population. By looking at anatomy, dimensions, distensibility, successes and failures, a new device that better adapts its shape to the RVOT needs, could be designed [Chapter 10].

CHAPTER 7

RIGHT VENTRICULAR OUTFLOW TRACT RAPID PROTOTYPING MODELS

The objective of this chapter is to determine if MR imaging data can be used to create rigid models that are accurate representations of the RVOT anatomy and if such models can be used to refine the selection of patients for PPVI.

Twelve patients' MR data were analyzed and elaborated for input into a RP system. The accuracy of the proposed methodology (3D volume reconstruction from MR data and RP model building process) was verified using 5 objects of know dimensions. RVOT RP models were successfully built and presented to 2 experienced cardiologists, who were blinded to the outcome of the procedures. The cardiologists were retrospectively asked if they would have attempted PPVI. Their responses were compared with the documented decisions and outcomes of PPVI. The cardiologists made the correct decision, based on the known clinical outcome, respectively in 50% and 66% of the cases, using conventional MR assessment, and improved to 75% for both of them, with the availability of the 3D RP models. Rapid prototyping models allowed a complete appreciation of the 3D anatomy. They can help the selection of patients for PPVI more accurately than conventional MR, and they can also enable an in-vitro insertion of the PPVI device to test its positioning and anchoring into the RVOT prior to actual implantation. Moreover, different materials can be used to build compliant RVOT models which better mimic the distensible implantation site.

7.1 INTRODUCTION

As already explained in the introduction chapters and demonstrated in the previous chapter, the 3D morphology and size of the patient's RVOT play a key role in the selection of subjects for PPVI. There remain major difficulty in the case of patients with borderline anatomies and dimensions, and we have had some patients in whom PPVI has been attempted, but has not been successful. Our experience suggests that this is due to both misinterpretation of the 3D MR data and also the texture and distensibility of the RVOT [Chapter 6]. Thus, the purpose of this part of my thesis was to determine if MR data can be used to create RP rigid models that are an accurate representation of the RVOT and pulmonary trunk anatomy, and if such models can be used to refine the selection of patients for PVVI. Indeed, the use of realistic, RP models should improve the perception of the RVOT 3D morphology, which is generally always presented to the clinician on a 2D computer screen. Through the testing of direct and indirect model building process chains, several types of materials have been used to meet transparency, compliance and strength specifications of RVOT models. Furthermore, if necessary, trial implant of the device could be realized in the RVOT RP model prior to the actual PPVI procedure.

7.2 RAPID PROTOTYPING APPLICATIONS

The importance of RP in the biomedical sector has been steadily increasing during the last decade. Models of anatomical parts in plastic materials have been built by several techniques (stereolithography, laser sintering, fused deposition, ink-jet printing) from anatomic data acquired through CT and MR imaging. Different uses of RP models have been widely reported in medical scientific literature and within cooperative research projects. In most cases, they have supported operations of orthopaedic, craniofacial and maxillofacial surgery, aimed at reconstructing bone tissues damaged by tumour, trauma, congenital malformations or acquired diseases. Specific applications can be grouped in three main categories [148,149]:

- Diagnostic visualization: the analysis of a physical model can help to detect pathologies which are difficult to recognize from medical images.

- Surgical planning: a model can help a surgeon in evaluating and rehearse complex operations, in order to save time at operation stage and reduce pain and risk for the patient.
- Implant fabrication: a physical model can be used as a pattern or template in the fabrication of prostheses customised to patient anatomy.

Amongst the most recent applications, growing interest is dedicated to the fabrication of vascular replicas, i.e. physical models reproducing the shape of cardiovascular system flow cavities (lumen). Traditionally, these models have been either crafted in blown glass or cast in silicone rubber from human or animal blood vessels. While the former solution is usually expensive, inaccurate and depending on the operator skill, the latter is unsuitable to the reproduction of organs from living subjects and to the fabrication of scaled models, often better than life-sized ones in the evaluation of fine morphological details. The integration of RP techniques with CAD-based reconstruction of 3D geometries from medical imaging data overcomes these drawbacks and provides optimal results with respect to accuracy, flexibility, responsiveness and cost.

Most cases documented in literature refer to vascular replicas for the experimental analysis of blood flow through optical fluid dynamic techniques such as laser Doppler anemometry and particle image velocimetry. This application involves the use of models built around an internal cavity, reproducing lumen shape, connected to a flow circuit by inlet and outlet pipes. Models are transparent in order to allow fluid velocity measurements by means of structured-light vision systems. In a first attempt of CAD integration, plastic replicas of aortic bifurcations have been built by computer numerical control machine after reconstructing vessel geometry from MR scans of a silicone cast from dissected tissue [150]. Compared to this solution, the introduction of RP techniques streamlines the process chain by avoiding the need to split vessel geometry at a parting line. Chong CK *et al.* [151], have created phantoms of arterial segments with anastomoses in silicone rubber from stereolithographic patterns, whose geometries were interactively modelled in a CAD environment from manual measurement on MR scans. Later experiences, supported by commercial software packages for 3D reconstruction, have led to the fabrication of replicas of carotid bifurcations from healthy or atherosclerotic subjects [152,153] and of the total cavopulmonary connection [154]. Process chains range from indirect methods, based on

the vacuum casting of silicone rubber around fused deposition modelled or stereolithographic patterns (possibly with intermediate models in low-melting metal alloy) to direct solutions based on clear epoxy resins for stereolithography. A further solution, involving a water soluble pattern manufactured by fused deposition modelling (FDM) and dipped into silicone-based liquid mixture has been proposed for the fabrication of compliant replicas of abdominal aorta [155].

RP models have also been used to support the complex decisions involved in the treatment of cardiovascular system diseases. For this kind of application, the shape of the model must reproduce the internal surface of the vessel. Replicas of aortic tracts with aneurysms have been built directly by stereolithography [156] or indirectly by vacuum casting of clear urethane resin in silicone moulds from stereolithographic or 3D-printed patterns [157]. Due to the high detail resolution required, vessel geometries have been mainly reconstructed from CT scans, although the resolution improvement of MR scans by image processing algorithms has also been attempted [158]. As a special application [159], models of pre-birth developing hearth lumen have been built by sterolithography after a complex process of software reconstruction by skilled graphical and clinical operators. Issues related to geometric reconstruction have been investigated in [160,161] through the testing of commercial or specifically developed software tools.

One of the roles unveiled by some of the above cited studies consists in the use of replicas of arteries, affected by special pathologies, in the planning of operations.

7.3 METHODS

7.3.1 Patients and Phantoms

Magnetic resonance data were acquired in 12 patients who had been referred for possible PPVI (mean age, 20 years; range, 9-39 years; 7 male, 5 female; 10/12 tetralogy of Fallot; 3 homograft conduit, 3 homograft monocusp patch, 6 transannular patch). These 12 patients were retrospectively selected from our PPVI programme. They were chosen to reflect the wide range of RVOT anatomy that we see in our practice. Eight of the patients went forward to catheterization with a view to PPVI, of which 4 had a successful outcome and 4 had an unsuccessful outcome. These patients represent those with borderline morphology and account for 25% of our PPVI patient population. The remaining 4 patients, who were turned down for PPVI based on RVOT size and

geometry, underwent surgery. The local research ethics committees approved the study, and all subjects (and/or a parent/guardian) gave informed consent to undergo MR imaging, and to use the acquired MR data for research purposes.

Patient	Gender	Age [years]	RVOT	Min MR dimension [mm]	Min model dimension [mm]
1	F	14	Transannular Patch	14×16	13×16
2	M	19	Transannular Patch	39×39	41×41
3	M	17	Transannular Patch	14×17	14×18
4	F	22	Homograft monocusp	15×15	16×17
5	F	14	Transannular Patch	32×37	31×37
6	M	12	13 mm Homograft	16×18	16×21
7	M	9	Homograft monocusp, LA appendage to back wall	17×19	16×20
8	M	17	Repaired age 4, Homograft	18×22	19×22
9	M	24	Homograft monocusp	20×20	18×19
10	F	39	23 mm Homograft	20×23	23×27
11	M	38	Transannular Patch	18×20	22×25
12	F	16	Transannular Patch	22×30	25×34

Table 7.1 Patient characteristics.

Magnetic resonance data were also acquired from 5 phantoms (60 mL syringe, hemispheric roll-on anti-perspiration bottle top (adidas®), universal hospital specimen bottle (NHS, UK), sweet box (tictac®), plastic salad square container), fully filled with saline and 1% gadolinium, in order to validate the reconstruction methodology. The shape of these phantoms was variously selected in order to test the ability of the reconstruction algorithm with different object curvatures. The phantom size was comparable with the human RVOT anatomy to enable evaluation of errors in the same range of dimensions.

Phantom	Phantom 'real'		Computer model		3D model	
	V [ml]	d [mm]	V [ml]	d [mm]	V [ml]	d [mm]
1. Syringe	60	26	62	27	59	27
2. Bottle top	55	47	55	47	55	47
3. Specimen bottle	45	34	44	32	42	33
4. Sweet box	20	13×36	21	13×36	21	13×36
5. Square container	100	55×55	101	55×56	100	56×56

Table 7.2 Phantom dimensions.

7.3.2 Magnetic Resonance Imaging and 3D Model Reconstruction

Magnetic resonance imaging was performed at 1.5T (Symphony – Maestro class, Siemens Medical Systems, Erlangen, Germany) using the same sequences as described in the previous chapters.

Magnetic resonance data were processed in Mimics as explained in the previous chapter and resulted in the generation of the patient blood volume without arterial wall thickness, i.e. the RVOT lumen. To create the 3D model of the implantation site, a wall of 2 mm virtual constant thickness was built around the blood volume, which was subsequently subtracted (Figure 7.1), leaving a shell structure. Thus, the standard stereolithography format STL (solid to layer) of the resulting structure could be imported into a RP system. This format is a triangulated surface representation of the 3D model, where the triangular elements approximate the surface of the object. In the presence of curved surfaces, this configuration allows the best approximation of the object real geometry (Figure 7.2).

The reconstruction time for the RVOT MR data of each patient was approximately 2-3 hours.

The 3D reconstruction process was also used to analyse the phantom MR data and create the STL files of these objects to be inputted into the RP system (Figure 7.3). In this case, the time of reconstruction was <30 mins.

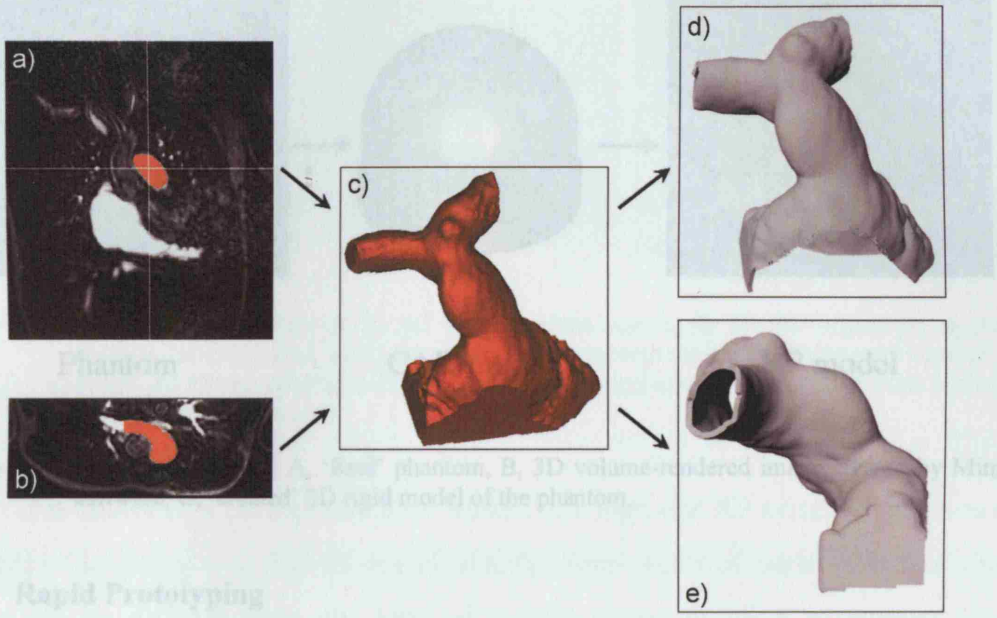

Figure 7.1 Original coronal (a) and reformatted axial (b) MR data showing segmentation mask (orange) of the RVOT after thresholding, region growing and manual editing. c) 3D reconstruction of the blood volume without arterial thickness. 3D reconstruction of the arterial wall (hollow structure) with 2 mm constant thickness in the d) anterior view and e) lateral view.

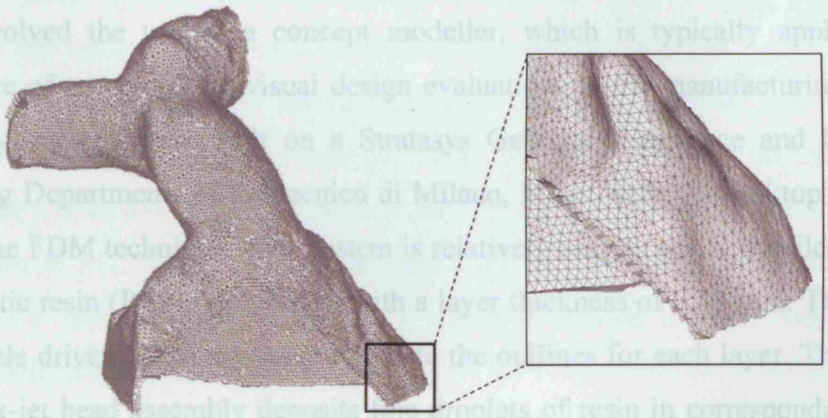

Figure 7.2 Standard stereolithography format STL of the RVOT and pulmonary bifurcation, with magnified segment demonstrating the triangulated surface representation of a 3D model. These data are exported to the rapid prototyping 3D printer.

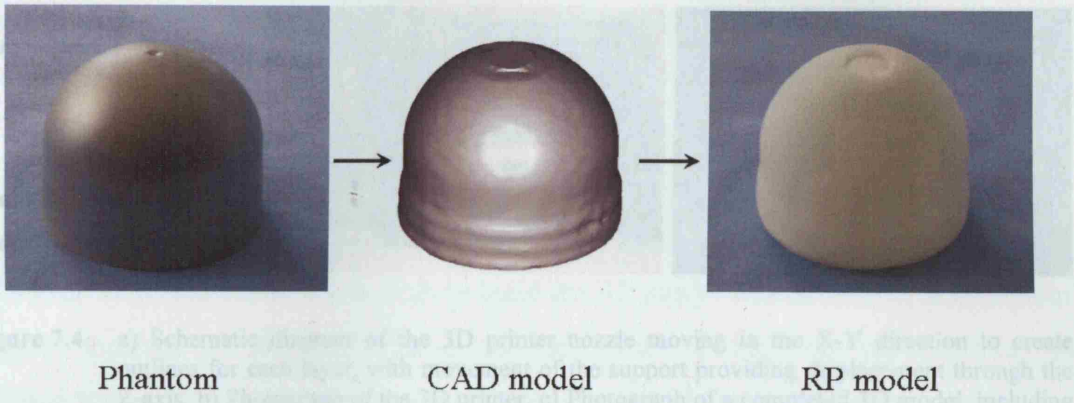

Figure 7.3 Phantom example. A, 'Real' phantom, B, 3D volume-rendered image created by Mimics software, C, 'created' 3D rigid model of the phantom.

7.3.3 Rapid Prototyping

Building cost is a critical factor in the selection of the RP technique and equipment. To date, manufacturing costs resulting from the use of most RP systems are too high to make medical models affordable in common diagnostic and surgical applications. The relatively large size of many anatomical parts requires the use of significant amounts of material and a long operation time of the RP system. The solution adopted in this project involved the use of a concept modeller, which is typically applied to the manufacture of mock-ups for visual design evaluations in the manufacturing industry. Specifically, models were built on a Stratasys Genisys (Aerospace and Mechanical Engineering Departments of Politecnico di Milano, Milan, Italy), a desktop RP system based on the FDM technique. This system is relatively easy to use and builds parts in a thermoplastic resin (P1500 polyester), with a layer thickness of 0.33 mm. The machine uses a nozzle driven by an x-y stage to create the outlines for each layer. The drop-on-demand ink-jet head assembly deposits fine droplets of resin in correspondence of the object outlines. An ultraviolet lamp immediately cures the deposited material. The third dimension is obtained by a displacement through the z-axis of the support stage. Successive layers are added until the object is completed (Figure 7.4). The software of the RP machine automatically calculates all support structures in the object overhanging regions, necessary for the standby of the model during the production phase. For a standard finish, the parts are easily cleaned of the support material with fingers.

Figure 7.4 a) Schematic diagram of the 3D printer nozzle moving in the X-Y direction to create outlines for each layer, with movement of the support providing displacement through the Z-axis. b) Photograph of the 3D printer. c) Photograph of a completed 3D model, including the supporting structures.

The choice of a concept modeller instead of a high-end RP system introduces the problem of ensuring a sufficient model quality. Fabrication of parts with fine shape details can be difficult with this kind of system whose building parameters (layer thickness, operation speeds) may sacrifice surface quality to achieve short building times. However, common experience in the use of concept modellers suggests that, even in the presence of thick layers, surface quality can be controlled by a careful selection of object orientation during the building process. This problem is non trivial since anatomical parts, unlike most manufactured objects, lack regular surfaces and symmetries that can restrict the choice of allowable orientations.

Orientation selection for the fabrication of artery models was carried out with the help of a CAD optimization method, which aimed at drawing the best possible surface quality from low-end RP systems in the fabrication of medical models. From the triangle mesh in STL format, which represented the part shape, the method was able to suggest one or more building orientations, which optimized a given combination of different quality measures:

- The degree of surface stair-stepping inherent to the layered manufacturing principle common to all RP techniques.
- The occurrence of visible marks left on the model surface after the removal of support structures.
- Loss of integrity of awkwardly oriented fine shape details.

Once such measures were defined as a function of the normal direction to triangle facets, a global measure of the part quality could be evaluated for each possible building orientation. In the selection of an optimal orientation, the proposed method combined a

numerical search of local maxima for the quality measure in a continuous domain with a visual evaluation of candidate solutions. This allowed us to consider the overall amount of defects on part surface along with the defect distribution on specific interest regions.

The selection procedure was implemented in an interactive software tool. Figure 7.5 shows the use of the tool in the selection of building orientation for an artery replica. The suggested orientation allowed us to build the RP model with a minimum amount of support material on the inside vessel surface, which would have been difficult to remove without damaging model surface. The grey-level graphical display enabled the recognizing of local variations of a process-dependent quality measure related to surface stair-stepping and support marks, which was estimated from experimental data.

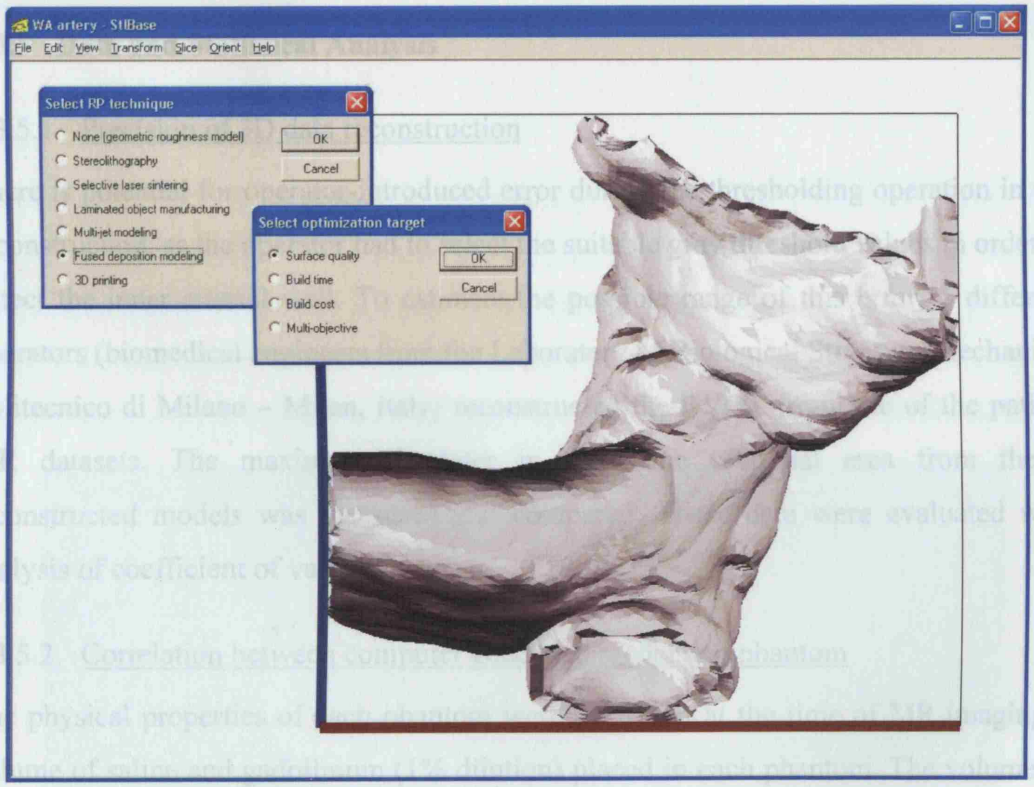

Figure 7.5 Selection of build orientation.

7.3.4 Assessment of Clinical Utility

In all patients, a decision as to whether PPVI should be attempted was made, from the clinical history and the MR data, by a consensus decision of cardiologists, cardiothoracic surgeons and intensivists at our institution [Section 3.3.1]. If PPVI was attempted (n = 8), the success or failure of PPVI was then regarded as the end-point. If

PPVI was not attempted (n = 4), this decision was regarded as the end-point. For all patients, I then retrospectively presented the 3D MR images alone or the 3D models alone, randomly, and in a blinded fashion, to 2 cardiologists, who were also blinded to the actual outcome of the procedures. The observers were given the dimensions of the RVOT and the MR report, when the MR images were presented, and a caliper to take their own measurements, when the models were presented. They were asked to state whether they would attempt PPVI based on the 3D MR image alone and on the 3D model alone. These decisions were then compared with the documented decisions and outcomes of PPVI, to establish the accuracy of 3D MR imaging and 3D modelling for selecting suitable patients for PPVI.

7.3.5 Data and Statistical Analysis

7.3.5.1 Precision of 3D data reconstruction

There is potential for operator-introduced error during the thresholding operation in the reconstruction, as the operator had to select the suitable gray threshold values in order to detect the inner arterial wall. To estimate the possible range of this error, 5 different operators (biomedical engineers from the Laboratory of Biological Structure Mechanics, Politecnico di Milano – Milan, Italy) reconstructed the RVOT from one of the patient MR datasets. The maximum diameter in the same sectional area from the 5 reconstructed models was measured and compared. These data were evaluated with analysis of coefficient of variation.

7.3.5.2 Correlation between computer generated model and phantom

The physical properties of each phantom were measured at the time of MR imaging – volume of saline and gadolinium (1% dilution) placed in each phantom. The volume of all 5 computer generated phantoms was measured using Mimics software measurement tools, and compared with the original volume of fluid placed into each phantom. The phantoms were built by RP technique, and their volumes (volume of water required to fill the RP model) compared with the volumes of the original phantom, to determinate the correlation between the real phantom and the RP model. The internal diameters were also measured from the original phantoms and the reconstructed models by mechanical caliper, and from the computer generated phantoms by Mimics electronic caliper.

7.3.5.3 Assessment of patient models

The narrowest diameter of the RVOT/pulmonary trunk was chosen and measured from both the 3D MR images (electronic calipers), and from the 3D RP models (mechanical calipers).

7.3.5.4 Statistical analysis

Statistical analysis was performed with program SPSS for Windows, version 12.0.1 (SPSS Inc., Chicago, Ill., 2003). All data were analyzed by using the Spearman Rank correlation and Bland Altman plots to assess correlation. A P value < .05 was defined as denoting a statistically significant difference.

7.4 RESULTS

7.4.1 Model Building

Three-dimensional RP models were successfully built for all 5 phantoms (Figure 7.6) and all 12 patients (Figure 7.7). Rapid prototyping building time for the models was 3-4 hours. Qualitative visual comparison of the resulting RP models with the input STL triangle meshes confirmed the capability of the FDM desktop system of maintaining the desired shape with acceptable surface roughness and without loss of significant details.

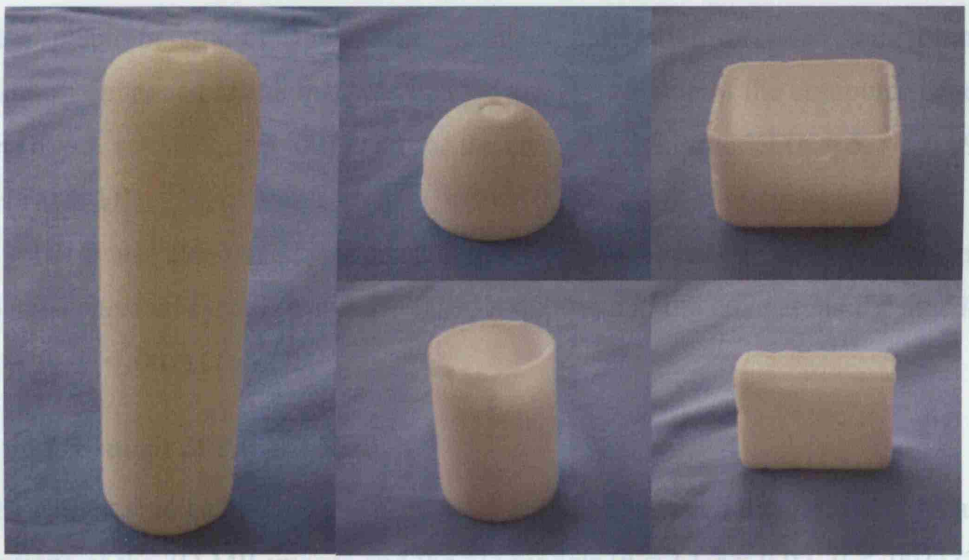

Figure 7.6 The five 3D phantom models.

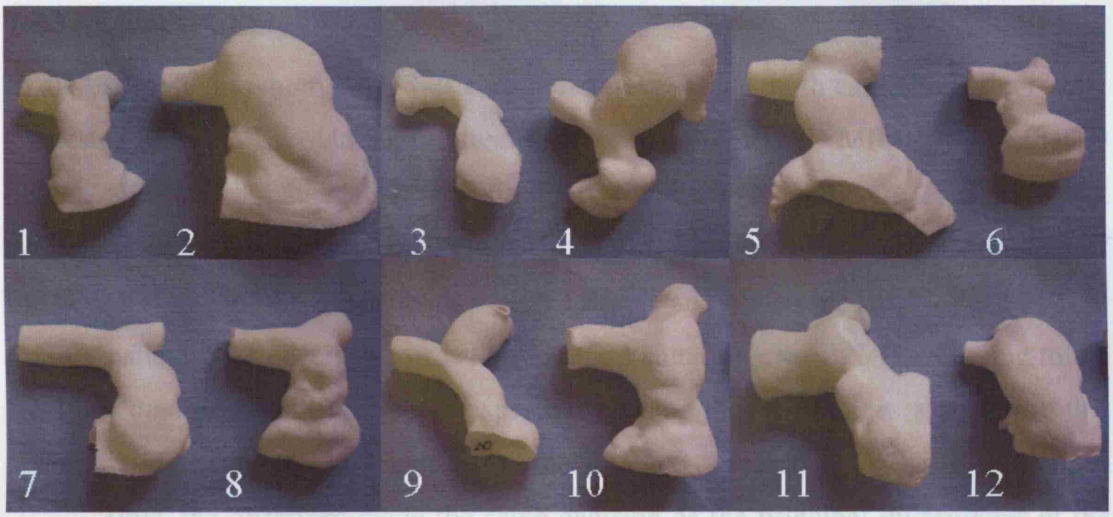

Figure 7.7 The twelve 3D patient models (RVOT and pulmonary bifurcation).

7.4.2 Precision of 3D Data Reconstruction

The coefficient of variation of the diameter measurements due to the MR data operator thresholding was 3.4%. For the critical diameter of 22 mm, this would lead to an average operator-induced error of approximately ± 0.75 mm, which would be clinically acceptable.

7.4.3 Correlation between Model and Phantom

For the phantom studies, there was excellent correlation between the volume of gadolinium-enhanced saline that was imaged and the volume of the computer-generated model ($n = 5$, $r = 0.99$, $P < .001$) and for the created 3D RP model ($n = 5$, $r = 0.99$, $P < .001$) (Table 1).

There was also excellent correlation between the diameter of each phantom, the computer-generated model ($n = 5$, $r = 0.99$, $P < .001$) and the created 3D RP model ($n = 5$, $r = 0.99$, $P < .001$) (Table 1).

7.4.4 Assessment of Patient Models

For the patient studies, there was excellent correlation between the narrowest measured dimensions of the 3D MR images and the 3D models ($n = 12$, $r = 0.97$, $P < .001$) (Table 2). There was a small positive systematic bias towards the models on the Bland-Altman plot (1.9 mm) (Figure 7.8).

7.4.5 Clinical Utility

In all 4 subjects in whom PPVI was considered not suitable, both cardiologists correctly suggested that PPVI should not be attempted, using either the 3D MR images or the 3D models. For the 8 patients for whom PPVI was attempted, 2 were considered not suitable after balloon sizing, and 2 patients had failed implantation due to instability of the device. Thus, of these 8 patients, 4 were suitable and 4 were unsuitable for PPVI. In these 8 patients, the observers correctly identified suitability for PPVI, according to the final outcome, in 4 and 2 patients, respectively, using the MR images alone, with this suitability increasing to 5 and 5, using the model alone (Table 3).

Thus, the observers made the same decision as the principal investigator at the time of cardiac catheterization, based on the known clinical outcome, in 67% and 50% respectively of the total patients using conventional MR assessment, which improved to 75% and 75%, with the availability of the 3D models. In both patients where PPVI was first attempted and then failed, the decisions were 50% correct with the MR images alone, but 100% correct using the models for both observers.

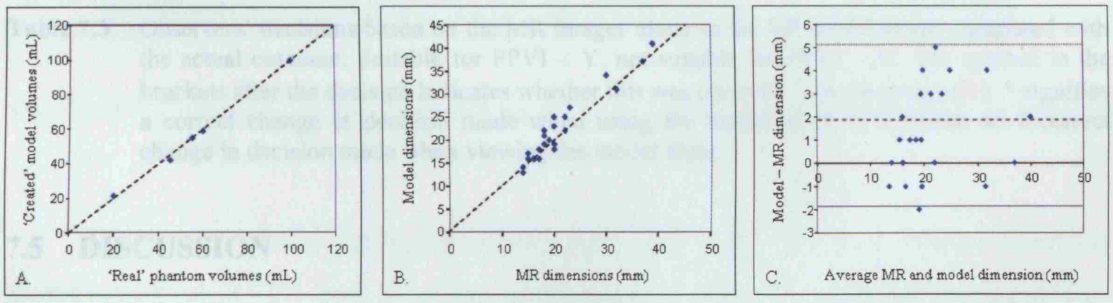

Figure 7.8 A) Plot of 'real' phantom volume against 'created' RP model volume (x = 0.99 y + 0.64, r = 0.99, P < .001). The dotted line represents the line of correlation. B) Plot of dimensions measured from the patients at MR against those measured from the 'created' RP models (x = 0.92 y + 0.68, r = 0.97, P < .001). The dotted line represents the line of correlation. C) Bland-Altman plot for the patient data, MR and model dimensions.

Patient	Proceed to PPVI	Success of PPVI	Cardiologist 1		Cardiologist 2	
			MR	Model	MR	Model
1	Y	N – after balloon sizing	Y (✗)	Y (✗)	Y (✗)	Y (✗)
2	N		N (✓)	N (✓)	N (✓)	N (✓)
3	Y	Y	Y (✓)	Y (✓)	Y (✓)	Y (✓)
4	Y	Y	Y (✓)	**N‡** (✗)	N (✗)	N (✗)
5	N		N (✓)	N (✓)	N (✓)	N (✓)
6	Y	Y	Y (✓)	Y (✓)	N (✗)	**Y*** (✓)
7	Y	Failed	Y (✗)	**N*** (✓)	N (✓)	N (✓)
8	Y	Y	N (✗)	N (✗)	N (✗)	**Y*** (✓)
9	Y	N – after balloon sizing	Y (✗)	**N*** (✓)	Y (✗)	Y (✗)
10	Y	Failed	N (✓)	N (✓)	Y (✗)	**N*** (✓)
11	N		N (✓)	N (✓)	N (✓)	N (✓)
12	N		N (✓)	N (✓)	N (✓)	N (✓)

Table 7.3 Observers' decisions based on the MR images alone or the RP model alone, compared with the actual outcome. Suitable for PPVI – Y, not suitable for PPVI – N. The symbol in the brackets after the decision indicates whether this was correct (✓) or incorrect (✗). * signifies a correct change in decision made when using the model alone. ‡ signifies an incorrect change in decision made when viewing the model alone.

7.5 DISCUSSION

In this study, I have demonstrated that CAD technique combined with imaging processing tools and RP can be used to create accurate models of the RVOT. I have shown that in borderline patients such models can help clinicians select patients for PPVI with increased certainty when compared to conventional MR imaging alone. Although RP is currently used widely in engineering and manufacturing industries [162], and in medicine to custom make prosthetic parts [163,164] to explain complex operations [165,166], and in preliminary studies of the cerebral vasculature [167], the application of RP to assess pathology of the great vessels from MR data has not been previously reported. A model of the studied anatomy, held in the hand, can be easily viewed from any angle. Furthermore, we believe it is easier to measure the dimensions

from the models than from the 3D MR data, and this may account for the small systematic bias we observed between the two techniques.

Rapid prototyping models can also be used for trial implantation of the device to test whether the positioning and anchoring of the stent in the outflow tract are correct and safe (Figure 7.9).

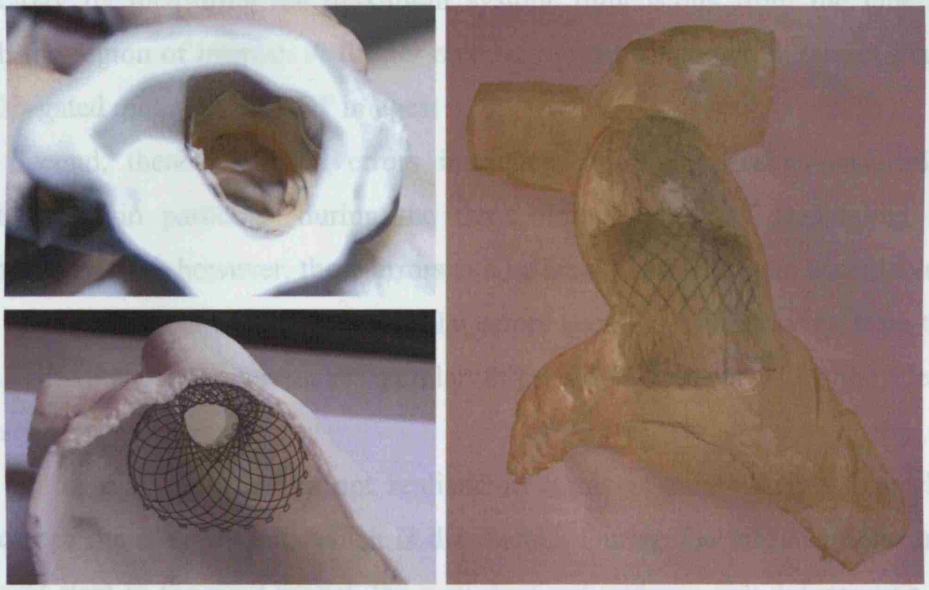

Figure 7.9 Fitting tests of the current device for PPVI and some new prototypes in different RP models.

The most common group of patients requiring pulmonary valve replacement has dilatation of the RVOT and therefore is not suitable for PPVI with the current device [Chapter 6]. In order to extend the indications for PPVI, new devices will need to be developed, and models of dilated outflow tracts may be used to help optimise these [80]. Indeed, prototypes of future new devices can be tested into the rapid prototyping model of relevant RVOTs prior to first-in-man implantation (Figure 7.9).

The application of RP modelling to other valves within the heart may also be useful for planning percutaneous interventions in the future [66,168,169]. In particular for the aortic valve, where the position of the coronary artery ostia and the relationship of the anterior leaflet of the mitral valve are crucial for safe deployment of a device.

There are limitations to this methodology: first, the MR images used to build the 3D models are not ECG-gated, and thus represent an average of the RVOT shape and size over the cardiac cycle [Chapter 4]. This can lead to an underestimation of the

maximum systolic dimension of narrowest diameter. This is underlined by the fact that there remain patients in whom the cardiologists felt that PPVI should be attempted, but at balloon sizing were felt not to be suitable for PPVI (n = 2). This limitation will be addressed when 3D gated MR-sequences become more widely available [105,106]. In current practice, we overcome the error introduced by the dynamic nature of the RVOT morphology by measuring the maximum systolic dimensions from the cine images through the region of interest. A further method of acquiring such a dataset may be to use ECG-gated multi-detector CT images.

Second, there are small errors introduced by the operator performing the reconstruction, in particular during the thresholding operation. Depending on the operator experience, however, these errors can be small, and within an acceptable range for RP model building. Furthermore, similar errors occur when measuring from the MR images, where the operator makes similar threshold judgments using the electronic calipers.

Third, rigid models are not realistic in terms of mimicking the mechanical behaviour of the arterial wall, which is distensible. During the virtual implantation of the valved stent in the rigid model, the wall does not undergo any deformation, unlike the real arterial wall. Transparency of the RP anatomical implantation site would also be useful to enable better visualization if pre-procedural trial of PPVI is attempted in the model (Figure 7.9).

7.6 COMPLIANT AND TRANSPARENT MODEL BUILDING

Compliant and transparent models cannot be manufactured with a straightforward use of RP techniques, due to limitations of currently available processes and materials. Desired material properties can be reached only with the resort to secondary processes after RP fabrication. As a consequence, models for detailed procedure planning are likely to require longer building time and higher cost than preliminary models for stent design.

An indirect process chain, customarily used in the manufacturing industry for small batch production of prototype plastic parts, was proposed to satisfy compliant and transparency requirements, without sacrificing time, accuracy and money. The process consisted in vacuum casting a liquid resin in a room-temperature vulcanised rubber mould, which was produced from the RP model built before with FDM technique. This

solution allowed maximum flexibility in the selection of the resin for the artery replica, since a wide choice of resin types and grades is available to get the desired combination of visual appearance and mechanical properties. Moreover, this method was relatively simple, quick and inexpensive, with the advantage of having a uniform thickness along the entire model surface. Compared to the pilot production of manufactured parts, the proposed application did not require a high surface finish on the pattern. Therefore, the mould could be built on a low-end RP system such as the FDM desktop modeller used before, without the need of extremely thin layers or post-finishing treatments.

Figure 7.10 shows a sample mould and one of the artery models that has been cast from it. The mould was composed by a cope, a drag and a core. Cope and drag carried the impression of the outer artery surface, and were prepared from a temporarily filled pattern. The core, which shaped the inner artery surface, was prepared by pouring liquid rubber into one of the pattern openings once all the others were closed.

Two different materials were used for the mould fabrication. The cope and the drag were cast in a polyurethane rubber with high hardness grade (80 Shore A), to maintain sufficient accuracy in cavity dimensions. Specifically, a rigid cavity allowed a firm support of the core while the liquid resin was poured into the mould, thus keeping the thickness of the cast part within a reasonable variation. The core was cast in a silicone rubber with much lower hardness (18 Shore A). This choice allowed an easy removal of the core from the openings of both pattern and cast part. This operation required a severe compression of the rubber core in order to reduce its dimensions to opening size. As confirmed by preliminary tests, the softer rubber was able to withstand the large deformations, and could also easily split in the presence of complex shapes and narrow openings. Rubber curing occurred at room temperature and with minimal heat development, thus keeping thermal stresses on the FDM pattern at an acceptable level.

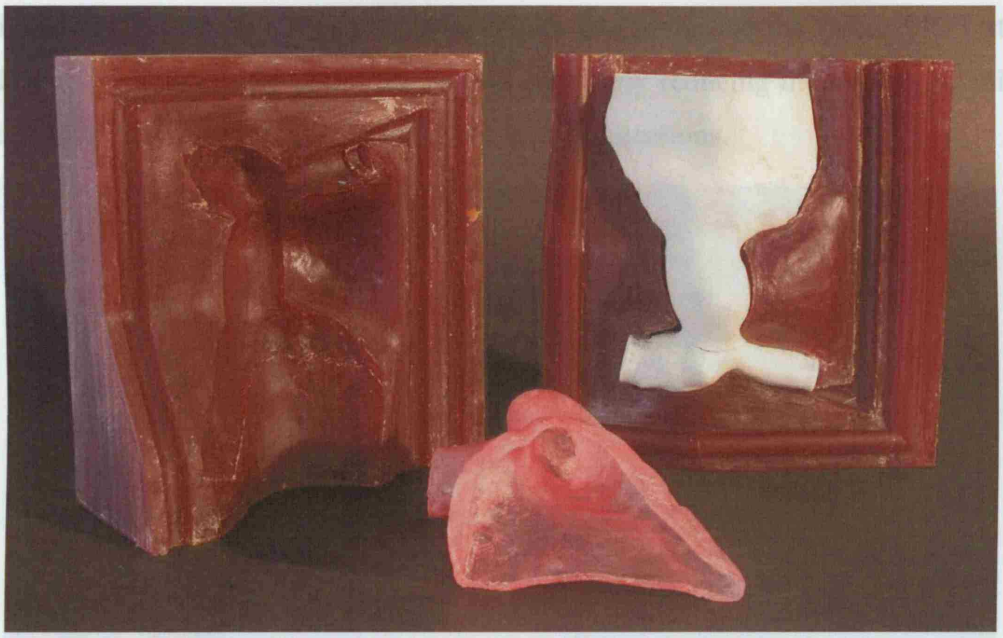

Figure 7.10 Rubber mould for compliant and transparent artery models.

Final artery models were cast in different types (Figure 7.11) of thermoset resins prepared from liquid components, which are mixed and degassed at room temperature before being poured into the mould. Among tested resins, the best results have been achieved with a polyurethane rubber with medium transparency properties and high compliance (Figure 7.12) and with a flexibilized epoxy resin, which provided a higher transparency with a lower and less persistent compliance than the previous material.

The resin curing process took about 8 hours for each cast object (cope, drag, core and final part). The total process time was in the order of few days.

7.7 CONCLUSION

In this chapter I have shown that individual patient data acquired from MR images can be used to build accurate 3D models of the RVOT. These RP models have 2 practical applications: 1) they can aid clinicians to select borderline patients for PPVI more accurately than 3D MR images, allowing for complete appreciation of 3D anatomy of the RVOT; 2) they provide a realistic environment in which to test the PPVI device. With the development of distensible and transparent models, this methodology will enable preclinical testing of new stents, which may be useful to treat the large number of patients that are currently unsuitable for PPVI as defined in Chapter 6. The RVOT

replicas have, therefore, the potential to aid in the design of the future PPVI stent, guiding its alterations and optimization, and ultimately reducing the number of animal experimental tests necessary prior to first-in-man applications.

Figure 7.11 Some examples of models built using different polymers (urethane, epoxy, silicons).

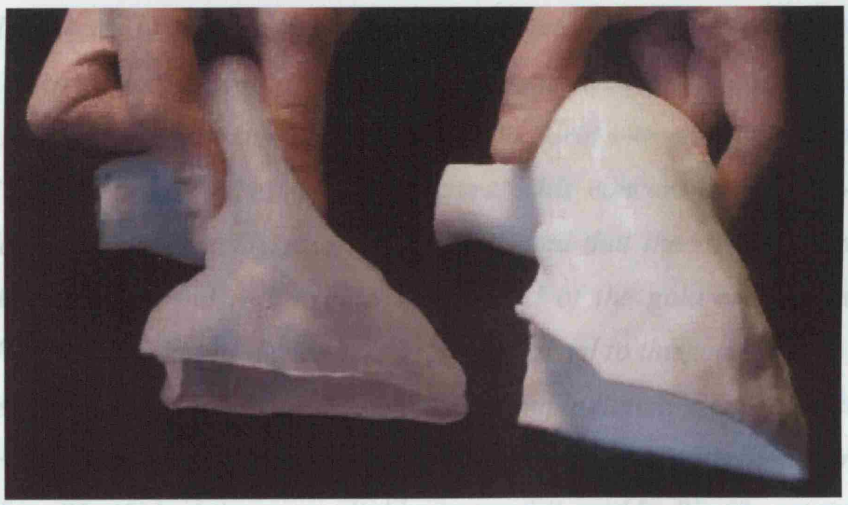

Figure 7.12 Example of a compliant RVOT model.

CHAPTER 8

CURRENT STENT FOR PERCUTANEOUS PULMONARY VALVE IMPLANTATION

The purpose of this chapter is to analyse factors responsible for stent fracture in PPVI using the finite element (FE) method.

Three different stent models were created: PL) platinum–10% iridium alloy stent – resembles the first generation PPVI device; PL-AU) same geometry, but with the addition of gold over the strut intersections – models the current stent; $PL_{1/2}$) same design as PL, but made of thinner wire. For $PL_{1/2}$, a stent-in-stent solution was applied. Numerical analyses of the deployment of these devices were performed to understand the stress distribution in static and dynamic conditions, and hence stent fracture potential. In PL the highest stresses occurred at the strut intersections, suggesting that this location may be at highest risk of fracture. This concurs with the in-vivo stent fracture data. Numerical analyses of PL-AU indicated that the stresses were lower at the strut intersections, but redistributed to the end of the gold reinforcements. This suggests that fractures in this device may occur just distal to the gold, as seen in clinical experience. $PL_{1/2}$ was weakest at bolstering the implantation site; however, when 2 stents were coupled, lower stresses were seen compared with PL alone. In terms of fatigue safety, PL-AU had the most reliable design followed by PL. The minimum safety occurred on $PL_{1/2}$, but 2 coupled $PL_{1/2}$ stents enhanced its fatigue performance. In conclusion, using FE analysis, we demonstrated that a stent-in-stent technique results in better device performance, which suggests a novel clinical strategy.

8.1 INTRODUCTION

The previous 2 chapters have described the results I accomplished in the investigation of the PPVI implantation site. Thus, the RVOT has been assessed with new engineering methodologies that allowed a better understanding of the environment in which PPVI is performed. This chapter will focus on the study of the device used for PPVI. Indeed, despite the clinical success of the PPVI programme, there remain a major technical issue with the current percutaneous device that needs to be addressed: stent fracture.

Stent fracture is a recognized complication following stent implantation for all cardiovascular applications [57,59,170-173]. Prevalence of stent fracture (up to 43%) has been described in bare stenting of the RVOT, with Palmaz Schatz and Palmaz Genesis laser-cut stainless steel stents [59]. In its most severe scenario, device embolization has been reported in 11%, though without death or acute hemodynamic compromise. Nearly 90% of fractured stents have a substernal location, which is identified as a high risk factor for fracture.

The purpose of this chapter is, therefore, to evaluate stent fracture in PPVI devices, by analysing the stress distribution, during the consecutive phases of stent inflation and compression, and by comparing different device designs. The extra strength provided by a second device in the 'stent-in-stent' technique was evaluated in contrast to the performance of single prostheses. Finite element analyses were used to perform the fracture study in static loading conditions. The results of the FE analyses were further used to quantitatively predict the fatigue life of the analyzed PPVI devices.

8.1.1 Stent Fracture in PPVI

We retrospectively reviewed 123 consecutive patients who underwent PPVI between September 2000 and May 2006, in order to analyze incidence, appearance and treatment options for stent fracture in our patient population (mean follow-up of 13.0±1.0 months). The early generation device, without gold reinforcement at the intersection struts, was implanted in the first 10 PPVI patients; the new design prosthesis – to date still in use – into the following 113 patients [79].

Stent fracture was detected in 26 patients (21.1%): 4/10 (40%) patients treated with the early generation device and 22/113 (19%) patients treated with the gold-

reinforced stent. Stent fracture developed between 0 and 843 days, with the highest incidence in the first 400 days (21/26, 80.8%). The fractures occurred during crimping of the stent onto the balloon in 2 cases (both early generation devices), following balloon dilatation in 3 patients, following implantation of a second percutaneous valve in 1, and spontaneously in 21 patients. The exact location of fractures in the PPVI patients was analyzed from both the frontal and lateral chest x-rays. The early generation stents fractured at the strut intersections. After reinforcing the weld with gold, these fractures were no longer seen. In fact, in the new design stent, fractures occurred more frequently next to the ends of gold brazed parts.

Stent fracture was classified based on chest x-ray appearance (Figure 8.1):

- Type I: fracture of one or more struts without loss of stent integrity;
- Type II: fracture with loss of stent integrity;
- Type III: fracture associated with separation of fragments and/or embolization.

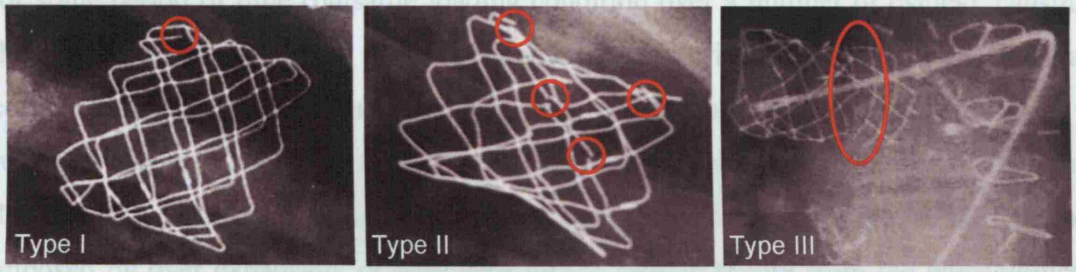

Figure 8.1 Stent fracture classification: Type I: stent fracture of ≥ 1 strut, no loss of stent integrity; Type II: stent fracture of ≥ 1 strut with loss of stent integrity; Type III: complete separation of segments and/or embolization of the stent (shown here, into the right PA).

At initial presentation, 20/26 patients had Type I, 5/26 Type II and 1/26 Type III stent fracture. Six patients had clinical consequences: the patient with Type III stent fracture had stent embolization into the right PA, which required surgical explantation of the PPVI device, and all patients, who initially presented with Type II stent fracture, had 2nd PPVI for relief restenosis [Section 8.1.2]. At the time of this analysis, 17/20 (85%) patients with Type I fracture at initial presentation were still under medical follow-up, with serial chest x-ray and echocardiography for surveillance. In the remaining 3/20, there was progression to Type II fracture – 1 had a second PPVI, while 2 were still waiting a second PPVI.

8.1.2 Stent-in-Stent Technique

In 6 patients, interventional management of the stent fracture was possible by repeat PPVI (stent-in-stent technique) for stabilization of the fractured parts, with successful haemodynamic results. The feasibility of stent-in-stent implantation has previously been demonstrated with different stents for a variety of indications in congenital heart disease [56,58,172]. Repeat PPVI represents the most promising approach to treat stent fracture. Multi-element devices can be produced combining stents of diverse material and design to take advantage of their different mechanical properties, reinforce the prosthesis and avoid fracture.

8.1.3 Fatigue Fracture

Fatigue is a special kind of failure in which fracture occurs not because an instantaneous load is applied, causing a crack to grow, rather because a stress is applied continuously for some period of time (pulsatile loading condition over a number of cycles), causing the cracks to gradually grow until they finally reach a critical level. Many mechanical components, which have been found safe under static loading conditions, can fail as a result of fatigue stresses that are below the material's ultimate strength. Thus, structural damage can occur from outright fracture of the stent, for example due to the loading imposed by over expansion, or over time due to fatigue failure from the physiological pulsatile contact pressures at the artery vessel walls [174-181]. Indeed, once the PPVI stent is inflated into the RVOT, it becomes immediately subjected to pressure cycles resulting from systolic and diastolic blood pressure change. Cyclic fatigue failure is particularly important in stent application as the heart beats at typically 70 times per minute – about 40 million times per year – necessitating that these devices are designed to last over 200 million loading cycles for a 5-year life.

To design against such fatigue failures, stents for all cardiovascular applications are currently assessed on the basis of testing for survival. For example, if a design life of 10^8 cycles is required, testing is performed to ascertain whether the stent will survive 10^8 cycles under accelerated simulated physiological loading [182]. In case of success, this is an inadequate approach, as the safety factors, which essentially tell us how close we are to failure, remain unknown. Indeed, this approach to fatigue design is not used in

most fields of engineering, where the probability of fatigue failure is instead assessed on the basis of testing for failure.

The symptoms of fatigue are cracks that result from permanent deformation in localised areas of the device. Such deformation usually results from stress concentration sites on the surface of a component, or a pre-existing, virtually undetectable defect on the surface. Finite element analyses can predict stress concentration areas, and can help design engineers predict how long their products are likely to last before experiencing the onset of fatigue. This is typically achieved for small components using the traditional stress/strain-life (S-N) approach, where design and life prediction rely on experimentally determined relationships between the applied stress S and the total life of the component (N = number of cycles of repetition leading to failure). Therefore, the stress level a material can endure for a specific number of cycles can be derived from the S-N curve [183].

8.2 METHODS

Inflation of the PPVI stent was performed in the FE code ABAQUS Standard, considering large deformation analyses, and material and geometrical nonlinearities, both for the quasi-static inflation and fatigue simulation of the PPVI stent.

8.2.1 Geometries and Meshes

Three stent geometries were created on the basis of data supplied from the company or obtained from measurements by means of caliper and optic microscope. The stent geometries were created to emulate the initial crimped status of the device onto the catheter balloon.

The first model – named PL – is characterized by 6 wires (wire diameter of 0.33 mm), each formed in 8 zig-zags. Individual wires are joined together at the crown points to create the full stent (Figure 8.2a). This geometry representes the early generation device used in PPVI.

The second model (PL-AU) has the same geometry as the previous one but includes also gold brazed areas in the shape of 0.076 mm thick sleeves around the platinum wire crowns (Figure 8.2b). This stent resembles the currently used device.

The third model ($PL_{1/2}$) has the same design as the PL device but with a wire diameter of 0.23 mm ($PL_{1/2}$ material mass was half the mass of the PL stent). This model was designed in order to evaluate and quantify the change in mechanical performance of a stent made from a thinner wire.

The biological valve mounted into the clinically used stent was not modelled in this study.

The FE model mesh was automatically generated. All stents were meshed with 10-node tetrahedrons in order to easily fit the complex geometries studied and give an accurate solution. The gold elements of the PL-AU model were tied to the platinum wires to avoid relative movement or separation between the 2 parts.

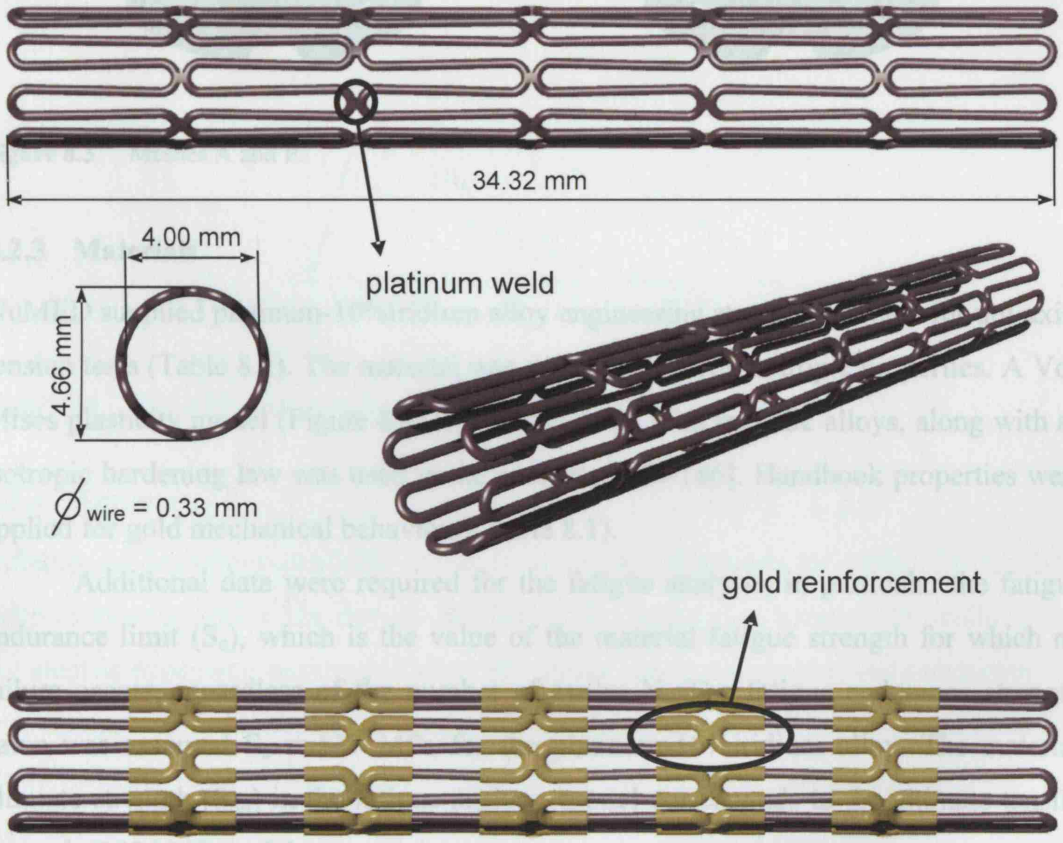

Figure 8.2 CAD model and dimensions of a) PL stent and b) PL-AU stent.

8.2.2 Mesh Sensitivity

Before running the analyses, a sensitivity test was performed on the PL model mesh to achieve the best compromise between limited calculation time and no influence of the element number on the results.

Five meshes with an increasing number of elements and nodes were tested (Figure 8.3 and Table 8.2).

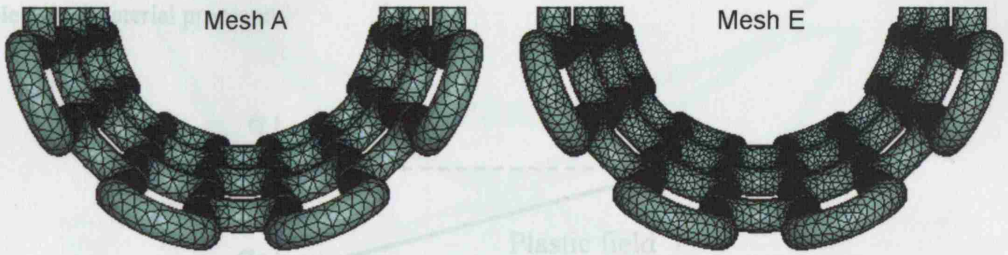

Figure 8.3 Meshes A and E.

8.2.3 Materials

NuMED supplied platinum-10%iridium alloy engineering stress-strain data for uni-axial tension tests (Table 8.1). The material was assumed to have isotropic properties. A Von Mises plasticity model (Figure 8.4), commonly used with metallic alloys, along with an isotropic hardening law was used in the analyses [184-186]. Handbook properties were applied for gold mechanical behaviour (Table 8.1).

Additional data were required for the fatigue analysis, in particular the fatigue endurance limit (S_e), which is the value of the material fatigue strength for which no failure occurs, regardless of the number of cycles N. The fatigue endurance strength value was assumed S_e = 517 MPa for the platinum-10%iridium alloy. The material ultimate strength (S_{ult}) in the fatigue analysis model corresponds to the ultimate tensile strength (1034 MPa) of the material.

	Platinum/10%Iridium	Gold
Young Modulus E [GPa]	224	80
Poisson ratio ν	0.37	0.42
Yield Strenght σ_0 [MPa]	285	103
Ultimate Tensile Strenght σ_R [MPa]	1034	181
Elongation at break ε_R	0.80	0.34

Table 8.1 Material properties.

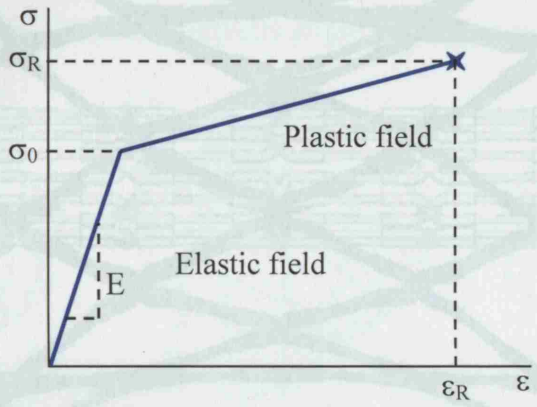

Figure 8.4 Schematic elasto-plastic stress (σ)-strain (ε) curve.

8.2.4 Analyses

Inflation of balloon-expandable stents is clinically performed by pressurization of a balloon inserted inside the device. Modelling the interaction between the balloon and the stent is expensive in terms of time and power calculation and is only important for analyses in which the transitory configurations are required [187]. The intention of this study was to look at the stent in its final configuration (when the balloon was completely inflated) and after balloon deflation. For these reasons, the balloon was not modelled in the simulations.

Computationally, inflation of the stent may be performed using either direct pressure applied to the internal surface of the stent or through prescribed boundary conditions. Attempts to expand the device with a pressure applied directly to the internal surface of the stent can prove difficult. Indeed the terminal parts of the stent are not constrained by other segments. Therefore, the deployed configuration could result in

unrealistic deformations ('dogboning' effect) of the device (Figure 8.5). Consequently, the stent was inflated using radial expansion displacements up to an internal diameter of 24 mm (maximum diameter reached by the device during actual PPVI). Once the stent had reached the desired diameter, the displacement constraints were removed to simulate the balloon deflation and allow the elastic recoil of the stent.

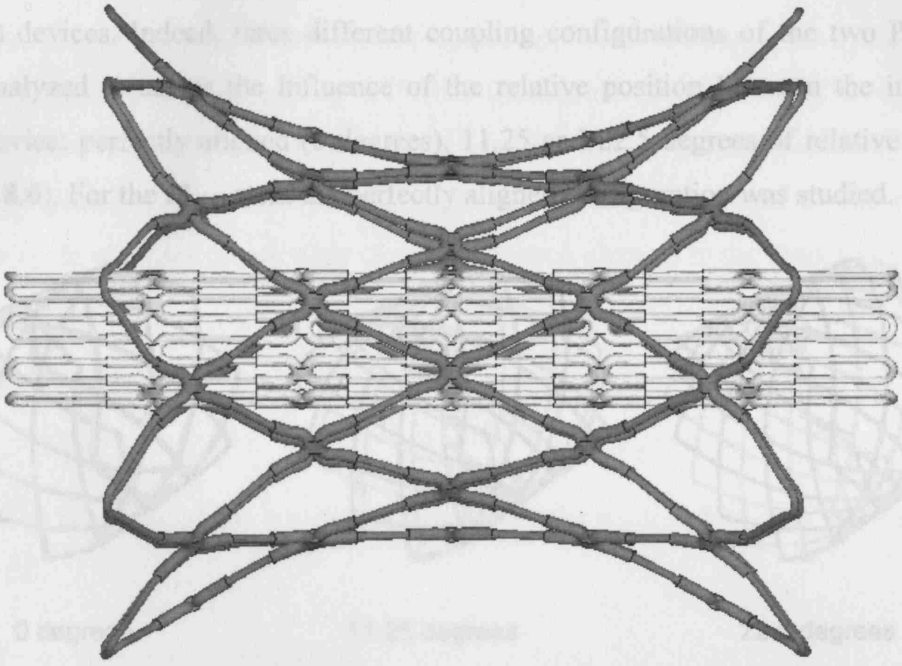

Figure 8.5 Deployed configuration (grey) of the PL-AU stent resulting from the application of a pressure directly to the internal surface of the device. The initial configuration of the stent is shown in white.

Lastly, in order to simulate the compression force experienced by the device due to the implantation site wall, a gradual pressure was applied to the external surface of the stent. This enabled evaluation of the stent strength to maintain the patency of the vessel.

To compare the performance of 2 coupled devices (stent-in-stent technique) against the single prosthesis, the inflation of two stents – one inside the other – was simulated. First, the outer stent was deployed up to 24 mm and released, as previously described. Next, the inner device was inflated up to 24 mm, making contact with the outer stent. The displacement constraints were removed to allow the material to recoil.

Finally, a pressure was applied to the external surface of the outer stent to evaluate the strength of the structure.

The interaction between the two devices was described by a contact algorithm (a detailed explanation of the contact algorithm available in the FE code is reported in Section 9.2.4) with friction – coefficient of sliding friction equal to 0.25 [188].

The stent-in-stent analysis was performed with two PL (2PL) and two $PL_{1/2}$ ($2PL_{1/2}$) devices. Indeed, three different coupling configurations of the two PL stents were analyzed to assess the influence of the relative position between the inner and outer device: perfectly aligned (0 degrees), 11.25 and 22.5 degrees of relative rotation (Figure 8.6). For the $PL_{1/2}$ stent the perfectly aligned configuration was studied.

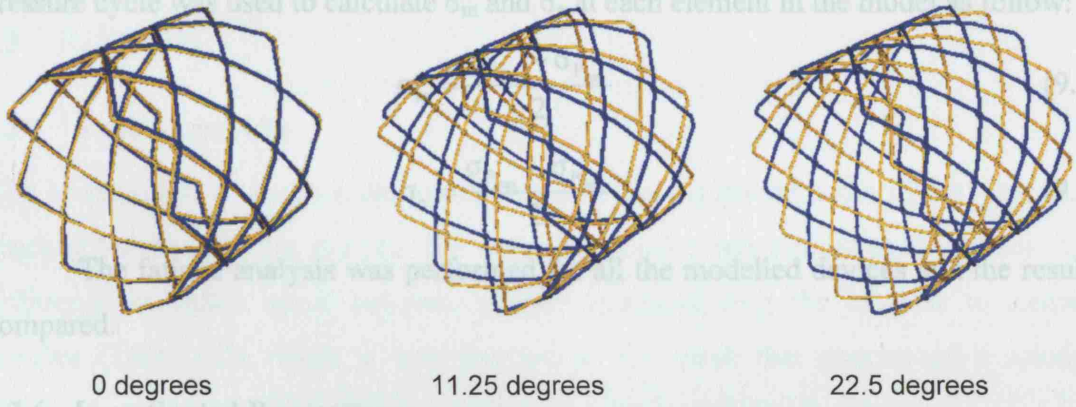

Figure 8.6 Three relative rotation degrees between the outer (blue) and inner (yellow) devices in the 2PL analyses at the end of stent inflation.

8.2.5 Fatigue Analysis

The objective of this analysis was to determine the fatigue stresses of the inflated stent design when subjected to cyclic external pressures. Several theories have been developed in order to establish a relationship between alternating stress (σ_a) and mean stress (σ_m) in a structure under cyclic load conditions and with specific material mechanical limits. The Goodman method, which is commonly used for ductile metallic alloys, was used for this study. This method uses a graphical approach for relating σ_a and σ_m with the material strength limits. An x-y plot is used where σ_m is plotted along the x-axis and σ_a is plotted along the y-axis. The fatigue endurance strength, S_e, is the limiting value of σ_a and is also plotted along the y-axis. A straight line (Goodman line)

is drawn from S_e to the material's ultimate strength, S_{ult}, along the x-axis. Values of σ_a and σ_m that fall above this line indicate possible fatigue failure.

The mean and alternating stresses in the PPVI stent, deployed and subjected to cyclic loading conditions, depends on the stress conditions at the maximum and minimum pressures applied during the cardiac cycle. The stent inflation FE analysis described in the previous section was therefore used to determine the maximum and minimum fatigue stresses. The external pressure applied to the stent was cycled from 0 MPa (minimum pressure P_{min}) to 0.1 MPa (maximum pressure P_{max}) to obtain the minimum and maximum stresses respectively for use in the fatigue analysis. The maximum principal stress component, σ, at the beginning and end of the pulsation pressure cycle was used to calculate σ_m and σ_a at each element in the model as follow:

$$\sigma_m = \frac{\sigma_{P_{max}} + \sigma_{P_{min}}}{2} \tag{9.1}$$

$$\sigma_a = \frac{\sigma_{P_{max}} - \sigma_{P_{min}}}{2} \tag{9.2}$$

The fatigue analysis was performed for all the modelled devices and the results compared.

8.2.6 Investigated Parameters

The following mechanical properties were measured:

- Elastic recoil (R) following virtual balloon deflation in the stent middle (R_{middle}) and peripheral ($R_{peripheral}$) sections. The elastic recoil was defined as:

$$R = \frac{D_{load} - D_{unload}}{D_{load}} \cdot 100$$

with D_{load} and D_{unload} equal to the stent diameter at the end of the loading and unloading step, respectively. The difference in the elastic recoil (ΔR) between peripheral and middle section of the stent was defined as:

$$\Delta R = R^{middle} - R^{peripheral}$$

- Von Mises equivalent stress (σ_{VM}) map at the end of virtual balloon inflation, deflation, and after application of the external pressure.
- Radial strength, represented by the plot of radial displacement resulting from the applied external pressure. The displacement was evaluated at both the peripheral and central nodes of the device.

- Goodman diagram plotted using S_e, S_{ult} and the value of σ_m and σ_a for each element of the stent models.
- Fatigue safety factor (FSF), which essentially quantified the proximity of σ_m and σ_a at any given numerical integration point of the stent models to the limiting Goodman curve, calculated as:

$$\frac{1}{FSF} = \frac{\sigma_m}{S_{ult}} + \frac{\sigma_a}{S_e}$$

- where σ_m and σ_a derived from the equations (9.1) and (9.2) respectively.
- Contour plot of the inverse of FSF depicting in red the zone with the maximum inverted value or the lowest FSF.

8.3 RESULTS

8.3.1 Mesh Sensitivity

Von Mises stress colour map and elastic recoil of the peripheral nodes of the stent were checked for the different meshes. The stress distribution was similar in all meshes. The difference in elastic recoil between meshes decreased with the increase in element number (Table 8.2). Mesh C was selected as the mesh that guaranteed a solution independent from the grid without a critical increase in calculation time.

The mesh of the gold parts, built around mesh C of the PT model, resulted in additional 116602 elements for the PL-AU stent.

The $PL_{1/2}$ mesh was made of 149703 elements and 304054 nodes.

	Spacing	Elements	Nodes	$R^{peripheral}$ [%]
A	0.17	85393	176424	1.58
B	0.15	95720	195365	1.57
C	0.12	166778	324518	1.55
D	0.115	218832	417126	1.55
E	0.1	284703	527852	1.54

Table 8.2 Mesh sensitivity analysis.

8.3.2 Elastic Recoil

Inflation by displacement control resulted in uniform radial expansion in all stent configurations. Upon balloon deflation, the R of the different devices was generally low, especially if compared to the values reported for stents used in different clinical indications [189-191].

As expected, $R_{PL_{1/2}} > R_{PL}$ because of the larger wire section of the PL stent, and $R_{PL} > R_{PL\text{-}AU}$ because of the gold reinforcement in the PL-AU stent (Table 8.3).

The difference in elastic recoil between the peripheral and middle sections was tiny for all the stents. The highest ΔR was in the $PL_{1/2}$ stent, where the peripheral sections recovered more than the central part. Pressure applied uniformly to the external surface of the stent revealed that the peripheral sections of the $PL_{1/2}$ device were also weaker than the central part in bolstering the arterial wall (Figure 8.7c)

The elastic recoil of the 2PL stent-in-stent analyses was almost the same in the three rotation configurations and $R_{PL} > R_{2PL}$. The coupled system can be imagined as a combination of two parallel springs. The force of recovery in the 2PL is bigger than with one single device. For the same reason, $R^{middle}_{PL_{1/2}} < R^{middle}_{2PL_{1/2}}$. However, $R^{peripheral}_{PL_{1/2}} > R^{peripheral}_{2PL_{1/2}}$: the coupling of two $PL_{1/2}$ stents reinforced the peripheral sections of the structure.

Model	$R^{peripheral}$ [%]	R^{middle} [%]	ΔR [%]
PL	1.55	1.38	0.17
PL-AU	1.38	1.16	0.22
$PL_{1/2}$	2.31	1.90	0.41
2PL – 0 degrees	1.71	1.50	0.21
2PL – 11.25 degrees	1.69	1.52	0.17
2PL – 22.5 degrees	1.70	1.58	0.12
$2PL_{1/2}$	2.14	1.95	0.19

Table 8.3 Elastic Recoil Values.

8.3.3 Stress Distribution

The Von Mises stress maps at the inflated diameter of 24 mm is presented in Figure 8.7a for the PL, PL-AU and $PL_{1/2}$ stents. The highest stresses occurred in localized regions of the devices – at the strut intersections – where a peak of approximately 660 MPa was detected. These stresses were primarily due to the bending of the wires close to the platinum welds as the struts opened during inflation. Stress values throughout the stent were typically lower, diminishing rapidly from the crowns to the straight parts.

After virtual deflation of the balloon, at the end of the elastic recoil (Figure 8.7b), σ_{VM} were lower everywhere due to the general unloading of the entire structure.

When compared to the PL device, the values of σ_{VM} at the strut intersections in PT-AU were slightly smaller, both at the end of the inflation step (Figure 8.7a) and virtual balloon deflation (Figure 8.7b). However, this difference was mostly evident when the external pressure was applied (Figure 8.7c), that is when the stent has to resist to the recovering force of the arterial wall.

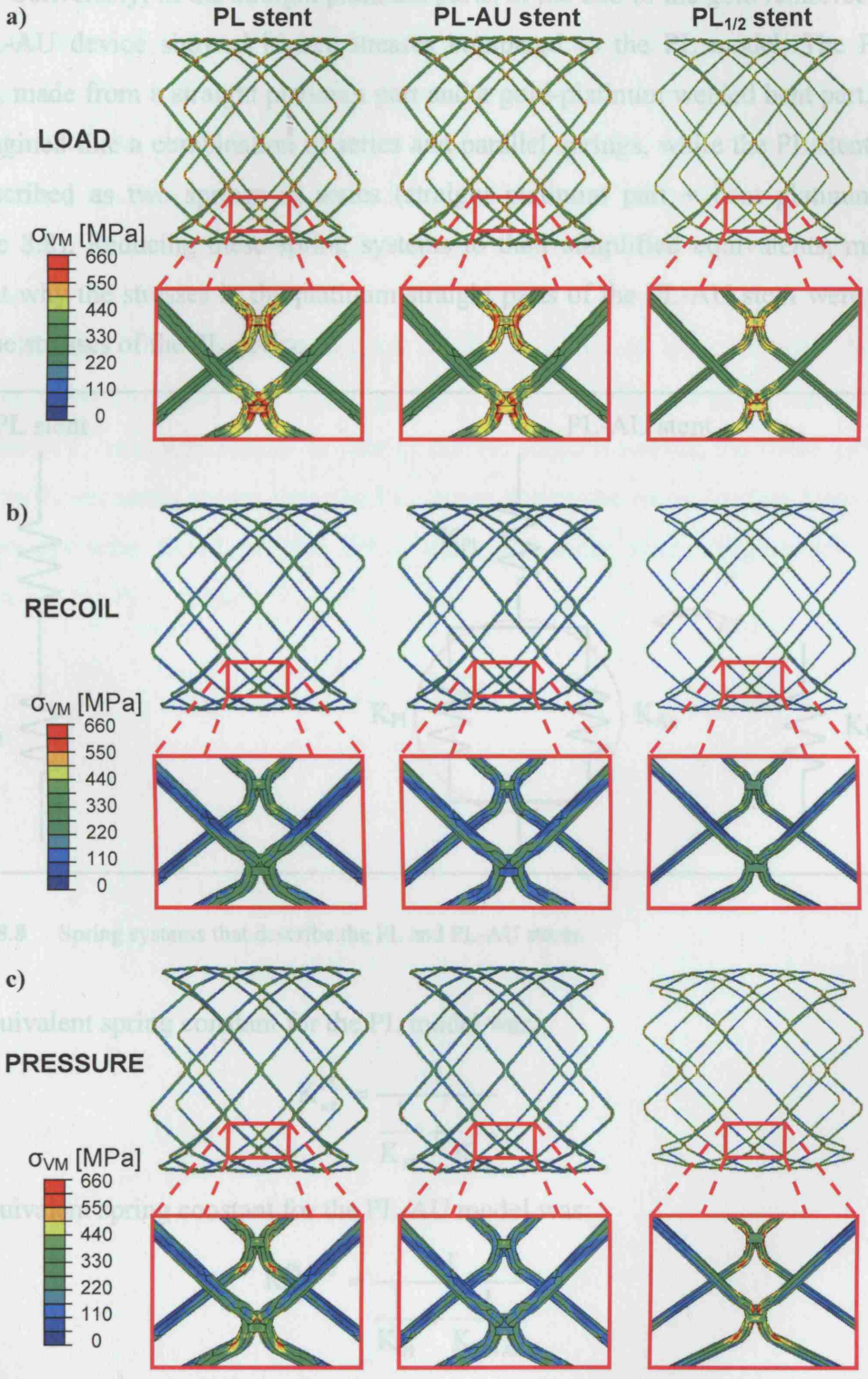

Figure 8.7 Von Mises stress (σ_{VM}) map in the PL, PL-AU (the gold elements were removed to visualize the stress distribution in the platinum elements) and $PL_{1/2}$ stents at a) end of the inflation, b) elastic recoil, and c) after application of a 0.2 MPa pressure to the external surface of the devices.

Conversely, in the straight platinum parts, at the end of the gold reinforcements, the PL-AU device showed higher stresses compared to the PL model. The PL-AU device, made from a straight platinum part and a gold-platinum welded bent part, could be imagined like a combination of series and parallel springs, while the PL stent could be described as two springs in series (straight platinum part + bent platinum part) (Figure 8.8). Reducing these spring systems to their simplified equivalents, makes it evident why the stresses in the platinum straight parts of the PL-AU stent were higher than the stresses of the PL device.

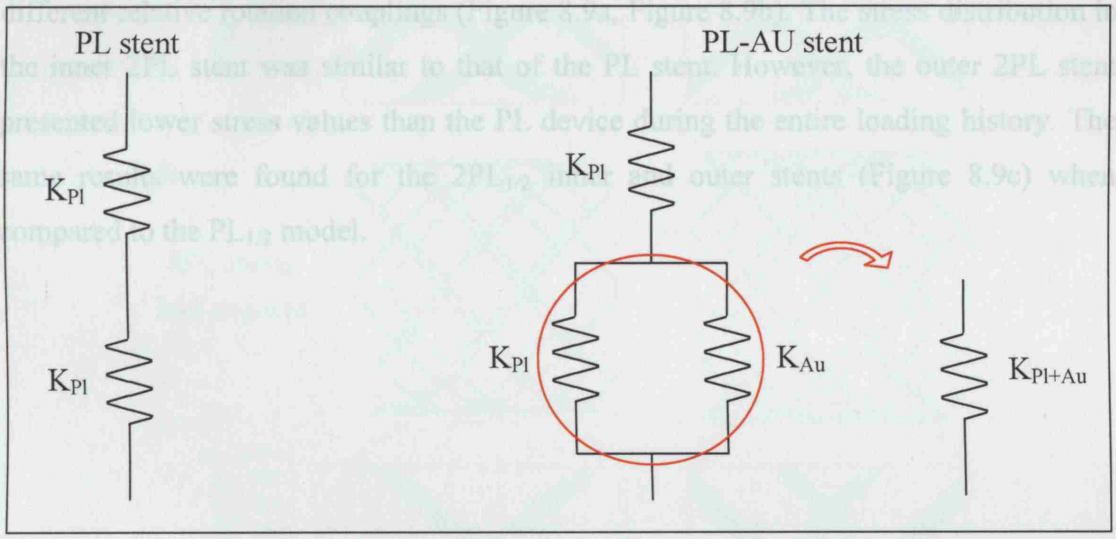

Figure 8.8 Spring systems that describe the PL and PL-AU stents.

The equivalent spring constant for the PL model was:

$$K_{eq}^{PL} = \frac{1}{\frac{1}{K_{Pl}} + \frac{1}{K_{Pl}}} \tag{9.1}$$

The equivalent spring constant for the PL-AU model was:

$$K_{eq}^{PL\text{-}AU} = \frac{1}{\frac{1}{K_{Pl}} + \frac{1}{K_{Pl+Au}}} \tag{9.2}$$

Since $K_{Pl+Au} = K_{Pl} + K_{Au}$, then $K_{Pl+Au} > K_{Pl}$. Therefore, from the equations 9.1 and 9.2, it derived that:

$$K_{eq}^{PL\text{-}AU} > K_{eq}^{PL} \tag{9.3}$$

In general, the spring equation

$$F = K \cdot x \tag{9.4}$$

relates the force (F) exerted by a spring to the distance (x) it is stretched by a spring constant, K. The inflation modality (displacement control exerted by the balloon inflated inside the stent) forced the two devices, PL and PL-AU, to the same rate of displacement (x) during the expansion. Since (9.3), then $F^{PT\text{-}AU} > F^{PT}$ and therefore the straight part of platinum in the PL-AU stent was more stressed then the same part of the PL stent.

The 2PL model gave analogous results in terms of σ_{VM} between the three different relative rotation couplings (Figure 8.9a, Figure 8.9b). The stress distribution in the inner 2PL stent was similar to that of the PL stent. However, the outer 2PL stent presented lower stress values than the PL device during the entire loading history. The same results were found for the $2PL_{1/2}$ inner and outer stents (Figure 8.9c) when compared to the $PL_{1/2}$ model.

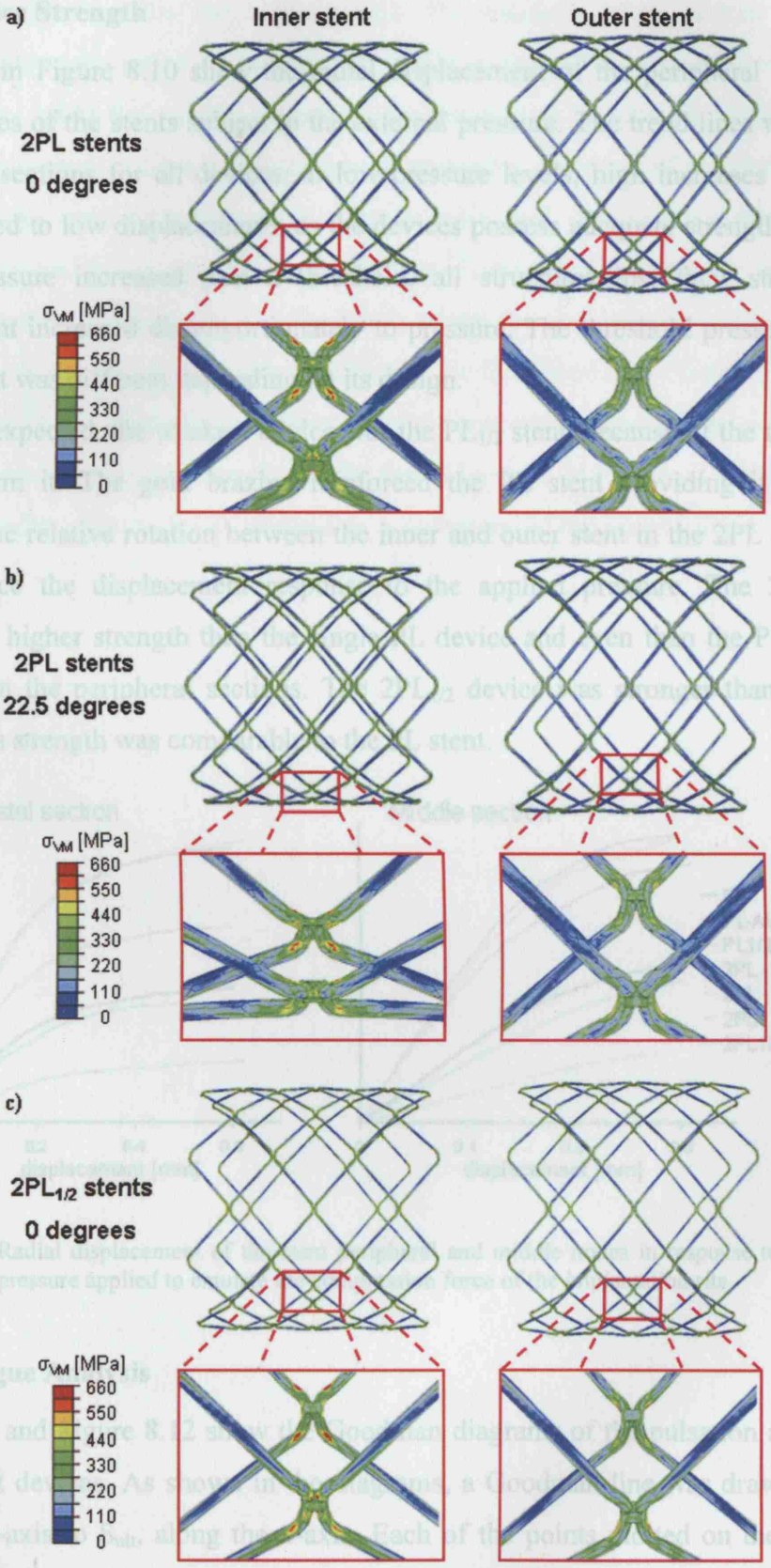

Figure 8.9 Von Mises stress (σ_{VM}) map of the inner and outer stents of the 2PL models for a) 0 degrees and b) 22.5 degrees configuration, and c) of the $2PL_{1/2}$ model, at 0.2 MPa of pressure.

8.3.4 Device Strength

The charts in Figure 8.10 show the radial displacement of the peripheral and middle section nodes of the stents subject to the external pressure. The trend lines were similar in the two sections for all devices: at low pressure levels, high increases in pressure corresponded to low displacements, as the devices possess adequate strength. However, as the pressure increased past a threshold, all structures lost their strength, and displacement increased disproportionately to pressure. The threshold pressure for each type of stent was different depending on its design.

As expected, the weakest device was the $PL_{1/2}$ stent, because of the thinner wire used to form it. The gold brazing reinforced the PL stent providing it with extra strength. The relative rotation between the inner and outer stent in the 2PL devices did not influence the displacement response to the applied pressure. The 2PL model presented a higher strength than the single PL device and even than the PL-AU stent especially in the peripheral sections. The $2PL_{1/2}$ device was stronger than the single $PL_{1/2}$ and its strength was comparable to the PL stent.

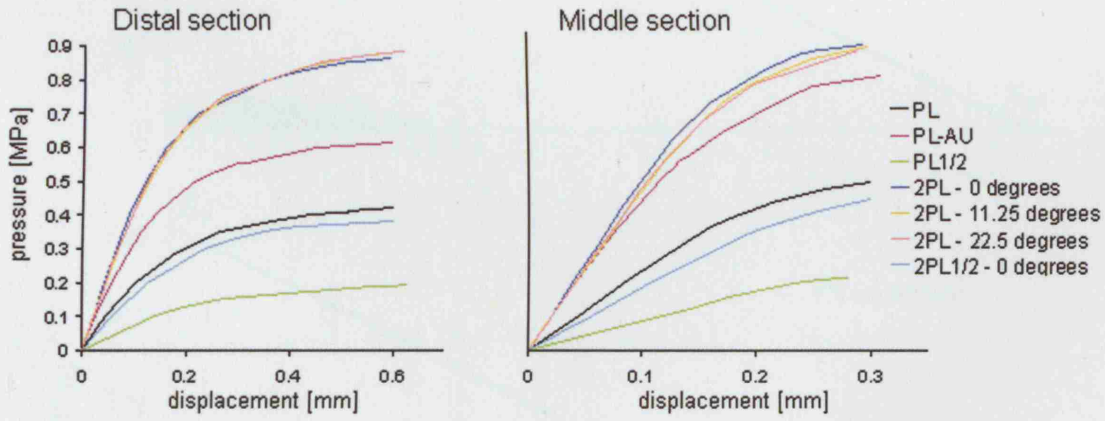

Figure 8.10 Radial displacement of the stent peripheral and middle nodes in response to the external pressure applied to emulate the compression force of the implantation site.

8.3.5 Fatigue Analysis

Figure 8.11 and Figure 8.12 show the Goodman diagrams of the pulsation analysis for the different devices. As shown in the diagrams, a Goodman line was drawn from S_e, along the y-axis to S_{ult}, along the x-axis. Each of the points plotted on the Goodman diagram represented σ_m and σ_a for one of the elements in the FE model (calculated at the centroid of the element). The majority of the points fell well below the line in all

diagrams, indicating that the regions with the smallest safety factors were very localized. During the pulsation loading, the inside surface of the zig-zaged wires was in compression, while the outside surface of the bends was in tension, for all modelled devices. These areas, where the stress was compressive, were not of concern for fatigue because cracks only propagate under tensile loads and compressive stresses in the region of a crack do not produce more damage. The critical regions for fatigue were, therefore, on the outside surface of the bends where the peak tensile stresses occurred. The points of the PL-AU device distribution in the Goodman diagram were more concentrated in the area close to the origin if compared to the PL device plot. The greater dispersion of points was drawn for the $PL_{1/2}$ stent. However, 2 of these devices coupled together (Figure 8.12) resulted in a gathering of the points closer to the safer zone.

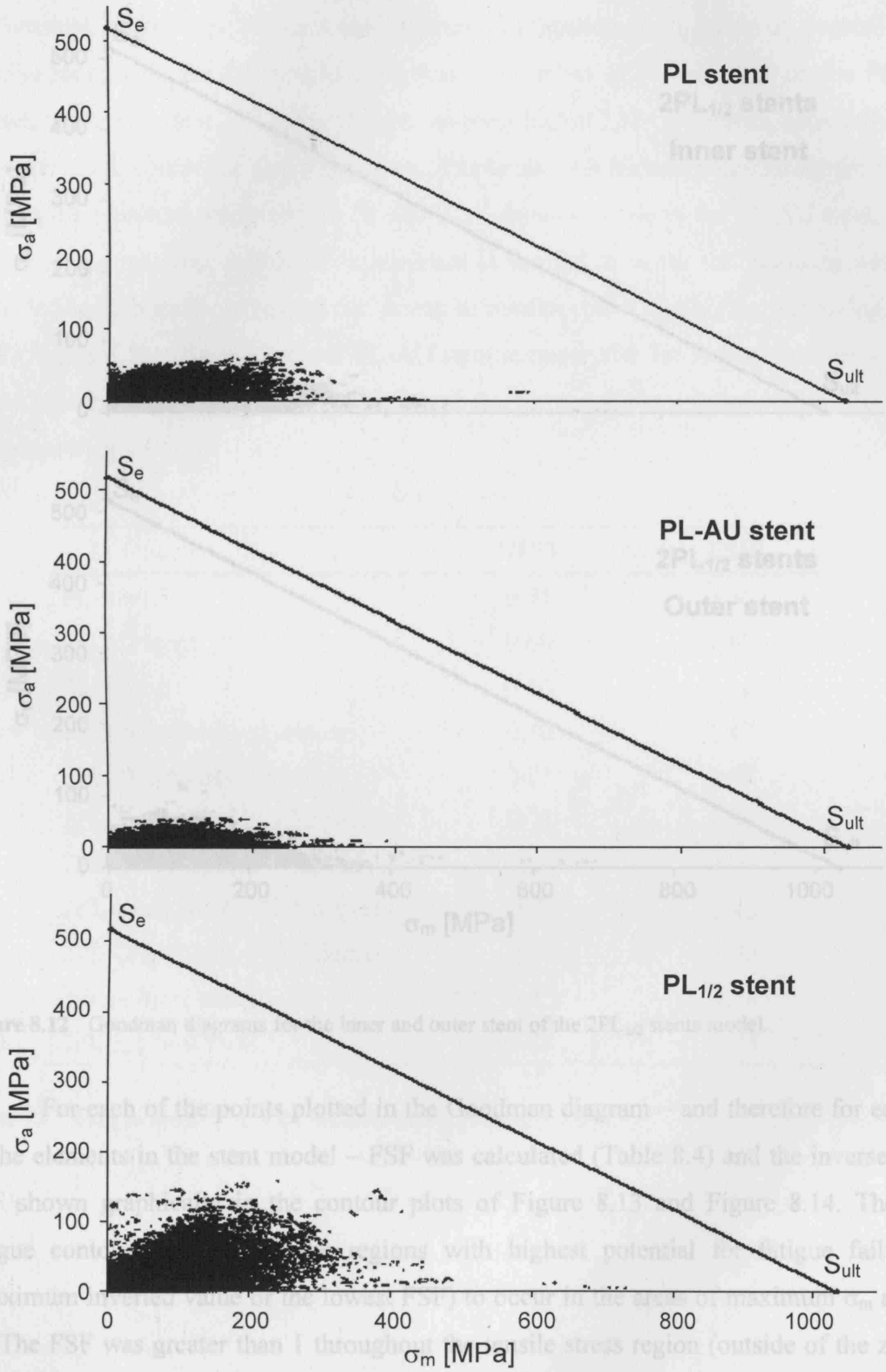

Figure 8.11 Goodman diagrams for the PL, PL-AU and $PL_{1/2}$ stents.

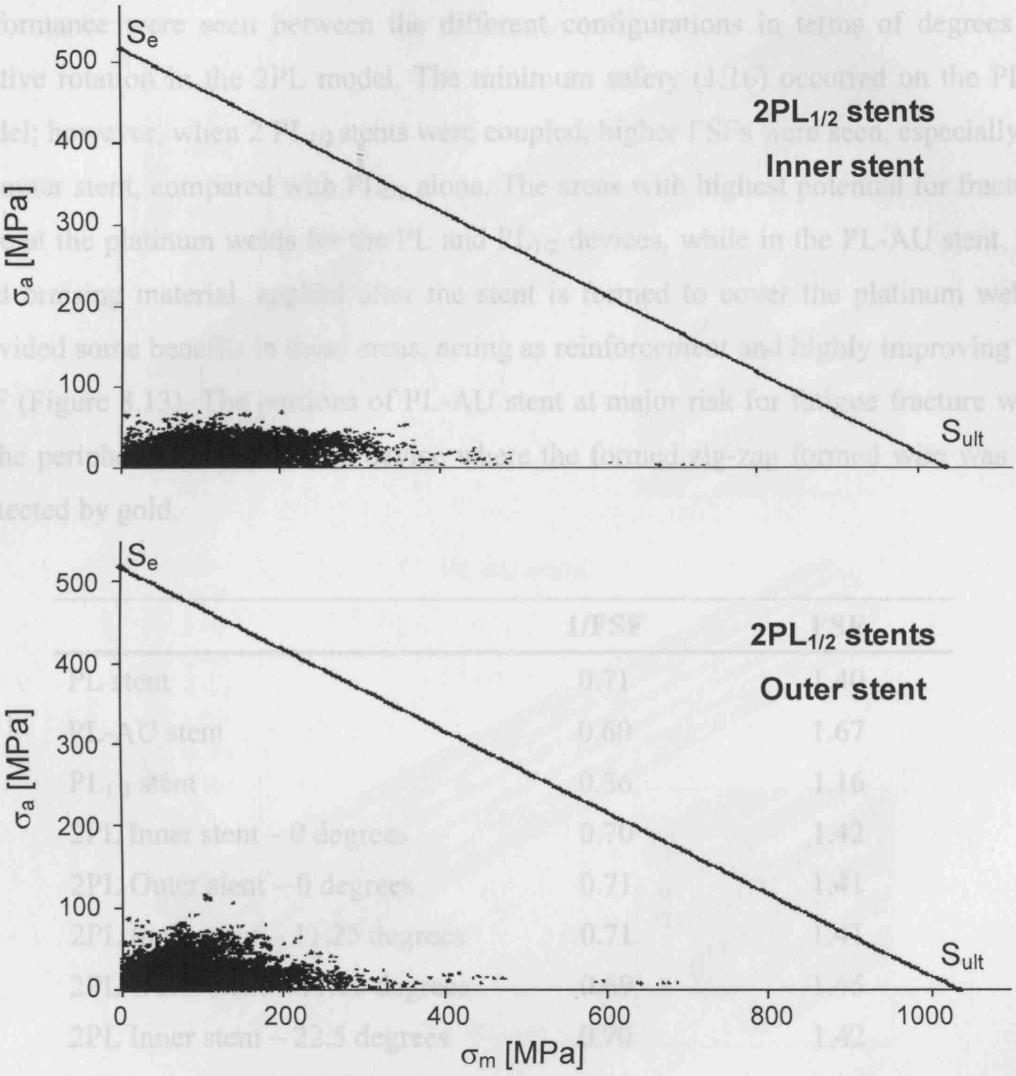

Figure 8.12 Goodman diagrams for the inner and outer stent of the $2PL_{1/2}$ stents model.

For each of the points plotted in the Goodman diagram – and therefore for each of the elements in the stent model – FSF was calculated (Table 8.4) and the inverse of FSF shown graphically in the contour plots of Figure 8.13 and Figure 8.14. These fatigue contour plots depict the regions with highest potential for fatigue failure (maximum inverted value or the lowest FSF) to occur in the areas of maximum σ_m and σ_a. The FSF was greater than 1 throughout the tensile stress region (outside of the zig-zags) of all studied stents (Table 8.4). The PL-AU model had the most reliable design followed by the 2PL model – 22.5 degrees – where 2 PL stent coupled together enhanced the fatigue performance of the PL stent alone. Small differences in fatigue

performance were seen between the different configurations in terms of degrees of relative rotation in the 2PL model. The minimum safety (1.16) occurred on the $PL_{1/2}$ model; however, when 2 $PL_{1/2}$ stents were coupled, higher FSFs were seen, especially in the outer stent, compared with $PL_{1/2}$ alone. The areas with highest potential for fracture were at the platinum welds for the PL and $PL_{1/2}$ devices, while in the PL-AU stent, the gold braising material, applied after the stent is formed to cover the platinum welds, provided some benefits in these areas, acting as reinforcement and highly improving the FSF (Figure 8.13). The portions of PL-AU stent at major risk for fatigue fracture were at the peripheral sections of the device where the formed zig-zag formed wire was not protected by gold.

	1/FSF	**FSF**
PL stent	0.71	1.40
PL-AU stent	0.60	1.67
$PL_{1/2}$ stent	0.86	1.16
2PL Inner stent – 0 degrees	0.70	1.42
2PL Outer stent – 0 degrees	0.71	1.41
2PL Inner stent – 11.25 degrees	0.71	1.41
2PL Outer stent – 11.25 degrees	0.69	1.45
2PL Inner stent – 22.5 degrees	0.70	1.42
2PL Outer stent – 22.5 degrees	0.69	1.45
$2PL_{1/2}$ Inner stent	0.85	1.18
$2PL_{1/2}$ Outer stent	0.78	1.28

Table 8.4 Fatigue safety factors for the different stent configurations.

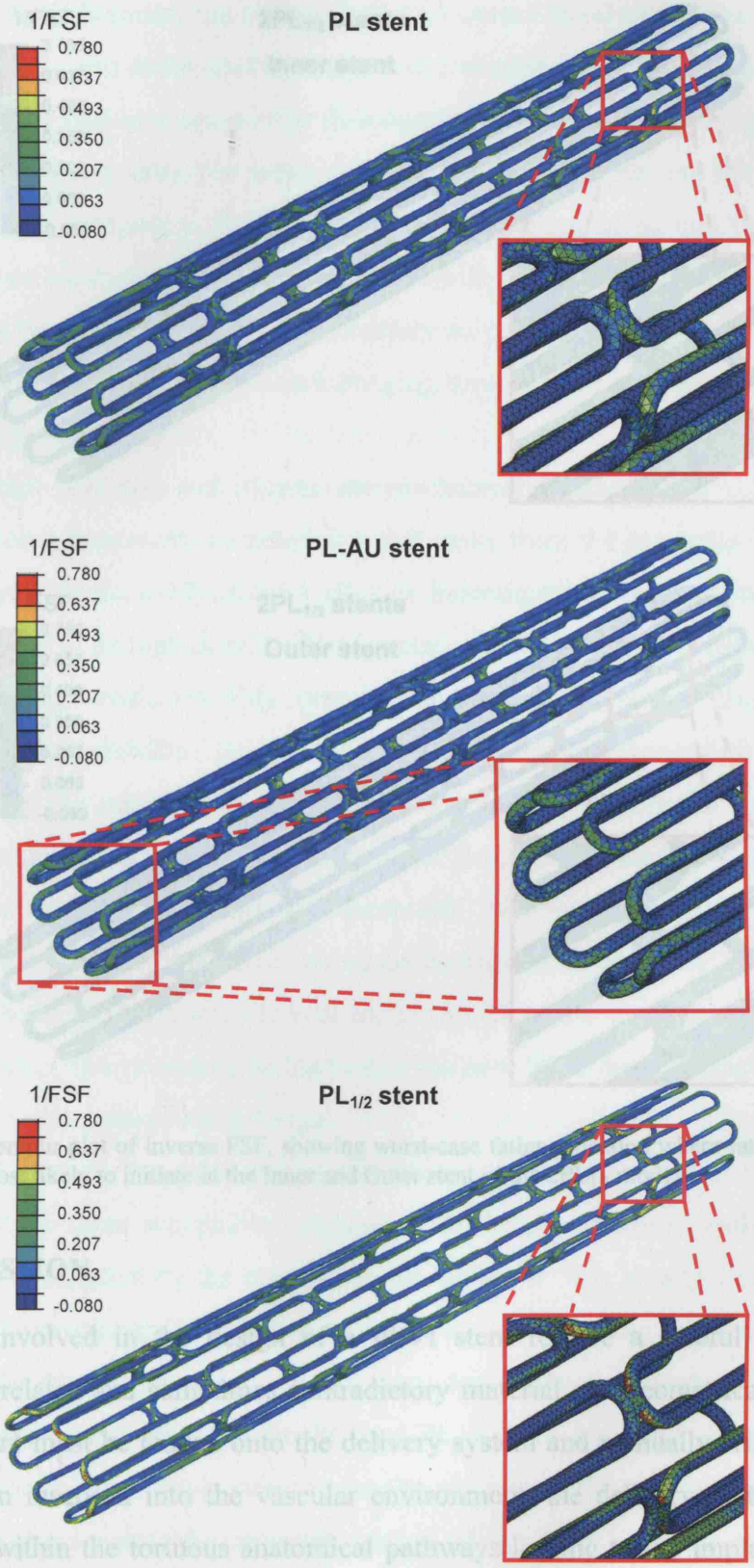

Figure 8.13 Contour plot of inverse FSF, showing worst-case fatigue location where fatigue cracks are most likely to initiate in the PL, PL-AU and $PL_{1/2}$ stents.

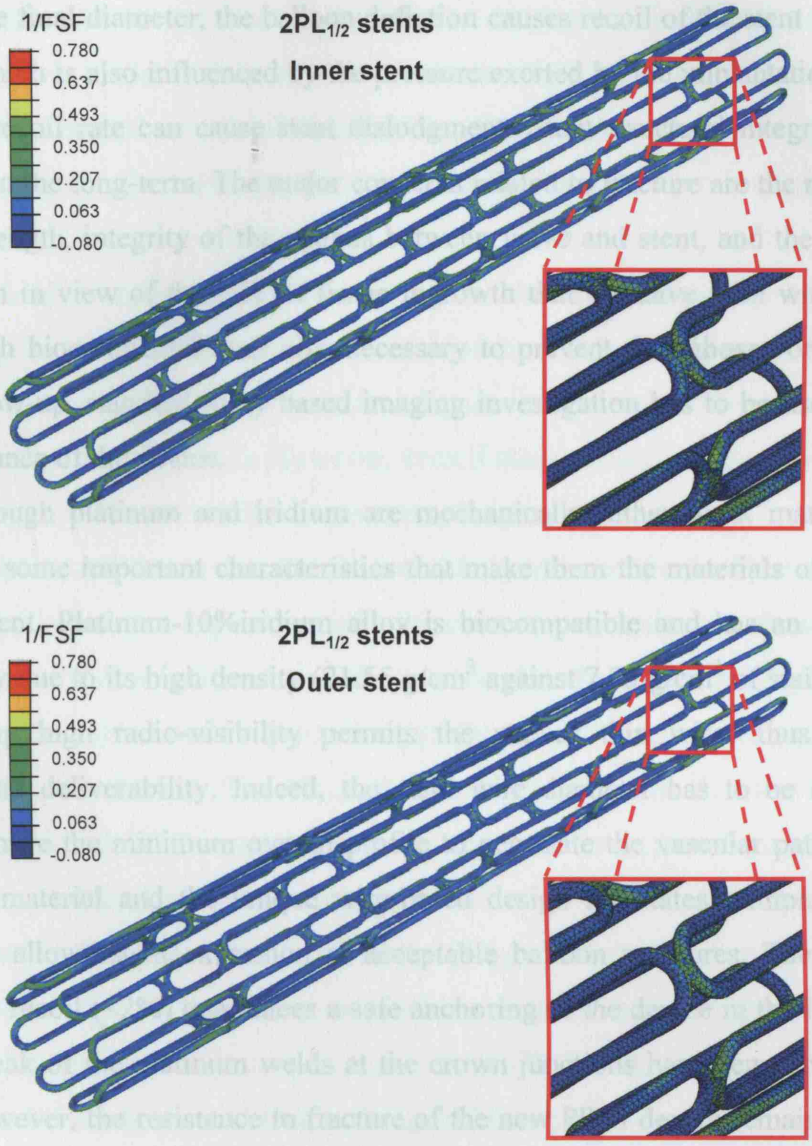

Figure 8.14 Contour plot of inverse FSF, showing worst-case fatigue location where fatigue cracks are most likely to initiate in the Inner and Outer stent of the $2PL_{1/2}$ model.

8.4 DISCUSSION

The targets involved in the design of a PPVI stent require a careful compromise between interrelated and sometimes contradictory material and geometrical properties. The PPVI stent must be loaded onto the delivery system and manually crimped on the balloon. Upon insertion into the vascular environment, the delivery system must be manipulated within the tortuous anatomical pathways leading to the implantation site. The delivery of the device to the optimal position requires good visibility under fluoroscopy. Stent deployment is gained by gradual inflation of the balloon. Upon

acquiring the final diameter, the balloon deflation causes recoil of the stent to a smaller diameter, which is also influenced by the pressure exerted by the implantation site wall. High stent recoil rate can cause stent dislodgment. Stent structural integrity must be guaranteed in the long-term. The major concerns related to fracture are the maintenance of radial strength, integrity of the sutures between valve and stent, and the risk of late embolization in view of the lack of tissue ingrowth that we have seen with the PPVI stent. A high biocompatibility is also necessary to prevent thromboses or restenoses. During follow-up, standard x-ray based imaging investigation has to be used to assess the performance of the device.

Although platinum and iridium are mechanically rather weak materials, they also present some important characteristics that make them the materials of choice for the PPVI stent. Platinum-10%iridium alloy is biocompatible and has an exceptional radio-opacity due to its high density (21.55 g/cm^3 against 7.95 g/cm^3 of stainless steel). The resulting high radio-visibility permits the use of thin wires thus improving flexibility and deliverability. Indeed, the stent wire diameter has to be as small as possible to have the minimum overall profile to negotiate the vascular pathways. The use of this material and the unique wire-based design facilitates crimping onto the balloon and allows stent expansion at acceptable balloon pressures. The reasonably small elastic recoil (<2%) guarantees a safe anchoring of the device in the implantation site. The break of the platinum welds at the crown junctions has been solved by gold brazing. However, the resistance to fracture of the new PPVI device remains the major concern of this stent material and design.

This FE study has proved that the maximum stresses reached in the device during inflation remain acceptable (platinum-10%iridium ultimate tensile strength of 1034 MPa, data supplied by the manufacturer). However, it is clearly visible from the computational analyses that the stress increases according to the expansion diameter; the safety of the device, therefore, is highly dependent on the magnitude of deployment.

The comparison between the PL and PL-AU models after external pressure application showed much lower stress in the PL-AU stent at the strut intersections. This is because in these points the resistant section of the PL-AU device is larger. The relatively weak gold actually reinforces the weld sections of the stent. However, it is possible to note a redistribution of σ_{VM} in the straight platinum sections, at the end of

the gold reinforcements: the structure is loaded at these points more than when there is no reinforcement, because of the reinforcement itself. Indeed, the gold reinforcement creates geometrical and material discontinuities. This suggests that fractures in the PL-AU device may occur just distal to the gold brazed elements, as proven from patient x-ray investigation.

The fatigue analysis strengthened the idea that the gold brazes act as a solid reinforcement for the stent platinum welds. Indeed the regions at highest risk of fracture in the PL-AU device were at the peripheral parts of the stent, where the platinum-10%iridium wires are uncovered. However, even if these peripheral parts had lower FSF compared to the weld areas in the same stent, the potential of fatigue fracture for this stent, PL-AU, was still lower than the chance of fatigue failure for the PL model.

The limited recent experience with the stent-in-stent technique demonstrate not only that repeat PPVI is safe and feasible, but also that the implantation of a previous device before the valved one may act functionally to bolster the vessel and ensure the integrity of the valved stent. The $2PL_{1/2}$ device compared to the PL stent showed the same ability to withstand the external pressure, the same stress distribution in the inner stent, but favourable, lower stress values in the outer device. Because of its wire diameter, the two $PL_{1/2}$ stent employed in the $2PL_{1/2}$ model present the same material mass as the PL stent, but the thinner wire allows easier crimping, better deliverability and greater flexibility. The recoil is higher in the $2PL_{1/2}$ device than the PL stent. However, the FE study showed that as the gold brazing reinforces the platinum wires, the elastic recoil is reduced. In terms of fatigue failure, the $PL_{1/2}$ model was the worst among the models analysed, but 2 of these stents coupled together could enhance the fatigue performance of the $PL_{1/2}$ stent alone. The $2PL_{1/2}$ model FSF was, however, lower than the PL stent FSF, but gold reinforcement at the strut intersections could help further reduce the potential for fracture of $2PL_{1/2}$ model. Therefore, it is reasonable to conclude that a coupling of two PL-AU devices made of a thinner wire would result in better performance. In clinical practice, the stent-in-stent technique could be performed either sequentially or as a single step approach. In our experience, sequential stenting can be performed safely (6 patients – no embolization). For the single step approach (no performed to date), the delivery system would be of similar size as the two stents are half the size of the previous single device, and thus additional complications of a higher

French delivery system would be avoided. Therefore, the multi-element stent with gold reinforcement is a possible solution to reduce the chance of device fracture in PPVI and increase the success of this procedure, without theoretically compromising its technical ease. The FE analysis of this device was not carried out because of the large number of nodes and elements required by the mesh of this model, which exceeds the performance of the computer used in this study.

The pressure to compress the stents modelled in this study to a smaller diameter (Figure 8.10) is high if compared to data reported from mechanical tests in endovascular stents [192,193], where however the device is subject to punctual loads. The pressure in this FE model is uniformly applied along the stent circumference. Therefore, higher pressure values guaranteed to be on the safe side in the computational analysis.

In-vivo, the stent conforms its shape to the implantation site [79]. Angiographic pictures of PPVI patients show that the shape of the *in-vivo* stent differs from the theoretical cylindrical profile. Therefore, the force that the stent may be subjected to by the implantation site and the surrounding tissues are not uniform around the circumference. This can cause high-stress concentrations in some parts of the stents and increase the risk of fracture. Clearly the main limitation of this study is the absence of the implantation site model [137,140]. The next step will be the development of FE models of realistic RVOT geometries, which can be obtained from post processing of MR images as discussed in the previous 2 chapters. By simulating the interaction between the stent and the real implantation site model, it may be possible to evaluate the deformed shape of the device and the real distribution of stresses to which the prosthesis is subjected.

8.5 CONCLUSION

Stent fracture is the major technical complication related to PPVI. In this chapter, I have used the FE method as a technique to analyse and compare existing stents in order to understand the mechanical reasons for their fracture and to optimize their design. Importantly, these FE analyses have identified potential areas for failure in the stent, that correspond to those areas that fracture in clinical practice. However, the mechanical limit values that are indicators of possible fracture have not been reached in the FE analyses and the current stent for PPVI should not fail. Also the bench testing carried

out before the introduction of the device first-in-man, and in which the PPVI stent was fatigue tested over million of cycles showed no fracture. However, both tests do not consider the *in-vivo* loading conditions the stent is subject to in the real PPVI situation. These may be the discriminating factor in fracture occurrence. Thus, the current experimental set-up is not properly designed and the FE analyses, although give important indications, are not robust enough. Therefore, the interaction between the stent and the RVOT will be studied next on clinical data analyses and further modelled with the aid of FE method [Chapter 9].

The multi-element stent herein presented is a new concept that could solve the problem of fracture in PPVI devices. Indeed, the coupling of two stents, made from thin wires, resulted in high strength and low stresses, which guaranteed better resistance to fracture, without affecting other fundamental device properties such as easy crimping, deliverability and low elastic recoil. This novel technique has been put forward as a patent and has potential applications not only in valved stent technology but also in all biomedical fields where stents are employed to sustain tubular structure, including, for example, peripheral artery and venous stents, repair of abdominal aortic aneurysms, and treatment of gastrointestinal and urological conditions.

The multi-element stent may be a solution to enhance the mechanical performance of the PPVI device. However, the design of the multi-element stent would still be based on the current generation device and this new model could only be used to treat the same cohort of patients, who have RVOT dimensions smaller than 22mm in diameter. The demand for a larger device, that overcomes the geometrical limitation of the current generation stent, would not be answered by the multi-element model developed in this chapter and the range of patients who can benefit from PPVI procedure would still remain extremely limited. A first attempt towards the next generation PPVI stent, with an innovative design that can broaden the applications of PPVI, is reported in Chapter 10.

CHAPTER 9

STENT/IMPLANTATION SITE INTERACTION

The analysis of the interaction between the PPVI stent and the implantation site is the subject of this chapter. Biplane fluoroscopy images from patients were used to reconstruct the 3D shape and deformation of the stent in situ. Asymmetries were measured in all directions and early systolic and diastolic configurations were compared.

Following this, the stent/implantation site interaction was modelled using FE analyses. FE contact analysis is a non trivial problem, and simplified hypotheses were introduced. Although a simplified FE modelling of stent/implantation site interaction was adopted, it was able to give useful information about the influence of the RVOT on the stent mechanical performance. When deployed into the RVOT, the stent did not show a uniform shape. This made the stent weaker in bolstering the arterial compression recoil forces and the stresses on the struts higher than when the stent is uniformly loaded, increasing the risk of fracture. Further studies have to be performed to overcome the current limitations of FE modelling in solving contact problems.

9.1 INTRODUCTION

During the development phase of the current PPVI device, simple bench testing and animal experiments were performed as part of routine preclinical testing. These *in-vitro* and *in-vivo* experiments predicted valve degeneration with no stent fracturing. However, in our clinical practice, the opposite occurred – good valve function, ~20% stent fractures.

In the current bench experiments for fatigue testing, the PPVI stents are placed in a distensible cylindrical tube, where they are tested with cyclic pressures over millions of cycles, and no stent fractures are seen. This is most likely because the human *in-vivo* loading conditions are incorrectly reproduced with this experimental apparatus. Animal experiments are also of limited value because they are not representative of human pathological anatomy. The FE analysis performed in Chapter 8 on the actual device showed that the probability of fracture depends on the radial expansion of the stent and on its design. The current stent, once expanded up to 24mm diameter, does not reach the material ultimate tensile stress and has a considerable high safety factor in fatigue testing. Therefore, fracture should not occur. However, the loading conditions assumed for the FE analyses performed in the previous chapter are simplified and not representative of the real situation, where the final shape of the stent *in situ* is far away from being uniformly cylindrical. In order to better understand and predict the stent mechanical performance and durability, the implantation site morphology has to be included into the FE model to enable correct *in-vitro* testing.

The group of patients described in the previous chapter [Section 8.1.1] was further investigated. Fluoroscopy images of the PPVI procedure or follow-up chest x-rays of these 123 patients were reviewed to detect independent variables that might be associated with risk of stent fracture [79]. The following factors were identified and analysed with multivariate Cox regression:

- RVOT type: 'native' – any part of circumference formed by native tissue – as opposed to homograft or other valved or non-valved conduit.
- Presence of pre-existing bare stent in RVOT.
- Sub-sternal location of the PPVI.
- Post dilatation with high-pressure balloon to relieve residual stenosis.

- Recoil of PPVI (qualitatively, PPVI diameter in frontal or lateral plane with fully inflated balloon greater than diameter post balloon deflation).
- RVOT calcification: absent, partial or circumferential calcifications along the RVOT, judged with fluoroscopy.
- Compression of PPVI, assessed as ratio of anteroposterior (AP) and lateral PPVI diameters at proximal, mid and distal site.
- Asymmetry of PPVI, assessed as ratio of anterior and posterior border lengths on lateral projection, and left and right lateral border lengths on AP projection.

In 97/123 patients, the original fluoroscopy images of PPVI procedure or chest x-rays performed after the procedure, were available for review. The PPVI dimensions were measured after calibration with the markers on angiographic catheters (Multitrack, NuMed).

Four factors were associated with higher risk of stent fractures: PPVI into "native" RVOT (B=2.6, P=0.04), non-calcified RVOT (B=-1.0, P<0.01; Log-rank test, p<0.001), presence of PPVI recoil during balloon deflation (B=1.6, P=0.01) and high proximal AP-to-lateral PPVI diameter ratio (B=6.2, P=0.03) as indicator of proximal PPVI compression. All these factors might implicate higher stresses on the PPVI stent. Thus, substernal calcified conduits may be less subjected to cyclic stress. Indeed, these conduits which are circumferentially calcified and adherent to sternum lack mobility and deformation, remaining rigidly immobile behind the sternum, despite the continuous movement of the cardiac chambers during the cardiac cycle.

This first analysis of stent/implantation site interaction, mainly based on a qualitative assessment of patient fluoroscopy images and x-rays, addressed my research towards a more complete and exhaustive study of the 3D stent shape and deformations *in situ*. In particular, in this chapter, the shape and deformations during the cardiac cycle of the current PPVI stent implanted in the RVOT are evaluated. Two patients were selected from those who were treated with PPVI and subsequently experienced stent fracture. Fluoroscopy images have been used to reconstruct the 3D shape of their *in-vivo* stent. A FE model of the interaction between the stent and the implantation site of one of these patients has been investigated. This work is preliminary and the main computational difficulties related to the solution of contact problems in FE analyses are discussed in detail.

9.2 METHODS

9.2.1 Fluoroscopy Systems

Fluoroscopy is routinely used in PPVI for intra-operative localization of patient anatomy and balloon device position. One or 2 x-ray projections of an object are usually not sufficient to reconstruct a 3D object. Several x-ray projections of the same object from different angles are needed to create a good 3D approximation of the object. If only a few x-ray projections are available, some *a priori* knowledge has to be incorporated in the reconstruction process. In the fluoroscopy images, the outline of the stent is easy to visualize due to the high density of the platinum-10%iridium alloy. The geometry of the stent is well known and presents the advantage to be simple, allowing the zig-zag wires to be described by segments. Therefore, the 2D x-ray projections from the fluoroscopy images acquired during the transcatheter procedure were used to create 3D models of the stent *in-situ*, at different times of the cardiac cycle.

An integral component of all conventional digital x-ray imaging systems is the image intensifier, which converts the x-rays into visible radiation that forms the patient image [194]. The image intensifier allows the operator to reduce the dose of x-radiation received by the patient, by amplifying the intensity of the image received. The image intensifier, however, introduces 2 types of spatial distortions:

- Spiral distortion is caused by the magnetic fields surrounding the image intensifier and results in image distortion with a characteristic S-shape (Figure 9.1).

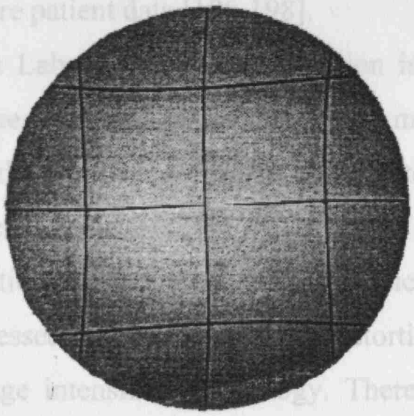

Figure 9.1 Digital x-ray image of wire test object illustrating S-distortion [195].

- Pincushion distortion is due to the construction of the image intensifier that projects the radiation from a curved input screen to the flat output screen. This geometrical distortion is observed as a displacement outwards of a given image point from the ideal location (Figure 9.2).

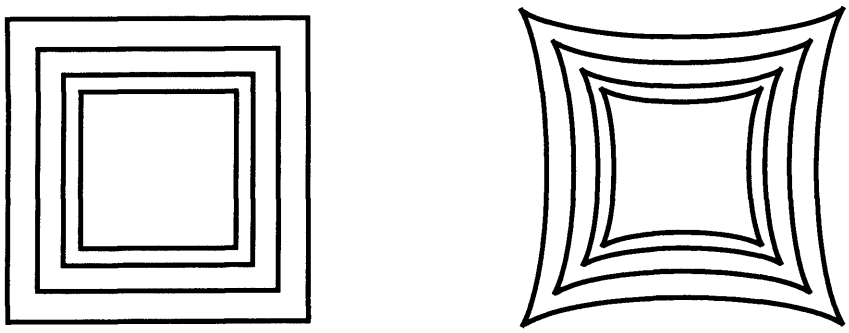

Figure 9.2 Ideal (left) and pincushion distorted (right) image.

The spiral distortion can be corrected with little effort and all image intensifiers manufactured by the major imaging technology companies feature this [195].

The pincushion distortion may be corrected by dedicated real time software. However, this software requires a lot of computing power, especially when highly dynamic studies are performed. Therefore, this error is usually not intrinsically corrected by the imaging acquisition systems. In order to be able to extract quantitative data from the x-ray images, distortion correction is usually needed. This is done using calibration grids and phantoms that are imaged with the imaging system in the same configuration used to acquire patient data [196-198].

The Catheterization Laboratory at our Institution is equipped with an Axiom Artis biplane system (Siemens, Erlangen, Germany) and more recently with a newer, more sophisticated system that features digital flat panel detectors in both planes which replace the image intensifier components. The flat detectors convert the light generated by the absorbed x-ray radiation directly into a digital electrical signal. The flat detection area with individually addressed pixel eliminates the distortions and artifacts associated with the conventional image intensifier technology. Therefore, this system provides excellent image quality (high spatial and contrast resolution) and accuracy at minimum radiation [199-203].

9.2.2 Patient Selection

In this chapter, I retrospectively analysed the PPVI fluoroscopy data of the 36 patients who experienced stent fracture between September 2000 and August 2007. The first 31 patients underwent PPVI in the catheterization laboratory equipped with the old Axiom Artis biplane system. The procedure was performed using the flat detector system in the remaining 5 patients.

In the group of patients who underwent PPVI in the old catheterization laboratory, the correction of the pincushion error by post-processing the distorted images on the basis of phantom imaging acquisition was not feasible. Indeed, the phantom images have to be acquired with the fluoroscopy system in the same position (x-ray source-detector distance, arm primary and secondary angles, table-detector distance) as the patient during the procedure. However, this position could not be retrieved from the fluoroscopy data of the patients in our retrospective analysis. Therefore only the patients who underwent PPVI using the flat detector system (n=5) were considered.

Furthermore, the arm position of the fluoroscopy system during the PPVI procedures limited furthermore the number of patient data that could be utilized for 3D reconstruction. The primary angle and secondary angle define the geometric orientation of the imaging system arms with respect to the patient (Figure 9.3). Zero degree primary and secondary angles correspond to an AP projection. This means that the resulting images are projections of the 3D device structure in two orthogonal 2D images, thus making the manual reconstruction of the 3D stent shape easier. Only 2 patients had orthogonal biplane images (AP projection) and therefore were finally selected for the 3D reconstruction (patient A and B). The characteristics of these 2 patients are reported in Table 9.1.

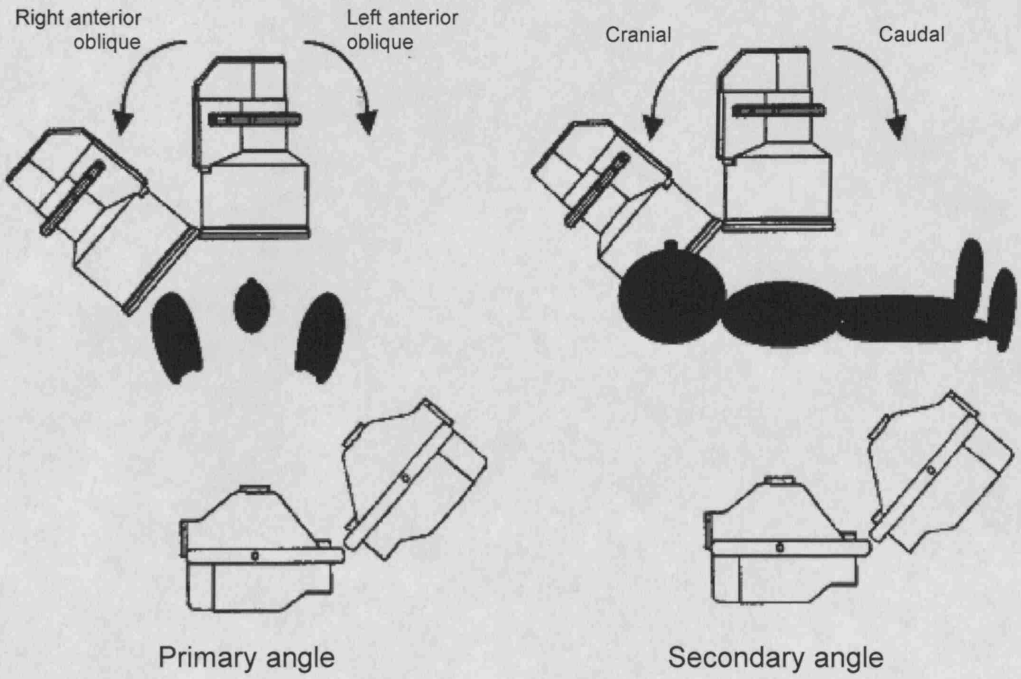

Figure 9.3 Schematic illustration of a fluoroscopy system [204]. The primary angle diagram is viewed from the patient's feet.

Characteristic	Patient A	Patient B
Gender	Male	Female
Age at implant [years]	38	25
Primary diagnosis	Aortic valve disease	Aortic valve disease
Outflow tract type	Homograft	Homograft
Calcification	Absent	Absent
Deployment balloon diameter	20 mm	20 mm
RVOT pressure post-PPVI	15 (syst) - 5 (diast) mmHg	24 (syst) - 15 (diast) mmHg
Time of fracture [days]	112 (spontaneous)	83 (spontaneous)
Type of fracture	I	II
Fracture management	Medical follow-up	Second PPVI

Table 9.1 Characteristics of the 2 patients selected for the stent/implantation site interaction study.

9.2.3 Reconstruction of Stent Shape and Deformations

From the cardiac cycle, the frames equivalent to the maximum (in early systole) and minimum (in diastole) RVOT dimensions were visually selected for each patient in order to evaluate the maximum deformation of the device. The corresponding x-ray images were enhanced with different post-processing techniques in order to increase the contrast and better visualize the stent outline. The 2 orthogonal projections were calibrated and registered. The intersection points between the struts that form the stent, where the zig wires are welded together to form the length of the device, were marked in the 2 fluoroscopy images and projected, using parallel rays, into the space (Figure 9.4). The points at the intersection of the rays departing from the 2 orthogonal images determined the position in 3D of the stent crowns. These points were then joined by straight segments which represented the zig-zags of the device (Figure 9.5).

To evaluate the accuracy of this 3D reconstruction method, the length of the reconstructed straight segments was measured and compared to the real length of the stent strut (5.72 mm). The error [%] was calculated as the difference (absolute value) between the single segment measure and the real length divided by the real length.

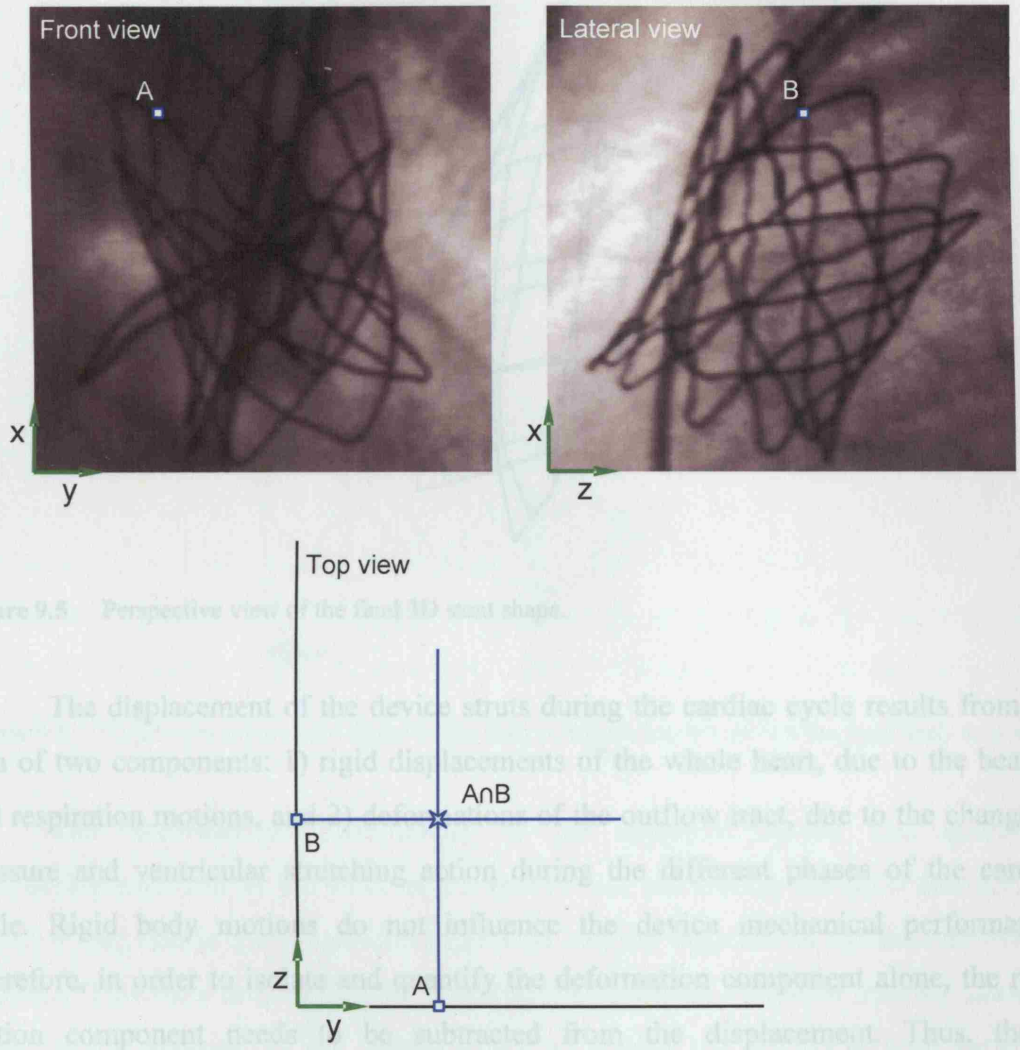

Figure 9.4 Example of the 2 orthogonal projections (from and lateral view) from fluoroscopy images of a patient post-PPVI. The points of weld between the stent wires were marked in the 2 images (A and B) and projected in the space (top view). The intersection point (A∩B) determines the position in space of the selected weld point.

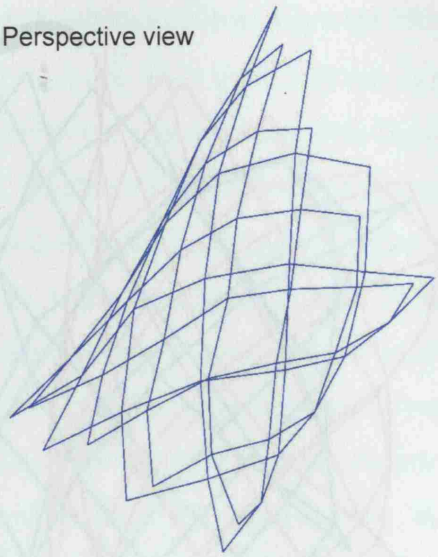

Figure 9.5 Perspective view of the final 3D stent shape.

The displacement of the device struts during the cardiac cycle results from the sum of two components: 1) rigid displacements of the whole heart, due to the beating and respiration motions, and 2) deformations of the outflow tract, due to the change of pressure and ventricular stretching action during the different phases of the cardiac cycle. Rigid body motions do not influence the device mechanical performance. Therefore, in order to isolate and quantify the deformation component alone, the rigid motion component needs to be subtracted from the displacement. Thus, the 2 reconstructions (early systole and diastole) of the device were superimposed and the rigid displacement component subtracted by rigid translation and rotation of one of the stent configurations onto the other (Figure 9.6).

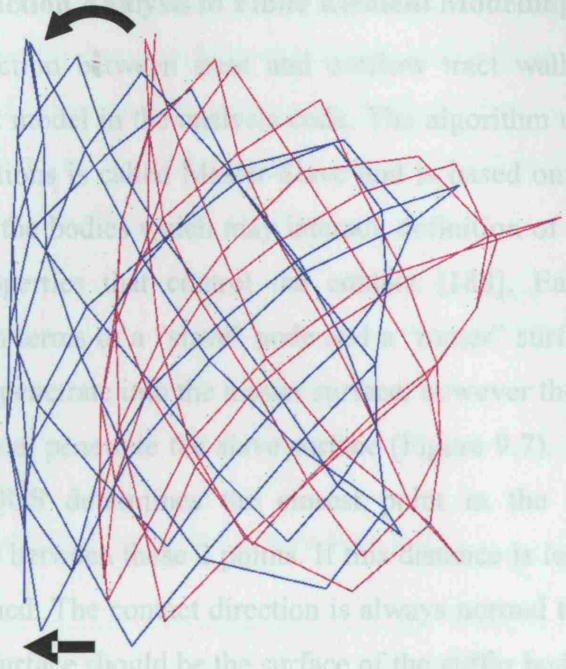

Figure 9.6 Rigid translation and rotation of the stent configuration to subtract the rigid body motion.

The circumferential asymmetry of the deployed device was quantified considering each cell of the stent as a rhombus and calculating the ratio between the rhombus diagonal in the longitudinal direction and the diagonal in the circumferential direction. This ratio in a PPVI stent uniformly deployed at 20mm of internal diameter (equal to the diameter of the balloons used to deploy the device in both patients), measures 1.19 for all cells. This value was calculated from diagonal measurements obtained during the expansion of the FE PL model of Chapter 8.

The radial asymmetry was measured in terms of ratio between the maximum and minimum diameters – D_{max} and D_{min} respectively – at each of the welding sections and the terminal sections of the 2 stent. This parameter was plotted in a chart in order to visualize the variations of the stent shape between early systole and diastole.

The longitudinal asymmetry was calculated standardizing each section of the deployed device to a circle and calculating the maximum difference between the diameters of these circles. The difference was divided by the average diameter of the standardized stent shape.

9.2.4 Contact Interaction Analysis in Finite Element Modelling

Simulating the interaction between stent and outflow tract wall in FE requires the definition of a contact model in the analysis code. The algorithm used by ABAQUS to model contact interactions is called Master-Slave and is based on the definition of the surfaces belonging to the bodies which may interact, definition of the contact pairs and definition of the properties that control the contact [188]. Each potential contact condition is defined in terms of a "slave" node and a "mater" surface. The slave nodes are constrained not to penetrate into the master surface; however the nodes of the master surface can, in principle, penetrate the slave surface (Figure 9.7). For each node of the slave surface, ABAQUS determines the closest point in the master surface, and calculates the distance between these 2 points. If this distance is less than a limit value, the contact is established. The contact direction is always normal to the master surface. Generally the master surface should be the surface of the stiffer body or the surface with the coarsest mesh, if the 2 surfaces are on structures with comparable stiffness.

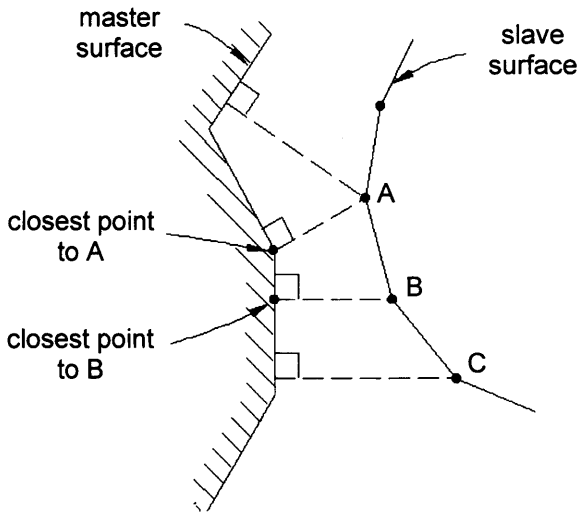

Figure 9.7 Contact and interaction discretization [188].

In ABAQUS, different mechanical contact properties are available that define the relationship between the pressure transmitted in the interaction and the distance of the 2 interacting surfaces. A 'softened' contact relationship, in which the contact pressure is an exponential function of the clearance between the surfaces, was chosen in this thesis (Figure 9.8). This contact relationship is useful for numerical reasons because it can make easier to resolve the contact condition. In the softened contract pressure-

overclosure relationship, the surfaces begin to transmit contact pressure once the clearance between them, measured in the contact normal direction, reduces to c_0 (Figure 9.8). The contact pressure transmitted between the surfaces then increases exponentially as the clearance continues to diminish. Once in contact, the 2 surfaces are allowed any arbitrary motion, separation, sliding and rotation.

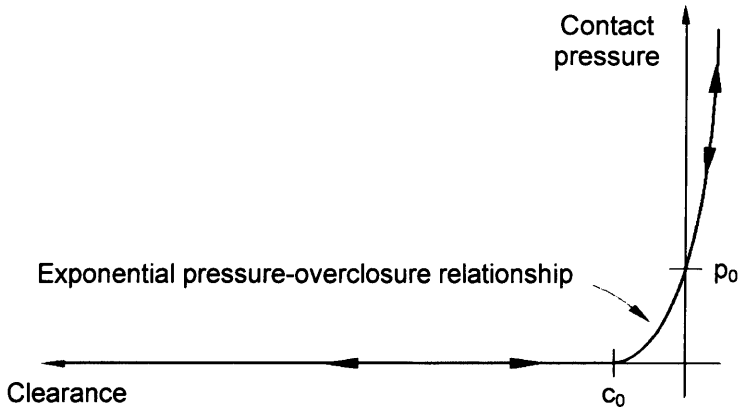

Figure 9.8 Exponential softened pressure-overclosure relationship in ABAQUS [188].

9.2.5 Finite Element Stent/Implantation Site Interaction Analysis

Magnetic resonance images pre-PPVI of Patient B data were used to create a FE model of the implantation site. Indeed, the 3D RVOT geometry from this patient's MR data was reconstructed using the methodology developed in Chapter 6. The mesh for this volume was produced with 3-node triangular shell elements (43980 elements and 131932 nodes), because the thickness of the homograft was considered to be significantly smaller than the other dimensions.

The material properties to describe the mechanical behaviour of the homograft RVOT were derived from literature data [205-213]. Material data vary according to the type of homograft: arterial segment, venous segment and/or sample from different positions in the vascular system. This information was not available for patient B, therefore, average values were assumed and a simple isotropic, linear elastic model was adopted to describe the RVOT material behaviour (Young modulus = 3 MPa, $\nu = 0.3$).

Boundary conditions for the implantation site model included zero displacement of the nodes belonging to the RVOT base and branch ends to avoid rigid body motions.

The PL stent model developed in the previous chapter was used for the interaction study and its crimped, initial configuration was placed inside the RVOT

model. This stent model was called PL_{RVOT} in the interaction analysis to allow an easier comparison of the results with the PL model of the previous chapter and avoid misunderstanding.

For the contact algorithm, the external surface of the PL_{RVOT} model was defined as slave surface, whilst an area of the internal surface of the RVOT model was selected as master surface, since PL_{RVOT} mesh was the finest if compared to the RVOT mesh. When surfaces are in contact they usually transmit shear, as well as normal forces across their interface. The relationship between these 2 force components is described by friction. However, since the RVOT surface is generally smooth and blood is interposed between the 2 surfaces, this phenomenon was neglected in the FE modelling.

Three different simulations were run for the analysis of the stent/implantation site interaction.

First, the stent model was placed in the same position in the RVOT as the real PPVI device site (Figure 9.9, left). The stent was expanded, as explained in the previous chapter, under prescribed radial displacements up to 20mm of internal diameter. This simulated the action of the inflation balloon, which, during the actual procedure in this patient, was deployed up to this final dimension. The prescribed displacements were subsequently removed thus allowing the elastic recoil of the device + outflow tract wall.

Second, the stent was moved further up into the distal part of the RVOT (Figure 9.9, right) and expanded in the same way as the first analysis. This made the calculation related to the contact problem between the PL_{RVOT} device and the implantation site model less demanding for the FE code.

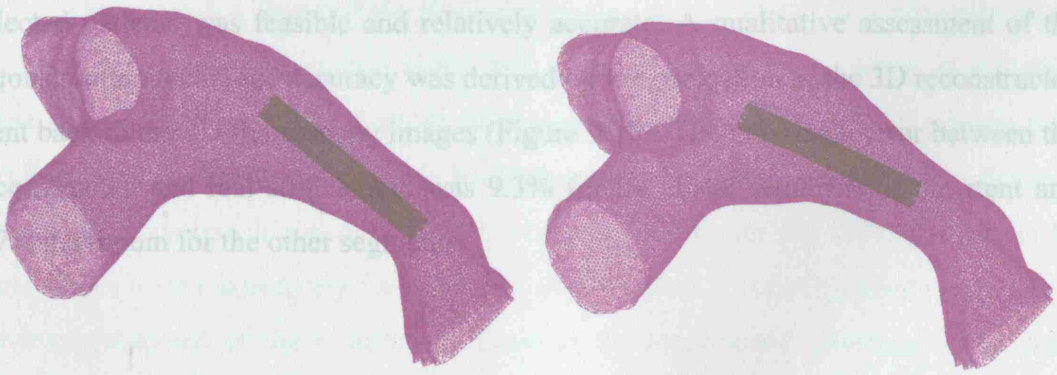

Figure 9.9 Position of the PL stent into the RVOT model for the first and third interaction analysis (left), and for the second interaction analysis (right).

Finally, the RVOT model was assumed to be rigid and was, therefore, modelled as a rigid surface (no displacements or deformations). The PL_{RVOT} device was placed back to its original site (Figure 9.9, left) and the inflation was achieved by pressure load in order to allow asymmetrical deformations of the stent. A displacement controlled inflation in the presence of a rigid surface as a boundary would have not allowed the stent to configure its shape to the morphology of the RVOT. Therefore, a direct pressure was applied to the internal surface of the stent, excluding the peripheral rings, to avoid the dogboning effect (Figure 8.5). Once the device was fully expanded, the pressure was reset to zero to enable the stent elastic recoil, and a new pressure was applied to the external surface of the stent to evaluate the stent strength.

The first FE analysis was run as a feasibility study of the interaction between a realistic, deformable RVOT model and the PPVI device. The second model represented an approximation of the real device position of implantation, but was used to evaluate recoil (R) and stresses (σ_{VM}) in a simplified contact problem. The third simulation was used to assess the shape, stresses and strength of the PL_{RVOT} device when deployed in an asymmetrical configuration. A fatigue analysis was also performed for the PL_{RVOT} model on the basis of a cyclic pressure (0 – 0.1 MPa) applied to the external surface of the stent.

9.3 RESULTS

9.3.1 Biplane Fluoroscopy Reconstructions

The 3D reconstruction of the stent shape from biplane fluoroscopy images of the 2 selected patients was feasible and relatively accurate. A qualitative assessment of the reconstruction technique accuracy was derived by the projection of the 3D reconstructed stent back to the 2D fluoroscopy images (Figure 9.10). The maximum error between the reconstructed and real strut length was 9.3% for the distal segments of the stent and 7.7% maximum for the other segments.

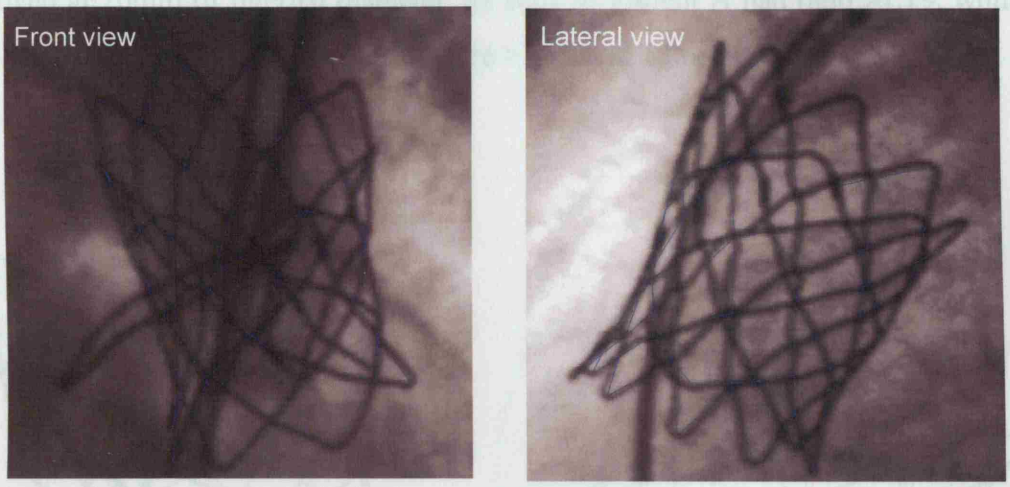

Figure 9.10 Result of the 3D stent reconstruction overlapped to the 2D fluoroscopy images.

The manual reconstruction of the 3D stent *in-situ* in early systole (blue) and diastole (magenta) are shown in Figure 9.11 and Figure 9.12 for patient A and B respectively. The rigid body motion component has been subtracted from the total device displacement. The x, y and z components – their direction referred to Figure 9.4 – of the translation vector for the rigid transformation from diastolic to early systolic configuration were 0.48, 0.16 and -1.43mm for patient A, and 2.39, -2.52 and -0.4mm for patient B. The rigid rotation was 3° around the x axis for patient A, and -4° around the y axis for patient B. Once the rigid body motion component was subtracted, the difference between the 2 configurations – early systole and diastole – was small in both patients, thus indicating an overall small deformation of the device structure due to the pulsatile pressure (10mm Hg and 9mmHg for patient A and B respectively, Table 9.1).

The expanded shape of the device implanted in the RVOT was not uniform, in all 3 directions: circumferential, radial and longitudinal direction. Some of the stent struts were widely open whilst others were at an early stage of expansion (Figure 9.11 and Figure 9.12). The maximum ratio between longitudinal diagonal and radial diagonal in the cells of patient A's stent was 2.17, whilst the minimum was 0.66. For patient B, these values were respectively 1.95 and 0.62. Ratio values >1 corresponded to cells with the major diagonal of the rhomboidal shape in the longitudinal direction of the stent (Front view Figure 9.11 I), whilst ratio values <1 to cells with the major diagonal of the rhomboidal shape in the circumferential direction (Front view Figure 9.11 II). Considering that 1.19 ratio corresponds to the ratio of cells in a stent uniformly

deployed at 20mm of internal diameter, 21 cells of Patient A had ratio >1.19, while 19 cells <1.19. In patient B, 27 cell ratios were >1.19 and 13 cells <1.19.

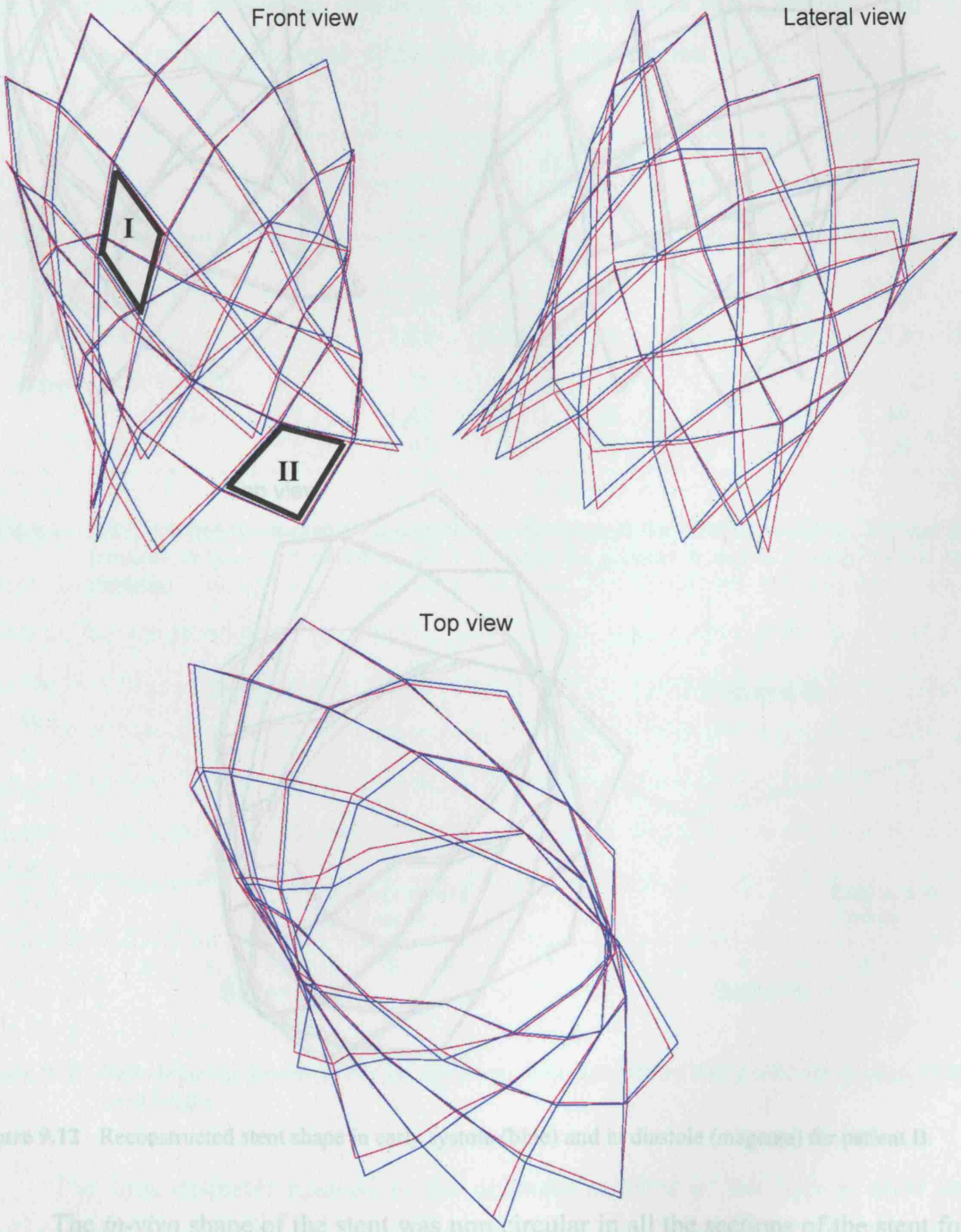

Figure 9.11 Reconstructed stent shape in early systole (blue) and in diastole (magenta) for patient A. In the frontal view the black lines outline the shape of the rhomboidal cells: I) major diagonal in the longitudinal direction of the stent; II) major diagonal in the circumferential direction.

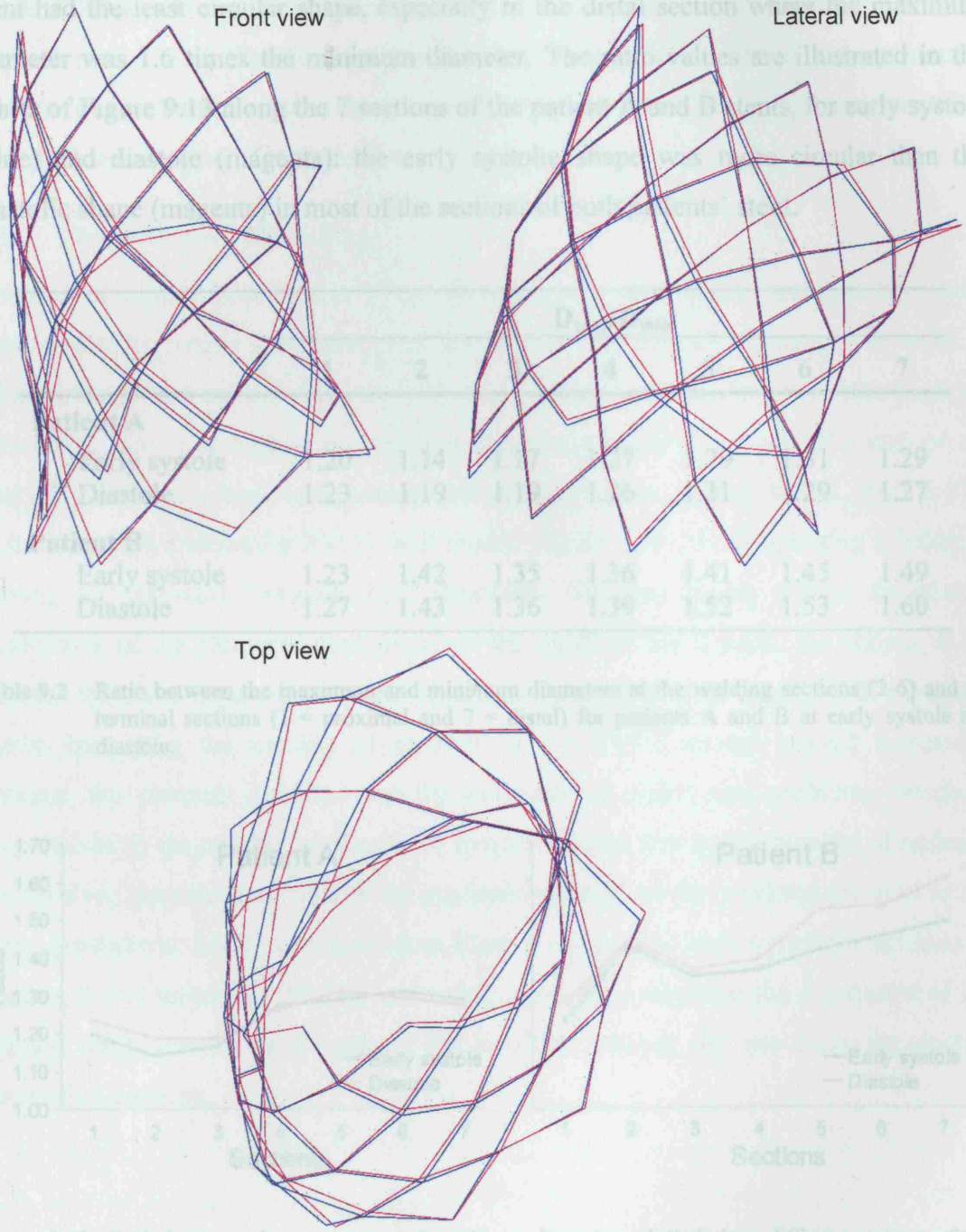

Figure 9.12 Reconstructed stent shape in early systole (blue) and in diastole (magenta) for patient B.

The *in-vivo* shape of the stent was non circular in all the sections of the stent for both patients, as seen in the figures and shown by the ratios between the maximum and minimum diameters (Table 9.2). Ratio values close to 1 corresponded to a section shape closer to a circle while higher values were related to more compressed sections. The section which was the closest to a circle was section 2 of Patient A's stent. Patient B

stent had the least circular shape, especially in the distal section where the maximum diameter was 1.6 times the minimum diameter. The ratio values are illustrated in the charts of Figure 9.13 along the 7 sections of the patient A and B stents, for early systole (blue) and diastole (magenta): the early systolic shape was more circular than the diastolic shape (magenta) in most of the sections of both patients' stent.

	D_{max}/D_{min}						
	1	**2**	**3**	**4**	**5**	**6**	**7**
Patient A							
Early systole	1.20	1.14	1.17	1.27	1.29	1.31	1.29
Diastole	1.23	1.19	1.19	1.26	1.31	1.29	1.27
Patient B							
Early systole	1.23	1.42	1.35	1.36	1.41	1.45	1.49
Diastole	1.27	1.43	1.36	1.39	1.52	1.53	1.60

Table 9.2 Ratio between the maximum and minimum diameters at the welding sections (2-6) and the terminal sections (1 = proximal and 7 = distal) for patients A and B at early systole and diastole.

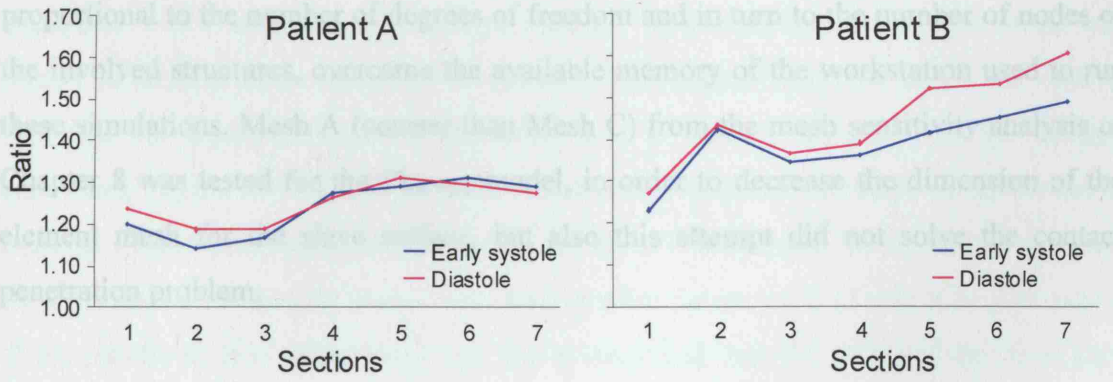

Figure 9.13 Ratio between the maximum and minimum diameters plotted along different sections of the stent length.

The final diameter reached at the different sections of the device, once the section shapes were standardized to circles, varied along the stent length. This indicated asymmetry in the longitudinal directions. The stents were more expanded at the terminal sections compared to the central portion: the maximum difference in standardized diameter along the length was 31.7% for patient A and 38.7% for patient B. In both

patients there were no significant variations of the section standardized diameters between systole and diastole, implying that the stented RVOT does not change overall dimensions (perimeter), due to the internal pressure variation, but only shape, identified by the change in ratio of each section.

9.3.2 Finite Element Modelling

Solution of contact problems in FE analyses is non trivial. Many attempts have been carried out, by tuning the parameters that govern the contact algorithm, in order to achieve the numerical convergence and the equilibrium for each part of the analysed structures. The first simulation required long calculation times and the end of the analysis was not reached due to contact convergence issues. Indeed, the PL stent at 87% of its expansion crossed the RVOT wall model (Figure 9.14), thus indicating a failure in solving the interaction between the 2 structures. This was mainly due to the relative dimensions of the elements used to create the mesh of the 2 parts. As shown in the picture, the stent tetrahedrons were significantly smaller than the RVOT triangular shells. Increasing the number of element in the RVOT model proved impossible because the memory required by the software to solve the problem, which is proportional to the number of degrees of freedom and in turn to the number of nodes of the involved structures, overcame the available memory of the workstation used to run these simulations. Mesh A (coarser than Mesh C) from the mesh sensitivity analysis of Chapter 8 was tested for the PL_{RVOT} model, in order to decrease the dimension of the element mesh for the slave surface, but also this attempt did not solve the contact penetration problem.

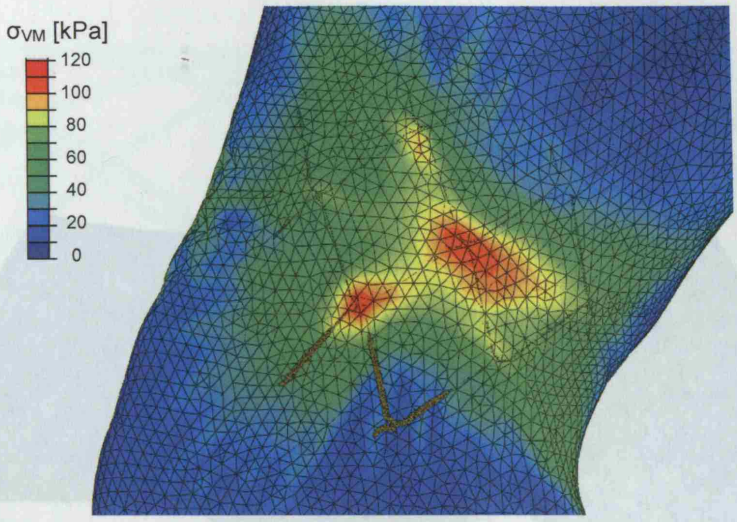

Figure 9.14 The PL_{RVOT} stent crossed the RVOT wall during the expansion in the first analysis. This phenomenon is show in the zoom picture, where part of the RVOT model has been removed.

The second simulations resulted in full expansion of the stent, up to an internal diameter of 20mm. The expanded stent was in contact with the implantation site only in the proximal area, where stresses can be noted on the RVOT wall (Figure 9.15). The maximum increase in the RVOT perimeter of those interface sections was 5.39% (initial perimeter = 62.16mm and expanded perimeter = 65.51mm) and the RVOT shape was forced to deform from elliptical to circular. The elastic recoil of stent and RVOT followed the deployment phase: the stent, free to deform according to the loading conditions imposed by the RVOT wall, resulted in a non circular shape in the proximal sections (Table 9.3), where contact with the RVOT was made. In the distal part, the stent preserved its circular shape, with also smaller values of R (Table 9.3). The recoil of the middle section of the stent was less accentuated than the recoil of the distal part (both of them are not in contact with the RVOT wall).

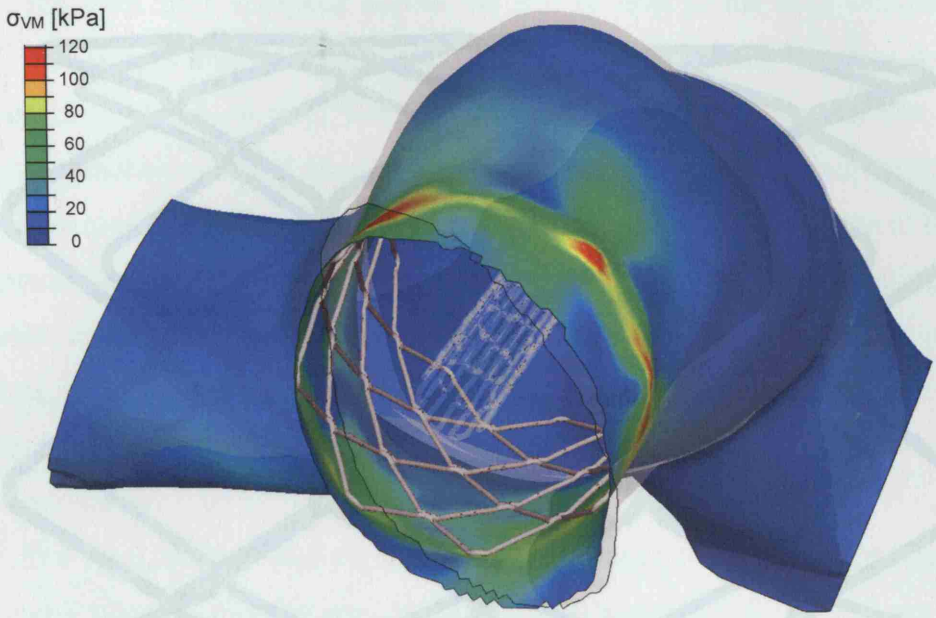

Figure 9.15 Expanded PL_{RVOT} stent and, in transparency, the initial configuration. Part of the RVOT model has been deleted to enable the sight of the device inside it.

Stent section	D_{max} [mm]	D_{min} [mm]	R_{min} [%]	R_{max} [%]
Proximal	19.53	17.61	2.35	11.95
Middle	19.76	19.48	1.20	2.60
Distal	19.59	19.09	2.06	4.56

Table 9.3 Maximum and minimum internal diameters at each section of the deployed stent after recoil of the coupled structure and the values of recoil calculated along the same diameters. Obviously, the minimum recoil (R_{min}) is measured in correspondence to the maximum diameter (D_{max}) and vice-versa.

The strut intersections, at the welding points, generally presented higher stress values than the straight platinum parts of the wire, as seen also for the PL stent of Chapter 8 uniformly loaded in the radial direction. However, depending on the position on the device, σ_{VM} were not uniformly distributed across all welded areas, with values up to 870 MPa at some intersections of the proximal sections, substantially higher than the σ_{VM} in the distal sections (450 MPa). The maximum σ_{VM} in the PL_{RVOT} model was higher if compared to the PL model of Chapter 8.

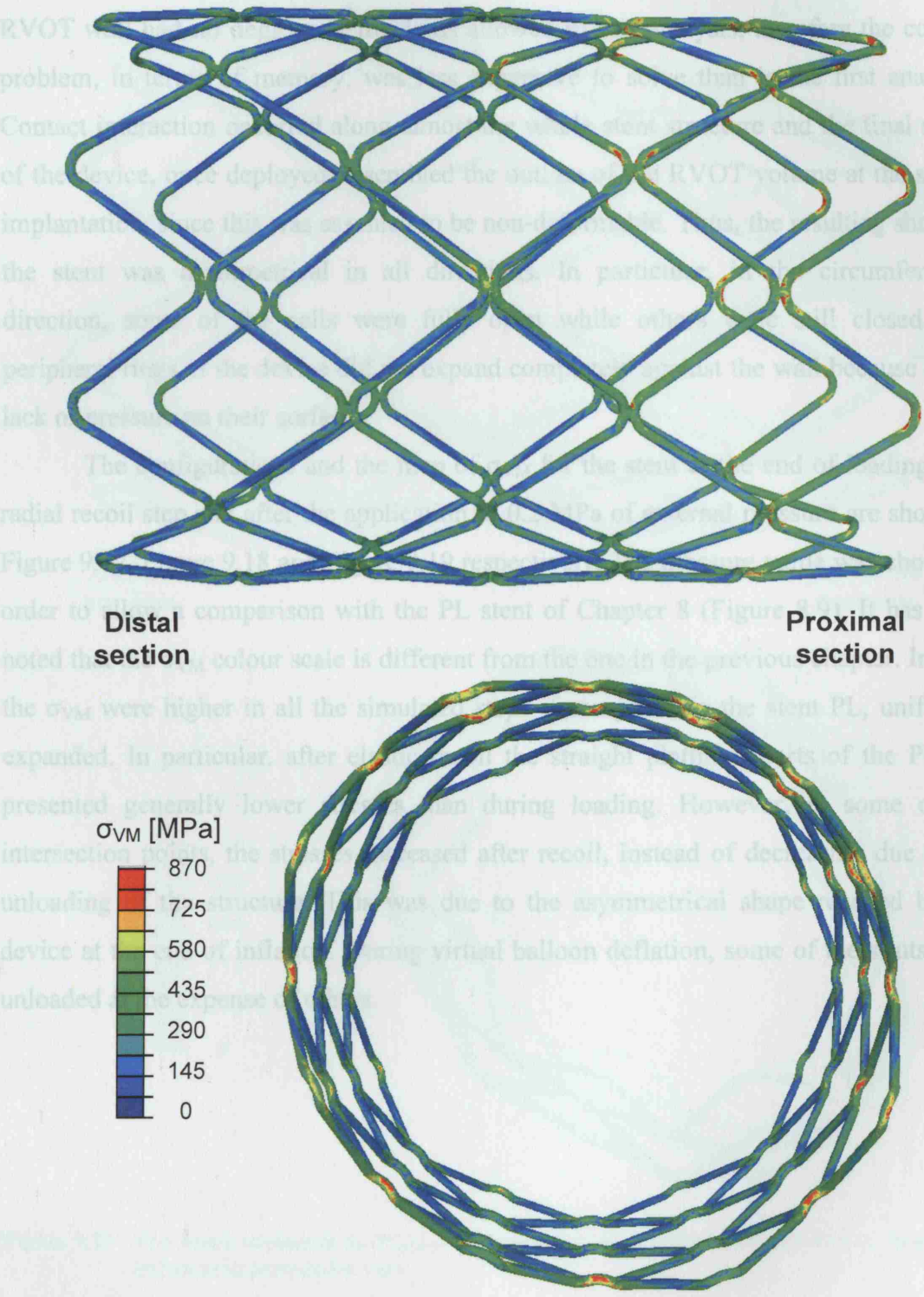

Figure 9.16 Von Mises stresses on the PL_{RVOT} stent structure (perspective view) once deployed and released into an RVOT distal position.

The stent fully deployed against the RVOT wall in the third simulation. The RVOT wall had no degrees of freedoms allowed in this analysis; therefore the contact problem, in terms of memory, was less expensive to solve than in the first analysis. Contact interaction occurred along almost the whole stent structure and the final shape of the device, once deployed, resembled the outline of the RVOT volume at the site of implantation, since this was assumed to be non-deformable. Thus, the resulting shape of the stent was asymmetrical in all directions. In particular, in the circumferential direction, some of the cells were fully open while others were still closed. The peripheral rings of the device did not expand completely against the wall because of the lack of pressure on their surfaces.

The configurations and the map of σ_{VM} for the stent at the end of loading step, radial recoil step and after the application of 0.2 MPa of external pressure are shown in Figure 9.17, Figure 9.18 and Figure 9.19 respectively. The pressure value was chosen in order to allow a comparison with the PL stent of Chapter 8 (Figure 8.9). It has to be noted that the σ_{VM} colour scale is different from the one in the previous chapter. Indeed, the σ_{VM} were higher in all the simulated steps if compared to the stent PL, uniformly expanded. In particular, after elastic recoil the straight platinum parts of the PL_{RVOT} presented generally lower stresses than during loading. However, in some of the intersection points, the stresses increased after recoil, instead of decreasing due to the unloading of the structure. This was due to the asymmetrical shape reached by the device at the end of inflation. During virtual balloon deflation, some of the struts were unloaded at the expense of others.

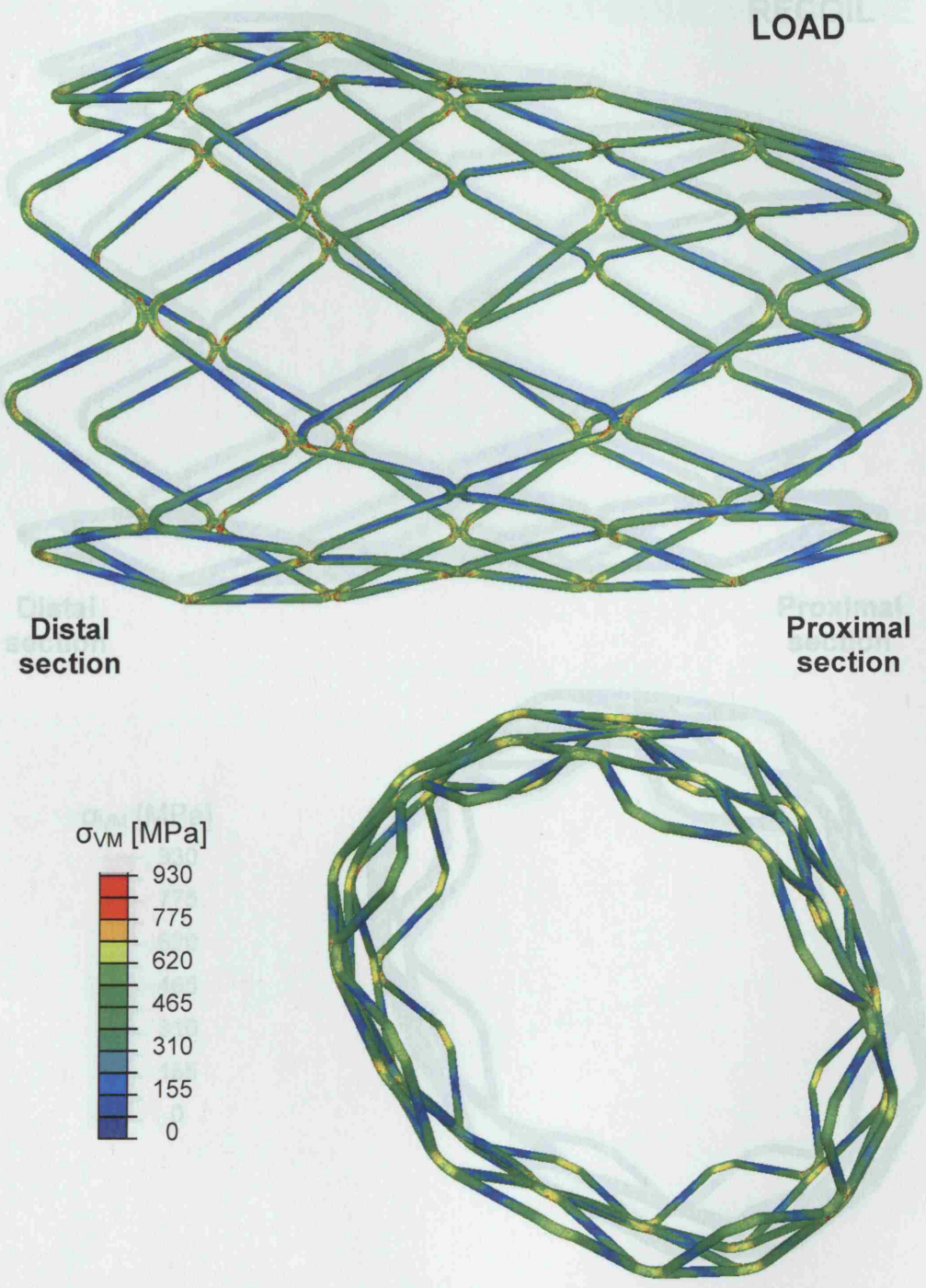

Figure 9.17 Von Mises stresses in the PL_{RVOT} stent once it is deployed into the rigid RVOT, in a lateral and an axial perspective view.

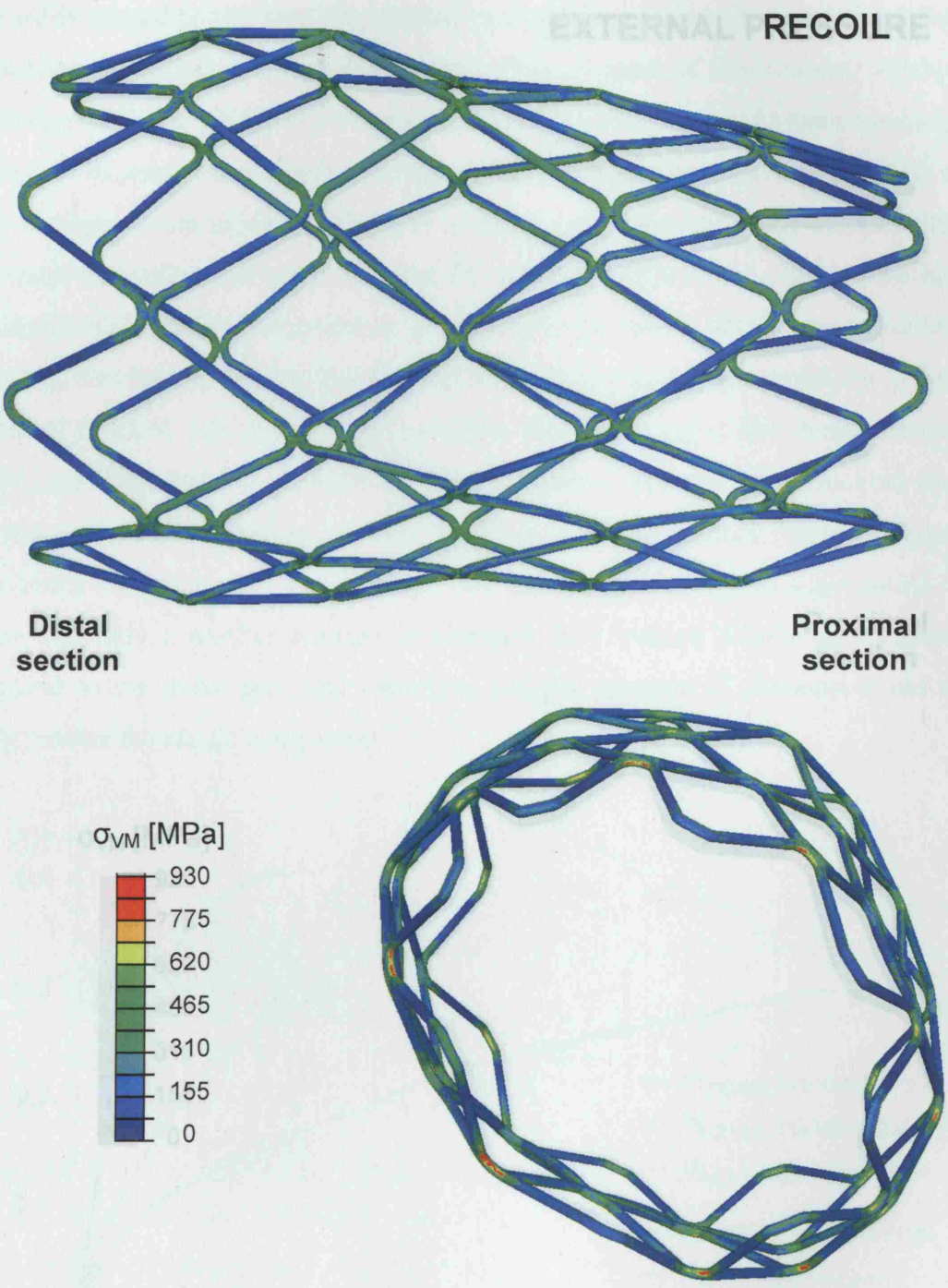

Figure 9.18 Von Mises stresses in the PL_{RVOT} stent after elastic recoil, in a lateral and an axial perspective view.

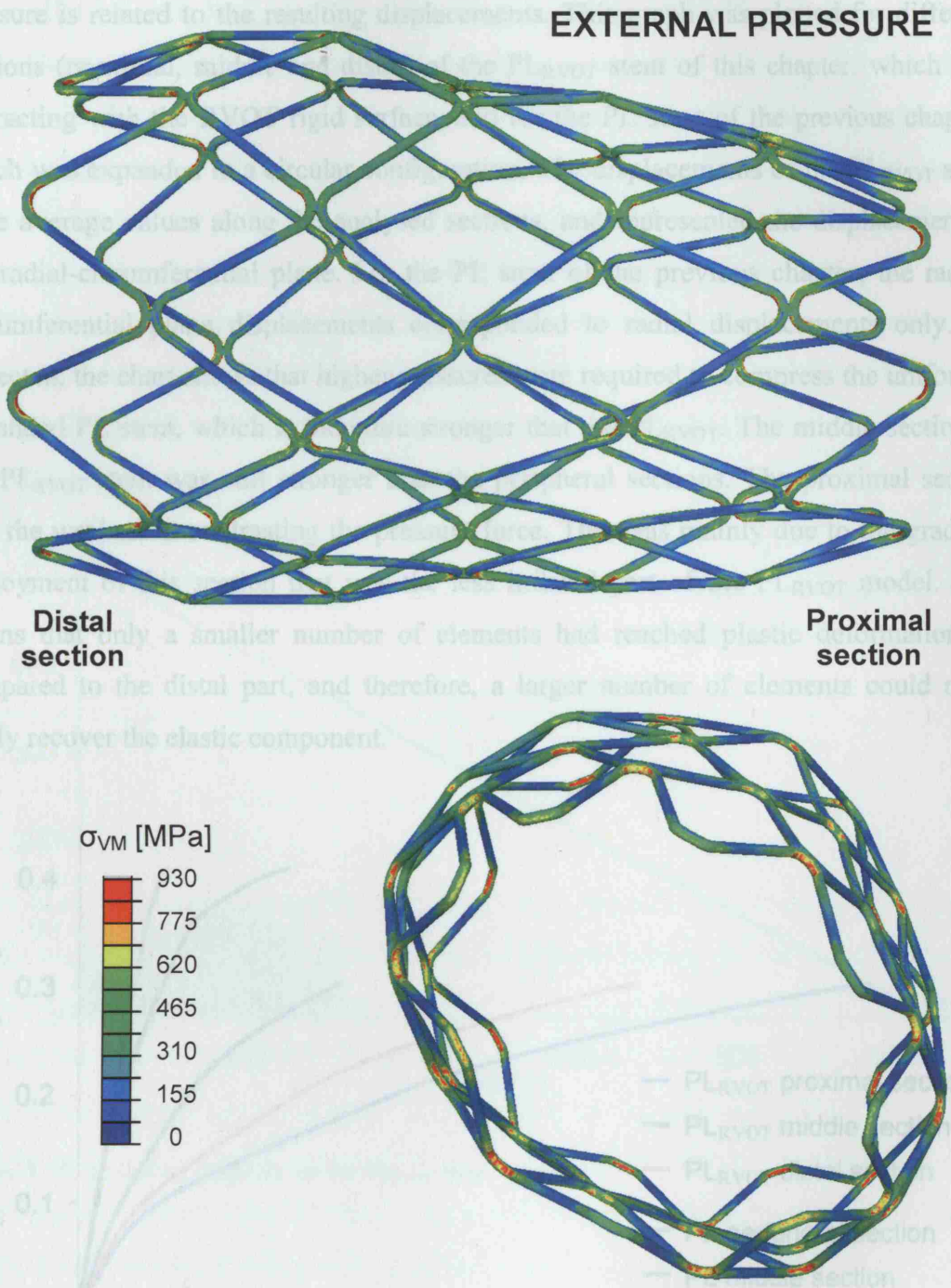

Figure 9.19 Von Mises stresses in the PL_{RVOT} stent after the application of 0.2 MPa of pressure to the external surface of the stent, in a lateral and an axial perspective view

The application of the external pressure was used to mimic the RVOT wall elastic recoil (not possible in this simulation because the wall was assumed to be rigid) and allowed to evaluate the strength of the PL_{RVOT} stent in bolstering the RVOT loads. The strength is represented in the chart of Figure 9.20, where the applied external

pressure is related to the resulting displacements. This graph was plotted for different sections (proximal, middle and distal) of the PL_{RVOT} stent of this chapter, which was interacting with the RVOT rigid surface, and for the PL stent of the previous chapter, which was expanded in a circular configuration. The displacements of the PL_{RVOT} stent were average values along the analysed sections, and represented the displacement in the radial-circumferential plane. For the PL stent of the previous chapter, the radial-circumferential plane displacements corresponded to radial displacements only. As expected, the chart shows that higher pressures were required to compress the uniformly expanded PL stent, which is therefore stronger that the PL_{RVOT}. The middle section of the PL_{RVOT} stent was still stronger than the peripheral sections. The proximal section was the weakest in contrasting the pressure force. This was mainly due to the grade of deployment of this section that was the less inflated part of the PL_{RVOT} model. This means that only a smaller number of elements had reached plastic deformations if compared to the distal part, and therefore, a larger number of elements could more easily recover the elastic component.

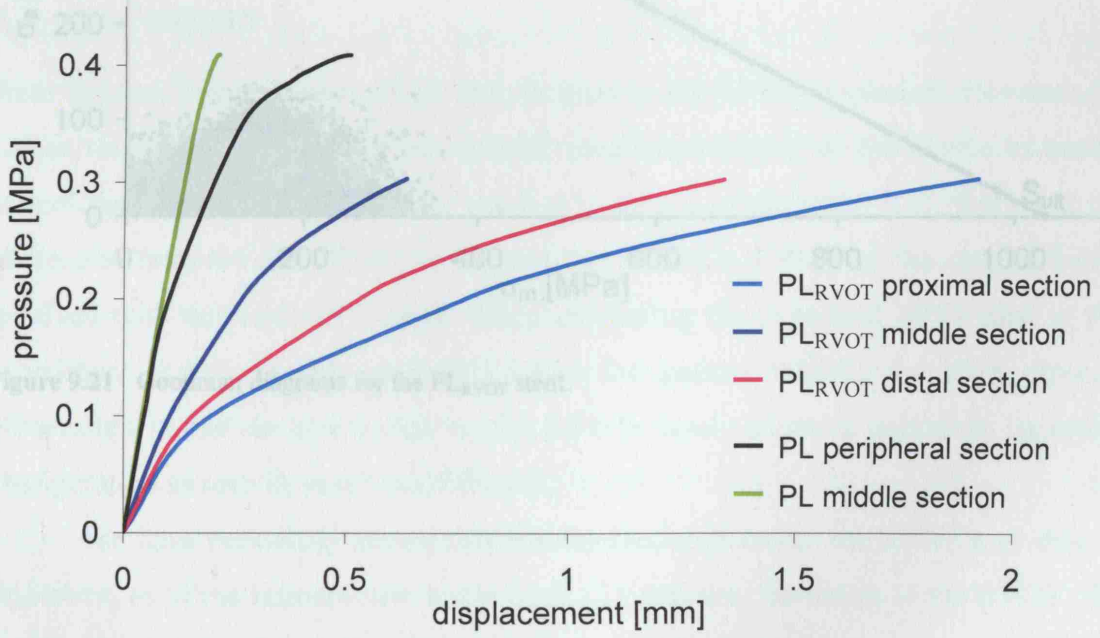

Figure 9.20 Displacement of the PL_{RVOT} stent nodes at proximal, middle and distal section, in response to the external pressure applied to emulate the compression force of the RVOT. The same characteristic is reported for the PL stent of the previous chapter that was uniformly loaded along the circumference.

The pulsatile load applied to the external surface of the PL_{RVOT} device resulted in the Goodman diagram of Figure 9.21. All the σ_m - σ_a points fell below the Goodman line but the scattering was wider than the plot drawn for the PL stent of the previous chapter, indicating a higher number of areas on the PL_{RVOT} stent at risk of fatigue fracture. The inverse of FSF is shown graphically in the contour map of Figure 9.22 (a different scale was used in this plot if compared to Figure 8.11 to capture the higher 1/FSF values in this case). The areas with highest potential for fracture were still at the platinum welds where FSF was equal to 1.13. This is not only lower than FSF for the PL stent, but also the minimum FSF amongst all the stent models analysed in Chapter 8, even $PL_{1/2}$.

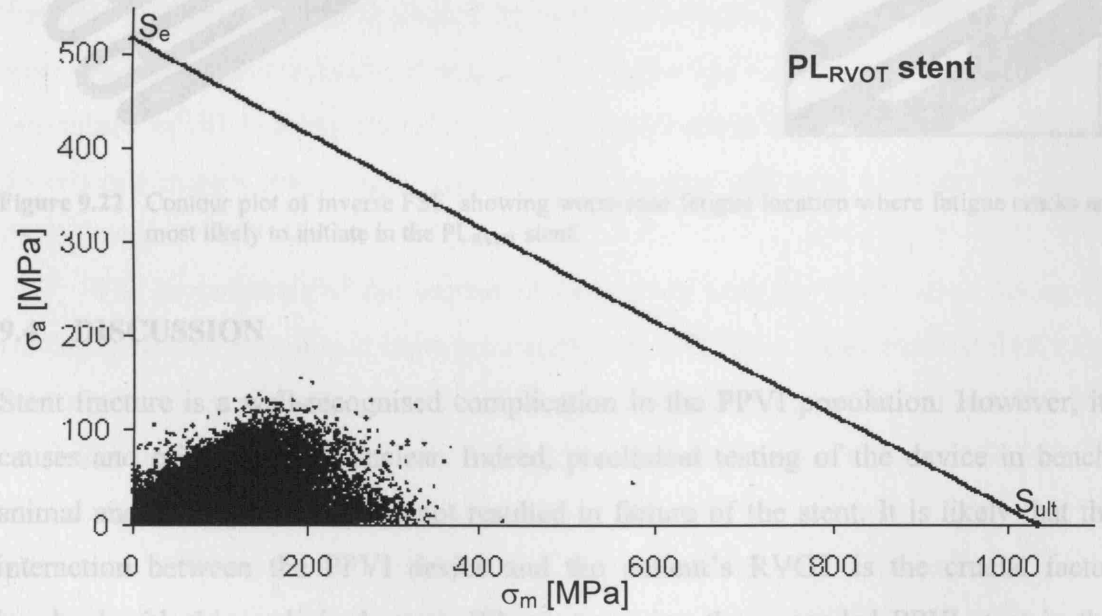

Figure 9.21 Goodman diagrams for the PL_{RVOT} stent.

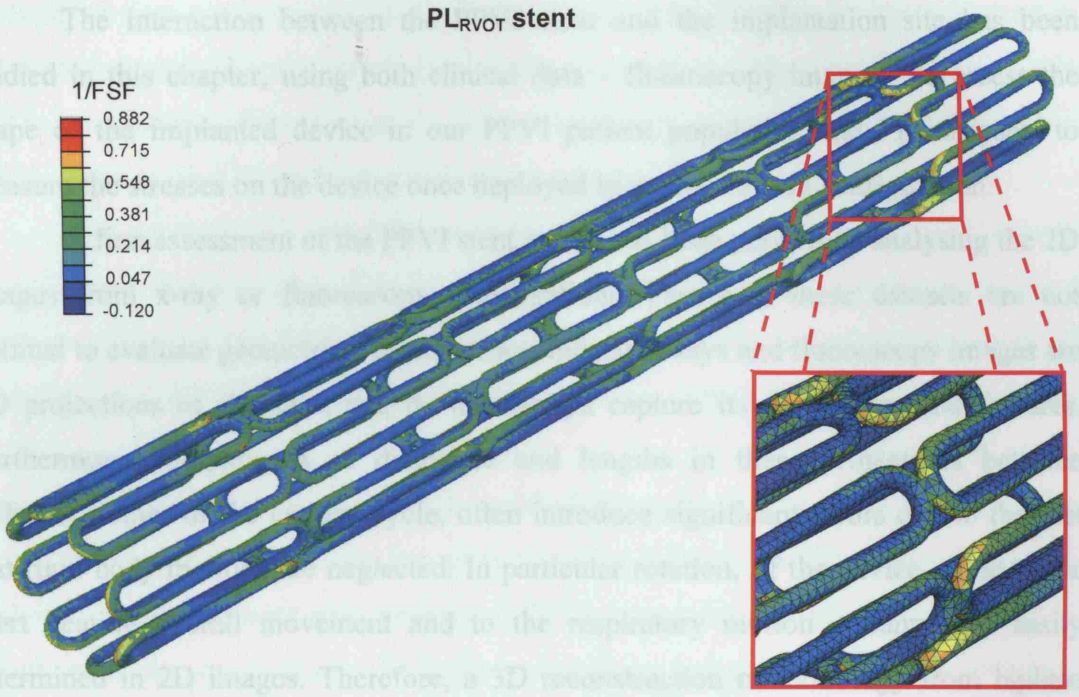

Figure 9.22 Contour plot of inverse FSF, showing worst-case fatigue location where fatigue cracks are most likely to initiate in the PL$_{RVOT}$ stent.

9.4 DISCUSSION

Stent fracture is a well-recognised complication in the PPVI population. However, its causes and origin are still unclear. Indeed, preclinical testing of the device in bench, animal and FE experiments has not resulted in failure of the stent. It is likely that the interaction between the PPVI device and the patient's RVOT is the crucial factor involved with this undesired event. When comparing the expanded PPVI stent in the experiment setting to the 'real' PPVI into the patient RVOT, the most obvious observation is that the stent shape in the RVOTs rarely shows a uniformly deployed configuration as seen in bench and FE tests.

We have previously shown that this interaction between the RVOT and stent is important, as in our retrospective analysis of 123 patients, the nature of the RVOT, the calcification extent, the grade of elastic recoil and the deployed shape were the factor associated with higher risk of stent failure in the 26 patients who fractured. All these parameters depend on the interaction of the device with the implantation site, which therefore cannot be neglected in the analysis of device failure.

The interaction between the PPVI stent and the implantation site has been studied in this chapter, using both clinical data – fluoroscopy images – to assess the shape of the implanted device in our PPVI patient population and FE analyses, to measure the stresses on the device once deployed in a non-uniform configuration.

A first assessment of the PPVI stent *in situ* has been performed analysing the 2D images from x-ray or fluoroscopy investigations. However, these datasets are not optimal to evaluate geometrical asymmetries. Indeed, x-rays and fluoroscopy images are 2D projections of the stent and do not always capture its most important features. Furthermore, comparisons of diameters and lengths in these projections between different frames of the cardiac cycle, often introduce significant errors due to the fact that rigid body motions are neglected. In particular rotation, of the device – due to the heart beating overall movement and to the respiratory motion – cannot be easily determined in 2D images. Therefore, a 3D reconstruction methodology from biplane fluoroscopy images has been developed in this chapter and used to assess the *in situ* PPVI device.

The asymmetries of the implanted stent along with its deformation during the cardiac cycle can be assessed more accurately in the 3D stent reconstruction than using 2D images. Circumferential, radial and longitudinal asymmetries were quantified in 2 PPVI stents of patients who experienced fracture and were proven to be significant in all three directions.

The PPVI stent uniformly deployed at 20mm of internal diameter, as in theory should have been the case for the 2 analysed patients, has a ratio of 1.19 between the diagonal in the longitudinal direction and circumferential direction of the rhombus selected to describe the stent cell shape. More than half of the cells were at the beginning of the expansion progression while the others were over-deployed. Neither radial nor longitudinal expansions were uniform. The stent sections were mainly elliptical with the peripheral rings more deployed than the central rings.

The rigid body motion of the device during the cardiac cycle was large and relevant, especially if compared with the actual deformations of the stent structure, due to the overall heart movement. However, the rigid displacements are not relevant to the likelihood of stent fracture. This cannot always be perceived in the visual assessment of 2D images, and stent deformations can be highly over or underestimated, especially

when large displacements are in place. Importantly, the changes in internal pressure between diastole and early systole (~10mmHg of variation in the stented RVOT, Table 9.1) in both patients did not cause an increase in the perimeter of the RVOT, but only a change in its section shape from elliptical to more circular.

The analysis of the 3D reconstructed devices from fluoroscopy clearly demonstrates that the interaction of the device with the RVOT influences the final deployed shape of the PPVI stent. A combination of asymmetrical expansion in all directions and RVOT changes in loading conditions could result in fracture of the device.

The main limitation of the methodology developed for the 3D stent reconstruction from fluoroscopy images is related to the impossibility of a retrospective analysis for most patients who underwent PPVI. In the future, this problem could be solved with the registration of phantom fluoroscopy data at the same set up – fluoroscopy system and table – as the actual PPVI procedure. This would help correct for image intensifier errors if the procedure is performed with non flat detector panels. An orientation of the fluoroscopy arms different from the AP was felt not suitable for the manual reconstruction methodology developed in this study. The reconstruction would be feasible but it would require a laborious elaboration, considering that the lines to project the 2D images in the 3D space will not be orthogonal to the 2D image, but with an angle that corresponds to the arm angulations during the procedure. Furthermore, this is not easily achievable with generic CAD software because they usually work in 3 orthogonal planes. The phantom registration would be the solution to this additional problem and an automatic algorithm for the reconstruction of the 3D stent structure could be developed.

Modelling realistically the stent/implantation site interaction using the FE method has proven difficult, due to contact convergence problems for the FE code. Although simplified hypotheses needed to be adopted, the information gained from the FE analyses of these simplified cases was still valuable.

The analysis of the PL stent implanted in a distal position of the RVOT allowed the effect of the RVOT wall on the PPVI stent to be quantified. The device was in contact with the implantation site only in a small area. However, this minimal contact was already able to show the recoil of the stented RVOT when the prescribed

displacements were removed to mimic the balloon deflation. The analysis of the 2D fluoroscopy images showed that balloon recoil is one of the risk factors for stent fracture. In the FE contact simulations, the recoil of the stented RVOT (Table 9.3) was higher than the recoil of the free PL in Chapter 8, also after the application in the latter of the external pressure up to 0.2 MPa. This is because the RVOT wall material influences the loading process that results in a non-circular stent shape because of the morphology and distensibility of the RVOT wall. A smaller load is necessary to compress the device in only one direction rather than with a concurrently and uniformly distributed radial load. Moreover, this loading condition, even if smaller, causes higher stresses to the structure than a uniform load, due to the non symmetrical shape acquired by the stent. All these considerations, however, are related to the material properties used in the mechanical behaviour description of the RVOT wall. We showed that patients with native outflow tract and/or no calcification present higher risk of stent fracture. This implies that RVOT material characteristics are very specific to each individual patient and average values cannot be used. Modelling different patients' RVOT with standard material properties would disregard the influence of the RVOT material on stent fracture, already demonstrated to be an important risk factor. A better characterization of the material mechanical behaviour is therefore necessary.

The results of the PL stent deployed in the distal part of the RVOT gave an indication of the influence of asymmetrical deployment in the device's mechanical performance. However the final asymmetry reached in this position was mainly in the radial direction and still moderate, if compared with the fluoroscopy data of this patient. Therefore the PL_{RVOT} model was deployed into the rigid RVOT surface with resulting shape asymmetries in all directions. Again, these asymmetries were less accentuated than the real asymmetries measured from the fluoroscopic 3D reconstructions. However, the FE expansion of the device in this non uniform shape was useful to assess the mechanical behaviour of the device compared to the uniformly expanded PL model of Chapter 8. At the same level of applied external pressure, the compression of the PL_{RVTO} was higher than the PL. The PL_{RVOT} is weaker than the PL stent in resisting external forces. The stress values at the end of deployment, elastic recoil and pressure application were significantly higher in the PL_{RVOT} than in the PL model of Chapter 8, implying that when the stent is not uniformly deployed, the risk of reaching the

endurance limit of the material is significantly higher. Moreover, during the cyclic loading condition the PL_{RVOT} stent worked at higher mean stresses, increasing the possibility of fracture. Not only FSF was smaller but also the distribution of σ_m - σ_a on the Goodman diagram was more scattered.

The FE modelling of stent/implantation site interaction proposed in this chapter showed the importance of these analyses. The introduction of the RVOT model in the FE evaluation of the maximum stresses reached by the stent in its life time showed the magnitude error that can be made in measuring these characteristics when the RVOT is neglected. The simulation of simple contact conditions was feasible; however the method requires further development in order to advance this field.

9.5 CONCLUSION

This chapter introduces the first study of stent/implantation site interaction in PPVI. The methodology developed in this chapter to reconstruct the 3D shape and deformation of the stent from biplane fluoroscopy images is innovative and proved its value. Indeed, the RVOT plays a significant role in the final shape and mechanical behaviour of the stent once implanted into it. Most of the stent morphological characteristics *in situ* were accurately quantified by the 3D reconstruction from fluoroscopy images, mainly in terms of stent geometrical asymmetries and deformations during the cardiac cycle. A comparison of these features between a group of patients who had a successful long term result and a cohort of patients who experienced fracture can give further indications regarding the parameters that are strictly involved in the risk of fracture. However in order to compare more patients data, the 3D reconstruction methodology needs to be further developed by using phantom registration and automatic algorithms.

An attempt to simulate the implantation of the stent into a selected patient RVOT by FE modelling is also reported. This analysis, even if it required the introduction of simplified assumptions, showed the need for inclusion of the interaction with the RVOT in the estimate of the stent mechanical performance. The stent when deployed in different asymmetrical configurations resulted in lower radial strength than the uniformly expanded case. The maximum stresses reached by the stent structure in the contact analyses were drastically higher, thus also increasing the potential of fatigue fracture.

The indications given by the FE analyses towards a higher risk of stent fracture for non-uniformly deployed stents are strong. However, the results in terms of elastic recoil and stresses on the PPVI stent interacting with the implantation site model depend on the patients' RVOT material characteristics. A better individual measurement of patient's RVOT distensibility properties is necessary and is one of the subjects for future work and advancement in PPVI as described in Section 11.2.1.

CHAPTER 10

SHAPE MEMORY ALLOY FOR PERCUTANEOUS PULMONARY VALVE IMPLANTATION STENT

Shape memory alloys, and in particular nitinol, are good candidates for next generation PPVI stent, since they combine biocompatibility and resistance to fracture with the ability to undergo large, completely reversible deformations.

The aim of this chapter is to optimise the mechanical performance of a nitinol ring for use in the next generation PPVI stent. Nine different designed were analysed using the FE method. The FE simulations allowed a comparison between the most important mechanical properties of each ring: suitability of the ring size to the catheter dimensions, maximum strains reached when crimped into the catheter, recovered shape when deployed into the RVOT, radial strength when subjected to a compressive force, and fatigue life measured under pulsation conditions of ±5% of the nominal diameter. The results of this comparison led to the design of an optimised ring with no overlapping of the zig-zag struts when crimped into the catheter and completely recoverable deformations when released, with enough force to be fixed into the RVOT wall without damaging its tissue and good strength to resist compressions, and with low potential for fatigue failure.

10.1 INTRODUCTION

The next generation PPVI stent, currently under investigation by Medtronic Inc., USA, will have to address the problems and limitations of the current design. In particular, the stent mechanical performance will have to be enhanced in order to avoid failure both in the short- and long-term. Chapter 8 described an FE methodology developed for the study of this problem. A possible solution to stent fracture may be to couple 2 stents, as proposed in Chapter 8. However, this device design cannot solve the other major limitation of the current generation stent, which is its ability to fit the RVOT of all patients. Therefore, a new design is necessary that will attempt to accommodate the whole range of dilated RVOTs, without compromising the deliverability through a catheter and the haemodynamics of the valve mounted into it.

Nitinol, thanks to its appealing, mechanical and biocompatible properties, is a good candidate to be the material of choice for the next generation of PPVI stents. Shape memory alloys are nowadays regularly used in bioengineering applications [138,214-219] because they combine important qualities such as biocompatibility, fatigue resistance, and MR compatibility, with the peculiar mechanical behaviour to undergo large completely recoverable deformations.

Nitinol, one of the commonest SMAs, is employed to fabricate a variety of medical devices: blood flow filters, ASD occluser devices, self-expandable stents, spinal vertebrae spacers, orthopaedic staples, plates for the recovery bones, surgical instruments such as baskets to remove kidney, bladder and bile duct stones, catheters, gripper, scissors and tongs for laparoscopic procedures [220-233]. The aim of these devices is to make interventional and endoscopic procedures as minimally invasive as possible, exploiting the features of nitinol. Section 10.2 of this chapter provides a brief explanation of SMA structure and its thermo-mechanical behaviour.

A first attempt to design a new device ('infundibular reducer') made of nitinol was performed in 2003. The geometry of the proposed device was constructed from a nitinol wire interlaced to form a criss-cross structure in the shape of a conduit, with a central restriction in diameter (Figure 10.1). The extremities of the stent (40mm diameter) ensured the anchoring of the device against the RVOT wall. The central part of the stent (20mm diameter) downsized the vessel diameter to the available bovine

valve diameters and acted as a supporting structure for this valve. This design, along with nitinol properties, makes large deformations of the structure possible. To guarantee the perfect sealing of this device, a membrane of polytetrafluoroethylene was sutured onto the outside of the self-expandable nitinol stent. The valve can be mounted into the restricted part of the self-expandable stent or a 2-step approach can be adopted, with subsequent implantation of the current generation device after the infundibular reducer has been inserted. Initial experience with this modified PPVI device was reported in 2004 in animal testing, as proof of concept, and is still under investigation by others [234,235].

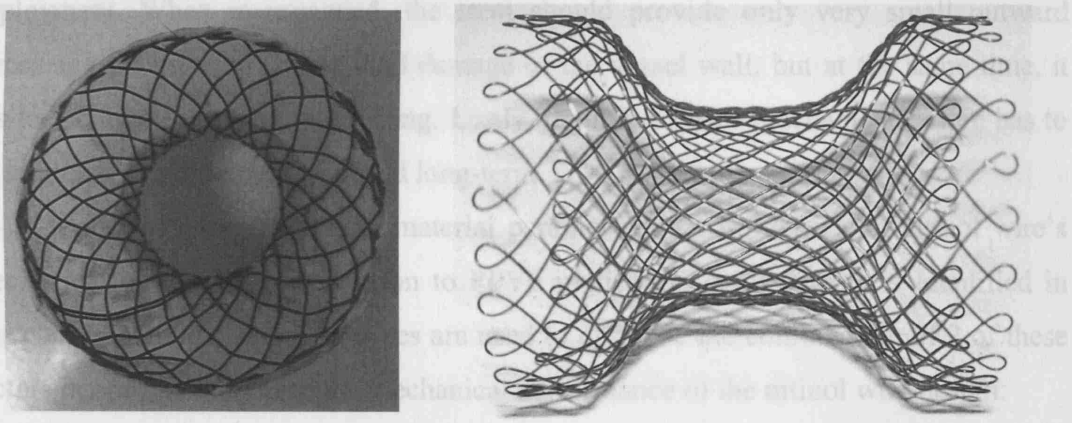

Figure 10.1 Design of the first proposed new nitinol stent for PPVI applications [80].

The major advantage of reducing the RVOT infundibulum by using a different stent design is that bovine jugular venous valves, which have been proven successful, could be used in the new device. However, the criss-cross structure, proposed as the initial solution for the stent, seemed not to have enough radial strength to achieve, and guarantee, the safe anchoring of the device into the RVOT. The development of this device design has been halted by the manufacturers at present.

Therefore, the zig-zag wire design used for the current stent has been reconsidered in the design of the next generation PPVI device, and coupled with the new material properties offered by SMAs. Nitinol zig-zag rings with different diameters could be linked together to form the infundibular reducer shape. At the extremities, rings with larger diameter would anchor the device into the RVOT, while the central rings, with smaller diameter, will hold the bovine venous valve in place (further details of this device currently remain confidential). The design optimisation of a nitinol wire

that could be employed as peripheral ring in the next generation PPVI stent is the objective of this chapter.

As described in Chapter 8, the design of an optimal stent for PPVI applications requires a compromise between different and contradictory requirements. In the case of nitinol, the rings have to undergo large displacements and deformations when crimped down into the delivery catheter. However, the strains once in the catheter must not be greater than the limit of elastic deformations accepted by the material, otherwise only a partial recover of the original shape will be accomplished. Furthermore, the zig-zag shapes need to avoid overlapping of the crowns, which can obstruct the device deployment. When re-expanded, the stent should provide only very small outward forces against the RVOT, to avoid damage of the vessel wall, but at the same time, it has to be highly resistant to crushing. Lastly, the risk of wire mechanical failure has to be minimized both in the short- and long-term.

A set of geometrical and material parameters that influence the nitinol wire's mechanical performance in relation to PPVI application requirements is identified in this chapter. Finite element analyses are used to optimise the combination of 2 of these factors in order to maximise the mechanical performance of the nitinol wire design.

10.2 SHAPE MEMORY ALLOY MECHANICAL BEHAVIOUR

Shape memory alloys are designed to undergo large, mechanically induced deformations that can be completely recovered by simple mechanical unloading (superelasticity property). These materials can exert and maintain a constant force over a wide range of deformations (wide plateau property). Furthermore, SMAs can acquire and memorise a certain shape, which is thermally activated (shape memory property). If plastically deformed, the original, memorized shape can be completely recovered by thermal loading.

The explanation of these peculiar behaviours can be found in the crystallography and thermodynamics of SMAs [236-238]. Shape memory alloy response depends on a thermo-elastic reversible transformation between 2 crystallographic phases, with different physical and mechanical properties: the austenite, A, characterized by a more ordered unit cell and stable at temperatures above A_f (martensite to austenite transformation finish temperature), and the martensite, M, characterized by a less

ordered unit cell and stable at temperatures below M_f (austenite to martensite transformation finish temperature), with $A_f > M_f$. In the temperature interval between A_f and M_f, both structural phases can exist. These critical temperatures generally depend on the material composition and the thermo-mechanical history of the alloy.

The transformation between austenite and martensite, and vice versa, takes place through reversible thermo-elastic transformations, functions of temperature and stresses. When the alloy is heated, martensite begins transforming into austenite (M→A). The set off temperature for this process is called A_s (martensite to austenite start temperature) and the ending temperature A_f. Similarly, when the alloy is cooled, austenite starts transforming in martensite (A→M), with M_s (austenite to martensite start temperature) setting off temperature and M_f ending temperature. Figure 10.2 shows the typical SMA relationship between temperature and austenite ratio. M_d is the limit temperature over which austenite, mechanically loaded, cannot transform in martensite anymore and is plastically deformed.

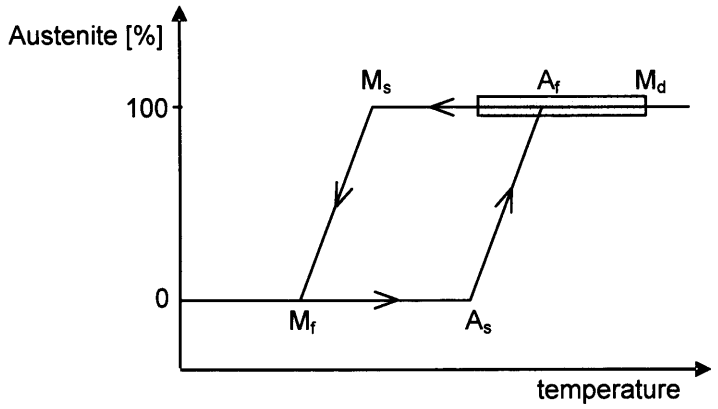

Figure 10.2 Transformation between martensite and austenite, and vice versa, at temperature changes. The area in grey represents the range of temperature ($A_s<T<M_d$) at which superelasticity effect occurs.

From a mechanical point of view, SMAs have 3 different behaviours depending on the operating temperature. At high temperature ($T > M_d$), the alloy, stable in the austenite phase, behaves as a normal metal: above the yield stress, the deformations are permanent (Figure 10.3, curve 1). When $A_f < T < M_d$, the austenite phase of the alloy is stable but a mechanical load causes a transformation from austenite to martensite with non-linear deformations that are completely recovered by mechanical unloading (superelasticity property). During loading-unloading the material response shows a

hysteretic cycle (Figure 10.3, curve 2): when the direct and inverse transformations take place, the stress remains mainly constant over a wide range of deformation respectively at the upper and lower plateau (wide plateau). However, if the deformations induced by the load are large (>5-7%), the alloy constitutive behaviour in martensite phase becomes elasto-plastic. Lastly, if the alloy is mechanically deformed at $T < A_f$, the martensite phase is subjected to linear deformations that are only partially recovered when the load is removed (Figure 10.3, curve 3). In this case, heating the alloy above A_f allows the recovering of the residual deformations (shape memory effect).

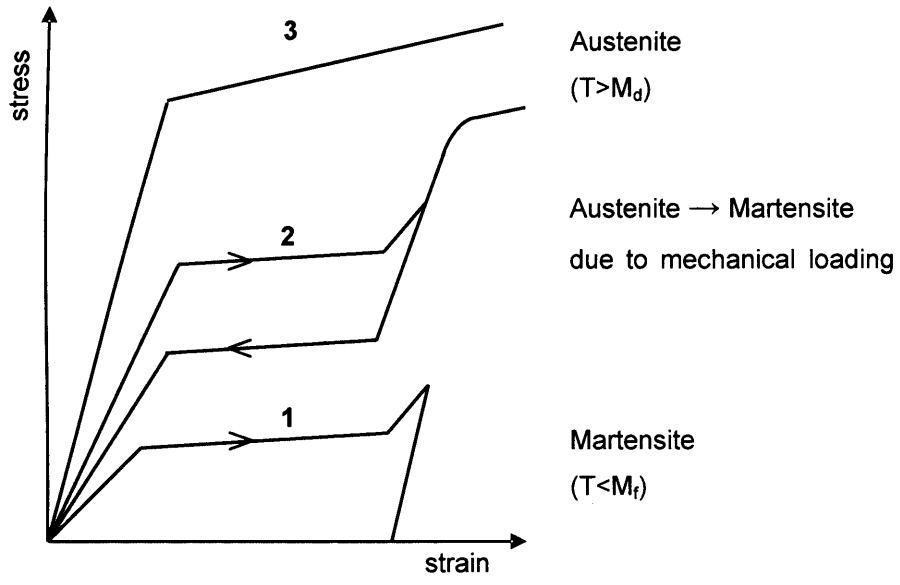

Figure 10.3 Characteristic stress/strain curves of SMAs in relation to the operating temperature: 1) above M_d, austenite mechanical behaviour is elasto-plastic; 2) For temperature above A_f, a mechanical load cases austenite to transform in martensite, but the deformation is completely recovered at unloading 3) martensite, stable at $T<M_f$, deforms at constant stress, and the deformation is only partially recovered.

Within the wide family of shape memory alloys, nitinol associates shape memory and superelastic effects, characterized by large plateau and stress hysteresis, with good resistance to corrosion, biocompatibility and fatigue resistance [215,239], magnetic resonance compatibility, kink resistance and dynamic interference [240]. The fatigue behaviour, in particular, provides great latitude for safe stent design since, conversely to the behaviour observed in conventional engineering materials, increasing mean strain often increases high-cycle fatigue life. This anomalous behaviour is generally attributed to any of a number of possible microstructural or mechanical effects

associated with the reversible stress-induced austenite-to-martensite phase transformation.

The combination of these features explains why nitinol alloys in the past 20 years have rapidly become the material adopted for several implantable devices, in particular vascular stents [241].

Nitinol stents exploit the superelasticity effect. Unlike the current PPVI device, nitinol stents do not need a balloon to be deployed (self-expandable). The device is produced in its deployed configuration and, in austenitic phase (A_f less than body temperature), is compressed onto a catheter, where a protective sheath keeps it compressed. During the crimping phase the material presents a nonlinear behaviour due to a stress-induced conversion of austenite into martensite. When, after the insertion of the stent into the body, the catheter tip reaches the desired implantation site, the sheath is retracted and the stent released. A reverse transformation from martensite to austenite occurs as a result of the instability of the martensite at zero stress for temperatures higher than A_f. Thus the stent expands into the implantation site, trying to recover its original undeformed shape.

10.3 METHODS

Design of experiments is an efficient statistical tool for optimising product design. The DOE approach selects a diverse and representative set of experiments, in which all factors are independent of each other, despite being varied simultaneously, and analyses the effects of the interactions between these factors. The result is a predictive model that shows the importance of all factors and their interactions, and highlights the optimum combination of factor settings, based on selected criteria.

In the study of a zig-zag nitinol wire for PPVI stent application, DOE was used to quantify the impact of 2 selected geometrical factors on the wire performance and to optimise their combination in order to realize the best ring design.

10.3.1 Geometry and Mesh

Nitinol zig-zag rings are usually formed by winding the straight wire over a series of pins, with various dimensions and relative distance, on a cylindrical mandrel of specific diameter. The wire is then aged at elevated temperature to "shape-set" at the designed

zig-zag ring profile and dimensions, and to release the strains. The open ends are joined together with a small weld to hold the finished wire in a closed loop shape.

CAD models of 9 zig-zag wires (named from 01 to 09) in their expanded shape were created (Figure 10.4). In all models, the following geometrical parameters were constrained:

- The wire diameter equal to 0.38mm.
- The zig-zags number of crowns (6).
- The ring internal, initial diameter, set up at 40mm. This should allow the implant of the new stent in most of the large RVOTs defined in Chapter 6.

Two variables were analysed by DOE: the diameter of the pins used for the zig-zag forming, and the distance of the pins along the cylindrical mandrel axis (Table 10.1).

The DOE analysis run in this chapter on the basis of these 9 ring designs will give the indications for the optimal wire design, according to the selected parameters. Therefore, the CAD model of the optimised ring (10) will also be created to test its mechanical performance and compare them with the other 9 models.

Finite element meshes were automatically generated with 10-node tetrahedrons, as in the wire in platinum-10%iridium stent models, and with the same element size.

Ring	Pin diameter [mm]	Pin longitudinal distance [mm]
01	1.02	5.08
02	2.54	5.08
03	1.02	12.70
04	2.54	12.70
05	0.70	8.89
06	2.86	8.89
07	1.78	3.50
08	1.78	14.28
09	1.78	8.89

Table 10.1 Values of the two variable factors (diameter of the pins and their longitudinal distance) for the 9 analysed rings.

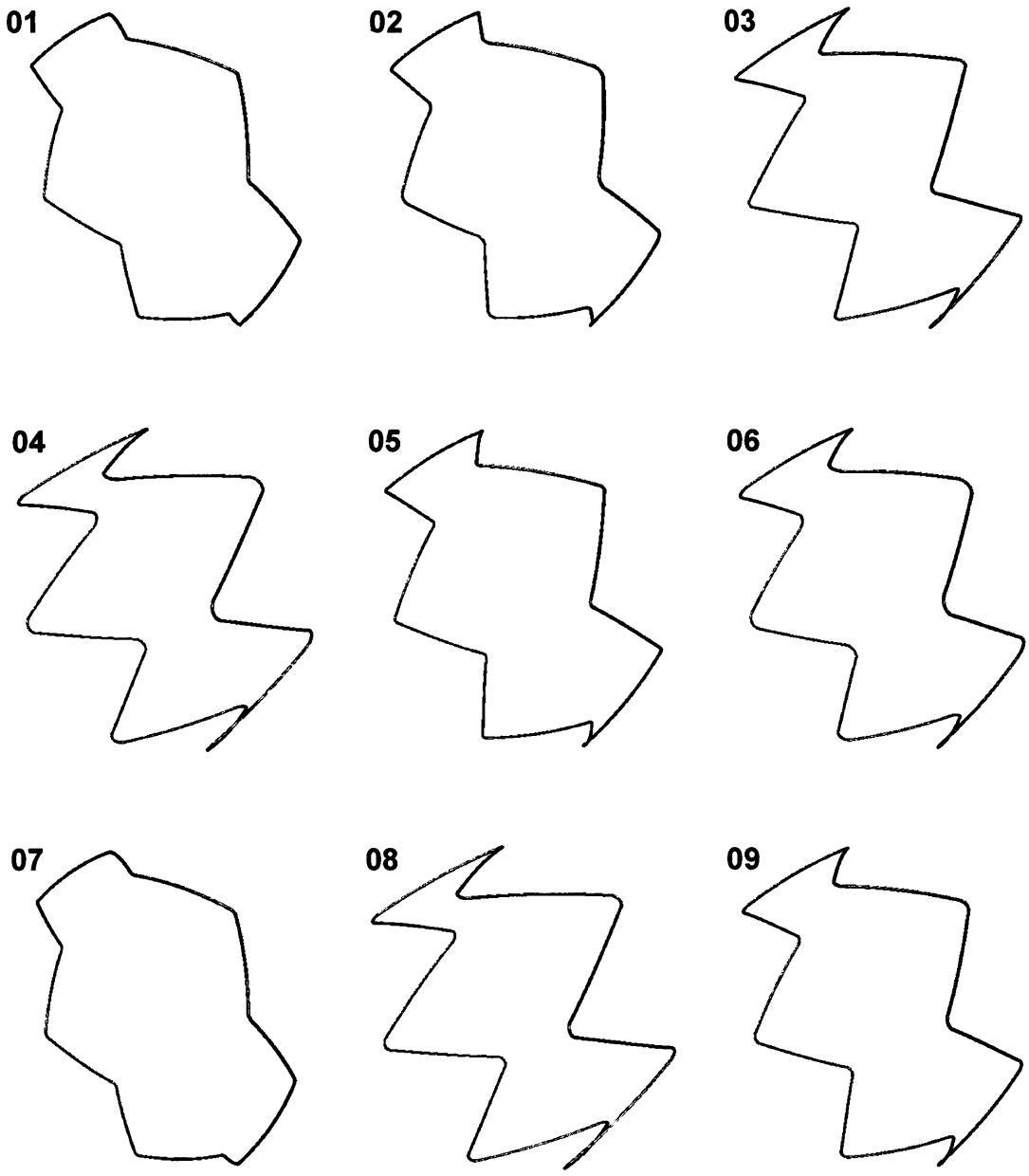

Figure 10.4 CAD model of the 9 analysed rings in their initial configuration.

10.3.2 Material Model

In the scientific literature, nowadays, there is an extensive number of publications about numerical models that accurately describe the thermo-mechanical response of SMAs [242-248]. However, the possibility of performing FE analyses of SMA devices with commercial codes is uncommon. An algorithm that captures the SMA super-elasticity effect is implemented in ABAQUS/Standard code through the user subroutine UMAT [249]. The characteristic uni-axial superelastic stress-strain curve of the UMAT material

is depicted in Figure 10.5, along with the main parameters of the constitutive model. Medium values of a generic nitinol alloy were chosen for these parameters (Table 10.2) [137]. All 9 analysed rings had the same material characteristics. The operating temperature of the rings was set at the body temperature (310.15 K = 37°C).

ABAQUS formulation of SMA does not model the plasticity in the martensite phase, that is the mechanical response of the material if the deformations induced by the loads are larger than the superelastic limit. However, this region of the material behaviour curve was not of interest in this study. The goal was to have a complete recovery of the mechanically induced deformations, thus allowing the stent to re-expand after releasing from the catheter. Therefore, only strains < 9% were assumed to be correctly modelled from the adopted material algorithm.

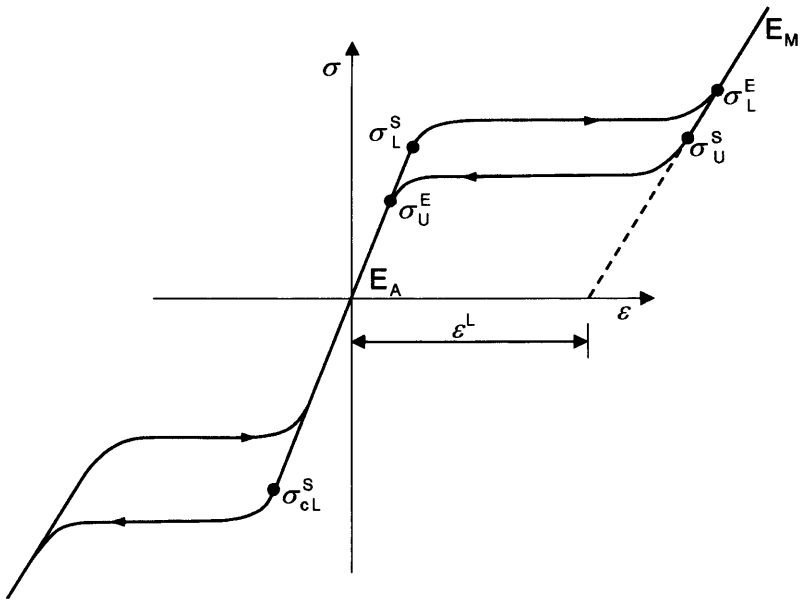

Figure 10.5 Uni-axial shape memory alloy behaviour. Explanation of the symbols is reported in Table 10.2.

Symbol	Description	Value
E_A	Austenite elasticity modulus	51 GPa
E_M	Martensite elasticity modulus	48 GPa
ε^L	Transformation strain	6 %
σ_L^S	Start of transformation loading	570 MPa
σ_L^E	End of transformation loading	670 MPa
σ_U^S	Start of transformation unloading	290 MPa
σ_U^E	End of transformation unloading	250 MPa
σ_{cL}^S	Start of transformation stress during loading compression	650 MPa

Table 10.2 Input values for the characteristic parameter of the SMA material model in ABAQUS.

For the fatigue analysis, the strain-life approach was adopted to predict the device safety. The key to this approach is to establish the constant life diagram using engineered fatigue samples that mimic the loading conditions an implant is subjected to *in-vivo*. Pelton *et al.* performed such testing on diamond stent-like specimens under *in-vivo* pulsatile bending loading conditions, at 10 million cycles [250]. Their results showed that, at mean strains ranging from 2% to 4%, nitinol fatigue endurance limit increases, when mean strain increases (Figure 10.6).

The life diagram from Pelton's study was used as fatigue limit for the nitinol material modelled in this chapter and to establish the safety factor of the rings. The diagram uses a graphical approach for relating the mean (ε_m) and alternating strain (ε_a) with the material fatigue limit, where ε_m is plotted along the x-axis and ε_a is plotted along the y-axis. Values of ε_a and ε_m that fall above the material fatigue limit indicate possible fatigue failure.

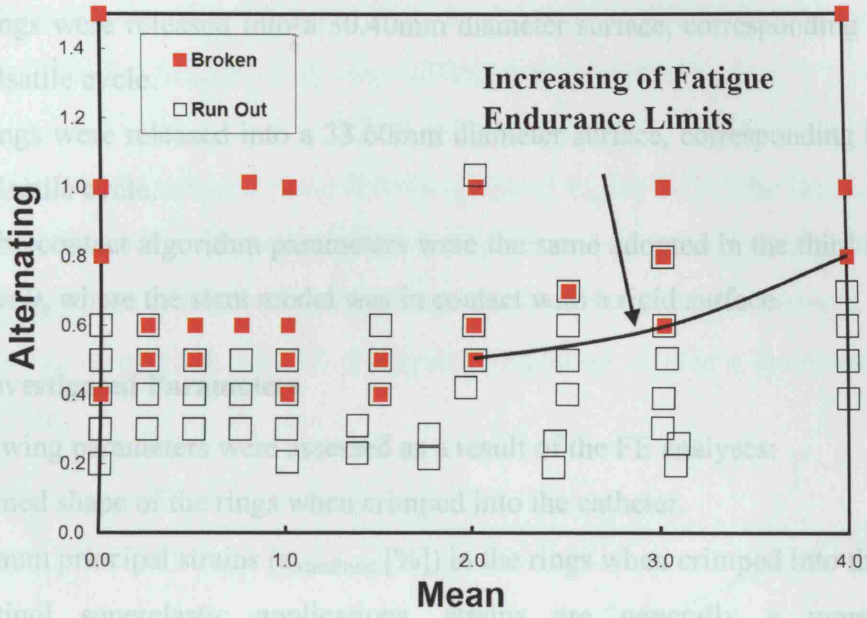

Figure 10.6 Fatigue testing results on diamond shaped specimens [250].

10.3.3 Analyses

In the FE analyses, the rings were first compressed from their initial geometry into the delivery catheter and then released to expand up to an operating, nominal diameter of 32mm (20% of compression respect to its initial diameter). This size was chosen to test the operating mechanical performance in a hypothetical RVOT. Once deployed into this RVOT, a radial pulsatile condition of ±5% of the nominal diameter was applied to test the ring fatigue behaviour.

The crimping of the nitinol rings was accomplished by prescribed radial displacements, up to a diameter slightly smaller than the delivery catheter size (18Fr = 6mm of internal diameter). At the end of the crimping step, the radial constraints were removed thus allowing the wires to recover their original shape. Contact with variable diameter, cylindrical, rigid surfaces was set up to study the configuration of the ring at the different phases of the loading cycle:

- The rings were released inside the catheter, represented by a cylindrical surface of 6mm diameter.
- The rings were released into a surface of 32mm diameter, equal to the selected operating diameter.

- The rings were released into a 30.40mm diameter surface, corresponding to -5% of the pulsatile cycle.
- The rings were released into a 33.60mm diameter surface, corresponding to +5% of the pulsatile cycle.

The contact algorithm parameters were the same adopted in the third simulation of Chapter 9, where the stent model was in contact with a rigid surface.

10.3.4 Investigated Parameters

The following parameters were assessed as a result of the FE analyses:

- Deformed shape of the rings when crimped into the catheter.
- Maximum principal strains ($\varepsilon_{MaxPrinc}$ [%]) in the rings when crimped into the catheter. In nitinol superelastic applications, strains are generally a more relevant characteristic than stresses. This is due to the peculiar mechanical behaviour of SMA, as described in Section 10.2. Therefore, in this chapter, strains and not stresses were reported to compare the FE results.
- Resistant force of the rings when compressed by an external pressure, measured at the operating diameter of 32mm. To calculate this force, a uniform pressure (ramp) was applied to the external surface of the ring. The pressures applied to the different rings to compress the diameter of 0.4% of the nominal diameter (0.128mm), where measured. The area where the external pressure was applied was different for each ring (they had different wire length). Therefore, to compare the strength of the different rings, the pressure values were multiplied by the areas to calculate the force.
- Fatigue characteristics of the rings under a ±5% radial pulsatile cycle. The maximum principal strains at the two pulsatile conditions were used to calculate ε_m and ε_a as follow:

$$\varepsilon_m = \frac{\varepsilon_{-5\%} + \varepsilon_{+5\%}}{2}$$

$$\varepsilon_a = \frac{\varepsilon_{-5\%} - \varepsilon_{+5\%}}{2}$$

To calculate the safety factor of the 9 ring models, the corresponding ε_m and ε_a were superimposed on the SMA life diagram (Figure 10.6). Based on the data showed in Figure 10.6, the fatigue boundary limit was extrapolated as follow:

- For $\varepsilon_m \leq 2\%$ (for example point A in the graph of Figure 10.7.), the fatigue limit was 0.40%. The fatigue safety factor (FSF_ε) was calculated as:

$$FSF_\varepsilon = 0.40\%/\varepsilon_a$$

- For $\varepsilon_m > 2\%$ (for example point B in the graph of Figure 10.7.), the fatigue limit line was assumed to be straight between the 2 points: C (2%, 0.4%) and D (4%, 0.6%). The fatigue safety factor for point B was calculated as the ratio between ε_a of point B_1 and ε_a. of point B, with B_1 orthogonal projection of B into the material fatigue limit line.

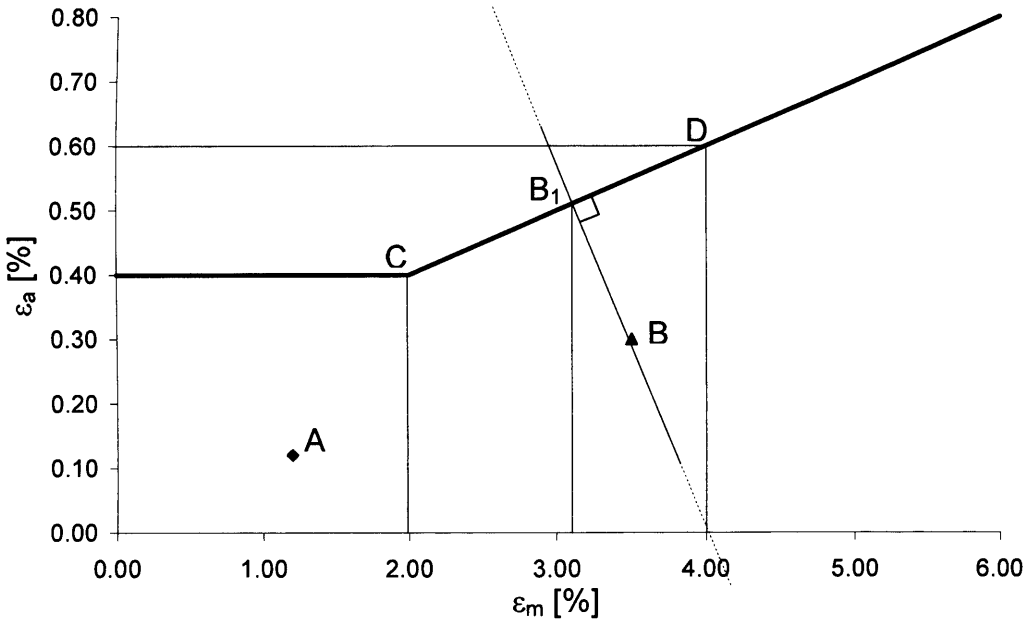

Figure 10.7 Extrapolation of the nitinol fatigue limit line from the fatigue graph of Figure 10.6.

10.4 RESULTS

10.4.1 Material Model

The uni-axial tensile stress-strain behaviour of the nitinol alloy modelled in this chapter, and operating at 37°C, is depicted in Figure 10.8. The simulation of the ring material property showed the typical superelastic behaviour. After an initial linear increase in stress with strain, large strains could be obtained with only a small further stress increase (wide plateau). The end of this plateau was reached at approximately 7% strain. Unloading from the end of the plateau region caused the stress to decrease rapidly until a lower plateau ("unloading plateau") was reached. Strain was recovered in this region

with only a small decrease in stress. The last portion of the deforming strain was finally recovered in a linear fashion. Beyond 7% of strains, the material curve would increase, with a slope dictated by the martensite elasticity modulus, up to infinite, because of the lack of a plasticity model at high strains. Strains up to 9% modelled with this material algorithm were considered acceptable for this study.

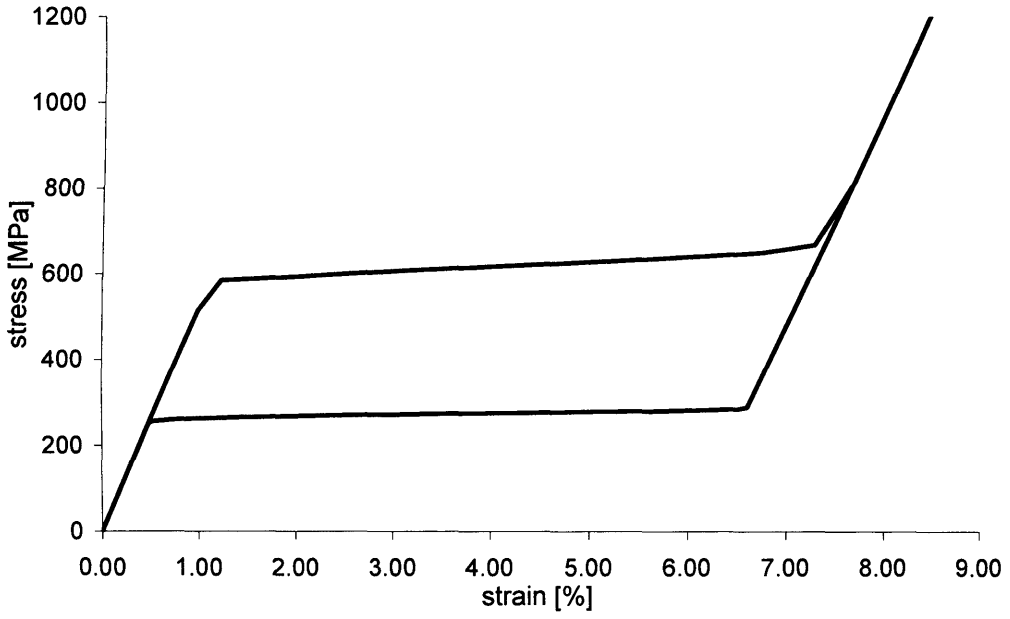

Figure 10.8 Uni-axial stress-strain behaviour of the nitinol modelled in FE and tested at 37°C.

The ring simulation cycle (crimping into the delivery catheter, release, expansion and interaction with the RVOT, and pulsatile conditions) can be explained following the curve of Figure 10.9. For this purpose, the axes were changed from stress-strain to force-diameter. The ring (point a, 40mm), of a given size larger than the RVOT wall, mimicked by the rigid surface at 32 mm diameter, was crimped into the delivery catheter (point b, 6mm) and released into the RVOT, expanding from point b until expansion (red curve) is stopped by impingement with the RVOT wall (point c, 32mm). At this point, further expansion of the ring was prevented. Because the ring did not expand to its memorised initial shape, it continued to exert a low outward force. At this point, the material has 2 different, possible responses:

- It will resist arterial recoil pressures, or any other external compression forces, with strong forces dictated by the loading curve from point c to d (blue colour).

- If expanded to a larger diameter, it will progress along the unloading curve towards e, maintaining the same force exerted against the RVOT wall.

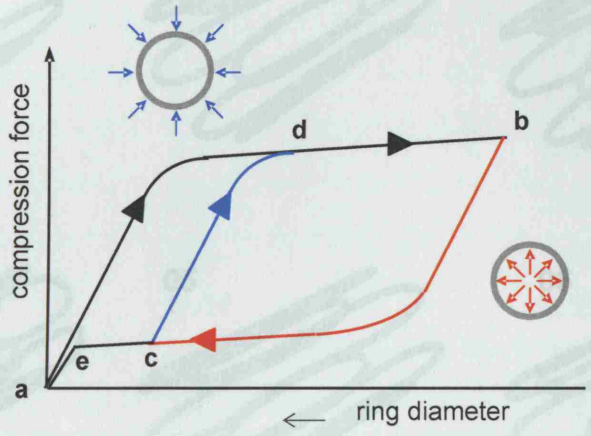

Figure 10.9 Schematic cyclic loading and unloading of the ring.

10.4.2 Shape and Strains into the Delivery Catheter

The 9 tested rings crimped into the delivery catheter resulted in the shapes of Figure 10.10. The figure shows that there was no overlapping of the zig-zag struts and therefore all ring designs may be suitable for the delivery catheter dimension. However, the strains in most of the models were considerable higher than the maximum strain allowed for the selected nitinol material to behave as superelastic (Table 10.3). Indeed, strain values higher than 9% were not realistic because the FE material model did not account for the plasticity behaviour of SMA above this deformation. Only rings 03, 04, 06 and 08 had maximum strains smaller than 9%, thus avoiding plastic deformations that could not be recovered when the device is released from the catheter.

In all cases, ring apices deformed toward the centre of the axis, with high tensile strains in the outer side of the crowns (in Figure 10.11 an example of the strain distribution: ring 08). The straight parts of the wires were only minimally deformed.

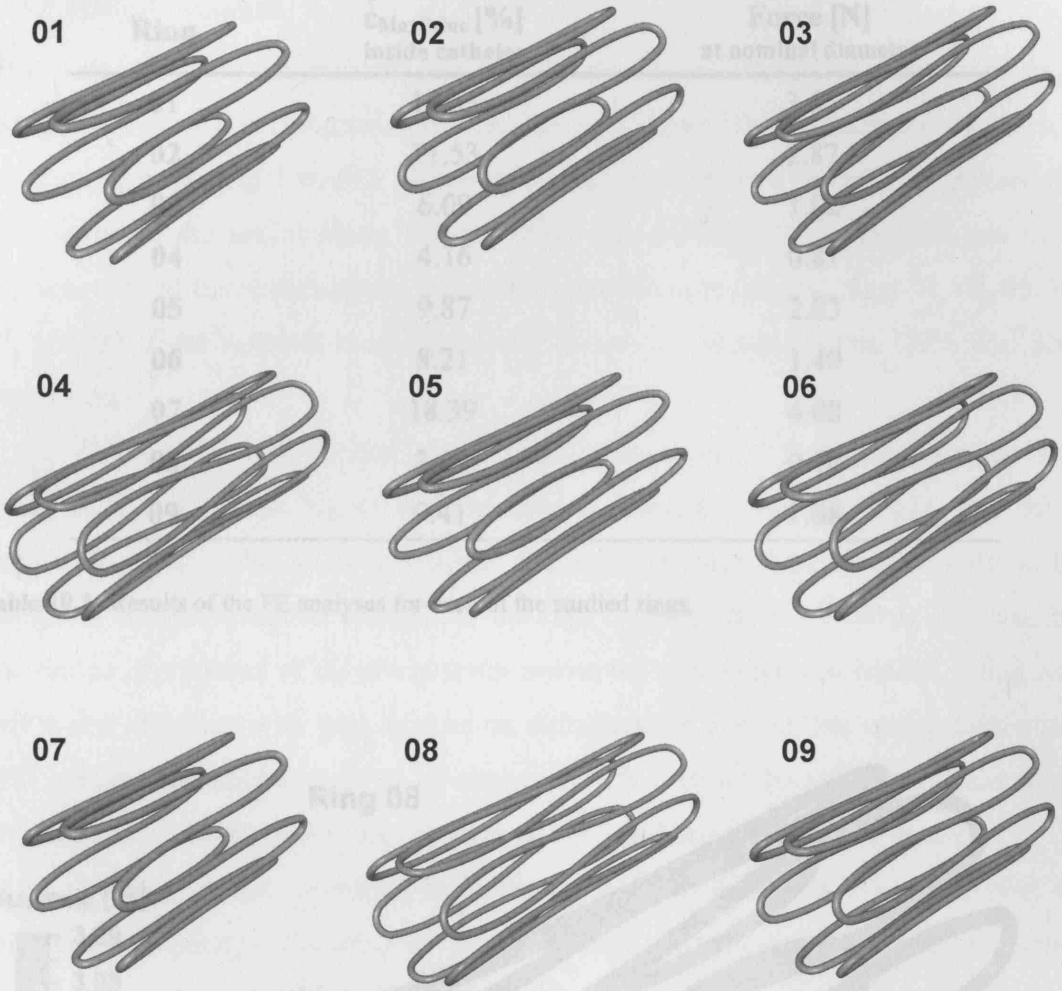

Figure 10.10 Deformed shape of the 9 rings when crimped into the delivery catheter.

Ring	$\varepsilon_{MaxPrinc}$ [%] inside catheter	Force [N] at nominal diameter
01	15.33	3.65
02	11.53	2.87
03	6.09	1.02
04	4.16	0.81
05	9.87	2.03
06	8.21	1.40
07	18.39	4.08
08	3.69	0.70
09	9.41	1.68

Table 10.3 Results of the FE analyses for each of the studied rings.

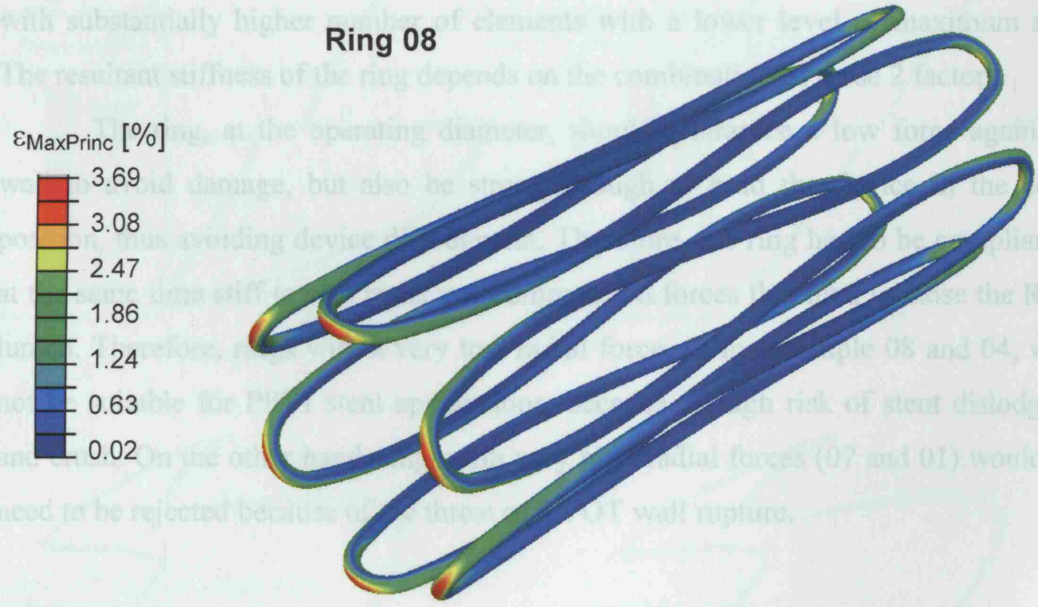

Figure 10.11 Example of the maximum principal strain distribution when ring 08 is crimped into the catheter.

10.4.3 Radial Strength

When released from the delivery catheter into the 32mm cylindrical surface, the rings recovered most of their original shape, as shown in Figure 10.12. The figure also depicts the maximum principal strains (different scales were adopted in order to capture the distribution of the strains along the ring structure). Indeed, all rings had strains <5%. The recovery of the deformations would have not been possible for rings 01, 02, 05, 06, 07, and 09 if the material model plasticity behaviour of superelastic SMA had been considered.

The radial forces exerted by the rings at the nominal diameter are reported in Table 10.3. Rings with higher residual strains were stronger than rings with lower strains. However, it has to be noted that the resistant force depended not only on the maximum stress/strain level reached by the ring elements at that nominal diameter, but also on the distribution of the stress/strain across the wire elements. Indeed, a ring with only a few elements with high maximum deformations can be less strong than a ring with substantially higher number of elements with a lower level of maximum strain. The resultant stiffness of the ring depends on the combination of these 2 factors.

The ring, at the operating diameter, should guarantee a low force against the wall to avoid damage, but also be strong enough to hold the device in the correct position, thus avoiding device dislodgment. Therefore, the ring had to be compliant but at the same time stiff to also resist any compression forces that tend to close the RVOT lumen. Therefore, rings with a very low radial force, as for example 08 and 04, would not be suitable for PPVI stent applications, because of high risk of stent dislodgment and crush. On the other hand, rings with very high radial forces (07 and 01) would also need to be rejected because of the threat of RVOT wall rupture.

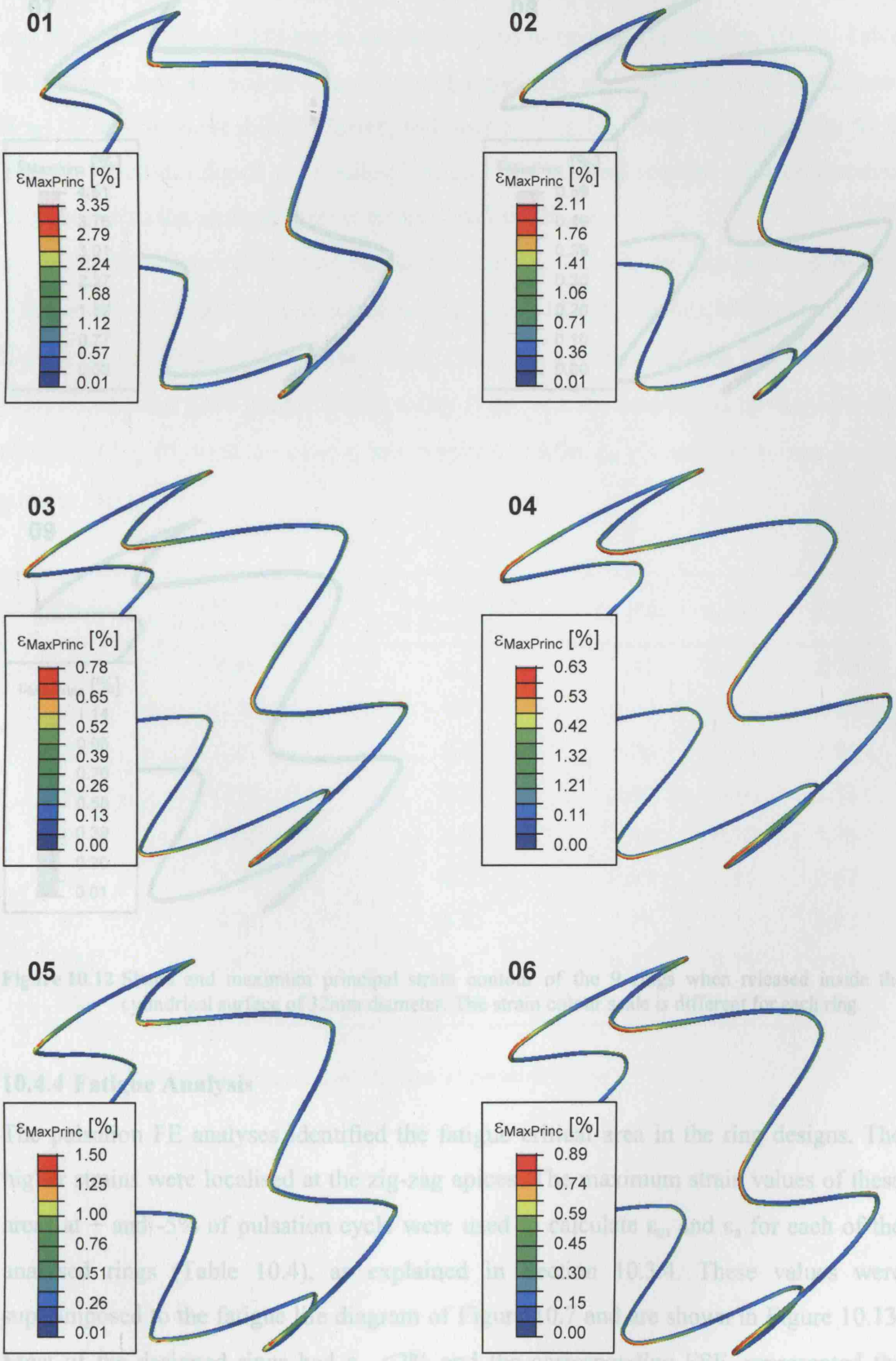
01
εMaxPrinc [%]
3.35
2.79
2.24
1.68
1.12
0.57
0.01
02
εMaxPrinc [%]
2.11
1.76
1.41
1.06
0.71
0.36
0.01
03
εMaxPrinc [%]
0.78
0.65
0.52
0.39
0.26
0.13
0.00
04
εMaxPrinc [%]
0.63
0.53
0.42
1.32
1.21
0.11
0.00
05
εMaxPrinc [%]
1.50
1.25
1.00
0.76
0.51
0.26
0.01
06
εMaxPrinc [%]
0.89
0.74
0.59
0.45
0.30
0.15
0.00

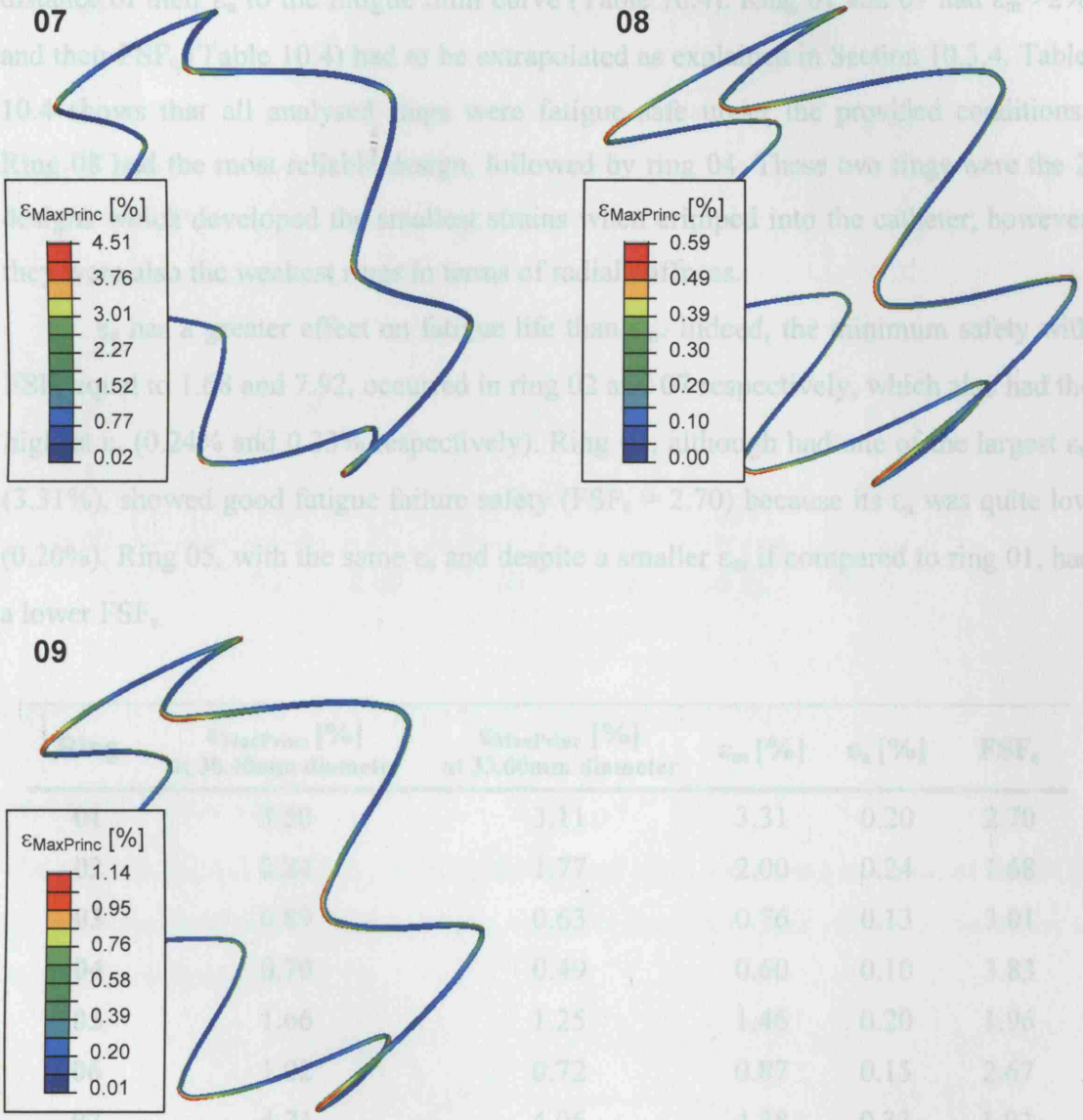

Figure 10.12 Shape and maximum principal strain contour of the 9 rings when released inside the cylindrical surface of 32mm diameter. The strain colour scale is different for each ring.

10.4.4 Fatigue Analysis

The pulsation FE analyses identified the fatigue critical area in the ring designs. The higher strains were localised at the zig-zag apices. The maximum strain values of these areas at + and -5% of pulsation cycle were used to calculate ε_m and ε_a for each of the analysed rings (Table 10.4), as explained in Section 10.3.4. These values were superimposed to the fatigue life diagram of Figure 10.7 and are shown in Figure 10.13. Most of the designed rings had $\varepsilon_m \leq 2\%$ and the corresponding FSF_ε represented the

distance of their ε_a to the fatigue limit curve (Table 10.4). Ring 01 and 07 had ε_m >2% and their FSF_ε (Table 10.4) had to be extrapolated as explained in Section 10.3.4. Table 10.4 shows that all analysed rings were fatigue safe under the provided conditions. Ring 08 had the most reliable design, followed by ring 04. These two rings were the 2 designs which developed the smallest strains when crimped into the catheter; however they were also the weakest rings in terms of radial stiffness.

ε_a has a greater effect on fatigue life than ε_m. Indeed, the minimum safety with FSF_ε equal to 1.68 and 7.92, occurred in ring 02 and 07 respectively, which also had the highest ε_a (0.24% and 0.33% respectively). Ring 01, although had one of the largest ε_m (3.31%), showed good fatigue failure safety (FSF_ε = 2.70) because its ε_a was quite low (0.20%). Ring 05, with the same ε_a and despite a smaller ε_m if compared to ring 01, had a lower FSF_ε.

Ring	$\varepsilon_{MaxPrinc}$ [%] at 30.40mm diameter	$\varepsilon_{MaxPrinc}$ [%] at 33.60mm diameter	ε_m [%]	ε_a [%]	FSF_ε
01	3.50	3.11	3.31	0.20	2.70
02	2.24	1.77	2.00	0.24	1.68
03	0.89	0.63	0.76	0.13	3.01
04	0.70	0.49	0.60	0.10	3.83
05	1.66	1.25	1.46	0.20	1.96
06	1.02	0.72	0.87	0.15	2.67
07	4.71	4.05	4.38	0.33	1.92
08	0.67	0.47	0.57	0.10	4.00
09	1.22	0.87	1.04	0.17	2.33

Table 10.4 Results of the fatigue analysis for each of the studied rings.

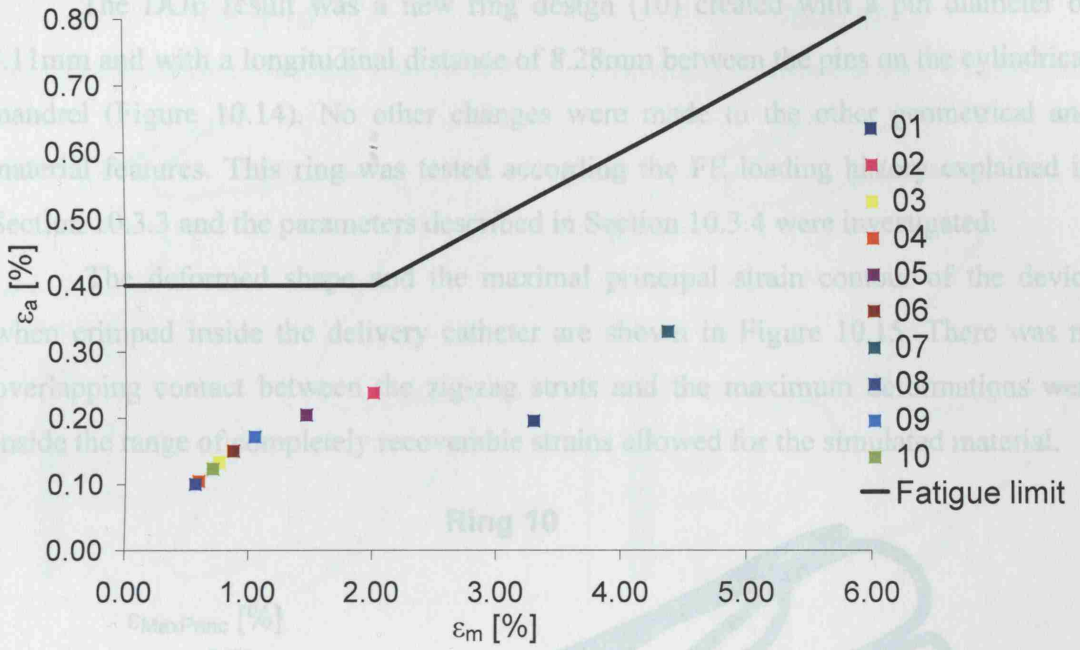

Figure 10.13 Fatigue graph for the 9 rings and the resulting optimised ring (10).

10.4.5 Optimised Ring

The results obtained from the FE analyses of the 9 rings were used as input for the DOE analysis. Acceptable limits and criteria were selected for each parameter in order to process the information.

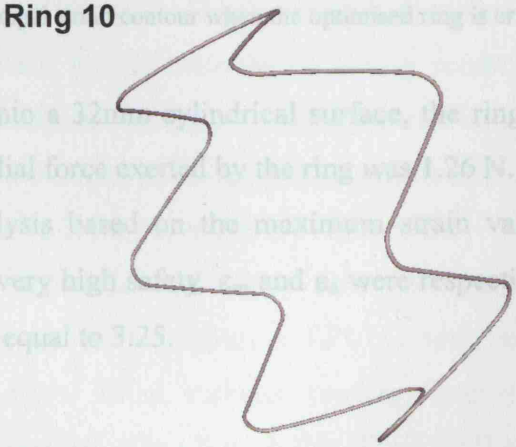

Figure 10.14 Optimised ring CAD model.

The DOE result was a new ring design (10) created with a pin diameter of 4.11mm and with a longitudinal distance of 8.28mm between the pins on the cylindrical mandrel (Figure 10.14). No other changes were made to the other geometrical and material features. This ring was tested according the FE loading history explained in Section 10.3.3 and the parameters described in Section 10.3.4 were investigated.

The deformed shape and the maximal principal strain contour of the device when crimped inside the delivery catheter are shown in Figure 10.15. There was no overlapping contact between the zig-zag struts and the maximum deformations were inside the range of completely recoverable strains allowed for the simulated material.

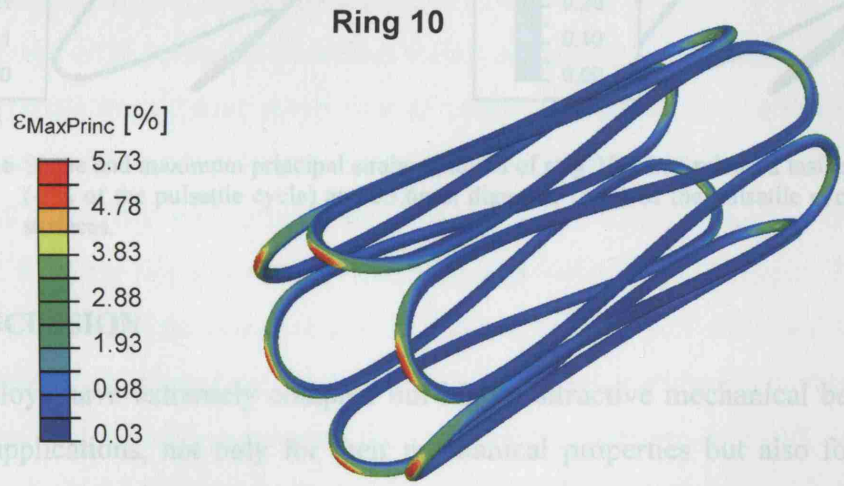

Figure 10.15 Maximum principal strain contour when the optimised ring is crimped inside the catheter.

When released into a 32mm cylindrical surface, the ring recovered most of its deformations and the radial force exerted by the ring was 1.26 N.

The fatigue analysis based on the maximum strain values at ±5% pulsation (Figure 10.16), showed very high safety. ε_m and ε_a were respectively 0.71% and 0.12% (Figure 10.13) with FSF equal to 3.25.

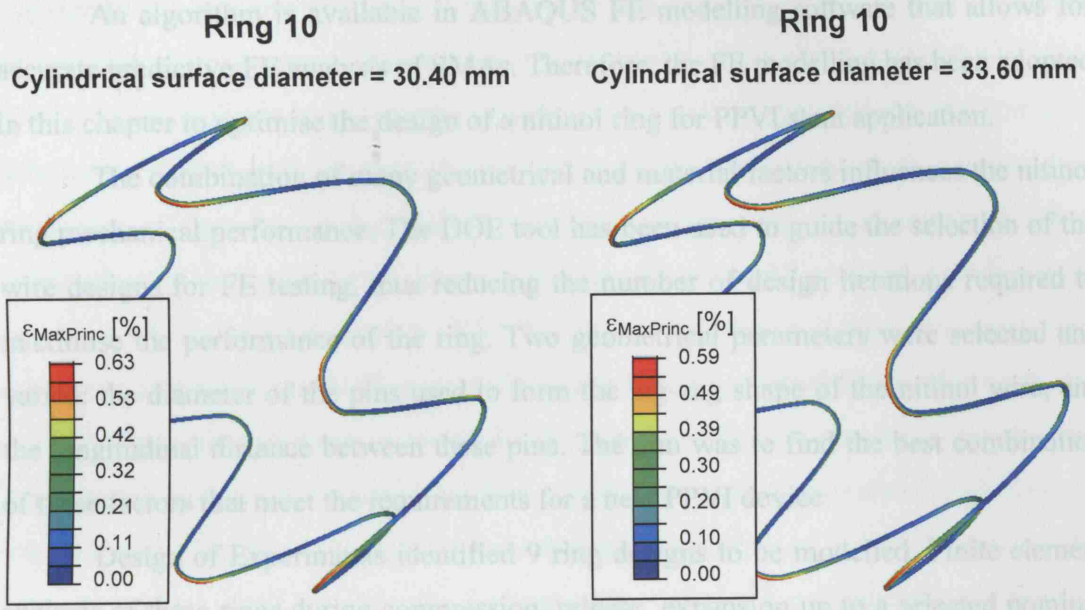

Figure 10.16 Shape and maximum principal strain contours of ring 10 when released inside the 30.40mm (-5% of the pulsatile cycle) and 33.6mm diameter (+5% of the pulsatile cycle) cylindrical surfaces.

10.5 DISCUSSION

Nitinol alloys have extremely complex but highly attractive mechanical behaviour for medical applications, not only for their mechanical properties but also for their bio-compatibility. However, the many benefits of these materials come at a cost and the complexity of their properties makes them difficult to process and maximise their potential. Traditional bench testing methods of device prototypes can be very time consuming and cannot always reveal the potential failures. Finite element modelling can greatly reduce testing and the time to device production by allowing the examination of a great number of designs before a prototype is even created.

Nitinol's unique non-linear and highly reversible characteristics make this a material well suited for the next generation PPVI device, subject to a variety of deformations resulting from initial catheter loading, deployment, and placement procedures which may adversely affect fatigue life. The nitinol stent will respond to the need for a new device that adapts its shape to large implantation sites and avoids fracture in the *in-vivo* cycling encountered in the implantation site environment, vascular dilations associated with normal cardiac rhythms, as well as a variety of other deformations experienced in the RVOT anatomical location.

An algorithm is available in ABAQUS FE modelling software that allows for accurate predictive FE analysis of SMAs. Therefore, the FE modelling has been adopted in this chapter to optimise the design of a nitinol ring for PPVI stent application.

The combination of many geometrical and material factors influences the nitinol ring mechanical performance. The DOE tool has been used to guide the selection of the wire designs for FE testing, thus reducing the number of design iterations required to maximise the performance of the ring. Two geometrical parameters were selected and varied: the diameter of the pins used to form the zig-zag shape of the nitinol wire, and the longitudinal distance between these pins. The aim was to find the best combination of these factors that meet the requirements for a new PPVI device.

Design of Experiments identified 9 ring designs to be modelled. Finite element analysis of these rings during compression, release, expansion up to a selected nominal diameter, and additional pulsating cycle after deployment allowed prediction of the mechanical behaviour and fatigue life of the 9 rings. The inadequacy of some ring designs in fulfilling the new device criteria was shown by the FE results. Furthermore, directions to optimise the ring design were given by the analysis of these results. A final most favourable ring model was created (ring 10) and analysed by FE method.

This ring dimensions should allow the next generation of PPVI devices to fit most of the large RVOTs that up to date are not suitable for percutaneous treatment with the current stent. Indeed, the ring optimised in this study was supposed to operate at a nominal diameter of 32mm. From the analysis of the RVOT morphology and dimensions in Chapter 6, 42 patients out of the 83 reviewed had morphology suitable for PPVI (type I morphology was excluded for the high risk of device dislodgment in the RV), but only 11 underwent the transcatheter procedure. Thirty-five of these 42 patients with suitable anatomy had also RVOT diameter <32mm. This means that a new PPVI stent created with ring 10, would increase the number of treatments from 13% up to 39%.

The dimensions of the wire used to form the ring were suitable for delivery of the device through the catheter already in use for the current procedure. The nitinol wire diameter (0.38mm) was bigger than the diameter of the platinum-10%iridium wire employed for the current generation device (0.33mm). However, nitinol stents, compared to the current device for PPVI, do not need a balloon to be deployed and the

catheter has to host the stent only. Furthermore, the crimping of this ring did not cause any overlap of its structures that could compromise its correct releasing (Figure 10.15).

The strains resulting from the crimping of ring 10 into the delivery catheter were acceptable (<6%) and enabled the recovery of the deformations to ensure good anchoring of the ring to the RVOT wall and maintenance of an adequate vessel scaffolding. Indeed, its oversize dimension (40mm) at initial formation guaranteed the released ring deployed against the RVOT wall, modelled as a 32mm cylindrical rigid surface, and at this nominal diameter to keep exerting an outward force. Moreover, ring 10 at the operating diameter responded with a good stiffness in resisting the crushing pressure applied to its external surface. These concurrent compliant and stiffness characteristics are due to the peculiar mechanical behaviour of nitinol. Thanks to this property, nitinol stents may become the treatment of choice for distensible and dynamic implantation sites, because they can better follow the wall deformations during the cardiac cycle. Indeed, the use of the current device in the presence of native and/or non-calcified RVOTs is not advisable, because of the high risk of fracture [Section 9.1]. During the deployment of the nitinol stent in the RVOT, the nominal strains at the end of the expansion are highest in a calcified implantation site (high ε_m), but the cyclic loadings are smaller (small ε_a) as the elastic modulus of calcific tissue is higher than that of either native tissue or fibrotic wall. In a compliant RVOT, the vessel expands more, in response to the stent expansion force, reducing the stent nominal deformations (small ε_m). Furthermore, the high compliance of the RVOT wall is blocked by the nitinol stent stiffness, thus reducing the systolic/diastolic loading and resulting in low cyclic strains (small ε_a).

The fatigue analysis of ring 10 tested at ±5% of its nominal diameter resulted in a significantly high FSF. Because of the unusual way it deforms, nitinol has a fatigue behaviour that is quite atypical of metals in general. In a strain-controlled environment like the highly distensible RVOTs, nitinol excels. Indeed all the tested rings, with fatigue ε_m up to 4.38% and ε_a up to 0.33%, had FSF > 1.65 for a maximum of 10 million cycles. However, the fatigue limit line for this study was only extrapolated from experimental data with ε_m close to 4%. Therefore, tests at ε_m between 4 and 6% are necessary to establish the fatigue limit and strain-life relationship at this ε_m and to validate the extrapolation.

Other geometrical and material factors should be included in the DOE analysis to maximise the mechanical behaviour of the nitinol ring, and other nominal diameters should be tested to mitigate migratory and fracture concerns. The study carried out in this chapter was mainly an example to exploit and show the FE method potential in optimising stent design. Other aspects involved in the design of the next generation nitinol stent will be the subject of future analyses performed with the methodology herein developed.

In Chapter 9, an FE methodology has been introduced to study the stent/implantation site interaction. Once this methodology is finalized and the main geometrical and material parameters optimised in a new final stent design, the FE interaction analysis could be used to determine the impact of the new stent attributes on selected realistic RVOTs, as well as the impact that the RVOT wall has on the mechanical behaviour of the nitinol stent. Furthermore, the performance of the new device deployed at non-uniform conditions could be tested. This new predictive data will provide an additional mechanism by which the performance of a new stent to be used in PPVI could be maximised. This iterative process will be carried out without extensive and costly testing efforts in bench and animal models.

10.6 CONCLUSION

Shape memory alloys have an extremely complex behaviour, depending on thermal and mechanical loading, and as such these materials comprise a range of exceptional mechanical properties of great interest for the next generation PPVI stent. In fact, shape memory alloys, and in particular nitinol, can completely recover large, mechanically induced deformations; they can exert a low expansion force, but at the same time strongly resist a compressive force; and their fatigue behaviour dramatically outperforms all conventional metals. This means that a nitinol stent for PPVI application could solve the problems of treating large RVOTs, as well as risk of fracture.

Because of its complex behaviour, a careful study is necessary to achieve the best compromise between all the positive properties of nitinol, whilst limiting its undesired behaviours. Finite element modelling can help in this task by analysing the

performance of many different rings in order to eliminate the designs that do not work, before prototypes are created and tested.

Using FE analysis and the ABAQUS nitinol superelastic material model, it was possible in this chapter to optimise the design of a ring for PPVI stent applications. This methodology can be applied to study the other rings that form the stent whole structure in order to maximize the complete device performance.

In the future, when the optimal design for the next generation stent will be finalized, a prototype of this new device could be tested in RP models of representative patient RVOTs, as the ones developed in Chapter 7. The robustness of the optimised design would be therefore further tested as explained in the future work of Chapter 11.

CHAPTER 11

CONCLUSIONS AND FUTURE WORK

11.1 OVERVIEW

The aim of this thesis was to improve the understanding of the mechanisms of PPVI, in order to enhance this minimally invasive technique and increase the number of patients who can benefit from this procedure. The research presented has successfully addressed a number of issues related to PPVI, by focusing on 3 key components: the implantation site, the device and the interaction between these two structures. The latter determines the success/failure of the procedure, but also defines the limits for its clinical application. Indeed, the current device is only suitable for patients with specifically defined anatomy. Selection of patients is critical both to ensure procedural success and to guarantee long-term positive outcome.

At the beginning of my research, I focused on the study of the implantation site morphology [Chapter 6]. My aim was to identify sub-groups of RVOT morphology that would be suitable for PPVI and to document their prevalence in our patient population using basic mathematical rules and anatomical parameters. Based on 3D reconstruction of 83 patients' RVOTs from MR data, a morphological classification was created, according to visual assessment of the 3D volumes and detailed measurements. A pyramidal morphology was most prevalent (49%) and related to the presence of a transannular patch. Percutaneous pulmonary valve implantation was not performed in patients with this morphology, which is unsuitable because of the high risk of proximal dislodgment. This finding has influenced the approach of surgeons to primary repair of congenital heart disease. Thus, in our institution, there is a preference for placing smaller patches, and where possible homograft conduits, instead of large patches that cause a pyramidal outflow tract shape to develop. It is most likely that, in the future, there will be fewer patients seen with this pyramidal morphology and consequently a higher proportion suitable for PPVI. Furthermore, the need for a valved stent that may be able to deal with this wide range of morphologies has emerged. The morphological classification developed during this research can guide the anatomical and dimensional requirements that the next generation device will need to fulfil.

Establishing the precise morphology of the proposed implantation site with the currently available techniques (echocardiography, MR, CT imaging) is extremely valuable, but I demonstrated [Chapter 7] that in borderline cases it can still be difficult

to perceive 3D anatomy that is presented on a 2D computer screen, and we have had several cases in which the transcatheter procedure has been attempted, but has not been successful. I demonstrated that the use of 3D RP models results in more accurate selection of patients for PPVI than conventional imaging assessment alone. Rapid prototyping models provide a complete appreciation of the 3D anatomy and size of the implantation site, as an object held in the hand can be easily viewed from any angle, and dimensions accurately measured. Moreover, these models enable trial implantation of the device to test whether the positioning and anchoring of the stent in the RVOT are correct and safe. Therefore, in borderline cases, a RP model of the patient's potential implantation site is built and used by the clinicians in the decision process regarding the suitability for transcatheter procedure. The RP models of some patient RVOTs, selected among the ones which represent the currently untreatable morphologies, could be used as bench test for the new device in order to understand its anatomical and dimensional suitability, its position and anchoring to the RVOT wall, and the shape of the valve mounted into it when the stent is deformed in the implantation site.

Chapter 6 and 7 enabled me to gain a fully understanding of the implantation site, identify RVOT morphologies in which the device may not be suitable (and hence define how new devices have to be designed), and use mathematical tools to define and classify the implantation sites. In Chapter 8, I focused on the PPVI stent itself and in particular on a common complication of this device, stent fracture, which can lead to major clinical events. The aetiology of these fractures is likely to be multi-factorial and depend on both the nature of the stent as well as the characteristics of the implantation site. My first approach to this clinical problem was to study the mechanical properties of the current device using FE modelling. A comparison of different innovative solutions was developed in order to identify an ideal balance between recoil, fracture resistance, radial strength, satisfactory biocompatibility and radio-opacity. This led to the development of multiple element stents (stent-in-stent), which appear to be an effective solution to reduce the rate of device fracture and increase the success of the percutaneous procedure, without compromising its technical ease (patent pending).

The FE analysis of the current stent identified the areas at potential risk for fracture, as seen in clinical practice. However, these FE analyses only mimicked a free stent uniform expansion. Therefore, they are not exhaustive because they do not account

for the interaction with the patient RVOT, as is also the case with the bench preclinical testing to date.

The stent/implantation site interaction has been studied in Chapter 9 through 3D reconstructions of the *in situ* stent shape from biplane fluoroscopy images, and through FE modelling. The reconstruction of the 3D shape and deformation of the stent from biplane fluoroscopy images accurately defined and quantified most of the stent morphological characteristics *in situ*. The clinical data clearly showed that the PPVI stent rarely results in a uniform expansion. Asymmetries are present in all directions and may be a discriminatory factor in PPVI stent fracture occurrence. The implantation of the stent into a selected patient RVOT by FE modelling was complicated. This analysis required the introduction of simplified assumptions to numerically solve the contact problem. However, the FE simulation underlined the need for inclusion of the interaction with the RVOT in the estimate of the stent mechanical performance. The asymmetrical expansion causes a decrease in radial strength, and an overall significant increase in the structure stresses and, therefore, in the potential for fatigue fracture. This finding has influenced the set up of preclinical tests that are performed on the devices. Thus, the current stent has been recently fatigue re-tested following the indication given by my research. A non-uniform loading condition was adopted in the bench test and stent fracture now occurred.

The proposed multi-element stent of Chapter 8 may be a solution for stent fracture. However, the design of the multi-element stent, based on the current device, is still not suitable to treat the numerous patients who have large RVOTs. A first attempt towards the next generation PPVI stent, with an innovative design that can broaden the applications of PPVI, was reported in Chapter 10. Nitinol alloy has been selected as the material of choice for the next generation device since it comprises a range of interesting mechanical and biocompatibility properties. Finite element modelling was used to analyse the mechanical performance of many different rings for use in the new PPVI stent in order to guide the optimisation process towards a robust final ring design. This optimised ring can recover large, mechanically induced deformations, allowing for easy crimping and releasing of the stent into the RVOT. It can exert a low expansion force, against the RVOT wall, that should not damage the tissues, but at the same time strongly resists a compressive force. Its fatigue behaviour dramatically outperforms all

conventional metals. The methodology developed in this chapter may be used to study all the rings that will form the final stent structure, in order to guarantee adaptability to most RVOT morphologies and to maximise its mechanical performance.

11.2 FUTURE WORK

The research presented in this thesis has covered a broad range of topics, spanning from MR 3D reconstructions and RP building of RVOT anatomies, through to the study of stent mechanical performance and its interactions with the implantation site.

For clarity, areas for future work have been categorized in three main sections: improvements to the RVOT classification presented in Chapter 6, improvement to the RP models developed in Chapter 7 and their use in testing new devices, and improvements to the FE modelling methodology of Chapter 9 for use in stent/implantation site interaction analyses. A brief outline for future work on each topic now follows.

11.2.1 Improvements to the Right Ventricular Outflow Tract Classification

The RVOT classification presented in Chapter 6 and its mathematical formulation have shown to be an accurate instrument for the correct identification of morphological sub-types for PPVI. However, the distensibility of the RVOT during the cardiac cycle is not assessed using this methodology. Patients with borderline size of the RVOT are at high risk of device dislodgment if their RVOT distends significantly, as stability of the PPVI stent cannot be assured. Furthermore, our experience to date suggests that stent fractures are more commonly seen following PPVI in non-calcified, and therefore more distensible and mobile RVOTs. Both the dynamic nature of the outflow tract and the wall thickness (consistent with calcification) may be assessed employing new imaging modalities. As extensively described before, we have predominantly used MR imaging in our assessment of the implantation site to date. However, MR imaging is less good at imaging metal and calcium. This can limit the assessment of patients both before and after device implantation. Hence, although associated with a radiation dose, CT imaging is now clinically indicated in many of our patients. New MR sequences and CT algorithms could be implemented and tested to achieve the highest spatial/temporal resolution. The aim would be to record accurate 3D RVOT volumes at a sufficient

number of frames to capture the critical phases of the cardiac cycle. The datasets originating from these scans could then be analysed and 3D RVOT volumes reconstructed for each frame of the cardiac cycle, using the developed methodology. Right ventricular outflow tract pressures are usually measured during catheterisation. These pressure data coupled with the RVOT 3D volume deformations during the cardiac cycle could enable the evaluation of the RVOT distensibility, as a general compliance indication but also localized along different cross sections of the outflow tract. Primary diagnosis, RVOT type and morphology, surgical history and treatment outcomes will be documented for all patients. Principal Component Analysis, a useful statistical tool that has found application in fields such as face recognition and image compression and is commonly used to find patterns in large datasets, could be used to classify the wide spectrum of RVOT morphologies and distensibilities, present in patients late after surgical repair of congenital heart disease, into types with similar characteristics and behaviour. The characteristic sub-groups of this classification could finally be used to guide the design of new devices for PPVI and give useful indications for future changes in surgical approaches to early repair. Moreover, the distensibility data could be imputed into the RVOT material model for FE analyses. In this way, this property would be characteristic for each individual patient and not an average data from the literature.

11.2.2 Improvements to the Rapid Prototyping Models

Chapter 7 describes the use of RVOT RP models to help patient selection for PPVI and to qualitative test the device stability. The use of these models in the preclinical experimental set up could be taken forward. Different materials to build the models could be studied and tested in order to identify the one which best simulate the RVOT distensibility properties as calculated from section 11.2.1, for each selected patient. The distensible, realistic RVOT phantom could then be placed into a mock circulatory loop, which operates over a range of heart rates and cardiac outputs that mimic the physiological and pathological conditions, and the device could be implanted inside this phantom. Thus, the device post-implantation mechanical performance would be evaluated under dynamic load conditions and into a fixture that has realistic morphology and distensibility characteristics. The function and hydrodynamics of the valve sutured into the stent (flow rate, pressure drop, effective valve orifice area) and

the stent shape and deformation, once placed into the mock loop, could be measured at the patient fluid dynamics condition.

11.2.3 Improvements to the Finite Element Models

Chapter 9 shows the feasibility of the stent/implantation site interaction FE analyses. However, simplified cases had to be analysed because of the difficulty for the FE code to process and solve contact problems. Recently, in the upgraded version of FE code used for the computational analyses in this thesis (ABAQUS/Standard), new algorithms have been implemented that allow for different mechanical contact properties to be modelled. New relationships and conditions have been defined between the slave and master surface of the contact pair and between the pressure transmitted in the interaction and the distance of the 2 interacting surfaces.

These improvements in the FE code should allow a realistic analysis of the interaction between the stent and the RVOT wall. This could advance the understanding of stent fracture in the PPVI population. Individual RVOT wall material properties obtained as explained in Section 11.2.1 could be inputted into the RVOT FE model of a selected subject. The PL-AU stent model could be expanded in the correct position inside the RVOT FE model, and to the same final diameter as during the actual PPVI procedure. The final stent configuration could be compared with the real shape of the device *in situ*, as assessed by biplane fluoroscopy image analysis [Chapter 9]. Finally, a pressure, equal to the difference between systolic and diastolic pulmonary pressure, measured at the time of PPVI procedure, could be applied to the RVOT internal surface and the risk of fatigue failure assessed. The robustness and validity of the stent/implantation site interaction FE model could be tested by comparison with the real stent fracture events in the PPVI patient population. If proven successful, FE analyses could be used to predict the stent mechanical performance and fatigue life in each patient referred for PPVI *a priori*, and therefore help patient selection for this procedure.

Furthermore, the FE model of the RVOT could be used to test the next generation PPVI stent in order to maximise its mechanical performance. This RVOT model, realistic in terms of morphology and dimensions, would be used to study the adaptability of the nitinol stent shape into a wide range of possible RVOT anatomies.

Moreover, realistic loading conditions could be simulated in the FE model to analyse the stent mechanical behaviour and assess its fatigue life expectancy.

Ultimately, FE models may be used to investigate the results of PPVI for each individual patient before the actual procedure is performed. Using FE analyses, it may be possible to predict, from the pre-implant morphology and deformations of the RVOT, in which patients the device will succeed/fail.

11.3 CONCLUSION

The research described in this thesis brings together many disciplines to create realistic, virtual and real models of the implantation site and device. The use of computational modelling in device development and in the clinical environment may accelerate the design and optimisation of new devices for transcatheter procedures. Translating the 3D assessment of patient anatomy and dynamics into FE models will allow the selection of patients with suitable implantation sites, and the reliable prediction of device stability and durability. Ultimately, this may lead to a reduction in the number of manufactured prototypes and animal experiments used in phase 0 and 1 trials prior to first-in-man implantation, to a shortening of the learning curve for implantation site selection, and therefore to a decrease in the number of procedural and device failures not only for PPVI, but also in all valve replacement applications in the future. Indeed, the methodologies developed in this thesis may be beneficial to a wide range of device/anatomical implantation site interactions. For example, following the success of PPVI, many groups have attempted to develop transcatheter valvular devices, mainly focusing on the aortic valve, due to its bigger market size. However, to date, percutaneous aortic valve implantation has proven difficult in human subjects and has been associated with significant mortality (up to 60%) and morbidity in the early experience. The more complex morphology and the higher loading conditions in the left heart make the transcatheter procedure technically more challenging. In retrospect, a deeper understanding of the implantation site morphology and loading conditions would have significantly increased the survival rate in first-in-man percutaneous aortic valve implantation.

BIBLIOGRAPHY

1. Brown EN, Peterson ML, Grande-Allen KJ. Biological systems and materials: A review of the field of biomechanics and the role of the Society for Experimental Mechanics. Experimental Techniques 2006; 30(2):21-29.

2. Schneck DJ; Bronzino JD. Biomechanics - Principles and Applications. CRC Press; 2003.

3. Pietrabissa R, Luisi VS. What is the role of biomechanics in cardiac surgery? Cardiol Young 2004; 14 Suppl 3:1-3.

4. Yacoub MH, Cohn LH. Novel approaches to cardiac valve repair: from structure to function: Part I. Circulation 2004; 109(8):942-950.

5. Yacoub MH, Cohn LH. Novel approaches to cardiac valve repair: from structure to function: Part II. Circulation 2004; 109(9):1064-1072.

6. Yacoub M, Nerem R. Introduction. Bioengineering the heart. Philosophical Transactions of the Royal Society B-Biological Sciences 2007; 362(1484):1253-1255.

7. Everett AD, Lim DS, Peeler BB, Vricella LA. Illustrated Field Guide to Congenital Heart Disease and Repair. First ed. Scientific Software Solutions; 2004.

8. Macmahon B, Mckeown T, Record RG. The incidence and life expectation of children with congenital heart disease. Br Heart J 1953; 15(2):121-129.

9. Moller JH, Taubert KA, Allen HD, Clark EB, Lauer RM. Cardiovascular health and disease in children: current status. A Special Writing Group from the Task Force on Children and Youth, American Heart Association. Circulation 1994; 89(2):923-930.

10. Mitsuno M, Nakano S, Shimazaki Y, Taniguchi K, Kawamoto T, Kobayashi J et al. Fate of right ventricular hypertrophy in tetralogy of Fallot after corrective surgery. Am J Cardiol 1993; 72(9):694-698.

11. Kirklin JK, Westaby S, Blackstone EH, Kirklin JW, Chenoweth DE, Pacifico AD. Complement and the damaging effects of cardiopulmonary bypass. J Thorac Cardiovasc Surg 1983; 86(6):845-857.

12. Taggart DP, Hadjinikolas L, Wong K, Yap J, Hooper J, Kemp M et al. Vulnerability of paediatric myocardium to cardiac surgery. Heart 1996; 76(3):214-217.

13. Taggart DP, Hadjinikolas L, Hooper J, Albert J, Kemp M, Hue D et al. Effects of age and ischemic times on biochemical evidence of myocardial injury after pediatric cardiac operations. J Thorac Cardiovasc Surg 1997; 113(4):728-735.

14. Lange PE, Onnasch DG, Bernhard A, Heintzen PH. Left and right ventricular adaptation to right ventricular overload before and after surgical repair of tetralogy of Fallot. Am J Cardiol 1982; 50(4):786-794.

15. Rebergen SA, Chin JG, Ottenkamp J, van der Wall EE, de RA. Pulmonary regurgitation in the late postoperative follow-up of tetralogy of Fallot. Volumetric quantitation by nuclear magnetic resonance velocity mapping. Circulation 1993; 88(5 Pt 1):2257-2266.

16. Marx GR, Hicks RW, Allen HD, Goldberg SJ. Noninvasive assessment of hemodynamic responses to exercise in pulmonary regurgitation after operations to correct pulmonary outflow obstruction. Am J Cardiol 1988; 61(8):595-601.

17. Graham TP, Cordell D, Atwood GF, Boucek RJ, Boerth RC, Bender HW et al. Right ventricular volume characteristics before and after palliative and reparative operation in tetralogy of Fallot. Circulation 1976; 54(3):417-423.

18. Jonsson H, Ivert T, Brodin LA. Echocardiographic findings in 83 patients 13-26 years after intracardiac repair of tetralogy of Fallot. Eur Heart J 1995; 16(9):1255-1263.

19. Horneffer PJ, Zahka KG, Rowe SA, Manolio TA, Gott VL, Reitz BA et al. Long-term results of total repair of tetralogy of Fallot in childhood. Ann Thorac Surg 1990; 50(2):179-183.

20. Harrison DA, Harris L, Siu SC, MacLoghlin CJ, Connelly MS, Webb GD et al. Sustained ventricular tachycardia in adult patients late after repair of tetralogy of Fallot. J Am Coll Cardiol 1997; 30(5):1368-1373.

21. Schamberger MS, Hurwitz RA. Course of right and left ventricular function in patients with pulmonary insufficiency after repair of Tetralogy of Fallot. Pediatr Cardiol 2000; 21(3):244-248.

22. Warner KG, Anderson JE, Fulton DR, Payne DD, Geggel RL, Marx GR. Restoration of the pulmonary valve reduces right ventricular volume overload after previous repair of tetralogy of Fallot. Circulation 1993; 88(5 Pt 2):II189-II197.

23. Therrien J, Siu SC, McLaughlin PR, Liu PP, Williams WG, Webb GD. Pulmonary valve replacement in adults late after repair of tetralogy of fallot: are we operating too late? J Am Coll Cardiol 2000; 36(5):1670-1675.

24. Gatzoulis MA, Balaji S, Webber SA, Siu SC, Hokanson JS, Poile C et al. Risk factors for arrhythmia and sudden cardiac death late after repair of tetralogy of Fallot: a multicentre study. Lancet 2000; 356(9234):975-981.

25. Eyskens B, Reybrouck T, Bogaert J, Dymarkowsky S, Daenen W, Dumoulin M et al. Homograft insertion for pulmonary regurgitation after repair of tetralogy of fallot improves cardiorespiratory exercise performance. Am J Cardiol 2000; 85(2):221-225.

26. Warner KG, O'Brien PK, Rhodes J, Kaur A, Robinson DA, Payne DD. Expanding the indications for pulmonary valve replacement after repair of tetralogy of fallot. Ann Thorac Surg 2003; 76(4):1066-1071.

27. Harrison DA, Siu SC, Hussain F, MacLoghlin CJ, Webb GD, Harris L. Sustained atrial arrhythmias in adults late after repair of tetralogy of fallot. Am J Cardiol 2001; 87(5):584-588.

28. Wessel HU, Paul MH. Exercise studies in tetralogy of Fallot: a review. Pediatr Cardiol 1999; 20(1):39-47.

29. Gatzoulis MA, Till JA, Somerville J, Redington AN. Mechanoelectrical interaction in tetralogy of Fallot. QRS prolongation relates to right ventricular size and predicts malignant ventricular arrhythmias and sudden death. Circulation 1995; 92(2):231-237.

30. Bove EL, Byrum CJ, Thomas FD, Kavey RE, Sondheimer HM, Blackman MS et al. The influence of pulmonary insufficiency on ventricular function following repair of tetralogy of Fallot. Evaluation using radionuclide ventriculography. J Thorac Cardiovasc Surg 1983; 85(5):691-696.

31. Oku H, Shirontani H, Sunakawa A, Yokoyama T. Postoperative long-term results in total correction of tetralogy of Fallot: hemodynamics and cardiac function. Ann Thorac Surg 1986; 41(4):413-418.

32. Kondo C, Nakazawa M, Kusakabe K, Momma K. Left ventricular dysfunction on exercise long-term after total repair of tetralogy of Fallot. Circulation 1995; 92(9 Suppl):II250-II255.

33. Niezen RA, Helbing WA, van der Wall EE, van der Geest RJ, Rebergen SA, de RA. Biventricular systolic function and mass studied with MR imaging in children with pulmonary regurgitation after repair for tetralogy of Fallot. Radiology 1996; 201(1):135-140.

34. Niezen RA, Helbing WA, van der Wall EE, van der Geest RJ, Vliegen HW, de RA. Left ventricular function in adults with mild pulmonary insufficiency late after Fallot repair. Heart 1999; 82(6):697-703.

35. Reduto LA, Berger HJ, Johnstone DE, Hellenbrand W, Wackers FJ, Whittemore R et al. Radionuclide assessment of right and left ventricular exercise reserve after total correction of tetralogy of Fallot. Am J Cardiol 1980; 45(5):1013-1018.

36. Tulevski II, Hirsch A, Dodge-Khatami A, Stoker J, van der Wall EE, Mulder BJ. Effect of pulmonary valve regurgitation on right ventricular function in patients with chronic right ventricular pressure overload. Am J Cardiol 2003; 92(1):113-116.

37. Oosterhof T, Tulevski II, Vliegen HW, Spijkerboer AM, Mulder BJ. Effects of volume and/or pressure overload secondary to congenital heart disease (tetralogy of fallot or pulmonary stenosis) on right ventricular function using cardiovascular magnetic resonance and B-type natriuretic peptide levels. Am J Cardiol 2006; 97(7):1051-1055.

38. Lange PE, Onnasch DG, Heintzen PH. Valvular pulmonary stenosis. Natural history and right ventricular function in infants and children. Eur Heart J 1985; 6(8):706-709.

39. Nugent EW, Freedom RM, Nora JJ, Ellison RC, Rowe RD, Nadas AS. Clinical course in pulmonary stenosis. Circulation 1977; 56(1 Suppl):I38-I47.

40. Evans CL, Matsuoka Y. The effect of various mechanical conditions on the gaseous metabolism and efficiency of the mammalian heart. J Physiol 1915; 49(5):378-405.

41. Sholler GF, Colan SD, Sanders SP. Effect of isolated right ventricular outflow obstruction on left ventricular function in infants. Am J Cardiol 1988; 62(10 Pt 1):778-784.

42. Louie EK, Rich S, Levitsky S, Brundage BH. Doppler echocardiographic demonstration of the differential effects of right ventricular pressure and volume overload on left ventricular geometry and filling. J Am Coll Cardiol 1992; 19(1):84-90.

43. Gaynor SL, Maniar HS, Bloch JB, Steendijk P, Moon MR. Right atrial and ventricular adaptation to chronic right ventricular pressure overload. Circulation 2005; 112(9 Suppl):I212-I218.

44. Lazar JM, Flores AR, Grandis DJ, Orie JE, Schulman DS. Effects of chronic right ventricular pressure overload on left ventricular diastolic function. Am J Cardiol 1993; 72(15):1179-1182.

45. Louie EK, Lin SS, Reynertson SI, Brundage BH, Levitsky S, Rich S. Pressure and volume loading of the right ventricle have opposite effects on left ventricular ejection fraction. Circulation 1995; 92(4):819-824.

46. Yemets IM, Williams WG, Webb GD, Harrison DA, McLaughlin PR, Trusler GA et al. Pulmonary valve replacement late after repair of tetralogy of Fallot. Ann Thorac Surg 1997; 64(2):526-530.

47. de Ruijter FT, Weenink I, Hitchcock FJ, Meijboom EJ, Bennink GB. Right ventricular dysfunction and pulmonary valve replacement after correction of tetralogy of Fallot. Ann Thorac Surg 2002; 73(6):1794-1800.

48. Discigil B, Dearani JA, Puga FJ, Schaff HV, Hagler DJ, Warnes CA et al. Late pulmonary valve replacement after repair of tetralogy of Fallot. J Thorac Cardiovasc Surg 2001; 121(2):344-351.

49. Warner KG, O'Brien PK, Rhodes J, Kaur A, Robinson DA, Payne DD. Expanding the indications for pulmonary valve replacement after repair of tetralogy of fallot. Ann Thorac Surg 2003; 76(4):1066-1071.

50. Vliegen HW, van SA, de RA, Roest AA, Schoof PH, Zwinderman AH et al. Magnetic resonance imaging to assess the hemodynamic effects of pulmonary valve replacement in adults late after repair of tetralogy of Fallot. Circulation 2002; 106(13):1703-1707.

51. Bove EL, Kavey RE, Byrum CJ, Sondheimer HM, Blackman MS, Thomas FD. Improved right ventricular function following late pulmonary valve replacement for residual pulmonary insufficiency or stenosis. J Thorac Cardiovasc Surg 1985; 90(1):50-55.

52. Therrien J, Siu SC, McLaughlin PR, Liu PP, Williams WG, Webb GD. Pulmonary valve replacement in adults late after repair of tetralogy of fallot: are we operating too late? J Am Coll Cardiol 2000; 36(5):1670-1675.

53. Warner KG, O'Brien PK, Rhodes J, Kaur A, Robinson DA, Payne DD. Expanding the indications for pulmonary valve replacement after repair of tetralogy of fallot. Ann Thorac Surg 2003; 76(4):1066-1071.

54. Ensing GJ, Hagler DJ, Seward JB, Julsrud PR, Mair DD. Caveats of balloon dilation of conduits and conduit valves. J Am Coll Cardiol 1989; 14(2):397-400.

55. Zeevi B, Keane JF, Perry SB, Lock JE. Balloon dilation of postoperative right ventricular outflow obstructions. J Am Coll Cardiol 1989; 14(2):401-408.

56. Powell AJ, Lock JE, Keane JF, Perry SB. Prolongation of RV-PA conduit life span by percutaneous stent implantation. Intermediate-term results. Circulation 1995; 92(11):3282-3288.

57. Ovaert C, Caldarone CA, McCrindle BW, Nykanen D, Freedom RM, Coles JG et al. Endovascular stent implantation for the management of postoperative right ventricular outflow tract obstruction: clinical efficacy. J Thorac Cardiovasc Surg 1999; 118(5):886-893.

58. Sugiyama H, Williams W, Benson LN. Implantation of endovascular stents for the obstructive right ventricular outflow tract. Heart 2005; 91(8):1058-1063.

59. Peng LF, McElhinney DB, Nugent AW, Powell AJ, Marshall AC, Bacha EA et al. Endovascular stenting of obstructed right ventricle-to-pulmonary artery conduits: a 15-year experience. Circulation 2006; 113(22):2598-2605.

60. Bonhoeffer P, Boudjemline Y, Saliba Z, Merckx J, Aggoun Y, Bonnet D et al. Percutaneous replacement of pulmonary valve in a right-ventricle to pulmonary-

artery prosthetic conduit with valve dysfunction. Lancet 2000; 356(9239):1403-1405.

61. Hufnagel CA, Harvey WP, Rabil PJ, McDermott TF. Surgical correction of aortic insufficiency. Surgery 1954; 35(5):673-683.

62. Pavcnik D, Wright KC, Wallace S. Development and initial experimental evaluation of a prosthetic aortic valve for transcatheter placement. Work in progress. Radiology 1992; 183(1):151-154.

63. Andersen HR, Knudsen LL, Hasenkam JM. Transluminal implantation of artificial heart valves. Description of a new expandable aortic valve and initial results with implantation by catheter technique in closed chest pigs. Eur Heart J 1992; 13(5):704-708.

64. Bonhoeffer P, Boudjemline Y, Saliba Z, Hausse AO, Aggoun Y, Bonnet D et al. Transcatheter implantation of a bovine valve in pulmonary position: a lamb study. Circulation 2000; 102(7):813-816.

65. Cribier A, Eltchaninoff H, Bash A, Borenstein N, Tron C, Bauer F et al. Percutaneous transcatheter implantation of an aortic valve prosthesis for calcific aortic stenosis: first human case description. Circulation 2002; 106(24):3006-3008.

66. Boudjemline Y, Bonhoeffer P. Steps toward percutaneous aortic valve replacement. Circulation 2002; 105(6):775-778.

67. Boudjemline Y, Agnoletti G, Bonnet D, Behr L, Borenstein N, Sidi D et al. Steps toward the percutaneous replacement of atrioventricular valves an experimental study. J Am Coll Cardiol 2005; 46(2):360-365.

68. Khambadkone S, Coats L, Taylor A, Boudjemline Y, Derrick G, Tsang V et al. Percutaneous pulmonary valve implantation in humans: results in 59 consecutive patients. Circulation 2005; 112(8):1189-1197.

69. Grube E, Laborde JC, Gerckens U, Felderhoff T, Sauren B, Buellesfeld L et al. Percutaneous implantation of the CoreValve self-expanding valve prosthesis in high-risk patients with aortic valve disease: the Siegburg first-in-man study. Circulation 2006; 114(15):1616-1624.

70. Webb JG, Chandavimol M, Thompson CR, Ricci DR, Carere RG, Munt BI et al. Percutaneous aortic valve implantation retrograde from the femoral artery. Circulation 2006; 113(6):842-850.

71. Grube E, Schuler G, Buellesfeld L, Gerckens U, Linke A, Wenaweser P et al. Percutaneous aortic valve replacement for severe aortic stenosis in high-risk patients using the second- and current third-generation self-expanding CoreValve prosthesis: device success and 30-day clinical outcome. J Am Coll Cardiol 2007; 50(1):69-76.

72. Webb JG, Pasupati S, Humphries K, Thompson C, Altwegg L, Moss R et al. Percutaneous transarterial aortic valve replacement in selected high-risk patients with aortic stenosis. Circulation 2007; 116(7):755-763.

73. Cheatham JP. Stenting of coarctation of the aorta. Catheter Cardiovasc Interv 2001; 54(1):112-125.

74. Mertens L. Deciphering the mystery of the leaky pulmonary valve in a new era of interventional cardiology. Eur Heart J 2007; 28(15):1793-1794.

75. Bonhoeffer P, Boudjemline Y, Qureshi SA, Le BJ, Iserin L, Acar P et al. Percutaneous insertion of the pulmonary valve. J Am Coll Cardiol 2002; 39(10):1664-1669.

76. Coats L, Khambadkone S, Derrick G, Sridharan S, Schievano S, Mist B et al. Physiological and clinical consequences of relief of right ventricular outflow tract obstruction late after repair of congenital heart defects. Circulation 2006; 113(17):2037-2044.

77. Coats L, Khambadkone S, Derrick G, Hughes M, Jones R, Mist B et al. Physiological consequences of percutaneous pulmonary valve implantation: the different behaviour of volume- and pressure-overloaded ventricles. Eur Heart J 2007; 28(15):1886-1893.

78. Sridharan S, Coats L, Khambadkone S, Taylor AM, Bonhoeffer P. Images in cardiovascular medicine. Transcatheter right ventricular outflow tract intervention: the risk to the coronary circulation. Circulation 2006; 113(25):e934-e935.

79. Nordmeyer J, Khambadkone S, Coats L, Schievano S, Lurz P, Parenzan G et al. Risk stratification, systematic classification, and anticipatory management strategies for stent fracture after percutaneous pulmonary valve implantation. Circulation 2007; 115(11):1392-1397.

80. Boudjemline Y, Agnoletti G, Bonnet D, Sidi D, Bonhoeffer P. Percutaneous pulmonary valve replacement in a large right ventricular outflow tract: an experimental study. J Am Coll Cardiol 2004; 43(6):1082-1087.

81. Boudjemline Y, Schievano S, Bonnet C, Coats L, Agnoletti G, Khambadkone S et al. Off-pump replacement of the pulmonary valve in large right ventricular outflow tracts: a hybrid approach. J Thorac Cardiovasc Surg 2005; 129(4):831-837.

82. Boudjemline Y, Laborde F, Pineau E, Mollet A, Abadir S, Borenstein N et al. Expandable right ventricular-to-pulmonary artery conduit: an animal study. Pediatr Res 2006; 59(6):773-777.

83. Bloch F. The Principle of Nuclear Induction. Science 1953; 118(3068):425-430.

84. Bloch F. Nuclear Induction. Physica 1951; 17(3-4):272-281.

85. Bloch F, Hansen WW, Packard M. The Nuclear Induction Experiment. Physical Review 1946; 70(7-8):474-485.

86. Bloch F. Nuclear Induction. Physical Review 1946; 70(7-8):460-474.

87. Bloch F, Hansen WW, Packard M. Nuclear Induction. Physical Review 1946; 69(11-1):680.

88. Purcell EM, Torrey HC, Pound RV. Resonance Absorption by Nuclear Magnetic Moments in A Solid. Physical Review 1946; 69(1-2):37-38.

89. Purcell EM, Bloembergen N, Pound RV. Resonance Absorption by Nuclear Magnetic Moments in A Single Crystal of Caf2. Physical Review 1946; 70(11-1):988.

90. Purcell EM, Pound RV, Bloembergen N. Nuclear Magnetic Resonance Absorption in Hydrogen Gas. Physical Review 1946; 70(11-1):986-987.

91. Bogaert J, Dymarkowsky S, Taylor AM. Clinical cardiac MRI. Heidelberg: Springer-Verlag ed. 2005.

92. Anderson RH, Razavi R, Taylor AM. Cardiac anatomy revisited. J Anat 2004; 205(3):159-177.

93. Higgins CB, Byrd BF, III, Farmer DW, Osaki L, Silverman NH, Cheitlin MD. Magnetic resonance imaging in patients with congenital heart disease. Circulation 1984; 70(5):851-860.

94. Fletcher BD, Jacobstein MD, Nelson AD, Riemenschneider TA, Alfidi RJ. Gated magnetic resonance imaging of congenital cardiac malformations. Radiology 1984; 150(1):137-140.

95. Carr JC, Finn JP. MR imaging of the thoracic aorta. Magn Reson Imaging Clin N Am 2003; 11(1):135-148.

96. Greenberg SB, Crisci KL, Koenig P, Robinson B, Anisman P, Russo P. Magnetic resonance imaging compared with echocardiography in the evaluation of pulmonary artery abnormalities in children with tetralogy of Fallot following palliative and corrective surgery. Pediatr Radiol 1997; 27(12):932-935.

97. Martinez JE, Mohiaddin RH, Kilner PJ, Khaw K, Rees S, Somerville J et al. Obstruction in extracardiac ventriculopulmonary conduits: value of nuclear magnetic resonance imaging with velocity mapping and Doppler echocardiography. J Am Coll Cardiol 1992; 20(2):338-344.

98. Sampson C, Kilner PJ, Hirsch R, Rees RS, Somerville J, Underwood SR. Venoatrial pathways after the Mustard operation for transposition of the great arteries: anatomic and functional MR imaging. Radiology 1994; 193(1):211-217.

99. Shellock FG, Shellock VJ. Metallic stents: evaluation of MR imaging safety. Am J Roentgenol 1999; 173(3):543-547.

100. Taylor AM. Assessment of the pulmonary valve with magnetic resonance imaging. In: Hijazi ZM, Bonhoeffer P, Feldman T, Ruiz CE, editors. Transcatheter Valve Repair. Oxon: Taylor and Francis; 2006. 359-368.

101. Zur Y, Wood ML, Neuringer LJ. Motion-insensitive, steady-state free precession imaging. Magn Reson Med 1990; 16(3):444-459.

102. Pereles FS, Kapoor V, Carr JC, Simonetti OP, Krupinski EA, Baskaran V et al. Usefulness of segmented trueFISP cardiac pulse sequence in evaluation of congenital and acquired adult cardiac abnormalities. Am J Roentgenol 2001; 177(5):1155-1160.

103. Barkhausen J, Ruehm SG, Goyen M, Buck T, Laub G, Debatin JF. MR evaluation of ventricular function: true fast imaging with steady-state precession versus fast low-angle shot cine MR imaging: feasibility study. Radiology 2001; 219(1):264-269.

104. Muthurangu V, Taylor AM, Hegde SR, Johnson R, Tulloh R, Simpson JM et al. Cardiac magnetic resonance imaging after stage I Norwood operation for hypoplastic left heart syndrome. Circulation 2005; 112(21):3256-3263.

105. Razavi RS, Hill DL, Muthurangu V, Miquel ME, Taylor AM, Kozerke S et al. Three-dimensional magnetic resonance imaging of congenital cardiac anomalies. Cardiol Young 2003; 13(5):461-465.

106. Sorensen TS, Korperich H, Greil GF, Eichhorn J, Barth P, Meyer H et al. Operator-independent isotropic three-dimensional magnetic resonance imaging for morphology in congenital heart disease: a validation study. Circulation 2004; 110(2):163-169.

107. Miquel ME, Hill DL, Baker EJ, Qureshi SA, Simon RD, Keevil SF et al. Three- and four-dimensional reconstruction of intra-cardiac anatomy from two-dimensional magnetic resonance images. Int J Cardiovasc Imaging 2003; 19(3):239-254.

108. Evans AJ, Blinder RA, Herfkens RJ, Spritzer CE, Kuethe DO, Fram EK et al. Effects of turbulence on signal intensity in gradient echo images. Invest Radiol 1988; 23(7):512-518.

109. Sechtem U, Pflugfelder PW, White RD, Gould RG, Holt W, Lipton MJ et al. Cine MR imaging: potential for the evaluation of cardiovascular function. Am J Roentgenol 1987; 148(2):239-246.

110. Nayler GL, Firmin DN, Longmore DB. Blood flow imaging by cine magnetic resonance. J Comput Assist Tomogr 1986; 10(5):715-722.

111. Underwood SR, Firmin DN, Klipstein RH, Rees RS, Longmore DB. Magnetic resonance velocity mapping: clinical application of a new technique. Br Heart J 1987; 57(5):404-412.

112. Bogren HG, Klipstein RH, Firmin DN, Mohiaddin RH, Underwood SR, Rees RS et al. Quantitation of antegrade and retrograde blood flow in the human aorta by magnetic resonance velocity mapping. Am Heart J 1989; 117(6):1214-1222.

113. Firmin DN, Nayler GL, Klipstein RH, Underwood SR, Rees RS, Longmore DB. In vivo validation of MR velocity imaging. J Comput Assist Tomogr 1987; 11(5):751-756.

114. Meier D, Maier S, Bosiger P. Quantitative flow measurements on phantoms and on blood vessels with MR. Magn Reson Med 1988; 8(1):25-34.

115. Sechtem U, Pflugfelder PW, Cassidy MM, White RD, Cheitlin MD, Schiller NB et al. Mitral or aortic regurgitation: quantification of regurgitant volumes with cine MR imaging. Radiology 1988; 167(2):425-430.

116. Korperich H, Gieseke J, Barth P, Hoogeveen R, Esdorn H, Peterschroder A et al. Flow volume and shunt quantification in pediatric congenital heart disease by real-time magnetic resonance velocity mapping: a validation study. Circulation 2004; 109(16):1987-1993.

117. Simpson IA, Maciel BC, Moises V, Shandas R, Elias W, Valdes-Cruz L et al. Cine magnetic resonance imaging and color Doppler flow mapping displays of flow velocity, spatial acceleration, and jet formation: a comparative in vitro study. Am Heart J 1993; 126(5):1165-1174.

118. Kilner PJ, Firmin DN, Rees RS, Martinez J, Pennell DJ, Mohiaddin RH et al. Valve and great vessel stenosis: assessment with MR jet velocity mapping. Radiology 1991; 178(1):229-235.

119. Kilner PJ, Manzara CC, Mohiaddin RH, Pennell DJ, Sutton MG, Firmin DN et al. Magnetic resonance jet velocity mapping in mitral and aortic valve stenosis. Circulation 1993; 87(4):1239-1248.

120. Zienkiewicz C. The birth of the finite element method and of computational mechanics. International Journal for Numerical Methods in Engineering 2004; 60(1):3-10.

121. Zienkiewicz 0C, Taylor RL, Zhu JZ. The Finite Element Method - Its Basis and Fundamentals. 6th ed. Elsevier; 2005.

122. Bathe KJ. Finite element procedures. Upper Saddle River, New Jersey, Prentice Hall; 1996.

123. Stuhne GR, Steinman DA. Finite-element modeling of the hemodynamics of stented aneurysms. J Biomech Eng 2004; 126(3):382-387.

124. Hose DR, Narracott AJ, Griffiths B, Mahmood S, Gunn J, Sweeney D et al. A thermal analogy for modelling drug elution from cardiovascular stents. Comput Methods Biomech Biomed Engin 2004; 7(5):257-264.

125. Savage P, O'Donnell BP, McHugh PE, Murphy BP, Quinn DF. Coronary stent strut size dependent stress-strain response investigated using micromechanical finite element models. Ann Biomed Eng 2004; 32(2):202-211.

126. Beasley MP, Conrad SA. Analysis of pressure losses in the hemodialysis graft vascular circuit using finite element analysis. Conf Proc IEEE Eng Med Biol Soc 2007; 1:998-1001.

127. Malota Z, Nawrat Z, Kostka P. Computer and physical modeling of blood circulation pump support for a new field of application in palliative surgery. Int J Artif Organs 2007; 30(12):1068-1074.

128. Cacho F, Doblare M, Holzapfel GA. A procedure to simulate coronary artery bypass graft surgery. Med Biol Eng Comput 2007; 45(9):819-827.

129. Sacks MS, Mirnajafi A, Sun W, Schmidt P. Bioprosthetic heart valve heterograft biomaterials: structure, mechanical behavior and computational simulation. Expert Rev Med Devices 2006; 3(6):817-834.

130. Kim H, Chandran KB, Sacks MS, Lu J. An experimentally derived stress resultant shell model for heart valve dynamic simulations. Ann Biomed Eng 2007; 35(1):30-44.

131. Sun W, Abad A, Sacks MS. Simulated bioprosthetic heart valve deformation under quasi-static loading. J Biomech Eng 2005; 127(6):905-914.

132. Nicosia MA, Cochran RP, Einstein DR, Rutland CJ, Kunzelman KS. A coupled fluid-structure finite element model of the aortic valve and root. J Heart Valve Dis 2003; 12(6):781-789.

133. Benard N, Perrault R, Coisne D. Blood flow in stented coronary artery: numerical fluid dynamics analysis. Conf Proc IEEE Eng Med Biol Soc 2004; 5:3800-3803.

134. Wang W, Yang D, Qi M. Finite element analysis of the expansion behavior of coronary stents. Sheng Wu Yi Xue Gong Cheng Xue Za Zhi 2006; 23(6):1258-62, 1266.

135. Wang W, Yang D, Qi M. Finite element analysis of the mechanical property of the resistance to compressing of the coronary stent. Sheng Wu Yi Xue Gong Cheng Xue Za Zhi 2006; 23(5):1008-1012.

136. Migliavacca F, Petrini L, Montanari V, Quagliana I, Auricchio F, Dubini G. A predictive study of the mechanical behaviour of coronary stents by çomputer modelling. Med Eng Phys 2005; 27(1):13-18.

137. Migliavacca F, Petrini L, Massarotti P, Schievano S, Auricchio F, Dubini G. Stainless and shape memory alloy coronary stents: a computational study on the interaction with the vascular wall. Biomech Model Mechanobiol 2004; 2(4):205-217.

138. Petrini L, Migliavacca F, Massarotti P, Schievano S, Dubini G, Auricchio F. Computational studies of shape memory alloy behavior in biomedical applications. J Biomech Eng 2005; 127(4):716-725.

139. Petrini L, Migliavacca F, Auricchio F, Dubini G. Numerical investigation of the intravascular coronary stent flexibility. J Biomech 2004; 37(4):495-501.

140. Lally C, Dolan F, Prendergast PJ. Cardiovascular stent design and vessel stresses: a finite element analysis. J Biomech 2005; 38(8):1574-1581.

141. Prendergast PJ, Lally C, Daly S, Reid AJ, Lee TC, Quinn D et al. Analysis of prolapse in cardiovascular stents: a constitutive equation for vascular tissue and finite-element modelling. J Biomech Eng 2003; 125(5):692-699.

142. FDA. Draft Replacement Heart Valve Guidance. 1994.

143. FDA. Draft Guidance for the Submission of Research and Marketing Applications for Interventional Cardiology Devices: PTCA, Catheters, Atherectomy Catheters, Lasers, intravascular Stents. 1995.

144. Abel DB, Dehdashtian MM, Rodger ST, Smith AC, Smith LJ, Waninger MS. Evolution and future of preclinical testing for endovascular grafts. J Endovasc Ther 2006; 13(5):649-659.

145. Carvalho JS, Shinebourne EA, Busst C, Rigby ML, Redington AN. Exercise capacity after complete repair of tetralogy of Fallot: deleterious effects of residual pulmonary regurgitation. Br Heart J 1992; 67(6):470-473.

146. Davlouros PA, Kilner PJ, Hornung TS, Li W, Francis JM, Moon JC et al. Right ventricular function in adults with repaired tetralogy of Fallot assessed with cardiovascular magnetic resonance imaging: detrimental role of right ventricular outflow aneurysms or akinesia and adverse right-to-left ventricular interaction. J Am Coll Cardiol 2002; 40(11):2044-2052.

147. Uebing A, Fischer G, Bethge M, Scheewe J, Schmiel F, Stieh J et al. Influence of the pulmonary annulus diameter on pulmonary regurgitation and right ventricular pressure load after repair of tetralogy of Fallot. Heart 2002; 88(5):510-514.

148. Petzold R, Zeilhofer HF, Kalender WA. Rapid protyping technology in medicine-basics and applications. Comput Med Imaging Graph 1999; 23(5):277-284.

149. Zollikofer CPE, Deleon MSP. Tools for Rapid Prototyping in the Biosciences. Ieee Computer Graphics and Applications 1995; 15(6):48-55.

150. Friedman MH, Kuban BD, Schmalbrock P, Smith K, Altan T. Fabrication of vascular replicas from magnetic resonance images. J Biomech Eng 1995; 117(3):364-366.

151. Chong CK, Rowe CS, Sivanesan S, Rattray A, Black RA, Shortland AP et al. Computer aided design and fabrication of models for in vitro studies of vascular fluid dynamics. Proc Inst Mech Eng [H] 1999; 213(1):1-4.

152. Yedavalli RV, Loth F, Yardimci A, Pritchard WF, Oshinski JN, Sadler L et al. Construction of a physical model of the human carotid artery based upon in vivo magnetic resonance images. J Biomech Eng 2001; 123(4):372-376.

153. Bale-Glickman J, Selby K, Saloner D, Savas O. Experimental flow studies in exact-replica phantoms of atherosclerotic carotid bifurcations under steady input conditions. J Biomech Eng 2003; 125(1):38-48.

154. de ZD, Pekkan K, Kitajima H, Frakes D, Yoganathan AP. Single-step stereolithography of complex anatomical models for optical flow measurements. J Biomech Eng 2005; 127(1):204-207.

155. Wicker R, Cortez M, Medina F, Palafox G, Elkins C. Manufacturing complex compliant cardiovascular system models for in vitro hemodynamic experimentation using CT and MRI data and rapid prototyping technologies. Proc.ASME Bioengineering Conference , 469-470. 2001.

156. Winder RJ, Sun Z, Kelly B, Ellis PK, Hirst D. Abdominal aortic aneurysm and stent graft phantom manufactured by medical rapid prototyping. J Med Eng Technol 2002; 26(2):75-78.

157. Lermusiaux P, Leroux C, Tasse JC, Castellani L, Martinez R. Aortic aneurysm: construction of a life-size model by rapid prototyping. Ann Vasc Surg 2001; 15(2):131-135.

158. Elsaid K, Hosni Y, Elsaid H, Vick G.W. Biomodeling of congenital cardiovascular malformations from MRI: lessons learned. SME Tech.Paper. 2004.

159. Pentecost JO, Sahn DJ, Thornburg BL, Gharib M, Baptista A, Thornburg KL. Graphical and stereolithographic models of the developing human heart lumen. Comput Med Imaging Graph 2001; 25(6):459-463.

160. Medina F, Wicker RB. Geometric modeling of the human aorta for rapid prototyping using patient data and commercial software packages. Proc.ASME Summer Bioengineering Conference , 421-422. 2003.

161. Pili P, Murgia F, Pusceddu G, Franzoni G, Tuveri M. Physical human lumen carotid reconstruction: life-size models by rapid prototyping. Proc.SPIE Int.Soc.Optical Engineering 5031, 504-514. 2003.

162. Yan X, Gu P. A review of rapid prototyping technologies and systems. Computer-Aided Design 1996; 28(4):307-318.

163. Salako F, Aubin CE, Fortin C, Labelle H. Feasibility study of patient-specific surgical templates for the fixation of pedicle screws. Stud Health Technol Inform 2002; 88:419-422.

164. Cheah CM, Chua CK, Tan KH. Integration of laser surface digitizing with CAD/CAM techniques for developing facial prostheses. Part 2: Development of molding techniques for casting prosthetic parts. Int J Prosthodont 2003; 16(5):543-548.

165. Wagner JD, Baack B, Brown GA, Kelly J. Rapid 3-dimensional prototyping for surgical repair of maxillofacial fractures: a technical note. J Oral Maxillofac Surg 2004; 62(7):898-901.

166. Muller A, Krishnan KG, Uhl E, Mast G. The application of rapid prototyping techniques in cranial reconstruction and preoperative planning in neurosurgery. J Craniofac Surg 2003; 14(6):899-914.

167. Knox K, Kerber CW, Singel SA, Bailey MJ, Imbesi SG. Rapid prototyping to create vascular replicas from CT scan data: making tools to teach, rehearse, and choose treatment strategies. Catheter Cardiovasc Interv 2005; 65(1):47-53.

168. Boudjemline Y, Bonnet D, Sidi D, Bonhoeffer P. Percutaneous implantation of a biological valve in the aorta to treat aortic valve insufficiency - a sheep study. Med Sci Monit 2002; 8(4):BR113-BR116.

169. Boudjemline Y, Bonhoeffer P. Images in cardiovascular medicine. Percutaneous aortic valve replacement in animals. Circulation 2004; 109(10):e161.

170. Murugan SJ, Dickinson DF, Gibbs JL. Images in cardiology. Complete fracture of a right ventricle to pulmonary artery shunt. Heart 2005; 91(11):1441.

171. Scheinert D, Scheinert S, Sax J, Piorkowski C, Braunlich S, Ulrich M et al. Prevalence and clinical impact of stent fractures after femoropopliteal stenting. J Am Coll Cardiol 2005; 45(2):312-315.

172. Knirsch W, Haas NA, Lewin MA, Uhlemann F. Longitudinal stent fracture 11 months after implantation in the left pulmonary artery and successful management by a stent-in-stent maneuver. Catheter Cardiovasc Interv 2003; 58(1):116-118.

173. O'Laughlin MP, Slack MC, Grifka RG, Perry SB, Lock JE, Mullins CE. Implantation and intermediate-term follow-up of stents in congenital heart disease. Circulation 1993; 88(2):605-614.

174. Zarins CK, Arko FR, Crabtree T, Bloch DA, Ouriel K, Allen RC et al. Explant analysis of AneuRx stent grafts: relationship between structural findings and clinical outcome. J Vasc Surg 2004; 40(1):1-11.

175. Vaidyanathan R, Dunand DC, Ramamurty U. Fatigue crack-growth in shape-memory NiTi and NiTi-TiC composites. Materials Science and Engineering A-Structural Materials Properties Microstructure and Processing 2000; 289(1-2):208-216.

176. Schmidt W, P.Behrens, D.Behrend, K.-P.Schmitz. Measurement technology for the determination of mechanical properties of coronary stents according to the European Standard prEN 12006-3. Progress in Biomedical Research 4 1999; 1:45-51.

177. K.-P.Schmitz, D.Behrend, P.Behrens, Schmidt W. Comparative study of different stent designs. Progress in Biomedical Research 4 1999; 1:52-58.

178. Marrey RV, Burgermeister R, Grishaber RB, Ritchie RO. Fatigue and life prediction for cobalt-chromium stents: A fracture mechanics analysis. Biomaterials 2006; 27(9):1988-2000.

179. Robertson SW, Ritchie RO. A fracture-mechanics-based approach to fracture control in biomedical devices manufactured from superelastic Nitinol tube. J Biomed Mater Res B Appl Biomater 2007.

180. Ritchie RO. Fatigue and fracture of pyrolytic carbon: a damage- tolerant approach to structural integrity and life prediction in "ceramic" heart valve prostheses. J Heart Valve Dis 1996; 5 Suppl 1:S9-31.

181. Ritchie RO, Lubock P. Fatigue life estimation procedures for the endurance of a cardiac valve prosthesis: stress/life and damage-tolerant analyses. J Biomech Eng 1986; 108(2):153-160.

182. Lemmon JD. Valve testing: durability and beyond. In: Hijazi ZM, Bonhoeffer P, Feldman T, Ruiz CE, editors. Transcatheter Valve Repair. Oxon: Taylor and Francis; 2006. 359-368.

183. Stephens RI, Fatemi A, Stephens RR, Fuchs HO. Metal Fatigue in Engineering. New York: John Wiley and Sons 2001; 74-79.

184. Dumoulin C, Cochelin B. Mechanical behaviour modelling of balloon-expandable stents. J Biomech 2000; 33(11):1461-1470.

185. Poncin P, Proft J. Stent tubing: understanding the desired attributes. Proceedings of the Materials & Processes for Medical Devices Conference 2003.

186. Petrini L, Migliavacca F, Auricchio F, Dubini G. Numerical investigation of the intravascular coronary stent flexibility. J Biomech 2004; 37(4):495-501.

187. Wang WQ, Liang DK, Yang DZ, Qi M. Analysis of the transient expansion behavior and design optimization of coronary stents by finite element method. J Biomech 2006; 39(1):21-32.

188. ABAQUS 6.4. Prescribed Conditions, Constrains and Interactions. Analysis User's Manual. 2004.

189. Ratib K, Doshi SN, Townend JN. Double-stenting of an ostial left main-stem lesion for elastic recoil. Int J Cardiol 2005; 102(2):357-358.

190. Schmidt W, Andresen R, Behrens P, Schmitz KP. Characteristic mechanical properties of balloon-expandable peripheral stent systems. Rofo 2002; 174(11):1430-1437.

191. Grenacher L, Deutsch J, Lubienski A, Richter GM. Resistance to hoop stress in balloon expandable stents: evaluation in an ex vivo model. Invest Radiol 2003; 38(2):65-72.

192. Rieu R, Barragan P, Masson C, Fuseri J, Garitey V, Silvestri M et al. Radial force of coronary stents: a comparative analysis. Catheter Cardiovasc Interv 1999; 46(3):380-391.

193. Dyet JF, Watts WG, Ettles DF, Nicholson AA. Mechanical properties of metallic stents: how do these properties influence the choice of stent for specific lesions? Cardiovasc Intervent Radiol 2000; 23(1):47-54.

194. Webster JG. Medical Instrumentation - Application and Design. Houghton Mifflin Company; 1992.

195. Schueler BA, Hu X. Correction of image intensifier distortion for 3-D X-ray angiography. Medical Imaging 1995; 2432:272-279.

196. Shechter G, Shechter B, Resar JR, Beyar R. Prospective motion correction of X-ray images for coronary interventions. IEEE Trans Med Imaging 2005; 24(4):441-450.

197. Shechter G, Devernay F, Coste-Maniere E, Quyyumi A, McVeigh ER. Three-dimensional motion tracking of coronary arteries in biplane cineangiograms. IEEE Trans Med Imaging 2003; 22(4):493-503.

198. Henri Veisterä, Jyrki Lötjönen. Reconstructing 3D Boundary Element Heart Models from 2D Biplane Fluoroscopy. In: T.Katila et al. Springer-Verlag Berlin Heidelberg; 2001; 17-23.

199. Tsapaki V, Kottou S, Kollaros N, Dafnomili P, Kyriakidis Z, Neofotistou V. Dose performance evaluation of a charge coupled device and a flat-panel digital fluoroscopy system recently installed in an interventional cardiology laboratory. Radiat Prot Dosimetry 2004; 111(3):297-304.

200. Tsapaki V, Kottou S, Kollaros N, Kyriakidis Z, Neofotistou V. Comparison of a CCD and a flat-panel digital system in an Interventional Cardiology Laboratory. Radiat Prot Dosimetry 2005; 117(1-3):93-96.

201. Tsapaki V, Kottou S, Kollaros N, Dafnomili P, Koutelou M, Vano E et al. Comparison of a conventional and a flat-panel digital system in interventional cardiology procedures. Br J Radiol 2004; 77(919):562-567.

202. Vano E, Geiger B, Schreiner A, Back C, Beissel J. Dynamic flat panel detector versus image intensifier in cardiac imaging: dose and image quality. Phys Med Biol 2005; 50(23):5731-5742.

203. Fajadet J, Marco J, Bertel O, E.Straumann. Innovations in flat-detector cardiac angiography. MEDICAMUNDI 3 A.D.; 47(2):56-60.

204. Shechter G, Shechter B, Resar JR, Beyar R. Prospective motion correction of X-ray images for coronary interventions. IEEE Trans Med Imaging 2005; 24(4):441-450.

205. Yacoub MH, Kiffle CF. Homograft Heart Valves. Roy.Soc.Med. 1970.

206. Vesely I, Casarotto DC, Gerosa G. Mechanics of cryopreserved aortic and pulmonary homografts. J Heart Valve Dis 2000; 9(1):27-37.

207. Gournier JP, Adham M, Favre JP, Raba M, Bancel B, Lepetit JC et al. Cryopreserved arterial homografts: preliminary study. Ann Vasc Surg 1993; 7(6):503-511.

208. Adham M, Gournier JP, Favre JP, De La RE, Ducerf C, Baulieux J et al. Mechanical characteristics of fresh and frozen human descending thoracic aorta. J Surg Res 1996; 64(1):32-34.

209. Langerak SE, Groenink M, van der Wall EE, Wassenaar C, Vanbavel E, van Baal MC et al. Impact of current cryopreservation procedures on mechanical and functional properties of human aortic homografts. Transpl Int 2001; 14(4):248-255.

210. Groenink M, Langerak SE, Vanbavel E, van der Wall EE, Mulder BJ, van der Wal AC et al. The influence of aging and aortic stiffness on permanent dilation and breaking stress of the thoracic descending aorta. Cardiovasc Res 1999; 43(2):471-480.

211. Bia D, Pessana F, Armentano R, Perez H, Graf S, Zocalo Y et al. Cryopreservation procedure does not modify human carotid homografts mechanical properties: an isobaric and dynamic analysis. Cell Tissue Bank 2006; 7(3):183-194.

212. Bia D, Zocalo Y, Pessana F, Armentano R, Perez H, Saldias M et al. Differential functional coupling between human saphenous cryoallografts and arteries: importance of the arterial type and the biomechanical parameter evaluated. Artif Organs 2007; 31(11):809-818.

213. Pukacki F, Jankowski T, Gabriel M, Oszkinis G, Krasinski Z, Zapalski S. The mechanical properties of fresh and cryopreserved arterial homografts. Eur J Vasc Endovasc Surg 2000; 20(1):21-24.

214. Barras CD, Myers KA. Nitinol - its use in vascular surgery and other applications. Eur J Vasc Endovasc Surg 2000; 19(6):564-569.

215. Trepanier C, Leung TK, Tabrizian M, Yahia LH, Bienvenu JG, Tanguay JF et al. Preliminary investigation of the effects of surface treatments on biological response to shape memory NiTi stents. J Biomed Mater Res 1999; 48(2):165-171.

216. Virmani R. Self-expanding stent deployment strategies may be the key to reducing in-stent restenosis. Catheter Cardiovasc Interv 2002; 56(4):487-488.

217. Carter AJ, Scott D, Laird JR, Bailey L, Kovach JA, Hoopes TG et al. Progressive vascular remodeling and reduced neointimal formation after placement of a thermoelastic self-expanding nitinol stent in an experimental model. Cathet Cardiovasc Diagn 1998; 44(2):193-201.

218. Pelton AR, Stockel D, Duerig TW. Medical uses of nitinol. Shape Memory Materials 2000; 327-3:63-70.

219. Duerig TW, Pelton AR, Stockel D. The utility of superelasticity in medicine. Bio-Medical Materials and Engineering 1996; 6(4):255-266.

220. Bruckheimer E, Judelman AG, Bruckheimer SD, Tavori I, Naor G, Katzen BT. In vitro evaluation of a retrievable low-profile nitinol vena cava filter. J Vasc Interv Radiol 2003; 14(4):469-474.

221. Leask RL, Johnston KW, Ojha M. In vitro hemodynamic evaluation of a Simon nitinol vena cava filter: possible explanation of IVC occlusion. J Vasc Interv Radiol 2001; 12(5):613-618.

222. Simon M, Rabkin DJ, Kleshinski S, Kim D, Ransil BJ. Comparative evaluation of clinically available inferior vena cava filters with an in vitro physiologic simulation of the vena cava. Radiology 1993; 189(3):769-774.

223. Kong H, Gu X, Titus JL, Kim TH, Urness M, Han YM et al. Creation of an intra-atrial communication with a new Amplatzer shunt prosthesis: preliminary results in a swine model. Catheter Cardiovasc Interv 2002; 56(2):267-271.

224. Walsh KP, Maadi IM. The Amplatzer septal occluder. Cardiol Young 2000; 10(5):493-501.

225. Smits M, Huibregtse K, Tytgat G. Results of the new nitinol self-expandable stents for distal biliary structures. Endoscopy 1995; 27(7):505-508.

226. Tyagi S, Singh S, Mukhopadhyay S, Kaul UA. Self- and balloon-expandable stent implantation for severe native coarctation of aorta in adults. Am Heart J 2003; 146(5):920-928.

227. Dai KR, Hou XK, Sun YH, Tang RG, Qiu SJ, Ni C. Treatment of intra-articular fractures with shape memory compression staples. Injury 1993; 24(10):651-655.

228. Sanders JO, Sanders AE, More R, Ashman RB. A preliminary investigation of shape memory alloys in the surgical correction of scoliosis. Spine 1993; 18(12):1640-1646.

229. Wever DJ, Elstrodt JA, Veldhuizen AG, Horn JR. Scoliosis correction with shape-memory metal: results of an experimental study. Eur Spine J 2002; 11(2):100-106.

230. Ryhanen J, Niemela E, Kaarela O, Raatikainen T. Stabilization of acute, complete acromioclavicular joint dislocations with a new C hook implant. J Shoulder Elbow Surg 2003; 12(5):442-445.

231. Kourambas J, Delvecchio FC, Munver R, Preminger GM. Nitinol stone retrieval-assisted ureteroscopic management of lower pole renal calculi. Urology 2000; 56(6):935-939.

232. Song HY, Shin JH, Lim JO, Kim TH, Lee GH, Lee SK. Use of a newly designed multifunctional coil catheter for stent placement in the upper gastrointestinal tract. J Vasc Interv Radiol 2004; 15(4):369-373.

233. Sundaram CP, Ono Y, Landman J, Rehman J, Clayman RV. Hydrophilic guide wire technique to facilitate organ entrapment using a laparoscopic sack during laparoscopy. J Urol 2002; 167(3):1376-1377.

234. Mollet A, Basquin A, Stos B, Boudjemline Y. Off-pump replacement of the pulmonary valve in large right ventricular outflow tracts: a transcatheter approach using an intravascular infundibulum reducer. Pediatr Res 2007; 62(4):428-433.

235. Mollet A, Stos B, Bonnet D, Sidi D, Boudjemline Y. Development of a device for transcatheter pulmonary artery banding: evaluation in animals. Eur Heart J 2006; 27(24):3065-3072.

236. Otsuka K, Kakeshita T. Science and technology of shape-memory alloys. New developments. Mrs Bulletin 2002; 27(2):91-100.

237. Otsuka K, Ren XB. Recent developments in the research of shape memory alloys. Intermetallics 1999; 7(5):511-528.

238. Wayman CM. Shape Memory and Related Phenomena. Progress in Materials Science 1992; 36:203-224.

239. Thierry B, Merhi Y, Bilodeau L, Trepanier C, Tabrizian M. Nitinol versus stainless steel stents: acute thrombogenicity study in an ex vivo porcine model. Biomaterials 2002; 23(14):2997-3005.

240. Duerig TW, Pelton AR, Stockel D. Superelastic Nitinol for Medical Devices. Medical Plastics Biomater 2, 30-43. 1997.

241. Stoeckel D, Pelton A, Duerig T. Self-expanding nitinol stents: material and design considerations. European Radiology 2004; 14(2):292-301.

242. Auricchio F, Taylor RL, Lubliner J. Shape-memory alloys: Macromodelling and numerical simulations of the superelastic behavior. Computer Methods in Applied Mechanics and Engineering 1997; 146(3-4):281-312.

243. Peyroux R, Chrysochoos A, Licht C, Lobel M. Thermomechanical couplings and pseudoelasticity of shape memory alloys. International Journal of Engineering Science 1998; 36(4):489-509.

244. Souza AC, Mamiya EN, Zouain N. Three-dimensional model for solids undergoing stress-induced phase transformations. European Journal of Mechanics A-Solids 1998; 17(5):789-806.

245. Qidwai MA, Lagoudas DC. Numerical implementation of a shape memory alloy thermomechanical constitutive model using return mapping algorithms. International Journal for Numerical Methods in Engineering 2000; 47(6):1123-1168.

246. Auricchio F, Sacco E. Thermo-mechanical modelling of a superelastic shape-memory wire under cyclic stretching-bending loadings. International Journal of Solids and Structures 2001; 38(34-35):6123-6145.

247. Govindjee S, Miehe C. A multi-variant martensitic phase transformation model: formulation and numerical implementation. Computer Methods in Applied Mechanics and Engineering 2001; 191(3-5):215-238.

248. Peng X, Yang Y, Huang S. A comprehensive description for shape memory alloys with a two-phase constitutive model. International Journal of Solids and Structures 2001; 38(38-39):6925-6940.

249. ABAQUS 6.4. User Subroutines Reference Manual. Analysis User's Manual. 2004.

250. Pelton AR, Gong X-Y, Duerig TW. Fatigue Testing of Diamond Shaped Specimens. SMST-2003: Proceedings of the International Conference on ShapeMemory and Superelastic Technologies Pacific Grove, California: 2003.

LIST OF PUBLICATIONS ARISING DURING THIS THESIS

Original Peer Reviewed Articles Directly Related to This Work

- Schievano S, Coats L, Migliavacca F, Norman W, Fenton M, Frigiola A, Deanfield J, Bonhoeffer P, Taylor AM. variations in right ventricular outflow tract morphology following repair of congenital heart disease - Implications for percutaneous pulmonary valve implantation. J Cardiovasc Magn Reson 2007;9(4): 687-695.
- Schievano S, Migliavacca F, Coats L, Khambadkone S, Carminati M, Wilson N, Deanfield J, Bonhoeffer P, Taylor A. Rapid prototyping three-dimensional model building of the right ventricular outflow tract and pulmonary trunk from magnetic resonance data – Clinical utility for percutaneous pulmonary valve implantation. Radiology 2007;242(2):490-497.
- Schievano S, Petrini L, Migliavacca F, Coats L, Nordmeyer J, Lurz P, Khambadkone S, Taylor AM, Dubini G, Bonhoeffer P. Finite element analysis of stent deployment: understanding stent fracture in percutaneous pulmonary valve implantation. J Int Cardiol 2007;20(6):546-554.
- Armillotta A, Bonhoeffer P, Dubini G, Ferragina S, Migliavacca F, Sala G, Schievano S. Use of rapid prototyping models in planning of percutaneous pulmonary valved stent implantation. Proc Inst Mech Eng [H] 2007;221(4):407-416.
- Nordmeyer J, Khambadkone S, Coats L, Schievano S, Lurz P, Parenzan G, Taylor AM, Lock JE, Bonhoeffer P. Risk stratification, systematic classification and anticipatory management strategies for stent fracture after percutaneous pulmonary valve implantation. Circulation 2007;115(11):1392-1397.

Original Peer Reviewed Articles Not Directly Related to This Work

- Boudjemline Y, Schievano S, Bonnet C, Coats L, Agnoletti G, Khambadkone S, Bonnet D, Deanfield J, Sidi D, Bonhoeffer P. Off-pump replacement of the pulmonary valve in large right ventricular outflow tracts: a hybrid approach. J Thorac Cardiovasc Surg 2005;129(4): 831-7.
- Coats L, Khambadkone S, Derrick G, Sridharan S, Schievano S, Mist B, Jones R, Deanfield J, Pellerin D, Bonhoeffer P, Taylor A. Physiological and clinical consequences of relief of right ventricular outflow tract obstruction late after repair of congenital heart defects. Circulation 2006;113(17):2037-2044.
- Lurz P, Coats L, Khambadkone S, Nordmeyer J, Boudjemline Y, Schievano S, Muthurangu V, Lee TY, Parenzan G, Derrick G, Cullen S, Walker F, Tsang V, Deanfield J, Taylor AM, Bonhoeffer P. Six-year experience with percutaneous pulmonary valve implantation - Impact of evolving technology and learning curve on clinical outcome. Circulation 2008, in press.
- Vismara R, Laganà K, Migliavacca F, Schievano S, Coats L, Taylor AM, Bonhoeffer P. In vitro tests to evaluate the efficiency of percutaneous pulmonary valved stent in different right ventricular outflow tract morphologies. Artificial Organs 2008, in press.
- Schievano S, Nicosia M, Cochran RP, Khambadkone S, Einstein DR, Kunzelman K, Bonhoeffer P. Percutaneous mitral valve dilatation: single balloon versus double balloon - A finite element study. Submitted to EHJ.